THÈSE

Pour l'obtention du titre de :

Doctorat de l'Université de Lorraine

École doctorale C2MP : Chimie- Mécanique- Matériaux-Physique
Mention mécanique des matériaux

Présentée par :

Sunija Sukumaran

Design and preparation of a micro-harvesting device made of hybrid SMA/Piezoelectric polymer composite.

Thèse soutenue publiquement le 30 août 2021 à Nancy devant le jury.

Composition du jury

Président :	Etienne Patoor	Professeur des Universités - Georgia Tech Lorraine
Rapporteurs:	Karine Lavernhe-Taillard	Maîtresse de conférences - HDR - Université Paris Saclay
	Christine Galez	Professeure des Universités - Université Savoie Mont Blanc
Examinateurs:	Emilie Planes	Maîtresse de conférences - Université Savoie Mont Blanc
	Frédéric Thiebaud	Maître de conférences - Université de Lorraine
	Samir Chatbouri	Attaché Temporaire de Recherches - Université de Lorraine
Invités:	Nandakumar Kalarikkal	Professeur des Universités - Mahatma Gandhi Université, India
	Laurent Badie	Ingénieur de recherche - Université de Lorraine
	Etienne Tisserand	Professeur des Universités - Université de Lorraine
Encadrants:	Tarak Ben Zineb	Professeur des Universités - Université de Lorraine
	Didier Rouxel	Professeur des Universités - Université de Lorraine

Mis en page avec la classe thesul.

Acknowledgment

This thesis is the result of the collaboration between the Laboratory for the study of Microstructures and Mechanics of Materials (LEM3) from the University of Lorraine (UL) and the Jean Lamour Institute (IJL) from the University of Lorraine (UL) funded by Lorraine University of Excellence (LUE). I would like to express my sincere gratitude to everyone who participated in this work, directly or indirectly, and to everyone who supported me during these years.

Firstly, I would like to say great thanks to my thesis supervisors, Tarak Ben Zineb and Didier Rouxel, for their guidance and unconditional support throughout my work. Thank you for giving me the opportunity to be a part of this research area. You were able to transmit your knowledge to me through many discussions, which helped me acquire knowledge in different domains. Also, your scientific support and motivation during this period are clearly the main keys to the outcome of this work. Thanks to Karine Lavernhe-Taillard and Christine Galez for carrying out the task of rapporteurs, as well as to Etienne Patoor, Emilie Planes, for showing interest in my work and reviewing it. Many thanks to Frédéric Thiebaud for helping me with the experimental tests. Also, thanks to Samir Chatbouri, who helped me to learn and set up the electronic parts. His friendly nature always creates a good atmosphere for work. My sincere thanks to Laurent Badie, who trained me inside the cleanroom and was always ready to help with the experiments. Obviously, I cannot ignore his valuable comments and motivation throughout this journey. Many thanks to Etienne Tisserand for his experimental support with the electronic parts. Also, thanks to Jean Sebastien Lecomte for the DSC measurements.

I would like to thank my teachers, Nandakumar Kalarikkal and Sabu Thomas, who opened the way for me to do research. Nandakumar Kalarikkal deserves special recognition for his unwavering support and motivation. I really want to express my gratitude to the entire LEM3 team at Polytech Nancy. A big thanks to Guven Muslum. The numerical simulation wouldn't be performed without his assistance. Also, the project students; Izabela Gesla, Mehmet Emir Yilmaz, and Huseyin Eren Urtekin, for their outstanding work on the micro-energy harvesting system. Also, thanks to IJL internship students R. Amrane and others for their good work on mechanical system development.

I owed a big thanks to colleagues and friends with whom I shared the office. Especially, Nicolas Ulff, we always had a fruitful discussion and have had a good memory. Thanks to my friends: Kaushalya, Nitheesha Shaji, Snehamol Mathew, Asfina Rahim and Mohand Achour for always being there for me, even when things were tough. Last but not the least, I would like to express my sincere gratitude to my parents. Words are not enough to express my thanks to them. My father, Sukumaran, and my mother, Girija Sukumaran, for their continued effort and support, not only with my thesis but also in my life. Also, thanks to my wonderful sister Sujitha Sukumaran for being such a supportive person in my life.

Finally, I would like to thank all the people who helped me.

Thank you!

To my parents.

Table of Contents

List of figures viii
List of tables xiii
List of abbreviations xiv
General introduction 1
1. State of the art 5
1.1 Energy harvesting 5
1.2 Feasibility of energy harvesting via SMA/Piezoelectric polymer composite 6
1.3 State of the art of SMA/piezoelectric composite system 8
1.4 Introduction to piezoelectricity and principle 14
1.5 Piezoelectric materials and application in energy harvesting 16
1.6 Introduction to PVDF and its copolymer for piezoelectric energy harvesting 18
1.6.1 Stretching 21
1.6.2 Poling 21
1.6.3 PVDF for mechanical energy harvesting 24
1.7. Modeling of the ferroelectric and ferroelastic behaviors of piezoelectric materials 28
1.8 Introduction to shape memory alloys 31
1.8.1 Shape memory effect 32
1.8.2 Superelasticity 34
1.8.3 Modeling of the SMA thermomechanical behavior 36
1.9 Conclusion 41
2. Experimental characterization of the composite for energy harvesting 43
2.1 Processing of SMA/P(VDF-TrFE) composite 44
2.1.1 Materials and methods 45
2.1.2 Synthesis of P(VDF-TrFE) solution 45
2.1.3 Spin coating technique 45
2.1.4 SMA/(PVDF-TrFE) composite 47
2.1.5 Multi-layered SMA/(PVDF-TrFE) composite 48
2.1.6 Polarisation hysteresis 49
2.2. SMA/P(VDF-TrFE) composite with interface layer 51

2.2.1 PEN/P(VDF-TrFE) device 51
2.2.2 Polarisation hysteresis 52
2.2.3 SMA/Epoxy/PEN/P(VDF-TrFE) composite 53
2.2.5 Summary 54
2.3 Experimental characterization for energy harvesting 55
2.3.1 Mechanical energy harvesting performance 55
2.3.2 Output voltage 56
2.3.3 Output power 58
2.3.4 SMA/ P(VDF-TrFE) composite 59
2.3.7 Output voltage 61
2.4 Thermomechanical loading test in tensile machine for SMA/P(VDF-TrFE) device 62
2.4.1 Stress-strain -temperature 64
2.4.2 Voltage-strain-temperature 66
2.4.3 Summary 68
2.5 Micro energy harvester characterisation system 70
2.5.1 Support system and frame 72
2.5.2 Cooling and heating source 73
2.5.3 Optical lens system 73
2.5.4 Summary 74
2.6 Conclusion 75
3. Numerical analysis of the electro-thermo-mechanical response of the SMA/Piezo composite 78
3.1 Modeling of SMA behavior 79
3.2 Modeling of piezoelectric behavior 80
3.2.1 Linear model 80
3.3 Finite element simulation of the SMA/(PVDF-TrFE) composite 80
3.3.1 SMA thermomechanical properties 81
3.3.2 Piezoelectric properties 82
3.4 Finite element (FE) model of the device 82
3.4.1 Tensile and bending tests 83
3.5 SMA behaviour simulation with Chemisky-Duval's model 84
3.5.1 Superelastic effect 84
3.5.2 One-way shape memory effect 84

3.5.3 Assisted Two-way shape memory effect 85
3.6 Simulation of the two-layer composite material 86
3.6.1 Mesh and element type 86
3.7 Simulation results and discussion 87
3.7.1 One-way shape memory effect 88
3.7.2 Two-way shape memory effect 91
3.7.3. SMA/Piezoelectric polymer composite 92
3.8 Comparison between simulation and experimental analysis of the composite 94
3.9 Prototype geometry 96
3.10 Conclusion 97
4. Performance evaluation for piezoelectric energy recovery 100
4.1. Shaker test bench for piezoelectric energy recovery 101
4.1.1 Components of the shaker test bench 102
4.1.2 Study with the shaker test bench 105
4.2 Mechanical system for bending test 106
4.2.1 Principle of operation 106
4.2.2 Study with the mechanical bending system 107
4.3 Electronic circuits for piezoelectric energy harvesting: state of the art 109
4.3.1 Electrical modelling of the piezoelectric generator 110
4.3.2 Piezoelectric energy recovery standard circuits 112
4.3.3 Optimal recovery techniques 115
4.4 Practical application to our system 119
4.4.1 Equivalent electrical circuit of a piezoelectric generator 119
4.4.2 Choice of energy harvesting electronics 120
4.4.3 Simulation of the system with the LTC 3108 board 121
4.4.4 Simulation of the system with the LTC 3588-1 board 124
4.5 Conclusion 126
5. General conclusions and perspective 129
Appendices 135
Bibliography 143
Résumé français 165

List of figures

1.1 Schematic representation of the SMA-piezoelectric thin layer composite working principle. 7

1.2 The relationship showing the coupled effects of the combination of SMAs and the piezoelectric materials in a multifunctional device..... 8

1.3 (a) The model of SMA/PZT hybrid composite proposed by Namli and Taya (b) experimental study showing the obtained voltage and temperature responses. 10

1.4 Photographic images of the NiTiCu-MFC composite thermal energy harvester (b) NiTiCu ribbon/PZT laminated composites. (c) schematic view (left) and the photo (right) of the experimental harvester demonstrator. 11

1.5 (a). Schematic diagram showing the piezoelectric bimorph in a cantilever beam configuration and SMA wire attached to the beam at three different positions and a laser (b) schematic of a hybrid SMA/PZT harvester(c) SEM image of the cross-section of the NiTi/PZT hybrid composite (d) PZT thin film surface. 12

1.6 (a) Schematic representation of the composite (b) Photographic image of the SMA/PVDF composite, the reference PVDF sample alone(left) and the PVDF (110mm thick) + two NiTiCu (40 mm thick) ribbons on each side for patterned Cu tape (c) The open circuit output voltage of the PVDF+2NiTiCu composite and blank PVDF samples versus temperature, the voltage is measured with an electrostatic contactless voltmeter. (d) Thermal energy harvesting from the NiTi/ZnO composite. 12

1.7 Schematic drawing of the (a) direct (b) converse (c) shear piezoelectric effect..... 14

1.8 (a) Tensor directions used to describe the orientation of a crystal (b) illustration of 33 and 31 modes. 15

1.9 Various classes of piezoelectric materials. 17

1.10 Chemical Structure of PVDF 19

1.11 Chemical structural representation of the three main phases of PVDF 20

1.12 Poling of piezoelectric material (a) The material originally occurs a random orientation of molecular dipoles (b) by the application of an electric field causes the dipoles to align in the same direction of the field. (c) The remnant polarization and strain are retained after the complete removal of the electric field (d) Polarisation electric field (P-E) hysteresis loop of piezoelectric material. 22

1.13 Piezoelectric polymer poling systems: (a) direct contact method and (b) corona poling. 23
1.14 (a) Photograph of the rGO-Ag/PVDF composite film encapsulated in PDMS layer with Al electrodes on both sides (b) The voltage harvested, and power generated from rGO–Ag/PVDF nanocomposite across various resistances c) schematic representation and the digital image of the ZnO NRs/PVDF (d) voltage output and the schematic illustration of the charge generation in ZnO NPs /PVDF and ZnO NRs/PVDF composite respectively (e) Schematic representation of hot-pressing method for building sandwich-structured P-FTNx-P Composite (f) the structure and installation of cantilever-type PNG (g) The power generation of the PVDF and P-FTN15%-P FPEHs with different external load resistance..... 28
1.15 Ferroelectric and ferroelastic behaviors issued from a phenomenological approach.....30
1.16 Schematic diagram of shape memory effect (SME).....32
1.17 Schematic diagram of the phase transformation and temperature hysteresis of NiTi SMA.....33
1.18 (a) Schematic representation of the microscopic and macroscopic phase of one-way shape memory effect. (b) Stress-strain-temperature graph for NiTi SMA showing shape memory effect.....34
1.19 (a) Pseudoelastic loading path for SMA (b) Pseuodoelastic stress-strain diagram for NiTi SMA.....34
1.20 Comparison between experimental characterization and modeling results for tension and combined bending-torsion loading.....38
1.21 Comparison between the predicted SMA behavior and obtained experimental results (a) tension loading-unloading (b) tension-shear complex loading.....40
2.1 (a). Schematic diagram of the P(VDF-TrFE) solution preparation (b) Photographic image of the different steps in solution preparation setup. 46
2.2 SMA/Polymer composite film preparation (a) different steps of spin coating to form the polymer layer on SMA (b) Photographic image of the spin coater and the annealing steps for SMA/P(VDF-TrFE) composite. 47
2.3 Electrode deposition process (a) Image of the E-beam evaporator (b) The whole view of the cleanroom for material deposition (c) schematic representation of the electrode deposition and the image of the SMA/P(VDF-TrFE)/Cr/Al composite. 48
2.4 SMA/P(VDF-TrFE) multilayer composite structure and photographic image of the device top view and bottom layer view on the right. 49

2.5 Precision system applying A high voltage through the HVI with P(VDF-TrFE) samples connected. 50
2.6 Polarisation hysteresis loop of SMA/P(VDF-TrFE) composite (a) bottom layer (b) top layer. 50
2.7 Schematic diagram of the fabrication process of the flexible piezoelectric energy harvesters. Different steps of the processing of the PEN/P(VDF-TrFE) film and the photographic image of the original composite. 52
2.8 Polarization hysteresis loop of P(VDF-TrFE) on PEN..... 52
2.9 SMA/PEN/P(VDF-TrFE) composite multilayer structure with epoxy as an interface bonding layer and photographic image of the final device. 53
2.10 DSC curve for Ni55Ti 45 SMA showing transformation temperatures. 54
2.11 The experimental setup and the schematic representation for the piezoelectric energy harvesting. 56
2.12 Output voltage generated from the PEN/P(VDF-TrFE) composite subjected to different deformation (a) finger tapping (b) bending. 57
2.13 Schematically showing the working mechanism of the PEN/P(VDF-TrFE) composite..... 57
2.14 Power and current output of the PEN/P(VDF-TrFE) film. 58
2.15 Power output of the PEN/P(VDF-TrFE) film across various load resistors. 59
2.16 Output voltage generated from the SMA/PEN/P(VDF-TrFE) composite under finger tapping. 60
2.17 Oil bath heating system along with the sample and oscilloscope. 61
2.18 Output voltage generated from the SMA/P(VDF-TrFE) composite during thermal loading. 62
2.19 The tensile machine with its thermal chamber (b) Schematic representation of the dimension of the SMA/P(VDF-TrFE) composite. 63
2.20 The graphical representation of the evolution of the electric voltage under thermomechanical loading. 63
2.21 (a) Schematic diagrams of the tensile test (b) Tensile machine with SMA/P(VDF-TrFE) composite clamped inside the chamber. 64
2.22 (a) Stress-time curve with σ_{max}= 80 MPa (b) Stress-strain curve for the one-way shape memory effect. 65

2.23 3D representation of the stress-strain-temperature curve for one cycle of loading and heating of the SMA/P(VDF-TrFE) composite. 65
2.24 Output voltage generated by the SMA/P(VDF-TrFE) composite during the one-way shape memory effect. 67
2.25 3D representation of the Voltage-strain-temperature curve for one cycle of loading and heating of the SMA/P(VDF-TrFE) composite. 68
2.26 Schematic representation of the micro harvester experimental design model. 70
2.27 Schematic representations of the model of the micro harvester system in Catia software. 71
2.28 Designed model of the sample support on the left and the original photographic image of the support on the right. 72
2.29 Designed model showing the position of the sample support in the mainframe on the left and the original photographic image of the support placed in the frame on the right. 73
2.30 Schema of the optical lens system 74
3.1 SMA/P(VDF-TrFE) composite dimension 81
3.2 Boundary conditions for the tensile test. 83
3.3 Boundary conditions used for the bending test. 84
3.4 Loading during the one-way shape memory effect simulation 85
3.5 Mechanical loading during the one-way shape memory effect simulation. 85
3.6 Schematic representation of the simulation of the two-way shape memory effect. 86
3.7 Mesh of the model in the left and the number of elements in the thickness, two for the piezoelectric layer and four in the SMA layer. 87
3.8 Superelastic effect of SMA 88
3.9 Strain -Temperature graph for the tensile test one-way shape memory effect 89
3.10 Temperature -strain-stress 3D graph for one-way shape memory effect 89
3.11 Deflection of the SMA sample after unloading process (b) The sample retains its original shape after heating. 90
3.12 Strain-Temperature graph for bending test one-way shape memory effect 90
3.13 3D graph of Temperature-strain-stress for bending test one-way shape memory effect. 91
3.14 (a) Strain- Temperature graph for tensile test of two-way shape memory effect (b) Strain-Temperature graph for bending test of two-way shape memory effect. 92

3.15 Electrical potential vs temperature graph for P(VDF-TrFE) layers with different thicknesses (3µm to 6µm) under tensile loading. 93
3.16 Electrical potential-temperature graph for PVDF layers with different thicknesses under bending test. 93
3.17 Electrical potential evolution function of piezoelectric layer thickness (a) tensile (b) bending……94
3.18 SMA/Piezo hybrid composite subjected to a heating-cooling loading under constant tension pre-loading, (b) finite element mesh for the SMA/piezo composite contains four elements for the SMA layer and two elements for piezoelectric layer along with the thickness……95
3.19 Experimental and modeling stress versus strain curve……95
3.20 Evolution of the voltage-strain-temperature in the numerical model……96
3.21 (a) Finite element model of the disc configuration for the composite material (b) electric potential evolution function of temperature……97
4.1 Experimental setup for the mechanical shaker system for piezoelectric energy recovery. 102
4.2 P(VDF-TrFE) Piezoelectric film. 103
4.3 Schematic diagram for the shaker. 103
4.4 (P(VDF-TrFE) film holder view (a) Front view (b) Side view. 104
4.5 Front and back view of the mechanical test bench made in SolidWorks. 106
4.6 Arduino board and stepper motor. 107
4.7 The experimental setup of the mechanical bending system. 107
4.8 The generated output voltage from the piezoelectric P(VDF-TrFE) film. 108
4.9 Folding and unfolding of the P(VDF - TrFE) film by the mechanical folding system during handling. 108
4.10 Output voltage from the P(VDF-TrFE) film 109
4.11(a) Mechanical model with localized constants 110
4.12(a) Simplified electrical model of a piezoelectric element. 111
4.13 (a) Simple rectifier 112
4.14(a) Standard circuit for piezo energy harvesting. 113
4.15 Standard interface circuit with DC voltage linear regulator. 114
4.16 Standard interface circuit with battery charger system. 114

4.17(a) Internal circuit diagram of LTC3588 115
4.18 LTC3108 Boost converter for low voltage piezoelectric energy harvesting. 115
4.19 (a) P-SSHI interface circuit. 116
4.20 Pseudo period of the LC0 circuit. 116
4.21 S-SSHI interface circuit 117
4.22(a) SECE interface circuit 118
4.23 Electrical powers collected according to the charging resistor 119
4.24 Equivalent schematic of a direct mode piezoelectric device. 120
4.25 Simulation setup of the LTC 3108 board with an AC input. 122
4.26 Temporal Evolution of the output voltage and output current 122
4.27 Simulation circuit with LTC3588 board 124
4.28 Output voltage and output current for Iin = 2.20 µm and Vin = 5V 126

List of Tables

Table 1.1. Comparative study of PZT and P(VDF-TrFE) polymer. 18
Table 1.2. Output performance of the most recent PVDF energy harvesting device. 25
Table 3.1. The parameters used for the numerical modelling. 81
Table 3.2. Thermomechanical properties of the $Ni_{55}Ti_{45}$ SMA 82
Table 3.3. Properties of P(VDF-TrFE) polymer. 82
Table 4.1 Calculation parameters of the displacement performed by the mechanical shaker104
Table 4.2 Frequency sweep [10,50] Hz 105
Table 4.3 Frequency sweep [40,80] Hz. 105
Table 4.4. The harvesting and optimal load value for standard piezoelectric energy recovery circuit. 113
Table 4.5. The harvesting and optimal load value in P-SSHI method. 117
Table 4.6. The harvesting and optimal load value in S-SSHI method 117
Table 4.7. Evaluation of the LTC3108 board with different intensities. 123
Table 4.8. Parametric study of the LTC 3588-1 board. 125

List of Abbreviations

SMA	Shape Memory Alloy
NiTi	Nickel Titanium
PVDF	Polyvinylidene fluoride
P(VDF-TrFE)	Poly (vinylidene fluoride-trifluoroethylene)
PZT	Lead Zirconate titanate
MEMS	Microelectromechanical system
IoT	Internet of Things
PEN	Polyethylene naphthalate
D	Electric displacement
σ	Mechanical stress
Ɛ	Mechanical strain
P_s	Saturation polarization
P_r	Remnant Polarization
A_s	Austenite start temperature
A_f	Austenite finish temperature
M_s	Martensite start temperature
M_f	Martensite start temperature
Cr	Chromium
Al	Aluminium
V	Voltage
Q	Charge
I	Current
P	Power

General introduction

With the recent progress in material science, engineering, and micro/nanotechnologies new classes of materials are emerging with improved activities, new functions, and applications. Multifunctional, smart, or intelligent materials are particularly suited for many applications such as sensors, actuators, solar cells, microelectronic devices, energy harvesting devices[1,2]. In this regard, functional or "smart" materials like piezoelectric[3], pyroelectric[4], magnetoelectric and magnetostrictive materials[5], shape memory alloys (SMAs)[6,7] have immense research interest. The functional materials can vary physical or chemical properties like electrical conductivity, shape, Poisson's ratio, Young's modulus by responding to some stimuli such as light, temperature, chemical or by applying external mechanical, magnetic or electric loadings[8,9]. These properties make them suitable candidates for the design of advanced micro/nanoelectromechanical systems (MEMS/NEMS)[9,10]. MEMS systems find wide applications in the fields of energy harvesting devices due to the paradigm of the Internet of Things (IoT)[11,12].

Piezoelectric materials that can convert mechanical energy into electric energy are the most extensively used functional materials for small-scale energy harvesting[13,14]. Though other kinds of materials like SMAs are also used in different applications, including energy harvesting[15,16]. SMAs are a unique class of alloys that can recover their geometry upon the application of an external stimulus. That means after deformation, such an alloy has the ability to regain its actual shape at the desired characteristic temperature[17,18]. In addition, it can sustain a huge reversible strain ranging from 5-10%[9,19]. These specific characteristics of SMAs are known as the shape memory effect and superelasticity (pseudoelasticity). Different alloy compositions for SMAs are used depending on the specific requirements and applications, such as magnetic (Ni-Mn-Ga)[20], nickel-titanium-based (NiTi, NiTiNb, NiTiCu), iron-based (Fe-Mn-Si)[21] and copper-based (Cu-Zn-Al, Cu-Al-Ni)[22,23]. Among them, NiTi based SMAs are extensively used in a wide variety of applications as they exhibit strong shape memory effect (SME), superelasticity, corrosion resistance, low energy consumption and biocompatible nature[17,24]. Furthermore, NiTi SMAs thin films can be prepared by using standard deposition techniques like magnetron sputtering or arc deposition. This has aided their widespread application in MEMS/NEMS in recent years[25,26]. In this regard, SMAs are attractive for research as smart (or intelligent) and functional materials[17,27].

In the 1980's, the concept of smart hybrid composites emerged and found research interest[28]. SMA composite materials are developed by combining the SMAs in the form of wires, ribbons, thin films, or particles, embedded into the matrix materials such as polymers, fiber reinforced polymers, metals, or ceramics[29–31]. The physical properties of the composite matrix can be improved, such as damping property, actuation, stiffness, changes in vibrational frequency and internal strain energy of the material[15,32,33]. Several comprehensive analytical and numerical

(finite element) studies were reported on the thermomechanical behavior of SMAs[34,35]. However, SMAs are not broadly explored for energy harvesting applications. Chen et al.1992 reported combined characteristics of both shape memory alloys and piezoelectric ceramic composite and they called it "SMARTIES"[36]. They have proposed improved actuation and sensing properties. In this context, smart materials with different properties such as piezoelectric, pyroelectric effects, and shape memory effects found an interesting composite for energy harvesting applications. That is due to their multiphysical coupling properties are of high interest for the conversion of mechanical, thermal, and electrical energy. Hence, combining the conversion effects of these smart materials opens different ways for electrical energy generation either directly or in two or multiple steps. Several numerical and experimental studies were carried out based on SMA/piezoelectric composites, most of the studies so far reported in the literature being based on the SMA/piezoceramics composite. However, the usage of ceramics for the fabrication of such composite devices is not an ideal choice. Because ceramics possess some drawbacks which include rigidity, high density, high-temperature processing needed for thin-film fabrication, higher cost for manufacturing, lesser design flexibility. All of these constraints slow their application to many device applications, particularly energy harvesting applications[37,38]. Last but not least, they can't endure large deformation due to their brittleness.

In this regard, the choice of the coupled piezoelectric material plays an important role as it needs to provide the design flexibility (bending, twisting, fold) and should also maintain the original electronic and structural properties. Hence, piezoelectric polymers draw more attention because they can satisfy most of the above-mentioned characteristics. Also, they exhibit good mechanical flexibility, biocompatibility, ease of processing and fabrication, and are more resistant to mechanical shock[39,40]. Several piezoelectric polymers are reported and studied in the literature, which include PVDF and its copolymers, cellulose and its derivatives, polyurethanes (PU), polyimides (PI), polylactic acid (PLA)[3,41,42]. PVDF and its copolymers are well established and the most expansively studied materials among all other polymers due to their high piezoelectric coefficient, higher elastic compliance, electromechanical coupling, structural flexibility, good chemical resistance, and biocompatibility. In 2016, Gusarov et al[43] were the first to make a composite using SMA ribbon and PVDF polymer. PVDF polymers are more suitable for coupling with SMA, withstand high strains and are more flexible compared to ceramic-based materials. Among the PVDF based copolymer families P(VDF-TrFE) shows a high piezoelectric coefficient and is widely used for its ferroelectric properties[44,45]. The addition of nanofillers can improve several properties of the polymer matrix, including mechanical flexibility, dielectric and piezoelectric properties[46,47]. Other properties, such as low density, lightweight, low refractive index, and low cost, make it a promising candidate for various energy systems[37,48].

This thesis aims to develop a hybrid micro energy harvesting device by coupling a novel layered composite with a dimension of a few centimetres. The objective is to harvest thermal (waste heat) energy by utilizing the multiple energy conversion pathways offered by the composite

with stacking composed of NiTi SMA and piezoelectric P(VDF-TrFE) polymer thin layers. The work is mainly dealing with the development of the SMA/piezoelectric polymer composite and the modelling of the composite to figure out the various coupling effects of these smart materials. Therefore, in this thesis, we present a novel composite combining two functional materials with thermomechanical and electromechanical couplings of the SMA and piezoelectric polymer layers respectively. The series of steps that we are dealing with throughout the thesis contains the processing of the composite, the piezoelectric and electro-thermo-mechanical characterization. The second part deals with the modelling of the SMA and piezoelectric layer behavior properties, and of the composite effective behavior, and finally the electronic circuits for piezoelectric energy recovery.

The preparation and deposition of the P(VDF-TrFE) polymer layer on the NiTi SMA were carried out using the spin coating technique. Homogenous thin films of several micrometre thicknesses were deposited on SMA using the interface layer. The electrode layers of thickness in the nanometres range were deposited using an E-beam evaporator. The P(VDF-TrFE) layer was subjected to a high voltage polarisation (100 V/µm) using the contact method in order to achieve a significant piezoelectric coefficient. The piezoelectric energy harvesting performance of the P(VDF-TrFE) polymer thin film was measured by normal finger tapping and bending tests. Correspondingly, the thermal energy harvesting of the SMA/P(VDF-TrFE) composite was characterized by oil bath heating. The electro-thermo-mechanical behaviour of the composite was characterised by a tensile test machine having a heat chamber. Furthermore, a particular electro-thermo-mechanical characterisation system was designed to measure the electric response from the composite during the periodic thermal loading. The simultaneous heating and cooling of the composite can be done through laser beam heating and liquid nitrogen flux. The numerical simulation was performed using the finite element method to predict the global response of the composite by connecting the two steps of modelling. The first step involved the thermomechanical and electromechanical non-linear behaviour of the SMA and the piezoelectric layer respectively. The second step of modelling allowed us to derive the effective non-linear and multiphysical behaviour of the hybrid composite. Hence, the numerical finite element tool allows one to predict and optimize the harvesting process of the hybrid composite by determining the adapted number of layers and their thicknesses, the shape of the neutral surface and the appropriate applied mechanical pre-loading. Also, we have addressed an electronic circuit for the piezoelectric energy recovery from the film. The power conversion efficiency of the whole system strongly depends on the electronic circuit. The key problem with such a kind of system is converting the electronic charge into electric power because there are a few charges generated by the piezoelectric thin layer. We have developed a mechanical shaker system to generate vibrations for the film at different frequencies and amplitudes. Finally, in order to harvest the energy, we have implemented an integrated converter step-up like LTC3588 to store the produced energy in a battery for future usage.

The first chapter deals with the general concept of energy harvesting and the state of the art of the SMA/Piezoelectric composite. Then we will present the working mechanism of the SMA/piezoelectric polymer layer composite adopted for this thesis. In the following section, we will introduce the principle of piezoelectricity and different piezoelectric materials for energy harvesting. The PVDF and its copolymers will then be presented, as well as their application in mechanical energy harvesting. In addition, we briefly give the state of the art of modelling the behaviour of piezoelectric materials. Finally, in the first chapter, we introduce the shape memory alloy, its main properties and the SMA applications. Correspondingly, the modelling of the SMA's thermomechanical behaviour.

Chapter 2 will deal with the processing of the SMA/P(VDF-TrFE) composite and multi-layered manufacturing. Then, we will present the different mechanical, thermal and electro-thermo-mechanical characterization studies of the composite. Also, in this chapter, we will introduce a new characterization setup for the composite. The modelling of the composite, SMA and piezoelectric material is important to understand the different coupling behaviors of the composite and each layer. Therefore, these aspects will be presented in chapter 3. Chapter 4 will address the problem of piezoelectric energy recovery from an electronic point of view. Following that, we will present the selected solutions in terms of energy recovery boards with their conditioning circuits.

Chapter 1

State of the art

1.1 Energy harvesting 5
1.2 Feasibility of energy harvesting via SMA/Piezoelectric polymer composite 6
1.3 State of the art of SMA/piezoelectric composite system 8
1.4 Introduction to piezoelectricity and principle 14
1.5 Piezoelectric materials and application in energy harvesting 16
1.6 Introduction to PVDF and its copolymer for piezoelectric energy harvesting 18
1.6.1 Stretching 21
1.6.2 Poling 21
1.6.3 PVDF for mechanical energy harvesting 24
1.7. Modeling of the ferroelectric and ferroelastic behaviors of piezoelectric materials 28
1.8 Introduction to shape memory alloys 31
1.8.1 Shape memory effect 32
1.8.2 Superelasticity 34
1.8.3 Modeling of the SMA thermomechanical behavior 36
1.9 Conclusion 41

1.1 Energy harvesting

Nowadays, microelectronics and wireless technologies are extensively advanced in various fields. They are progressively embarked on board of the mobile, portable and wearable electronic systems[41,49,50]. Furthermore, the paradigm of the Internet of Things (IoT) is the most widely studied research area and has found increasing applications in many fields[51,52], in which the smart and simple devices are used with sensing and wireless communication abilities[53,54], whereas, their pervasive use in various applications raises the challenge of power supply. For example, sensors are arrayed in remote areas or health care devices are placed inside the human body. Hence, the recharging or replacement of batteries causes many difficulties[3,55]. Nevertheless, with the advancement in semiconductor and low-power integrated circuit technologies, many electronic devices are used as widespread. That includes smart electronic devices such as mobile phones and various kinds of sensors are prevalent everywhere in our daily lives. However, the power supply for these devices mostly depends on battery power for a long time[56,57]. In this regard, alternative power sources are required for the independent, maintenance-free, and continuous operation of such low-power smart electronics. Therefore,

the energy harvesting technique is being given more attention to solve issues related to batteries and provide a sustainable life for self-powered devices[58].

Persistent advancements in semiconductor manufacturing technologies have resulted in remarkable technological advancements in the field of small electronic devices, which include portable electronics, sensors, and transmitters. The size range was also reduced by a few magnitudes, hence the functionality and energy efficiency have been significantly improved[59]. Additionally, many electronic devices depend on the lifetime of battery power, and in many cases, it is very difficult to replace the batteries at the end of their lifespan, or it's unpractical in many applications like sensors arrayed in remote areas or inside the human body[60,61]. Accordingly, issues related to batteries, such as restricted life expectancy, substantial size, ecological pollutions, and high maintenance costs lead to the search for an alternative solution. In this aspect, harvesting energy from the ambient environment to power electronic devices draws more and more attention[62,63].

Energy harvesting, or energy scavenging, is the method of collecting energy from wasted energy sources such as heat, vibrations, and mechanical deformations, and converting it into useful electrical energy[64]. Several studies have focused on energy harvesters that may be ideal candidates for use in microelectromechanical systems (MEMS), smart structures, wireless sensors, biomedical implants, wearable electronics, or bendable devices[65–68], and are capable of utilizing various energy sources such as solar, wind, thermal energy, or mechanical vibrations[69]. In the case of low power electronic devices, the power generally lies in the µW or mW range.

This thesis is dedicated to the fabrication of a hybrid composite device for energy harvesting, consisting of a piezoelectric P(VDF-TrFE) polymer coupled with a NiTi shape memory alloy. The main goal is to fabricate a thin flexible multi-layered harvester that combines both the piezoelectric effect and the shape memory effect, thereby offering an enhanced output performance for energy generation.

1.2 Feasibility of energy harvesting via SMA/Piezoelectric polymer composite

This study proposes to develop a hybrid composite system for efficient energy harvesting using two different smart materials. There are a lot of studies focusing on harvesting energy from the ambient environment to power small-scale electronic devices autonomously. Hence, through this work, we are introducing a new method to show the feasibility of combining two smart materials for energy harvesting application. The principle of the composite of this work is based on the double energy conversion mechanism. We have fabricated a device using classical shape memory alloys (SMAs) of NiTi and a P(VDF-TrFE) piezoelectric polymer layer, two smart materials with multiphysical coupling properties attracting great attention because of their conversion capacity.

SMA can deliver mechanical energy under thermal loading. Piezoelectric materials generate an electric response when subjected to mechanical loading. Therefore, by the introduction of the concept of double energy conversion from thermal to mechanical to electrical the best suitable materials are shape memory alloys (SMAs) and piezoelectric polymers. We are focusing to develop a composite based on the coupling of these two smart materials to show the two-step energy conversion simultaneously. The thermal to mechanical energy conversion is induced by the reversible martensitic phase transformation occurring in SMAs. The mechanical to electrical energy conversion is induced by the reversible electrical polarisation variation in the piezoelectric polymer.

During heating induced by waste heat, due to the reverse martensite phase transformation SMA exhibits a large thermally induced strain[70], which in turn is transmitted to the piezoelectric layer and which produces an electrical response. Consequently, the thermally induced strain is effectively converted into useful electric energy. The working mechanism of the composite device is illustrated in Figure 1.1.

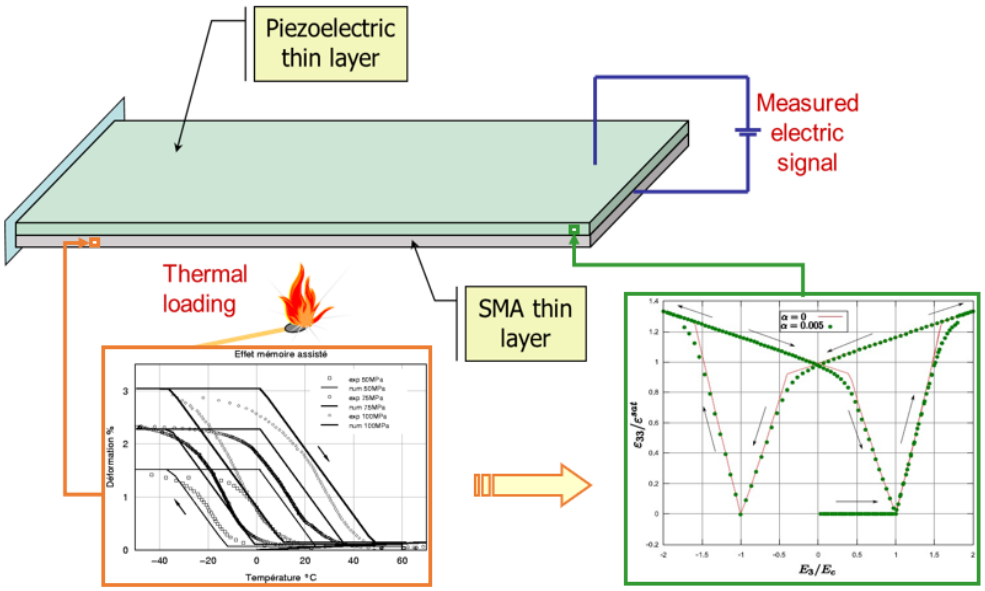

Figure 1.1 Schematic representation of the SMA-piezoelectric thin layer composite working principle.

In the following sections, we will introduce the state of the art of SMA/piezoelectric composites and the principle of piezoelectricity. After introducing different piezoelectric materials for energy harvesting, we selected P(VDF-TrFE) as the piezoelectric polymer layer for coupling with SMA. In addition, we will present the modelling behavior of piezoelectric materials. Then, the final section of the first chapter deals with SMA and its main properties, and with the modelling of the SMA thermomechanical behavior which is an important part of the thesis.

1.3 State of the art of SMA/piezoelectric composite system

The combined effect of smart materials is a promising approach for improved functionalities. A hybrid system composed of shape memory alloy (SMA) and piezoelectric materials provides significant enhancement of the characteristics of the composite system. For example, Gusarov et al.[43] demonstrated the hybrid PVDF/SMA laminated composite with an increased output energy of 200%. Also, the composite showed a 75% increase in output voltage compared to the pure pyroelectric output of PVDF. Typically, SMA possesses two phases called austenite and martensite. It has thermomechanical characteristics and the phase transformation occurs either by stress or temperature[9]. Piezoelectric materials generate an electric response when subjected to mechanical stress. Moreover, many of them can convert the temperature variation into electrical energy via the pyroelectric effect[13]. The coupling of different properties of the SMA and piezoelectric materials are presented in Figure 1.2.

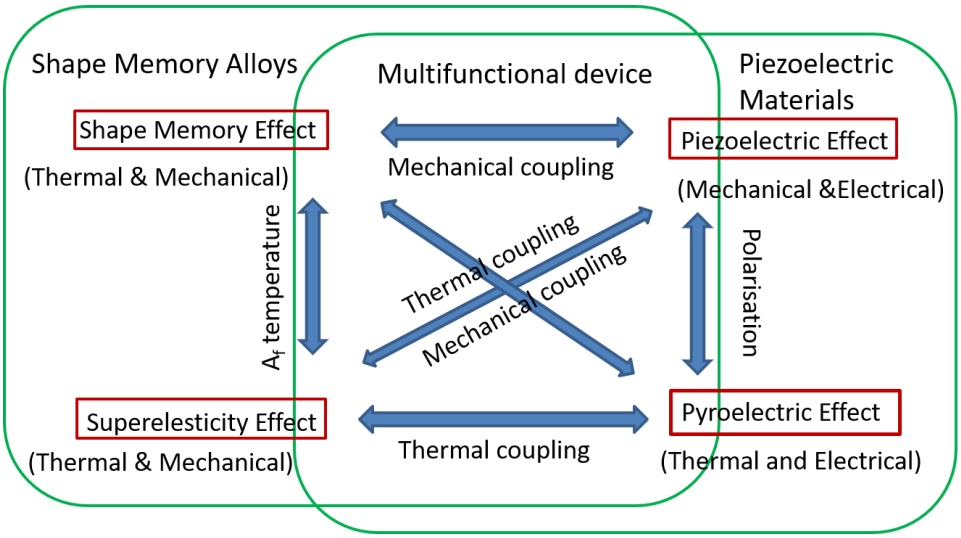

Figure 1.2 The relationship showing the coupled effects of the combination of SMAs and the piezoelectric materials in a multifunctional device.

Therefore, the hybrid device functions by coupling each of the effects in a synergetic way. SMA thermomechanical behaviour depends on certain characteristic temperatures and mechanical loading to attain the shape memory effect and superelasticity whereas the piezoelectric materials show a change in polarization by the action of mechanical stress and electric field or temperature corresponding to piezoelectric and pyroelectric effects, respectively.

As an example, the SMA with the shape memory effect is subjected to mechanical deformation and applying the thermal loading between a temperature above the transformation temperature A_f (austenite-martensite transformation finish temperature) and another one below M_f (martensite-austenite transformation finish temperature) can attain the phase transformation from austenite to martensite and vice versa. The heating induces the pyroelectric effect and the mechanical deformation results in the piezoelectric effect. Hence, the electric charge is created on the surface of the piezoelectric material. Taking into account

all these factors and the coupling effects, the design and manufacturing of such a hybrid composite system is found more interesting to study further.

Chen et al[36] 1992 was first reported the combined characteristics of SMA and piezoelectric ceramic composite and they called it “SMARTIES”. Combining SMAs with other structural or functional materials allows to design hybrid composites with specific properties or functions as strengthening, active modal modification, high damping, energy harvesting[71–73]. For example, Pyroelectric polymers and ceramics have been investigated for thermal to electric energy conversion [74,75]. However, their coupling capacity is very low with an inadequate conversion energy ratio. In this context, the addition of an SMA exhibiting thermomechanical coupling significantly increase the conversion capacity. The idea of combining SMA and Piezoelectric layers in hybrid composites considered for energy harvesting was initially proposed by Lagoudas and Bo [77]. The proposed simplified analytical model predicts the response of a hybrid composite with SMA, and piezoelectric layers subjected to a cylindrical bending. Garcia and Lobontiu[78] proposed an analytical model to evaluate the levels of actuation and sensing of multimorphs formed by sandwiching several layers of PZT and SMA materials. They showed the composite structure with a hybrid PZT-SMA trimorph can simultaneously act as a sensory actuator microdevice that can be used in small-scale MEMS applications. Shen, Han, Lee, Namli and Taya [79–82] extended such a development to the case of thermal loading in order to show that it is possible to deliver an electric voltage from an SMA/Piezo composite when subjected to thermal loading. Namli and Taya[81] designed both experimentally and analytically a thermal energy harvester composed of hybrid SMA-piezoelectric material. The PZT layer and SMA fiber were clamped inside a rigid frame subjected to a heating-cooling cycle under constant compression stress (Figure 1.3(a)). The study contains simplified analytical modeling of the shape memory effect of the SMA layer and of the linear piezoelectric behavior of the piezoelectric layer. It contains also the results of the experimental study. Figure 1.3 (b) shows the obtained electric signal function of the applied thermal loading and of its frequency. The authors reported that an electrical signal is obtained starting from a thermal loading with a frequency of 0.05 or 0.1 Hz and with temperature variation between -30°C and 110°C. The experimental results showed an output power of 8.6µW at 0.1 Hz. However, information such as the dimension of the harvester and the energy per cycle is missing in this study.

In 2011 Lebedev et al.[83] experimentally demonstrated thermal energy harvesting by using SMA/piezoelectric laminated composite. The laminated composite composed of 30 µm thick $Ti_{50}Ni_{25}Cu_{25}$ ribbons as an SMA layer with a first-order martensitic transformation and the Micro Fibre Composite (MFC) based on a PZT fibre layer as a piezoelectric material. Figure 1.4(a) represents the fabricated thermal energy harvester. The final prototype is made by gluing the SMA ribbon onto the MFC using cyanoacrylate. By the modulation of the heating current, the composites output voltage could be measured at different frequencies. The composite produced a maximum energy density of 30 mJ/cm^3 per phase transition.

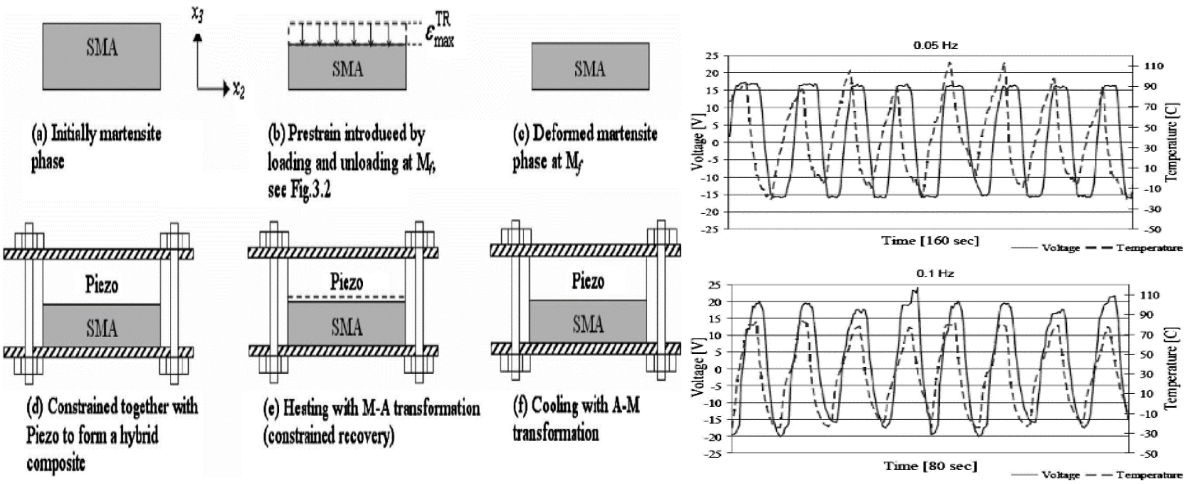

Figure 1.3 (a) The model of SMA/PZT hybrid composite proposed by Namli and Taya (b) experimental study showing the obtained voltage and temperature responses[81].

Zakharov et al.[84] demonstrated an original laminated NiTiCu/PZT composite for energy harvesting from small temperature variations. The SMA part is composed of 40 µm thick $Ti_{50}Ni_{25}Cu_{25}$ ribbons with a phase transformation temperature range of 50 to 80 °C. The commercial MFC is the piezoelectric layer, which consists of 100 µm diameter PZT fibers. The PZT fibers are aligned horizontally between the top and bottom electrodes and are covered with insulating Kapton films (Figure 1.4b). The harvester is made by assembling the SMA and piezoelectric layer in the form of a bilayer structure using cyanoacrylate glue. The same team also designed a mechanical structure that uses the thermally induced linear strain of the SMA to bend the PZT plate[84]. The "machine" with an active material of 0.2 cm^3 is able to harvest 90µJ and 60µJ during heating and cooling respectively by 35°C. The schematic representation of the machine harvester is shown in figure 1.4(c).

In 2013, the same group proposed an enhanced method for thermal energy harvesting by combining piezoelectric, pyroelectric and shape memory effect[85]. The generated voltage from the composite is measured while dipping the device in hot and cold water. The voltage measurements are done using an electrostatic non-contact voltmeter. The results exhibited a 50% of pyroelectric effect increase in a laminated structure. Avirovik et al.[86] developed a novel device design consisting of a piezoelectric bimorph and SMA wire heated remotely using a laser, which shows the dual functionality of both an energy harvester and an actuator (Figure 1.5a). The piezoelectric bimorph in a cantilever beam configuration is coupled with an SMA wire of diameter 100 µm. The SMA wire is attached to the beam at three different locations. In comparison with the reported energy harvesters, the energy conversion efficiency seems lower. However, the applicability as an actuator is proved.

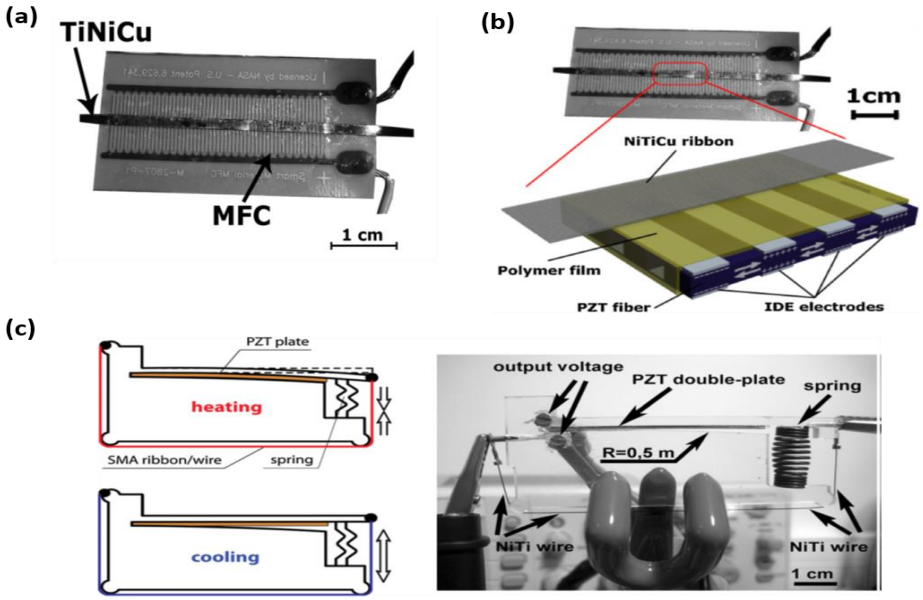

Figure 1.4 Photographic images of the NiTiCu-MFC composite thermal energy harvester of Lebedev et al. [83](b) NiTiCu ribbon/PZT laminated composites with Kapton covering and the SMA ribbons are glued onto the MFC (c) schematic view (left) and the photo (right) of the experimental harvester demonstrator, representing the SMA wire connected at its ends to the PZT plate[84].

Sato et al. [87] developed a novel hybrid composite with multifunctional properties using PZT thin film and NiTi SMA wire (150µm diameter). The PZT thin films are directly deposited on the surfaces of the NiTi SMA wires by employing the hydrothermal synthesis method. The piezoelectric thin films can withstand large deformation up to 5% because the thin films are formed by the layering of several crystals. Figure 1.5(c) and (d) show the SEM images of the cross-section of NiTi wire with uniform film formation along the NiTi surface and the surface of the PZT thin layers. Gosliga et al.[33] developed both finite element (FE) and analytical models to describe the dynamic behavior of the hybrid device combining the piezoelectric and shape memory effectS (Figure 1.5b). The FE model predicted electrical energy of 1.19 mJ for a single cycle of the output frequency of 494 Hz. Most of the studies reported so far deal with ceramic PZT based SMA piezoelectric composite.

Gusarov et al.[43] first made a composite by using 110µm thick PVDF and two 40µm thick NiTiCu ribbons and conductive epoxy as electrodes with patterned Cu tape for electrical contact (Figure 1.6 a &b). The Voltage output is measured with an electrostatic contactless voltmeter (Figure 1.6c). The authors showed that the post-stamp size (27.5 mm^3) harvester can achieve an energy density of 0.41 mJ/cm^3 with a temperature variation of 20 °C. Another related study is done by Radousky et al.[88] to harvest thermal and mechanical energy by combining ZnO nanowires and NiTi SMA. The thermoelectric device yielded an output voltage of ~0.65 V at room temperature bending and heating of the NiTi/ZnO device at 50 °C (Figure 1.6d).

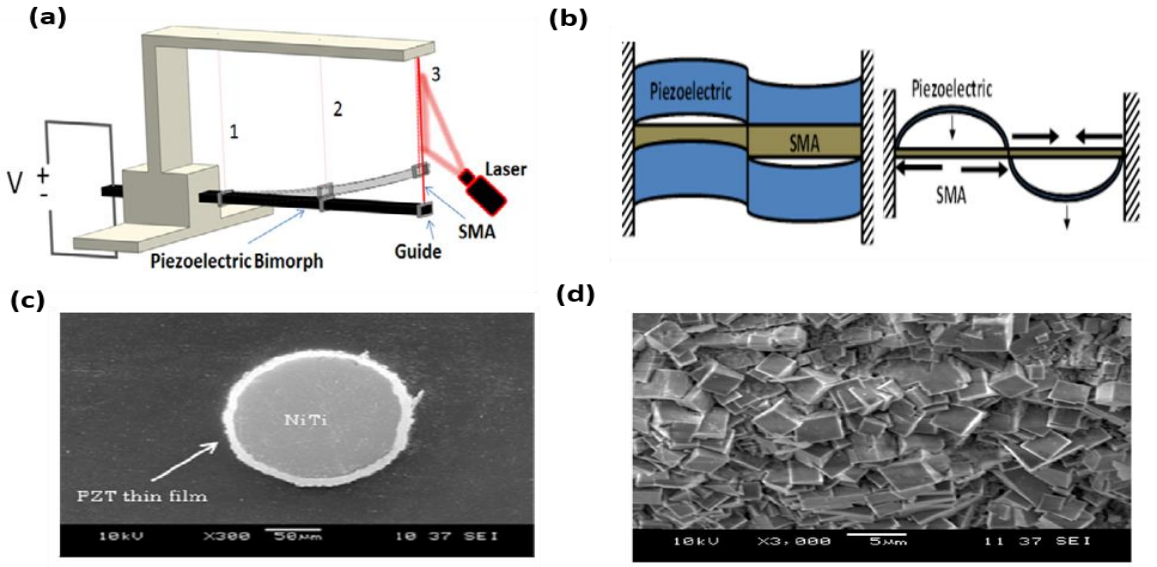

Figure 1.5 (a). Schematic diagram showing the piezoelectric bimorph in a cantilever beam configuration and SMA wire attached to the beam at three different positions and a laser[86] (b) schematic of a hybrid SMA/PZT harvester[33](c) SEM image of the cross-section of the NiTi/PZT hybrid composite (d) PZT thin film surface[87].

Most of the reported studies showed the experimental and simple numerical modelling of the SMA/PZT hybrid composite. Though, ceramic PZT may not be an optimal material choice for the fabrication of the flexible composite for energy harvesting applications. To the best of our knowledge, Gusarov et al. were the only authors to experimentally demonstrated the coupling of the SMA/PVDF composite. Nevertheless, these authors showed only the

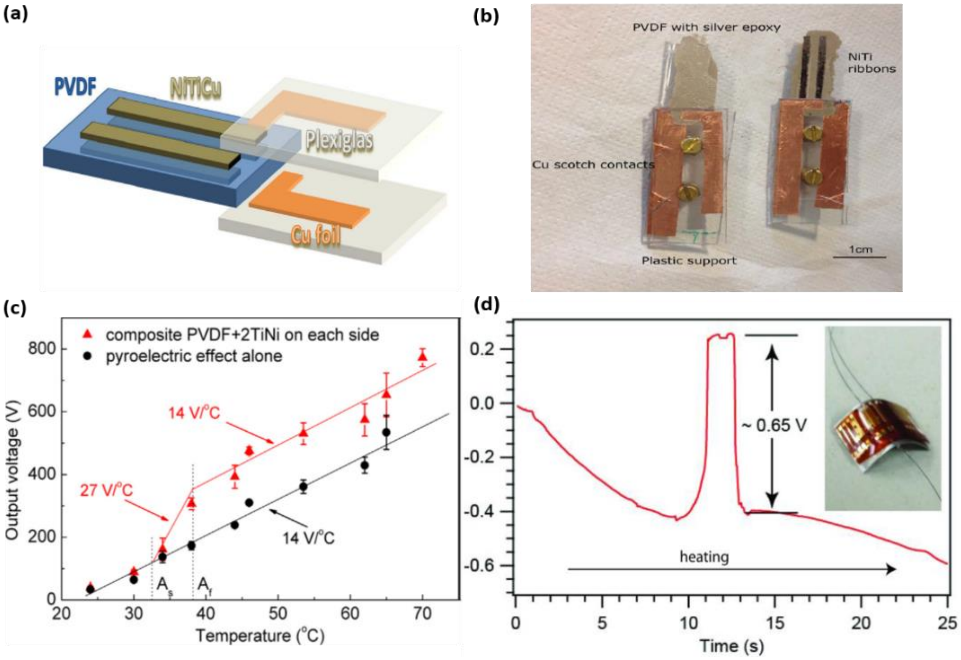

Figure 1.6 (a) Schematic representation of the composite (b) Photographic image of the SMA/PVDF composite, the reference PVDF sample alone(left) and the PVDF (110mm thick) + two NiTiCu (40 mm thick) ribbons on each side for patterned Cu tape[43] (c) The open circuit output voltage of the PVDF+2NiTiCu composite and blank PVDF samples versus temperature, the voltage is measured with an electrostatic contactless voltmeter. (d) Thermal energy harvesting from the NiTi/ZnO composite[88].

pyroelectric output voltage from the device, also the voltage obtained was measured with an electrostatic-contactless voltmeter. However, there are still possible improvements and studies that have to be done with this kind of hybrid composite. Henceforth, this work aims to go further in the development of the composite composed of SMA and piezoelectric polymer layers by developing a numerical and experimental optimization of the materials and the composite structure.

In order to fabricate a flexible composite device able to convert the thermal energy to electrical energy using the double energy conversion mechanism, the choice of the dimensions and characteristics of the materials play a major role. Piezoelectric polymers are more suitable for coupling with SMA due to their excellent flexible nature, high elastic compliance, and high energy conversion efficiency. Compared to ceramic materials, they can withstand much larger strain[48,89]. Therefore, they permit the full benefit of the output performance improvement from the SMA and its deformation according to the temperature. PVDF and its copolymers outperformed other well-known piezoelectric polymers in terms of piezoelectric and pyroelectric activity[90]. In comparison to PVDF polymer, the copolymer P (VDF-TrFE) has found more application in energy harvesting due to its numerous advantages, which include high crystallinity, higher remnant polarization, higher piezoelectric coefficient, and higher temperature stability[91,92]. In addition, P(VDF-TrFE) based polymers have found immense research application towards energy harvesting where thickness and flexibility are the key requirements.

In this regard, we use classical NiTi SMA and P(VDF-TrFE) as a piezoelectric polymer layer to fabricate the composite. Correspondingly, it is important to analyse the multiphysical coupling of both the material. Therefore, we deal with the numerical simulation of thermomechanical and electromechanical behaviour of SMA and piezoelectric materials respectively. Both the experimental and numerical analysis of the characterisation of the electro-thermo-mechanical behaviour of the composite is evaluated in this study. Therefore, before presenting the fabrication and characterisation of the SMA/P(VDF-TrFE) hybrid composite, we are going to briefly present the properties and application of both smart materials. In the following section, we introduce the principle and the main equations of these two "smart properties", the piezoelectric effect and the shape memory effect. Then, in the rest of this introductory chapter, we will introduce PVDF and its copolymer for piezoelectric energy harvesting and shape memory alloys and their properties. Furthermore, we will present the modelling of the thermomechanical and electromechanical behaviour of the SMA and piezoelectric material respectively.

1.4 Introduction to piezoelectricity and principle

The word 'piezoelectricity' is utilized to depict dielectric materials that create electrical charges across the boundaries when they are subjected to mechanical loading. The electric displacement is directly proportional to the applied mechanical stress. This effect is referred to as the direct piezoelectric effect[93]. If the stress is changed from tensile to compression an opposite electric charge (reverse direction) will develop (Figure 1.7a). When the material is placed in an electric field, it undergoes a mechanical strain or stress. This effect is named the indirect (or converse) piezoelectric effect[94]. In piezoelectric materials, the direction of deformation will change according to the electric field direction (Figure 1.7b). Shear piezoelectricity (Figure 1.7c) is linearly coupled with the shear mechanical stress or strain with the developed electric charges[95].

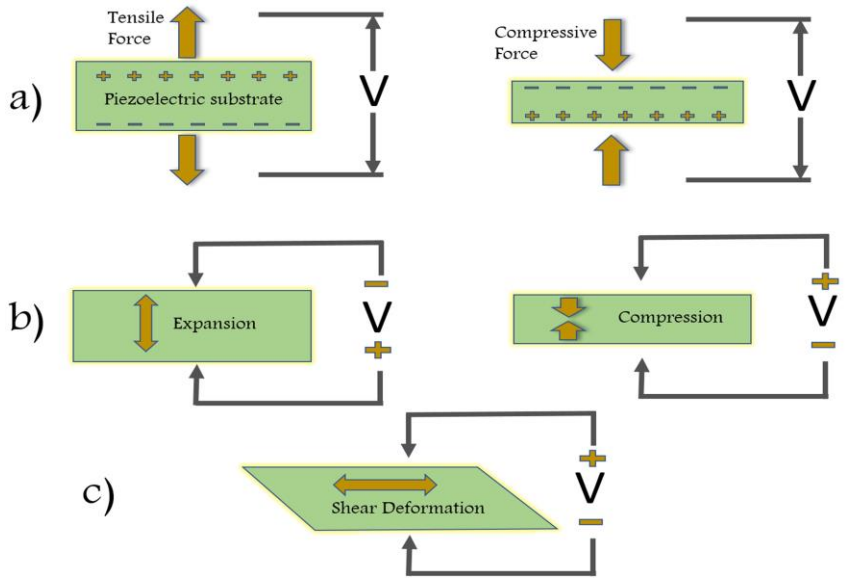

Figure 1.7 Schematic drawing of the (a) direct (b) converse (c) shear piezoelectric effect[37].

The constitutive equation for piezoelectric materials shows coupling between electrical and mechanical quantities, the direct piezoelectric effect is described by equation (1.1),

$$D_i = e_{ijk}\varepsilon_{jk} + k_{ij}E_j \qquad (1.1)$$

Equation (1.1) shows that an electric polarization and electric field is generated by mechanical stress. Where, $\underline{D}$ is the electric displacement vector, Ɛ is the strain tensor and $\vec{E}$ is the electric field. $\underline{\underline{e}}$ and $\underline{\underline{k}}$ are the third order piezoelectric coupling tensor and the second order permittivity tensor.

The converse or indirect piezoelectric effect can be described by the following equation 1.2,

$$\sigma_{ij} = C_{ijkl}\varepsilon_{kl} - e_{kij}E_k \qquad (1.2)$$

This shows that the piezoelectric material undergoes stress, thus a strain, under an applied electric field. Here, the mechanical stress σ is a second-order tensor and C is the fourth-order elastic tensor. These tensors are intrinsic to the piezoelectric material properties and in most cases, they present anisotropy with a different behavior between the polarization direction and the transverse plane.

Generally, we can define piezoelectricity as a cross-coupling between the elastic variables, stress (σ), strain (Ɛ), dielectric variables, electric charge density (D) and electric field (E). The piezoelectric materials are anisotropic in nature due to their crystallographic structure. According to the variation in the orientation of the crystals, the properties also vary. To designate well these orientations, three-axis and three rotations are used, as illustrated in figure 1.8(a). Axis 3 is placed along the thickness direction of the sample and axis 1 is placed in-plane along the longest side. The mechanical and electric parameters are tensors of different orders[96]. In order to differentiate the piezoelectric and elastic coefficient measured along different axes, they are represented in the form of a matrix. The piezoelectric coefficient is designated as d_{ij} (3× 6 matrix), where both the indices i and j refer respectively to the direction of the generated electrical charges and the direction of applied stress. The unit of the piezoelectric coefficient is expressed in Coulomb/Newton or meters/volt[97].

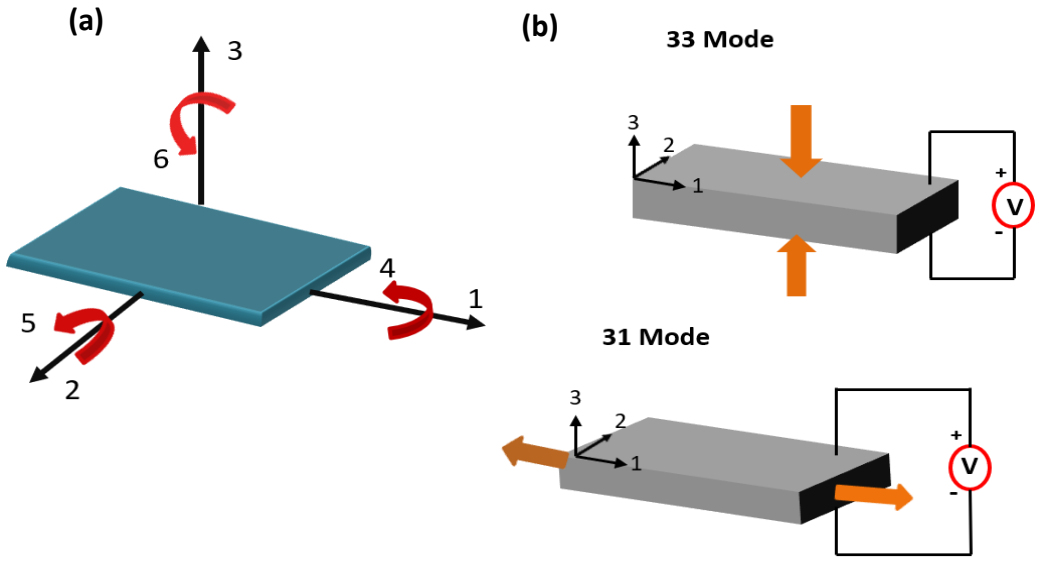

Figure 1.8 (a) Tensor directions used to describe the orientation of a crystal (b) illustration of 33 and 31 modes.

In piezoelectric materials, 31,33 and 32 piezoelectric coefficients modes are actively studied. In the 33 mode of operation, the electric polarization is generated in the same direction as the stress applied. On the other hand, in 31 mode, the electric polarization is developed in a

direction that is perpendicular to the direction of applied stress[98]. Figure 1.8.b graphically illustrates the two mode of operation.

Another important factor that plays a vital role in the electromechanical application is called the electromechanical coupling factor k, which determines the performance of the piezoelectric materials based on measuring the conversion efficiency of mechanical to electrical. It expresses the proportion between the input mechanical energy and the produced electrical energy from the piezoelectric material, in both directions[97,99].

$$k^2 = \frac{Produced\ electrical\ energy}{Input\ mechanical\ energy} \quad (1.3)$$

Or

$$k^2 = \frac{Produced\ mechanical\ energy}{Input\ elecric\ energy} \quad (1.4)$$

For most of the piezoelectric materials, the processing conditions and the crystal symmetry of the material will determine which elements of the dielectric constant, piezoelectric coefficient and elastic compliance tensor are non-zero. As for an example, in the case of an unstretched and polarised piezoelectric P(VDF-TrFE) copolymer coefficient matrices can be written as:

$$\begin{bmatrix}\sigma_{11}\\ \sigma_{22}\\ \sigma_{33}\\ \sigma_{12}\\ \sigma_{23}\\ \sigma_{13}\end{bmatrix} = \begin{bmatrix} C_{11} & C_{12} & C_{13} & 0 & 0 & 0\\ C_{21} & C_{22} & C_{23} & 0 & 0 & 0\\ C_{31} & C_{23} & C_{33} & 0 & 0 & 0\\ 0 & 0 & 0 & C_{44} & 0 & 0\\ 0 & 0 & 0 & 0 & C_{55} & 0\\ 0 & 0 & 0 & 0 & 0 & C_{66}\end{bmatrix}\begin{bmatrix}\varepsilon_{11}\\ \varepsilon_{22}\\ \varepsilon_{33}\\ 2\varepsilon_{12}\\ 2\varepsilon_{23}\\ 2\varepsilon_{13}\end{bmatrix} - \begin{bmatrix}0 & 0 & e_{13}\\ 0 & 0 & e_{32}\\ 0 & 0 & e_{33}\\ 0 & e_{42} & 0\\ e_{51} & 0 & 0\\ 0 & 0 & 0\end{bmatrix}\begin{bmatrix}E_1\\ E_2\\ E_3\end{bmatrix} \quad (1.5)$$

Nevertheless, variation in the value of different coefficients can appear in the above- described equation in PVDF and P(VDF-TrFE) copolymer, because of the fact that the electromechanical behavior and responses depend on several parameters such as polarization, stress/strain rates, temperature and hydrostatic pressure. Therefore, they can vary accordingly[98]. For example, let us consider the electromechanical response of P(VDF-TrFE) when it is subjected to the 33 mode of operation, that is through the thickness direction, therefore, both the electric field and stress are applied along the 33-direction.

1.5 Piezoelectric materials and application in energy harvesting

Mainly, the piezoelectric materials are classified into four different groups: single crystals, ceramics, polymers and polymer composites or nanocomposites[100]. Figure 1.9 shows the schematic representation of the main groups. The choice of a piezoelectric material will be based on several factors and applications. Such a choice is not only based on the piezoelectric

properties but there are other factors also associated with the material selection. That includes the design flexibility, frequency range, functionality of the application fields etc.[101].

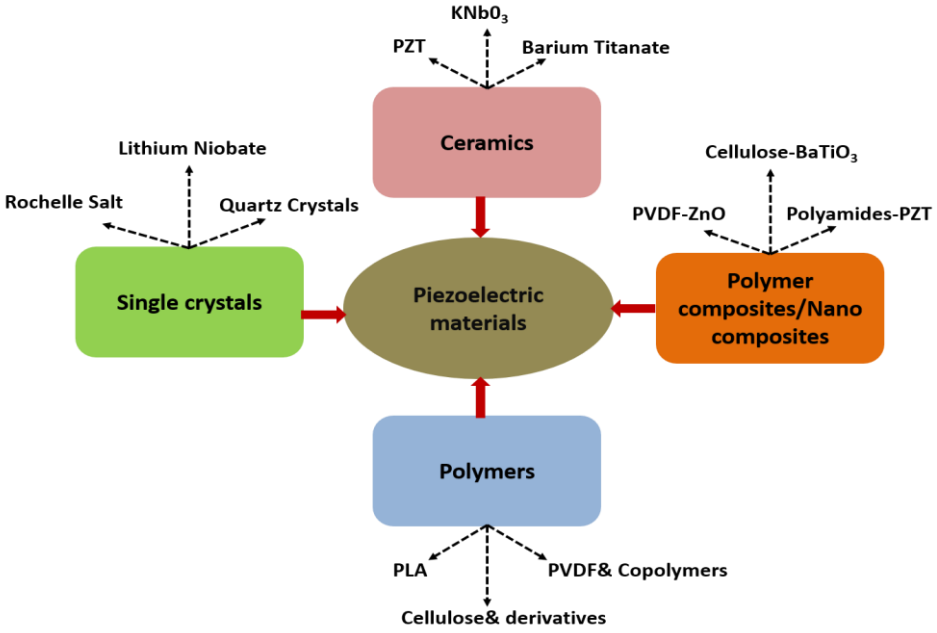

Figure 1.9 Various classes of piezoelectric materials.

Piezoelectric single crystals found applications mainly in the fields of sensors and actuators due to their higher piezoelectric coefficients[100] but the most used are ceramics. The widely used piezoelectric material in the field of energy harvesting is lead zirconium titanate (PZT) which has by far the best piezoelectric coefficients[64]. Nevertheless, the lead-based materials are toxic in nature and lead-free materials such as $BaTiO_3$, AIN and ZnO, although less efficient, are sometimes used as an alternative to PZT materials[3]. Despite the high piezoelectric coefficient and high electromechanical coupling of the piezoelectric ceramic materials, they present some drawbacks, which include rigidity, high density, high-temperature processing needed for thin-film fabrication, high cost for manufacturing, low design flexibility. All these limits their application towards energy harvesting devices[37,38]. Furthermore, and this is a crucial point in our case, they can't endure large deformation due to their brittleness. Moreover, the piezoceramic based devices required an additional nonpiezoelectric substrate layer for the fabrication of the energy harvester. This affects the degradation of the electromechanical coupling coefficient of the device[97,102]. As an example, a comparison between PZT and P(VDF-TrFE) is presented in Table 1.1.

As we are more focussing on energy harvesting devices to power small scale electronic devices, many of the applications, such as in microelectromechanical systems (MEMS), wireless sensors, biomedical implants, wearable and bendable electronic devices demand specific properties[103,104]. Therefore, the choice of the material plays an important role as it need to provide the design flexibility (bending, twisting, fold). It should also maintain the original electronic and structural properties. In this regards, piezoelectric polymers found more attention in the field of energy harvesting because they can satisfy most of the above-

mentioned characteristics. They exhibit good mechanical flexibility, biocompatibility, ease of processing and fabrication and are more resistant to mechanical shock[39,40].

Properties	PZT	P(VDF-TrFE)
Density (kg/m^3)	7.5[105]	1.82[105]
Relative permittivity (κ/κ_0)	1200[105]	12[105]
Acoustic impedance (10^6 kg m^{-2}s^{-1})	30[105]	2.7
Piezo-strain constant (pC/N)	$d_{31=}$ -110[105], d_{33}= 60-130[106]	$d_{31=}$ 23, $d_{33=}$ 24-38[105,107]
Electromechanical coupling constant (% at 1 KHz)	k_{31}= 30[105]	k_{31}= 20[105]
Dielectric constant	1180[107]	15-20[107]
Curie temperature (°C)	360[108]	120[109]

Table 1.1. Comparative study of PZT and P(VDF-TrFE) polymer.

There are several piezoelectric polymers reported and studied in literature for energy harvesting applications which include PVDF and its copolymers, cellulose and its derivatives, polyurethanes (PU), polyimides (PI), polylactic acid (PLA)[3,41,42]. PVDF and its copolymers are well established and most expansively studied materials among all other polymers due to their high piezoelectric coefficient, higher elastic compliances, electromechanical coupling, structural flexibility, good chemical resistance, biocompatibility. Additionally, the off-resonance figure of merit (d_{ij} g_{ij}) of PVDF is comparable to PZT ceramics, which is beneficial for energy scavenging[3,110]. Depending on the synthesis methods and the high voltage polarization, which is necessary to obtain the piezoelectric properties after shaping the polymer usually in thin layers, the piezoelectric coefficient of P(VDF-TrFE) is the highest (30 pC/N) among all piezoelectric polymers. Due to their other characteristics such as, low density, lightweight, low refractive index, low cost, PVDF and P(VDF-TrFE) are good candidates for different energy harvesting systems[37,48]. Another important property is that they can be fabricated with different design configuration and pattern electrodes on their surface. The polarisation can be done in the required portions according to the applications[48].

1.6 Introduction to PVDF and its copolymer for piezoelectric energy harvesting

For the reasons outlined above, PVDF and P(VDF-TrFE) are the most frequently utilized and quoted piezopolymer in electromechanical devices and energy harvesting devices. Considering the other existing ferroelectric semicrystalline polymers, they are vastly used and find more attractive research interest, because of their unique characteristics including fast-electro-mechanical response, high mechanical stability, low acoustic impedance and excellent piezo and ferroelectric response[111,112]. The other copolymers belong to PVDF family including poly (vinylidene fluoride-trifluoroethylene) (P[VDF-TrFE]), poly (vinylidene fluoride-

tetrafluoroethylene) (P[VDF-TeFE]), and poly (vinylidene cyanide-vinyl acetate) (P[VDCN-VAC]) and poly(vinylidene fluoride-hexafluoropropylene) (P[VDF-HFP]). They also exhibit all these characteristics[113,114].

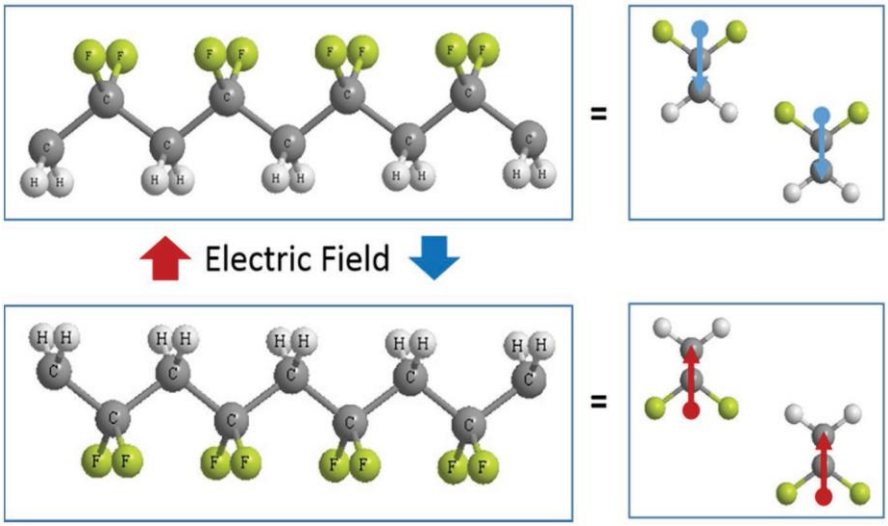

Figure 1.10. Chemical Structure of PVDF [38].

PVDF is a semi-crystalline polymer that is synthesized by the polymerization of the H2C = CF2 monomer (Figure 1.10). Various crystalline polymorphs namely α, β, γ, δ and ε are associated with PVDF, in which α, β, γ are the most studied polymorphs (Figure 1.11)[115]. The α and ε phases are non-polar because of the antiparallel alignment of the dipoles. The α phase is the most stable conformation with a semi-helical TGTG' (trans-gauche-trans-gauche) conformation. The β phase can be obtained by mechanical deformation and electrical poling of PVDF and it is polar. Each unit cell has two polymer chains with all trans (TTT) conformation the dipoles point to the same direction and net zero dipole moment. The γ and δ phases are also polar and have a conformation of TTTTGTTG' and TGTG' respectively. These two phases are also responsible for the piezo, pyroelectric characteristics of PVDF and its copolymers along with β phase. The same case with γ (T3GT3GT') conformation and shows polarity. Compared to other crystalline phases, the β phase shows a higher dipole moment thereby a higher electroactive (piezo, pyro and ferroelectric) properties[114,116,117]. Hence the improvement of β phase content in PVDF polymers with different methods is discussed widely in the literature[116,118,119]. Among the different copolymers of PVDF, (PVDF-TrFE) is able to form directly the polar phase by introducing the TrFE units to the PVDF which improves the piezoelectric effect. The additional fluorine atoms induce steric hindrance and avoid the formation of the non-polar α phase. Therefore (PVDF-TrFE) don't need any additional stretching or drawing of the polymer chain, which is a strong experimental advantage[120], even though poling is necessary to increase the piezoelectric effect. Correspondingly, PVDF and its copolymer solution can be prepared in a different liquid solvent. Therefore it offered various desired shapes and designs by extrusion, moulding or can easily coat on a substrate[121,122].

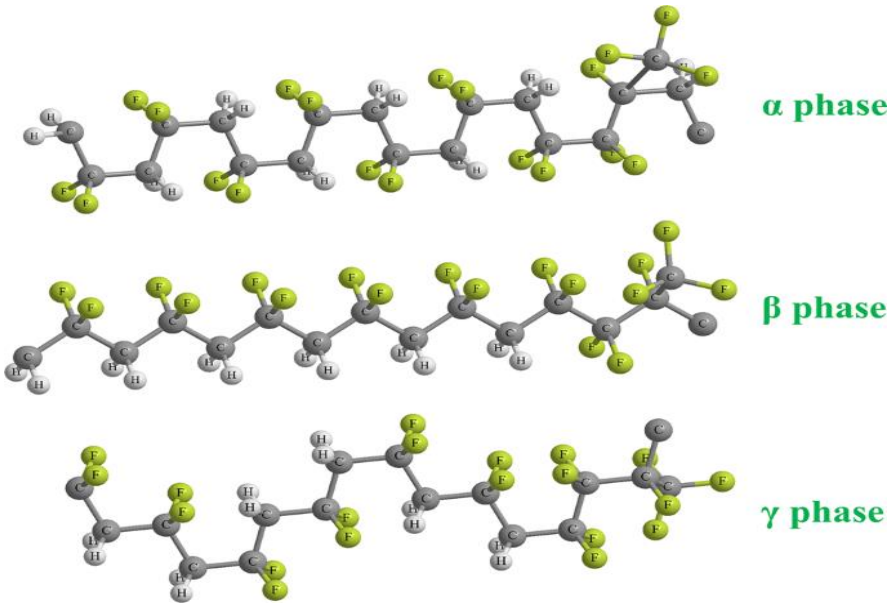

Figure 1.11. Chemical structural representation of the three main phases of PVDF[123]

There are various methods used to attain the electroactive phase of PVDF. Especially different synthesis methods have been developed in order to improve the crystal orientation which includes, as said, the addition of trifluoroethylene (TrFE) units[122,124]. Similarly, the addition of certain fillers, in particular nanofillers, enhances the structural, electrical, and thermal properties of the material. The β phase being responsible for the piezoelectric behavior of PVDF polymer, utmost of the literature studies showed that the β phase content in the polymer can be increased by the addition of certain fillers such as graphene, carbon nanotubes, metal oxides, clay, ceramic fillers, etc[125–127]. The substantial increase in the piezoresponse of the polymer mainly depends on their percentage and on the processing of the polymer. Wan et al. 2017[128] summarized the different groups and their improved piezoresponse . Also, the other important processing techniques are stretching and poling of the polymer.

Similar to other fluorocarbon polymers PVDF is also chemically inert. It is highly resistive to hydrolysis and a low degradation rate provides the biocompatibility of the polymer. Therefore, it found great application in biomedical implementation, biosensing, tissue engineering, and drug delivery. In addition, a PVDF based device can convert the small mechanical response in the body into readable electronic signals. As follows, it can be employed for in vivo and in vitro studies.

The drawbacks of PVDF based polymers include poor adhesion to other materials and the low thermal stability of piezoelectric properties. Indeed, it shows a decrease in piezoelectric coefficient above 80°C and losing the piezoelectric effect.

The stretching and poling mechanism plays an important role in this work. Thus, the following section gives a brief description of the two mechanisms.

1.6.1 Stretching

Crystalline phase transformation is essential to obtain the piezoelectricity in semicrystalline polymers like PVDF. The crystalline phase transformation can be effectually induced by thermal annealing, mechanical orientation, and the application of high voltage[129]. Stretching allows the polymer to fundamentally align the amorphous strands in the planar direction and thereby it's help for the uniform rotation of the crystallites by the application of an electric field in further steps[130]. The electrical and mechanical characteristics depend principally on whether the stretching is uniaxial or biaxial. Normally, a PVDF film has high α phase content with zero net dipole moment. While stretching the α phase is transformed into more β phase, where the fluorine atom is located on one side and the hydrogen on the other side. Therefore, it possesses a net dipole moment in a stacked direction. Temperature is also a factor during stretching, most of the studies showed that the transformation happens between 50°C and 140°C of temperature drawing[131,132].

1.6.2 Poling

A ferroelectric material comprises many individual units' cell and each with a corresponding electrical dipole. In which the regions where the unit cells possess equal polarization directions are named as ferroelectric domains. When a ferroelectric material is cooled below the curie temperature T_c, the domain polarizations are randomly oriented in the material and there is no net polarization[128]. In order to exhibit piezoelectricity in a material, a net polarization will achieve by reorienting the electrical dipoles in one direction. This process is usually known as poling. Thus, the poling or electrical alignment is very essential to convert an inactive polymer into a useful electromechanically active material for many applications. Poling can be obtained by the application of a high electric field E at an elevated temperature below T_C. Thereby the molecular dipoles of the polymer sustain and permanently align in the direction of the electric field[93,133].

Figure 1.12 demonstrates the schematic diagram of the poling process and the hysteresis curve of a piezoelectric polymer. Figure 1.12(a) showed the initial state of the material where the molecular dipoles are randomly oriented through the volume of the material. When the application of a high electric field causes spontaneous polarization within the material, the dipoles start to align in one direction (Figure 1.12b). After complete removal of the electric field, most of the dipoles are locked in a configuration of near alignment. The polymer now obtains a remnant polarization (P_r). The remnant polarization is retained after the complete removal of the electric field. The schematic representation of the orientation of the dipoles after poling process is indicated in Figure 1.12(c). The maximum possible value of the remnant

polarization is known as saturation polarization (P_s)[93]. Figure 1.12(d) represents the polarization- electric field (P-E) loop of typical piezoelectric material. The electric field is applied until the maximum saturation polarization is achieved and it is denoted as P_s. Reducing the field to zero governs the remnant polarization (P_r), and from there, reversing the field reaches a negative maximum (saturation) polarization and negative remnant polarization. The coercive electric field E_c represents the electric field where there is no net polarization due to the mutual compensation of the polarization of different domains. A high value of P_r is an important parameter to get high piezoelectric activity for energy harvesting application. The applied electric field is significantly influencing the final piezoelectric constant. After a certain value of an electric field, the piezoelectric coefficient saturates. Therefore, the poling time and temperature are important factors affecting the piezoelectric constant[93,95].

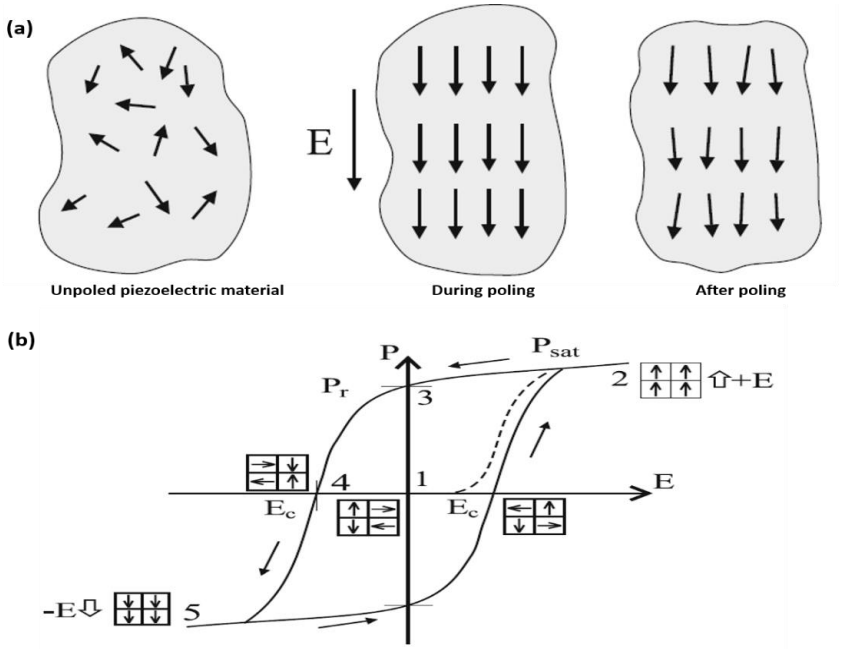

Figure 1.12 Poling of piezoelectric material (a) The material originally occurs a random orientation of molecular dipoles (b) by the application of an electric field causes the dipoles to align in the same direction of the field. (c) The remnant polarization and strain are retained after the complete removal of the electric field (d) Polarisation electric field (P-E) hysteresis loop of piezoelectric material[93].

To pole a material the most used methods are the direct or contact method and the non-contact method called corona poling. In the direct method, poling is done by depositing conductive electrodes on each side of the polymer and a high voltage is applied across the sample (Figure 1.13a). The sample is placed inside a vacuum chamber or immersed in an electrically insulating fluid to avoid its dielectric breakdown. The applied voltage ought to be DC, AD sinusoidal or triangular low-frequency waveforms[134]. In the case of piezoelectric polymers, the applied electric field is in the range of 5 to 100 MV/m. The final quality of the crystallite's alignment and subsequently the piezoelectric coefficient 'd' of the polymer significantly depends on certain parameters which include, the strength and time of the applied

electric field , the value and degree of uniformity of the applied temperature, the degree of impurity or voids between the electrodes and the uniformity of the polymer surface[135]. In some materials like PVDF, the crystalline orientation can be improved by the mechanical stretching performed prior to the poling process. Only this contact method allows to obtain the hysteresis curve of the piezoelectric material, such as the one shown in Figure 1.12(d), which is a valuable data to characterize the piezoelectric and ferroelectrical properties of our material.

Corona poling method offers some advantages, as large area samples can be poled without depositing any electrodes which help to reduce the risk of electrical breakdown of the sample. A typical corona poling system is demonstrated in Figure 1.13(b). A high voltage (8-20 kV) is applied through a conductive needle. Which is placed on the top of the grid with a specific distance(gap) and the sample is placed below on a ground plate. The grid voltage serves for the uniform distribution of the high voltage for a large area of the sample. The medium of the chamber should be vacuum or argon, or dry air. The gas molecules around the needle tip become ionized and are accelerated towards the sample surface which causes an electric field across the surface. The position of the grid and the applied voltage is controlling the amount of charge deposited on the polymer surface. The heat can be introduced through the hot plate which helps for better control of the poling system[37,136].

In comparison with the PZT, the processing temperature for the PVDF based polymers is much lower. In both these cases, the temperature range is lower than 300° C.

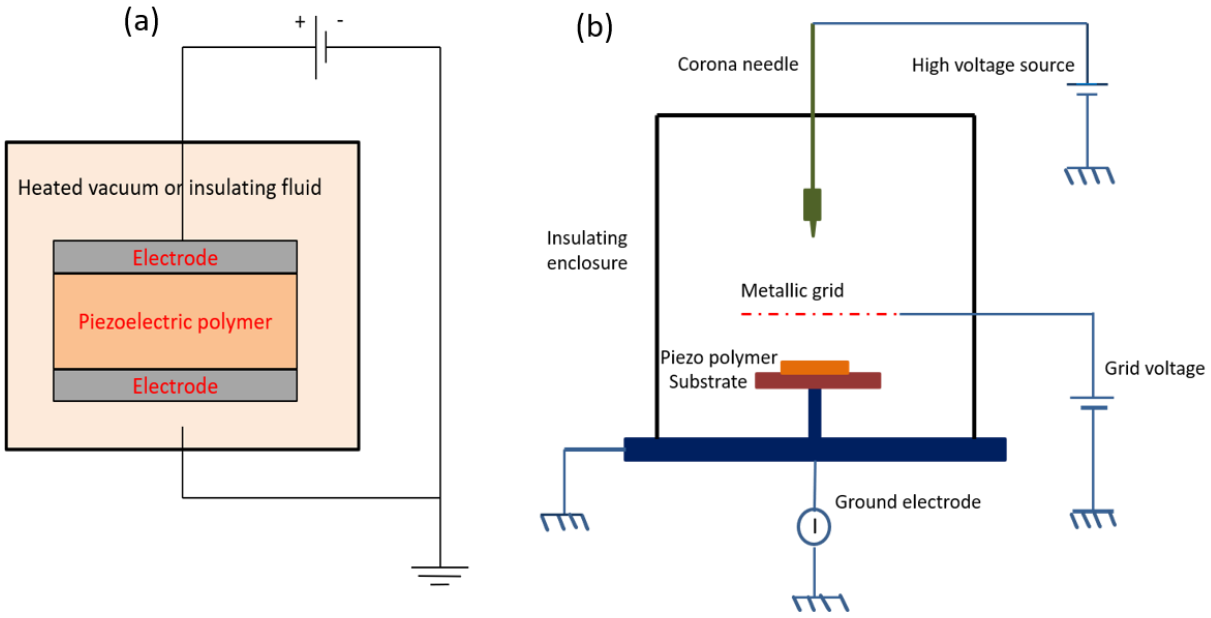

Figure 1.13 Piezoelectric polymer poling systems: (a) direct contact method and (b) corona poling.

1.6.3 PVDF for mechanical energy harvesting

PVDF and its copolymers are widely used for various mechanical energy harvesting such as vibration, stretching, raindrop energies. Here we are however focusing on the bendable, stretchable, and flexible PVDF devices and their different fabrication techniques to generate electricity to power small scale electronic devices. Therefore, to fabricate a hybrid flexible composite device, PVDF and its copolymers suit well because they can combine with different substrates and nanofillers. Nowadays wide studies are focused on the enhanced energy harvesting performance of PVDF based polymers. The following section presents some of the recent literature studies on the flexible PVDF and its copolymers-based generators.

Solvent casting is a simple process for the fabrication of PVDF and P(VDF-TrFE) thin films by mixing and stirring at the desired temperature. Dimethylformamide (DMF), N-methyl pyrrolidone (NMP), dimethyl sulfoxide (DMSO), or dimethylacetamide (DMAc) are utilized as polar solvents to dissolve P(VDF-TrFE) and the other copolymers[116,137]. The spin coating technique is an appropriate way to attain large-area uniform films and performance like mechanical stretching and improvement of the β phase crystal orientation. The processing conditions such as solution concentration, spin rotation speed (rpm) and annealing temperature also considered because these parameters contribute to the percentage of β-phase content in PVDF film[116]. Electrospinning is the most popular method for fabricating PVDF fibres, many research groups are actively working on electrospun PVDF fibres due to their various applications and better dielectric and piezoelectric constants[138]. The comparison of the output performance of PVDF energy harvesters in recent years is shown in Table 1.2.

Authors [Ref]	Materials Device size/thickness	Output performance		
		Voltage (V)	Current/current density	Power density/energy density
Yuan et al. 2020[139]	Multilayered P(VDF-TrFE) films (six 10 µm film)	88.62	353 µA	16.4 mW cm^{-2}
Pal et al 2020	PZT/MWCNT/PVDF) composite	20	-	29.1 mJ/cm^3
Yang et al 2020[140]	Polydopamine-modified BaTiO3/PVDF	9.3	86 nA	0.122 W/cm^2
Wankhade et al 2020[141]	PVDF–PZT nanohybrid system	55	-	36 µWcm^{-2}
Ng et al 2020[126]	2D MoS_2 Flakes/$BaTiO_3$ nanoparticles in PVDF	1.5	-	-

	matrix (1 cm^2)			
Hu et al 2019[142]	rGO/P(VDF-TrFe) composite (40mm×50mm)	8.3	0.6 µA	28.7 w/m^3
Kar et al 2019[143]	2D SnO_2 nanosheet/PVDF composite	42	6.25 $\mu A \cdot cm^{-2}$	4900 $W \cdot m^{-3}$
You et al 2019[144]	Aligned P(VDF-TrFE) fibres	12	150 nA	0.16 µW
Khadtare et al 2019[145]	PEDOT/Ag nanowires/ PVDF composite (1.5cm×2.5 cm)	7.02	1.11 µA	1.18 µW
Li et al 2019[146]	Electrospun ZnO Nanorods/PVDF composite	85	2.2 µA	-
Wu et al 2019[147]	P(VDF-TrFE) /graphene nanocomposite films (110 µm)	12.43	-	148.06 W/m^3
Parangusan et al 2018[148]	Electrospun PVDF-HFP/ Co-ZnO	2.8	-	-
Shi et al 2018[127]	Electrospun PVDF/Graphene nanosheet and $BaTiO_3$ nanoparticles (2.5 cm×2.5cm)	11	-	4.1µW
Sahatiya et al 2018[149]	Few layers MoS_2 /in situ poled PVDF nanofibers	50	30 nA	0.18 mW/cm^2
Jella et al 2018[150]	Stable MAPbI3-PVDF composite films (97.7 µm)	45.6	4.7 $\mu A/cm^2$	-

Table 1.2. Output performance of the most recent PVDF energy harvesting device.

As discussed above, PVDF and its copolymers serve as good candidates for energy harvesting due to their structural flexibility and ease of processing. Also, their high fracture strain (about 2%) makes them suitable and promising candidates for the design of bendable, stretchable, flexible energy harvesting systems. On the other hand, the ceramics and metal-oxides such as Zinc oxide (ZnO), Lead Zirconate Titanate, and Barium Titanate ($BaTiO_3$) showed an intrinsic fracture strain of less than1 %[55].

Several kinds of strategies are proposed and studied for manufacturing flexible PVDF based energy generators. Researchers are focused predominately on different piezoelectric materials such as $BaTiO_3$, ZnO, graphene, MoS_2, KNN, PZT to mix it with PVDF and its copolymers for the fabrication of piezoelectric nanogenerators. Here we are presenting the latest interesting results obtained in the last four years. We published ourselves a review article on recent applications of PVDF polymer device for energy harvesting application[3].

Hu et al 2018[151] designed a double-layered heterostructure with PVDF/$BaTiO_3$ composite. They have studied characteristics of double-layered BT/PVDF with the counterpart single layered film. The double layered design gives higher piezoelectric output in mechanical to electric conversion measurements, due to the accumulation of charges at the additional interlayer interface between the BT/PVDF layer and PVDF layer. It proved the enhanced electric capacity of the film, good interfacial adhesion, better flexibility, mechanical property, and cyclic endurance. The double-layer film with 20 % of volume fraction of BTNPs significantly increased the output voltage of 6.7 V and current of 2.4 μA. Fu et al[152] constructed a sensitive flexible piezoelectric nanogenerator based on a PVDF matrix with oriented $BaTi_2O_5$ nanorods (BT2). The nanorods were prepared by the molten salt method gave them strong polarity and further aligned in the horizontal direction in the PVDF matrix by hot pressing. This textured structure provides an increase in power generation in the cantilever beam mode. 5 vol% of BT/PVDF showed a higher power density of 27.4 $\mu W/cm^3$ and better mechanical properties under an acceleration of 10g. Through this experiment they also studied different conditions such as finger pressing, twisting, fist beating, bending, beating by bicycle spokes to harvest maximum energy from the PEG. The results proved that, when the harvester was repeatedly bent and struck by bicycle spokes, it can produce voltage up to 35 V(pk-pk). It is much higher compared to other conditions. The cantilever beam mode structure is well situated for converting energy from low-frequency vibrational mechanical energy from the normal activities of daily life into electricity. In a similar way, Shi et al 2018[127] exhibited a higher output voltage of 112 V during finger pressing and releasing of the PENG made by electrospun fiber composite with barium titanate (BT) nanoparticles (Nps) graphene sheets and PVDF. Also, the fibre mats composed of 0.15 wt% graphene nanosheets and 15 wt% BT nanoparticles give an open circuit voltage of 11V and electric power of 4.1 μW under a loading frequency of 2Hz and strain of 4 mm. The excellent output of the PNG is attributed to the synergetic effect of BT nps and graphene nanosheets on the piezoelectric performance of the nanocomposite.

Pusty et al 2019[89] demonstrated a flexible and self-poled piezoelectric generator based on rGO–Ag/ PVDF composite. The composite was synthesized by solution casting method by loading different weight percentages of rGO-Ag filler to the PVDF matrix Figure 1.14(a). The incorporation of the filler content greatly influenced the piezoelectric effect of the polymer. Hence, the PNG displayed a peak open circuit voltage of 18 V, a short circuit current of 1.05 μA, and a peak power density of ~ 28Wm^{-3}. Figure 1.14(b) shows the generated output voltage and power density across various resistances from the rGo-Ag/PVDF composite. Khalifa et al 2019[153] introduced a blend composite to enhance the piezoelectric properties. The blend composite consists of electrospun PANi (polyaniline)/HNT (halloysite nanotube)/ PVDF. The synergetic effect of HNT and PANi acted as nucleating agents and conductive filler in PVDF. When the application of different mechanical stresses the maximum voltage produced by the device is 7.2 V. The durable, flexible, sensitive nature of the nanogenerator opens the usage in wearable piezoelectric energy conversion applications. Jie Li et al 2019[125] presented modified ZnO NPs (by adding dispersant (n-propylamine, PA) and a silane coupling agent) / P(VDF-TrFE) composite by spin coating technique. The composite shows high crystallinity and a large specific surface area. The output voltage of the device is maintained at 2.40 V even after 1000 cycles of testing. On the other hand, Jingjing Li et al 2019[146] reported a novel flexible, high performance piezoelectric generator based on electrospun ZnO nanorods/PVDF composite membrane, the schematic representation of the composite membrane is depicted in Figure 1.14(c). Through their studies, it is evident that the ZnO nanorods effectively contribute to enhancing the piezoelectric charge when they deform with the PVDF membrane as well as act as a nucleating agent for the β phase. Thus, a large electrical throughput of open circuit voltage ~85 V and short circuit current ~2.2 μA were produced from the ZnO NR/PVDF fibre composite. Figure 1.14(d) presents the produced output voltage vs time for the pure PVDF, ZnO Nps/PVDF, and ZnO NR/PVDF.

Recently, Liu et al 2020[154] investigated a lead-free piezoelectric nanogenerator. They processed a new combination of doping material 0.5Ba ($Zr_{0.2}Ti_{0.8}$) O_3-0.5($Ba_{0.7}Ca_{0.3}$) TiO_3 (BZT-BCT) with a high piezoelectric coefficient of 620 pC/N. The BZT-BCT/P(VDF-TrFE) electrospun nanofiber mat is exhibited better output performance, which produces an output voltage of 13.01 V under cyclic tapping under 6N and 10 Hz. This PNG has the potential usage in wearable, implantable device, and self-powered sensors. Fu et al 2020[155] developed a unique sandwiched structure with high piezoelectric performance. The sandwich design is made with a PVDF film filled with FeTiNbO6 (FTN) semiconductor particles as an intermediate layer and a pure PVDF film as an upper and lower barrier layer. The compact composite (PVDF-FTN/PVDFx-PVDF (P-FTNx-P)) is fabricated by hot pressing technology. The schematic illustration of the synthesis of the sandwich structure of P-FTNx-P is given in Figure 1.14(e). The harvester delivers a high-power density of 110 μW/cm^3 and a large charge density of 75 μC/m^2 in cantilever mode. The photographic image of the cantilever type PNG and the graph for power density vs resistance is shown in Figure 1.14 f and g.

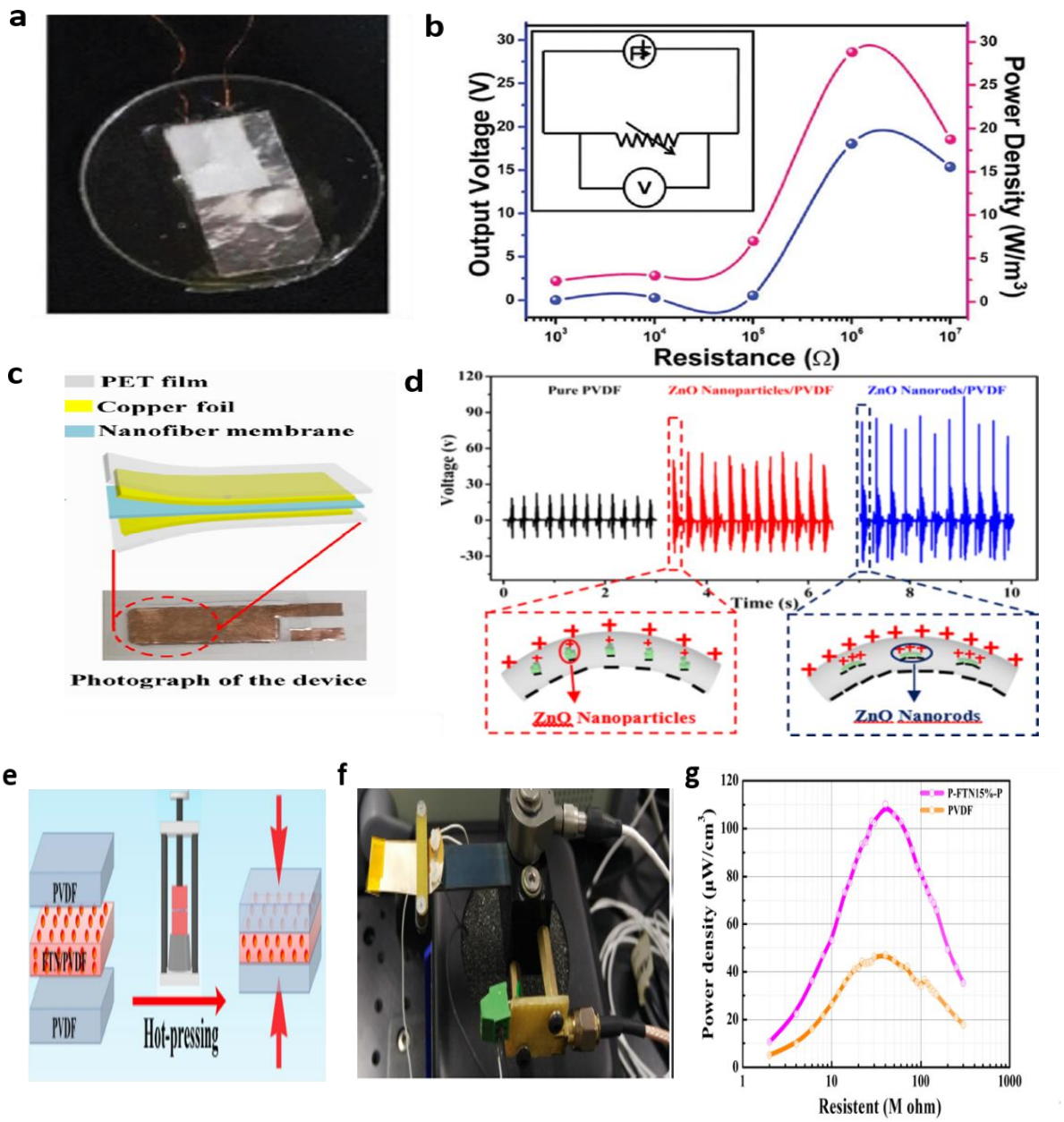

Figure 1.14. (a) Photograph of the rGO-Ag/PVDF composite film encapsulated in PDMS layer with Al electrodes on both sides (b) The voltage harvested, and power generated from rGO–Ag/PVDF nanocomposite across various resistances[89]. c) schematic representation and the digital image of the ZnO NRs/PVDF (d) voltage output and the schematic illustration of the charge generation in ZnO NPs /PVDF and ZnO NRs/PVDF composite respectively[146]. (e) Schematic representation of hot-pressing method for building sandwich-structured P-FTNx-P Composite (f) the structure and installation of cantilever-type PNG (g) The power generation of the PVDF and P-FTN15%-P FPEHs with different external load resistance[155].

1.7. Modeling of the ferroelectric and ferroelastic behaviors of piezoelectric materials

The modeling of piezoelectric material behavior concerns the linear and non-linear parts of this behavior. The linear part corresponds to the reversible electromechanical behavior induced by

the small and reversible variation of polarization under mechanical or electrical loading. Whereas the nonlinear part derives from the remnant ferroelectric and ferroelectric domain switching under high electromechanical loading. Voigt[165] was the first to propose, in 1910, a behavior model that accurately describes the linear part, namely piezoelectric behavior. This model is widely used now. It describes a relationship giving stress and electric displacement (polarization) as functions of strain and electric field, that was represented in equation 1.1 and 1.2.

Applying mechanical and electrical loading levels higher than given yield values activates the switching of ferroelectric and ferroelastic domains leading to a highly non-linear macroscopic behavior. Approaches widely adopted for describing elastic-plastic materials and SMA behaviors are also applied in order to derive the non-linear part of piezoelectric material behavior at different scales. They can predict specificities of such multiphysical behavior as anisotropy, large hysteresis, and saturation of electric polarization and strain [156]. The first phenomenological model was proposed by Chen in 1980[157,158]. It considers the remnant strain and polarization as internal variables taking into account the electromechanical loading history. However, this model is one dimensional and is limited to the case of electrical loading. A more sophisticated phenomenological model, consistent with thermodynamic laws, was proposed by Bassiouny et al. [159,160]. It is based on the concept of thermo-elasto-plasticity and is inspired by phenomenological descriptions adopted in ferromagnetism. It considers an additive decomposition of strain tensor and polarization vector into reversible and remnant parts. Internal variables are remnant strain (ε^R) and polarization (P^R). The adopted formulation applies the Clausius-Duhem inequality in order to derive the corresponding constitutive equations. Many models were proposed to enhance it [161–167]. The following equations correspond to an example of a nonlinear phenomenological electromechanical behavior model:

$$\begin{cases} \varepsilon_{ij} = \varepsilon_{ij}^{el} + \varepsilon_{ij}^{R};\ \varepsilon_{ij}^{R} = \varepsilon_{ij}^{P} + \varepsilon_{ij}^{F};\ D_i = P_i^{el} + P_i^{R} \\ \sigma_{ij} = C_{ijkl}\varepsilon_{kl}^{el} - e_{kij}E_k;\ D_i = e_{ikl}\varepsilon_{kl}^{el} + \kappa_{ij}E_j;\ P_i^{R} = P_i^{E} + P_i^{\sigma} \\ \varepsilon^{P} = \frac{3}{2}\varepsilon^{SAT}\frac{\left\|\overrightarrow{P^E}\right\|}{P^{SAT}}\left(\overrightarrow{e_{P^R}} \otimes \overrightarrow{e_{P^R}} - \frac{1}{3}\mathbf{I}\right);\ \dot{P}_i^{\sigma} = \frac{P^{SAT}}{2\varepsilon^{SAT}}e_j^0\dot{\varepsilon}_{ij}^{F};\ T_i = \sigma_{ij}e_j^{P} \end{cases} \quad (1.6)$$

Where, ε^{el} and P^{el} are the reversible deformation and polarization which occur when the electromechanical charge is removed. C and E are the fourth-order tensor of elasticity at constant electric field and the second-order dielectric permittivity at constant mechanical strain. The ferroelectric strain is denoted as ε^e. P^E is the remnant ferroelectric polarization induced by the electric field and P^σ is the mechanical depolarization induced by the ferroelastic reorientation of the domains, δ is the Kronecker tensor and e^p is the direction of remnant polarization, ε^f is the ferroelastic strain. The total strain and electric displacement present a reversible contribution related to the piezoelectric behaviour and remnant contribution related to ferroelectric and ferroelastic domain switching. This assumes the analogy between the

mechanical and the electric occurring mechanisms. The remnant strain and polarization derive from depolarization and ferroelasticity characterized respectively by the internal variables ε^R and P^E. ε^{SAT} and P^{SAT} are respectively the maximum remnant strain and polarization corresponding to a fully polarized material. The evolution laws of these two internal variables are presented in the following equations. They assume an elastic-plastic-like behavior with two loading surfaces, two hardening-like laws, and two normality conditions corresponding to the mechanical and electrical parts.

$$\begin{cases} f^{\sigma} = \sqrt{\frac{3}{2}\left(s_{ij}-\alpha_{ij}\right)\left(s_{ij}-\alpha_{ij}\right)} - (\sigma_c + ne_i^P E_i);\ f^E = \sqrt{(E_i - X_i)(E_i - X_i)} - E_c \\ \dot{\alpha}_{ij} = \frac{2}{3} h\dot{\varepsilon}_{ij}^F;\ \dot{X}_i = \beta \dot{P}_i^E;\ \sqrt{\frac{2}{3}\varepsilon_{ij}^R \varepsilon_{ij}^R} \le \varepsilon^{sat};\ \sqrt{P_i^R P_i^R} \le P^{sat} \\ \dot{\varepsilon}_{ij}^F = \dot{\lambda}^{\sigma} \frac{\partial f^{\sigma}}{\partial \sigma_{ij}} = \dot{\lambda}^{\sigma} \frac{3}{2}\left(\frac{s_{ij}-\alpha_{ij}}{\sigma_c + ne_i^P E_i}\right);\ \dot{P}_i^E = \dot{\lambda}^E \frac{\partial f^E}{\partial E_i} = \dot{\lambda}^E \left(\frac{E_i - X_i}{E_c}\right) \\ \dot{f}^{\sigma} = \frac{\partial f^{\sigma}}{\partial \sigma_{ij}}\dot{\sigma}_{ij} + \frac{\partial f^{\sigma}}{\partial \alpha_{ij}}\dot{\alpha}_{ij} + \frac{\partial f^{\sigma}}{\partial e_i^P}\dot{e}_i^P + \frac{\partial f^{\sigma}}{\partial E_i}\dot{E}_i = 0;\ \dot{f}^E = \frac{\partial f^E}{\partial E_i}\dot{E}_i + \frac{\partial f^E}{\partial X_i}\dot{X}_i = 0 \end{cases} \quad (1.7)$$

Finally, two conditions of consistency are applied in order to derive the constitutive equations describing the nonlinear electromechanical behavior of the piezoelectric material. These equations are numerically solved by a classical return mapping method combined to the Newton-Rapson technique [163,168]. f^E and f^{σ} are two electric and mechanical switching functions. Where X_i is equivalent to a kinematic hardening vector, E_c is the coercive electric field. σ_c are S_{ij} are the coercive and deviatoric stresses respectively. h is the numerical function defined as $h(x) = \frac{1}{2}(1 + \tanh(kx))$. Where λ^e and λ^{σ} are the ferroelectric and ferroelastic multipliers determined by the condition of consistency conditions $f^e=0$ and $f^{\sigma}=0$. β is the material constant and α is the numerical parameter.

Figure 1.15 shows an example of obtained numerical results issued from the solving of these constitutive equations. They show ferroelectric and ferroelastic behaviors induced by a compression loading under a constant electric field.

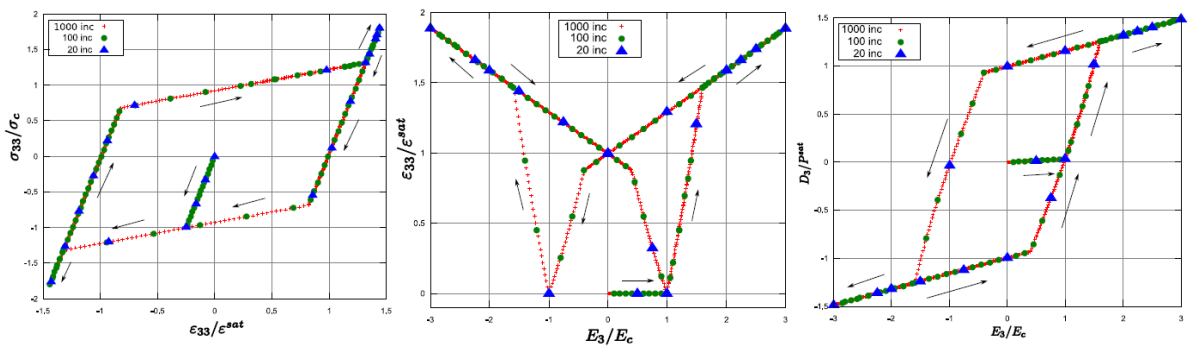

Figure 1.15. Ferroelectric and ferroelastic behaviors issued from a phenomenological approach [168].

The second family of models considers a local description of piezoelectricity and of the ferroelectric and ferroelastic domain switching at the microstructure scale. The piezoelectric linear constitutive equations have the same expression as in the case of the phenomenological approach. The nonlinear constitutive equations derived from the aforementioned micromechanical formulation initially developed for the plastic slip mechanism and extended to martensite variants and here to ferroelectric and ferroelastic domains. Each domain is characterized by its microstructure properties and a correspondent volume fraction assumed as an internal variable. The global remnant strain is the contribution sum of intrinsic switching strain for all ferroelectric and ferroelastic active domains weighted by their self-volume fractions. The assuming of free energy and dissipation expressions at the microstructure scale allow to apply the first and the second principle of thermodynamics in order to derive the local electromechanical constitutive equations. It will be then possible to deduce the corresponding effective electromechanical behavior at the RVE or macroscopic scale by considering analytical or numerical scale transition techniques as self-consistent, Mori-Tanaka or FE² homogenization methods. The literature presents a wide range of models based on such approach [156,163,169–175]. In the following an example of constitutive equations corresponding to the description of the electromechanical behavior of a piezoelectric single crystal based on a crystalline-plasticity-like approach [163,172]. The Gibbs free energy of this model presents the following expression:

$$\Psi = -\frac{1}{2}\sigma_{ij}(\varepsilon_{ij} - \bar{\varepsilon}_{ij}^{s}) - \frac{1}{2}E_n^0(\overline{D_n} - \overline{P_n^s}) - \frac{1}{2}\sum_{m,n} H^{mn} f^m f^n \qquad (1.8)$$

Where, $\sigma, \varepsilon, \bar{\varepsilon}^s, E_n^0, \overline{D_n}, \overline{P_n^s}, f^m, H^{mn}$ are respectively the stress tensor, the total and spontaneous strain tensors, the electric field, the total and spontaneous polarization vectors, the volume fraction of a given ferroelectric and ferroelastic domain (m) and the term of interaction matrix between concerned domains (n) and (m). Volume fractions of ferroelectric and ferroelastic domains are assumed as internal variables.

Most of the literature studies showed the combination of different materials and composite structures to enhance the performance of the harvester. Now active research approach is going on the development of the hybrid energy harvester. It is a developing area and a new direction in this field to combine piezoelectric materials with smart materials such as shape memory alloys with different functionalities. The following section is dealing with shape memory alloys, properties, and thermomechanical behavior models.

1.8 Introduction to shape memory alloys

Shape Memory Alloys (SMAs) belongs to a family of materials that can return to a predetermined shape upon heating. SMAs bear two phases, a high temperature phase called austenite (A) and a low-temperature phase named martensite (M)[17,24]. Austenite normally

occurs in cubic crystal structure while martensite has tetragonal, orthorhombic, or monoclinic crystal structures. The phase change from one structure to another does not emerge by the diffusion of atoms. It occurs through the process called shear lattice distortions; this transformation is known as martensitic transformation. The formed martensitic phase has different orientation directions and habit planes known as a martensite variant. Martensitic variants exist in two forms; twinned martensitic (M_t) and detwinned (M_d) martensites[24,176]. The phase transformation from austenite (parent phase) to martensite (product phase) and vice versa and the reorientation from one martensite variant to another are responsible for the unique behaviour of SMAs[17]. SMAs possess two distinct properties known as shape memory effect (SME) and superelasticity (pseudoelasticity). Additional less conventional SMAs properties are considered as two-way shape memory effect or caoutchoutic effect.

1.8.1 Shape memory effect

Shape memory effect (SME) is the property of SMA such as NiTi to recover its original shape over consequent heating after substantial distortion from its martensitic temperature state. This transformation is referred to the martensitic transformation which is a diffusionless solid-state phase transformation[177,178]. This phase change results in the change of crystal structure by the collective movements of the atoms in the solid. The movements are microscopic, which is less than the interatomic distance between the atoms[177]. The schematic representation of SME is shown in Figure 1.16.

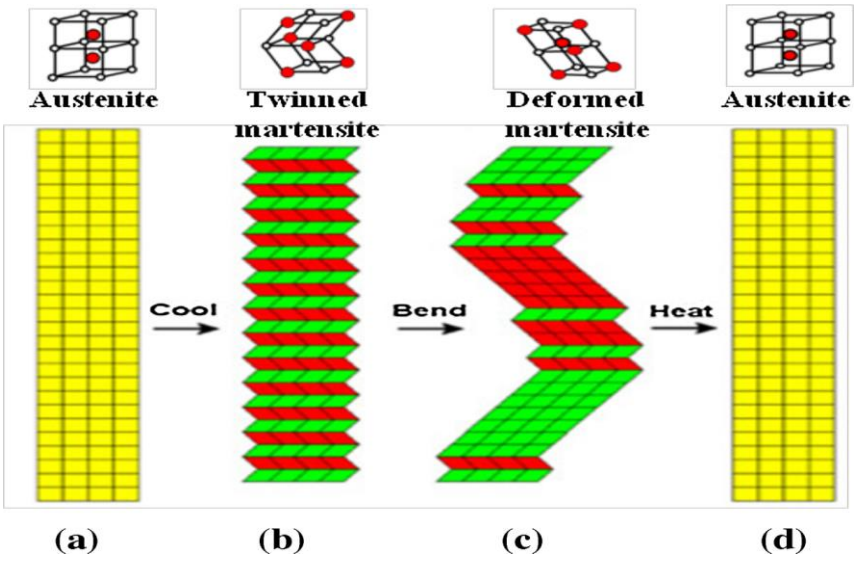

Figure 1.16 Schematic diagram of Shape memory effect (SME)[176].

The shape recovery is not occurring through a linear path, but it follows a hysteresis and nonlinear behaviour. The hysteresis arises since an additional force is necessary in order to overcome the elastic energy stored associated with the shape change during transformation[179,180]. There are four characteristic temperatures associated with the phase transformation. During the forward transformation without any loading condition, the

austenite state begins to transform into twinned martensite at the martensitic start temperature (M_s) and at martensitic finish temperature (M_f) it completes the transformation into martensite. The similar way during heating, the reverse phase transformation begins at the austenite start temperature (A_s) and at the austenitic finish temperature (A_f) the transformation is completed. Figure 1.17 illustrates the phase transformation of NiTi SMA[17,176].

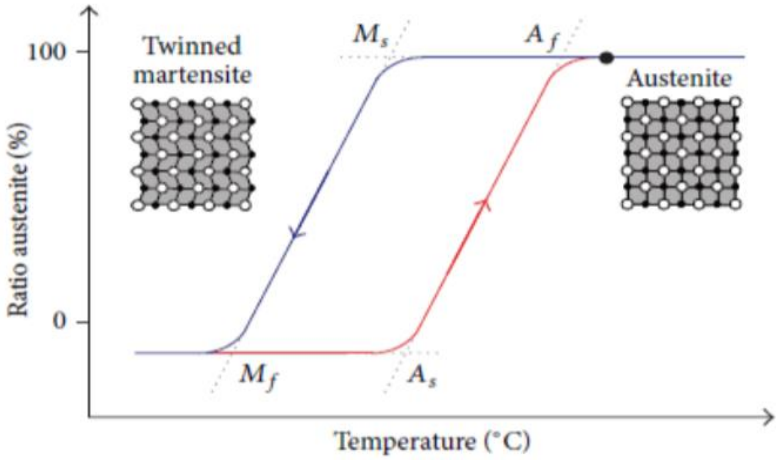

Figure 1.17. Schematic diagram of the phase transformation and temperature hysteresis of NiTi SMA[181].

SME behaviour can be represented by the thermomechanical loading path in a collective stress-strain-temperature region. The schematic representation of the associated microscopic and macroscopic phase change during SME behaviour is shown in Figure 1.18 (a) Schematic representation of the microscopic and macroscopic phase of one-way shape memory effect 181(b) Stress-strain- ^{temperature} graph for NiTi SMA showing shape memory effect184. Under a zero load, the cooling of the parent austenite phase below the forward transformation temperatures (Ms and M_f) lead to the formation of the twinned martensitic phase[17,182]. In this twinned martensitic state, the material is exposed to an applied load that is greater than the start stress level (σ_s), leading to the growth of certain martensitic variants. At a stress level (σ_f) the detwinning process is finished. The detwinned martensitic state is retained even the material is elastically unloaded from C-D (Figure 1.18b). The temperature reaches to As, (at E) the reverse transformation starts without the application of stress. This reverse transformation ends at temperature Af, the parent austenite phase only exists above this temperature.

By this way, the SMA recovered its original shape in the absence of permanent plastic strain caused during the detwinning process. Consequent cooling will again result in the martensitic phase and the whole cycle can be repeated. This phenomenon is known as the one-way shape memory effect or generally shape memory effect (SME)[176,183].

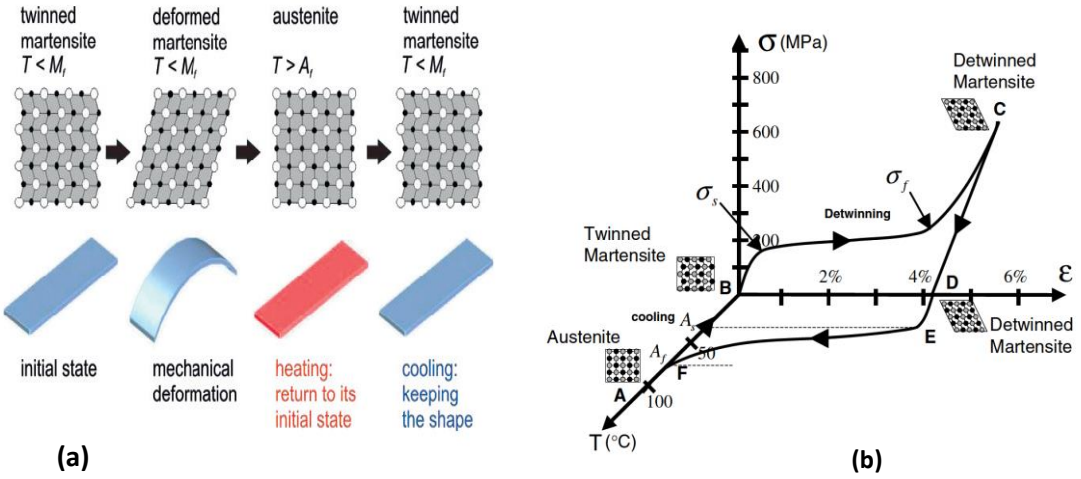

Figure 1.18 (a) Schematic representation of the microscopic and macroscopic phase of one-way shape memory effect [181](b) Stress-strain- temperature graph for NiTi SMA showing shape memory effect[184].

1.8.2 Superelasticity

Superelasticity, also known as pseudoelasticity is a reversible process occurred by the phase transformation between the austenite and martensite phases of SMA by the application of stress. The stress-induced martensite (SIM) gives rise to the formation of strain through loading and consequent unloading the strain is recovered at a constant temperature above A_f. The SIM is generally the martensite formed from austenite under applied stress[24,185,186]. A superelastic thermomechanical loading occurs normally at a higher temperature that is above A_f, where the parent austenite phase exists. Then it continues to form the detwinned martensite in the presence of an applied load, and at the end returns to the parent austenite phase with unloading till zero stress state. Figure 1.19 (a) shows the loading and unloading path for pseudoelastic behaviour of SMA[176,187].

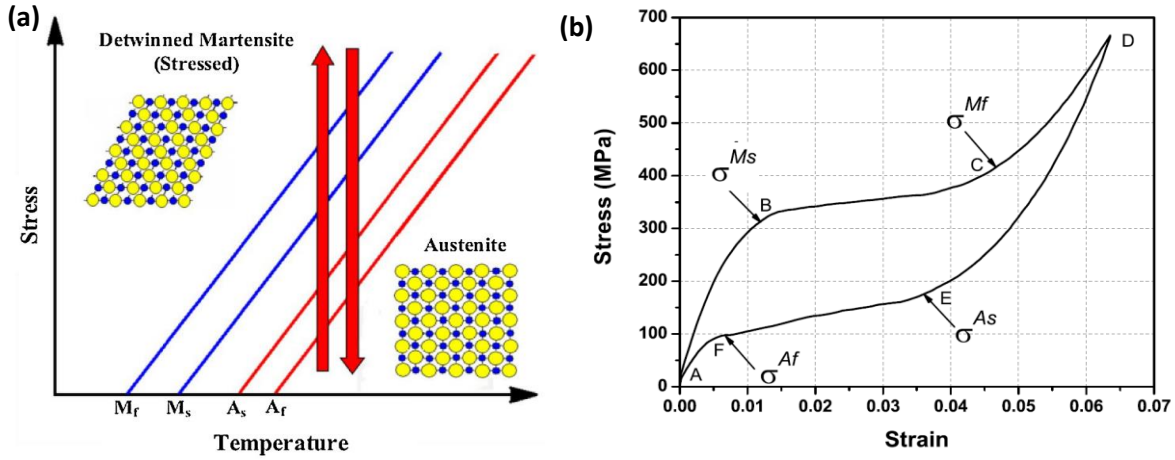

Figure 1.19 (a)Pseudoelastic loading path for SMA[187] (b) Pseudoelastic stress-strain diagram for NiTi SMA[24].

During mechanical loading, the transformation begins at a specific stress level from the parent austenite to martensite. The elastic loading path is indicated as A-B in the stress-strain graph (Figure 1.19b). At a specific load level, the stress level marked as σ_{Ms} represents the stress level inducing the starting of forward martensitic transformation as indicated in the phase diagram. This stress-induced transformation from austenite to martensite induces reversible inelastic strain. The transformation continues (B-C) until the stress level (σ_{Mf}) reached, which is indicated as the end of the transformation stress level. The consequent increase in stress would not cause any further transformation. Though, only the elastic deformation of detwinned martensite takes place from C-D. During unloading, the stress is decreased gradually, and the martensite elastically unloads along the path (D-E). Point E indicates the unloading path which intersects the austenite start surface at σ_{As}. This causes the reverse transformation from martensite to austenite. The unloading process is associated with the transformation strain recovery due to the reverse phase transformation. At the end of the transformation is denoted by the point at which the stress-strain unloading path rejoins the elastic region. Point F corresponds to the austenite with the stress σ_{Af}. During a complete pseudoelastic cycle, the forward and reverse transformation results in a hysteresis. This exhibits the energy dissipation in the martensitic transformation cycle. Depending on the SMA material, composition, and testing conditions the variation in transformation stress level and size of the hysteresis may occur.

The classical metals show the conventional elastic strain of about ~0.5 %. On the other hand, NiTi SMA can generate relatively large reversible strain up to about 8% without being plastically deformed. This is much higher than the classical metals. This phenomenon occurs when the deformation has been induced by the martensitic phase transformation[188].

There are also different transformations accompanying with shape memory such as rhombohedral (R-phase)[189], bainite and the rubber-like behaviour only at martensitic state[186,190]. These are not conferred more in this manuscript. Depending on the applications, the properties, and the requirements of SMA choice are very important. For example, MEMS and robotic applications need fast actuation therefore small hysteresis is preferred[185,191]. The composition of SMAs strongly depends on the transition temperatures (start and finish forward and reverse martensitic transformation temperaturres) and hysteresis size[191]. There are different characterization techniques used to determine the transition temperature such as differential scanning calorimetry (DSC) and dilatometry and they can be measured indirectly by a series of constant stress thermal cycling experiments[192,193]. The SMAs physical and mechanical characteristics such as Young's modulus, electrical resistivity, thermal conductivity and thermal expansion coefficient also change in between the two phases[194,195]. The austenite phase possesses higher Young's modulus because of its harder structure and on the other hand the martensitic structure is softer and easily deformed when an external force is applied[196,197].

1.8.3 Modeling of the SMA thermomechanical behavior

The first emerging thermomechanical constitutive models are empirical and one-dimensional[198,199]. Since, two-dimensional, and three-dimensional extensions are proposed based on more sophisticated formulations enhancing the accurate and complete description of the various specificities of the SMA thermomechanical behavior. Most of their formulations derive from micromechanical approaches, combined or not with scale transition techniques, statistic physics approaches, elastic-plastic model-like, and thermodynamic approaches assuming a given thermodynamic potential and dissipation expressions[200–202].

(a) Microscopic models

Thermomechanical behavior models based on thermodynamic approaches at the microscopic scale generally consider the Ginzburg-Landau or the molecular dynamic theories. They allow describing the effect of mechanisms related to the martensitic transformation occurring at the crystalline lattice scale. It corresponds to the martensite nucleation and its propagation and martensite variant reorientation. Models based on Ginzburg-Landau theory assume a polynomial expression of the free energy as a function of observable variables as temperature and strain. Initially proposed by Falk in 1980, [203,204] they were improved by many researchers in the coming years [205–207]. These models assume that the occurring instability of the thermodynamic equilibrium induces a martensitic phase transformation. The formulation of the thermodynamic equilibrium determines the structure and the motion of interfaces between martensite variants and between austenite and martensite phases. Researchers as Dhote et al., 2014, Levitas and Preston 2002, Wang and Melnik, 2007 [208–211] proposed extended and enhanced versions of these models. Models based on the molecular dynamic theory derive from a theoretical physic approach that emerged in the 1960s by Alder and Wainwright, 1959; Rahman, 1964 [212,213]. They consist to solve Newton's equations describing the particle motion within a network of a finite number of particles. The size and the shape of the particle network evolve in a dynamic manner in order to ensure, at each time, the balance between internal and applied stresses[214]. The main difference between available models based on such approach comes from the choice of the potential energy expression related to the interaction between particles.

The main considered expressions are those of Lennard-Jones (LJ)[215,216] and the embedded atom method (EAM) initially proposed by Daw et al.,1993[217]. Micro-macro models derive from the description of the martensitic transformation at the crystalline lattice scale. In the case of a polycrystalline microstructure, the introduction of a scale transition technique allows to describing the effective behavior of a given Representative Volume Element (RVE)[202,218–222]. Two kinds of micro-macro models are the most used. The first ones adopt formulation inspired from the crystalline plasticity whereas the second ones derive from micro-planes and micro-spheres approaches. Regarding models inspired from crystalline plasticity, different possibilities

of detwinning of the crystalline lattice, each characterized with a set of vectors (martensite variant) defining the habit plane normal and the detwinning direction. An intrinsic transformation strain and volume fraction characterize each variant and define its contribution to the resultant transformation strain. The assumption of free energy and dissipation expressions and the application of the first principle of thermodynamics and the Clausius-Duhem condition allow to manage the activation of the transformation process for each variant and the determination of the evolution of each variant volume fraction [202,221,223–226]. For polycrystalline SMAs, the introduction of a scale transition technique allows to derive the effective behavior starting from the local behavior of each grain (single crystal) [202,227–229]. The theory of micro-planes, initially proposed by Tailor in 1938, allows to describe the SMA thermomechanical behavior as a superposition of a succession of uniaxial behaviors in planes with different normal directions labeled "micro-planes" [230,231]. Additional kinematic or static conditions need to be ensured in order to derive the constitutive equations.

In the following an example of constitutive equations corresponding to the description of thermomechanical behavior of an SMA single crystal based on a crystalline-plasticity-like approach [202,232,233]. The Gibbs free energy of this model presents the following expression:

$$\Delta G\left(\sigma_{ij},T,f^{n}\right)=-\Delta G_{ch}-W_{élas.}-W_{\text{interf.}}+\sigma_{ij}\varepsilon_{ij}=\begin{pmatrix}-B\left(T-T_{ref}\right)f^{n}+\frac{1}{2}f^{n}\sum_{m}H^{nm}f^{m}+\\ \alpha\delta_{ij}\left(T-T_{0}\right)\sigma_{ij}+\frac{1}{2}\sigma_{ij}S_{ijkl}\sigma_{kl}-g\sigma_{ij}R_{ij}^{n}f^{n}\end{pmatrix} \qquad (1.9)$$

where $\Delta G_{ch},W_{élas.},W_{\text{interf.}},\sigma,\varepsilon,T$ and f^{n} are respectively the variation of chemical energy, elastic energy, interface energy, the stress and strain tensors, the material temperature and the volume fraction of a given martensite variant (n). The material parameters characterizing the single crystal are $S,\alpha,B,g,T_{0},T_{ref},R^{n},H^{nm}$ representing respectively compliance and thermal expansion tensors, a chemical factor related to phase transformation, distortion amplitude, room and reference temperatures, Shmid tensor characterizing the crystallographic properties of each martensite variant and the interaction parameters. The condition of the Clausius-Duhem allows to derive the following driving force governing the evolution of the volume fraction of each martensite variant:

$$\frac{\partial\Delta G}{\partial f^{n}}=-B\left(T-T_{0}\right)+\sum_{m}\left(H^{nm}f^{m}\right)-g\sigma_{ij}R_{ij}^{n}=F_{y}^{n} \qquad (1.10)$$

Considering the consistency conditions for each active variant, in combination with the thermos-elastic behavior, leads to the following constitutive equations describing the behavior of a single crystal SMA:

$$\dot{\sigma}_{ij}=\left(\left(C_{ijkl}-\sum_{n,m}\left(C_{ijrs}\tilde{\varepsilon}_{rs}^{n}\hat{H}_{nm}^{-1}\tilde{\varepsilon}_{pq}^{m}C_{pqkl}\right)\right)\dot{\varepsilon}_{kl}-\left(\alpha C_{ijkl}\delta_{kl}-\sum_{n,m}\left(C_{ijrs}\tilde{\varepsilon}_{rs}^{n}\hat{H}_{nm}^{-1}\left(Be^{m}+\alpha\tilde{\varepsilon}_{pq}^{m}C_{pqkl}\delta_{kl}\right)\right)\right)\dot{T}\right) \qquad (1.11)$$

with C is the stiffness elastic tensor and $\hat{H}_{nm} = H^{nm} + \tilde{\varepsilon}^n_{pq} C_{pqrs} \tilde{\varepsilon}^m_{rs}$, where $\tilde{\varepsilon}^n_{ij} = g R^n_{ij}$.

The comparison between the predicted thermomechanical behavior of a given single crystal SMA and the corresponding observed experimental response shows that this approach allows to well describe the SMA thermomechanical behavior under tension and combined bending-torsion loadings (Figure 1.20).

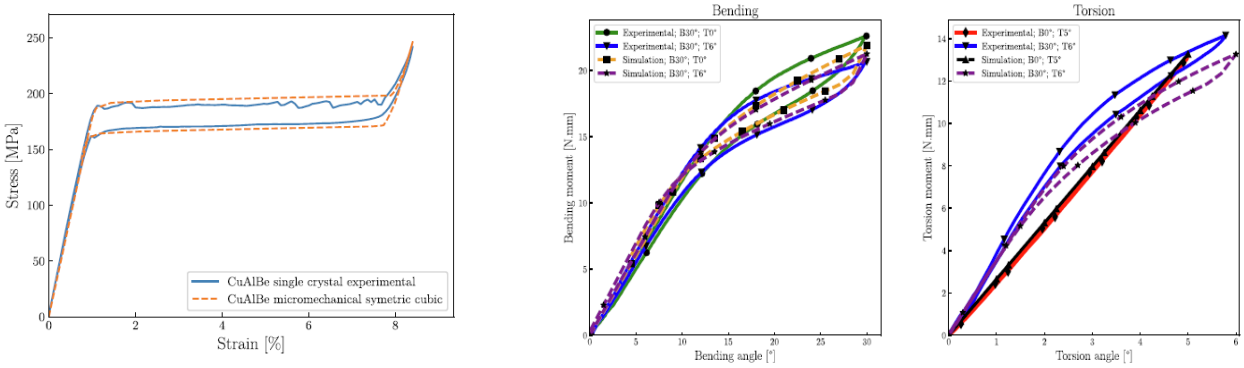

Figure 1.20. Comparison between experimental characterization and modeling results for tension and combined bending-torsion loadings [234].

(b) Macroscopic models

Macroscopic models describe, in a global and effective way, the thermomechanical behavior of an SMA polycrystalline RVE. Most of the available models are gathered in three families: (i) phenomenological models, (ii) models derived from an averaged thermodynamic approach and (iii) models based on the statistic physic theory at the macroscopic scale. Tanaka and Nagaki, 1982 [235] were the first to propose a macroscopic phenomenological thermomechanical model with internal variables describing the effect of martensitic transformation under uniaxial loading. Liang and Rogers, 1990 [199] and shortly thereafter Brinson, 1993[198] carried out its extension to tridimensional loading and proposed to distinguish the volume fraction of oriented martensite (mechanical martensite) from the self-accommodated martensite (thermal martensite). Thermomechanical models inspired from plasticity theory, consider the effective transformation strain as a plastic strain however reversible. These models assume that the average effect of interactions between martensitic variants operates as a complex plastic hardening. One or many loading surfaces derive from such formulation. Their association with the normality rule and the consistency condition allow determining transformation strain rate and therefore the constitutive equations governing the SMA thermomechanical behavior [236–242]. These models could consider loading surfaces with more complex shape in order to take into account the anisotropy of the martensitic transformation evolution. They also consider additional loading surfaces describing martensite reorientation and a complex evolution law related to effects of interactions between variants inspired from combined isotropic and kinematic hardenings [243–248]. Regarding models derived from an averaged thermodynamic approach, they assume expressions of the free energy and dissipation describing in an averaged

way effects of elasticity, martensitic phase transformation and martensite reorientation. Some of these available expressions come from a simplification of micromechanical formulations [249–253]. These expressions depend on control variables (stress or strain and temperature), on internal variables associated to different mechanisms (volume fraction of martensite, volume fraction of oriented and self-accommodated martensites, mean transformation strain, etc …) and material parameters associated with elasticity and phase transformation. The application of the first principle of thermodynamics and Clausius-Duhem conditions allows to determine driving forces associated with internal variables. The comparison of these driving forces to their corresponding yield forces allows deriving the constitutive equations of the SMA thermomechanical behavior. Additional proposed developments lead to the description of transformation saturation, inner loops related to partial transformation, and the effect of cyclic loading [246,254–259]. This kind of models presents an extension in the framework of large strains and geometrical nonlinearity [259–268].

In the following an example of constitutive equations corresponding to the description of thermomechanical behavior of a Polycrystalline SMA derived from an averaged thermodynamic approach [250,253,255]. The Gibbs free energy has the following expression:

$$\Delta G = \begin{vmatrix} -\frac{1}{2}\sigma_{ij}S_{ijkl}\sigma_{kl} - \sigma_{ij}\alpha_{ij}^{therm}\Delta T - \Delta T S^{A} - \sigma_{ij} f \overline{\varepsilon}_{ij}^{tr} - \sigma_{ij} f^{FA}\overline{\varepsilon}_{ij}^{twin} + B(T-T_0) f \\ +\frac{1}{2}H_f f^2 + \frac{1}{2} f H_{\varepsilon}\overline{\varepsilon}_{ij}^{tr}\overline{\varepsilon}_{ij}^{tr} + \frac{1}{2} f^{FA} H_{twin}\overline{\varepsilon}_{ij}^{twin}\overline{\varepsilon}_{ij}^{twin} + c_v\left((T-T_0) - T\log\frac{T}{T_0}\right) \end{vmatrix} \quad (1.12)$$

In this expression, σ and T are respectively the stress and the temperature that control the thermomechanical loading of the representative volume element (RVE). This Gibbs energy expression presents four internal variables that control the state of the RVE. Two internal variables f and $\overline{\varepsilon}^{tr}$ corresponding respectively to the volume fraction of martensite and the mean transformation orientation (strain) describe the martensitic transformation whereas f^{FA} and $\overline{\varepsilon}^{twin}$ are the two other internal variables describing the twinning of martensite and correspond to the volume fraction of twinned martensite and the associated mean twinning orientation (strain). S, α^{therm}, S^{A}, B, H_f, H_ε, H_{twin}, Cv and T_0 are material parameters corresponding respectively to the elastic and thermal expansion tensors, entropy of austenite, chemical parameter and three interaction parameters related to martensitic transformation and twinning, latent heat coefficient and the reference temperature. It is assumed that the volume fraction of twinned martensite depends on the global volume fraction and on the mean orientation strain as following:

$$\begin{cases} \dot{f} > 0 \Rightarrow \dot{f}^{FA} = \left(\dfrac{\varepsilon_{sat}^{tr} - \varepsilon_{eq}^{tr}}{\varepsilon_{sat}^{tr}}\right)\dot{f} \\ \dot{f} \le 0 \Rightarrow f^{FA} = kf \end{cases} \quad (1.13)$$

where $\varepsilon_{sat}^{tr}, \varepsilon_{equ}^{tr}$ and k are respectively the maximum mean transformation when the martensite is fully oriented, the von-Mises equivalent mean transformation strain and a material constant.

The number of internal variables is reduced to three. The application of the Clausius-Duhem inequality allows determining driving forces associated to each internal variable as following:

$$F_m^{\sigma} = \varepsilon_{ij} - S_{ijkl}\sigma_{kl} - \alpha_{ij}^{therm}\Delta T - f\,\overline{\varepsilon}_{ij}^{tr} = 0; \quad F_m^{T} = S - S^{A} + Bf - \alpha_{ij}^{therm}\sigma_{ij} + c_v \log\frac{T}{T_0} = 0$$
$$F_m^{f} = \sigma_{ij}\overline{\varepsilon}_{ij}^{tr} - B\left(T - T_0\right) - H_f\, f - \frac{1}{2}H_{\varepsilon}\overline{\varepsilon}_{ij}^{tr}\overline{\varepsilon}_{ij}^{tr} = F_y^{f}; \quad F_m^{\varepsilon^{tr}} = f\left(\sigma_{ij}^{d} - H_{\varepsilon}\overline{\varepsilon}_{ij}^{tr}\right) = fF_y^{\varepsilon} \qquad (1.14)$$
$$F_m^{\varepsilon^{twin}} = \sigma_{ij}^{d} - H_{twin}\overline{\varepsilon}_{ij}^{twin} = F_y^{\varepsilon^{twin}}$$

Where σ^d is the deviatoric stress tensor. The comparison of the driving force of each internal variable to its corresponding yield force and taking into account consistency conditions leads to identify the activated mechanisms and the system of equations to solve numerically in order to derive the thermomechanical behavior of the SMA. More details about this developed model and its specificities as the management of the inner loop related to partial transformation and/or twinning, saturation of transformation and twinning, tension compression asymmetry, etc…can be found in Chemisky et al 2011 and Duval et al. 2012 [250,255]. The following Figure 1.21 shows the capacity of SMA behavior prediction for this model under tension-compression and shear tension complex loadings.

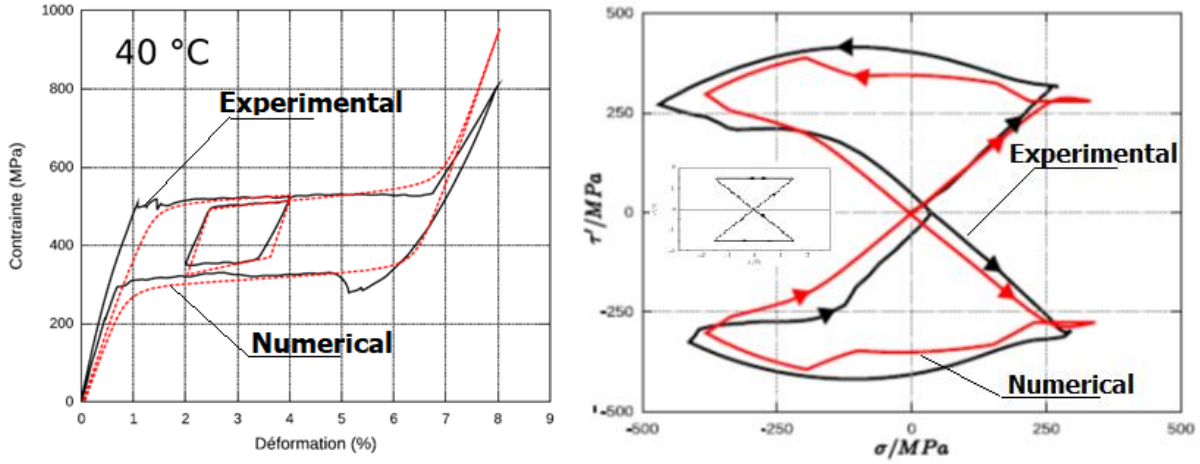

Figure 1.21. Comparison between the predicted SMA behavior and obtained experimental results for (a) tension loading-unloading and (b) tension-shear complex loading.

The last family of models considers the statistic physic theory[269] based on the local equilibrium of an SMA single crystal by combining the model detailed in by Boyd and Lagoudas[249]with the statistic physic theory to describe the reverse transformation recovery strain induced by heating. A homogenization technique with the assumption of homogeneous temperature through the RVE allowed deriving the effective behavior starting from the local behavior of each grain. Subsequently, Fischlschweiger and Oberaigner, 2012[270] developed model based on the statistic physic theory by analogy to magnetic domain switching in magnetic materials and considering an order parameter. They assumed that the thermodynamic equilibrium in the RVE level is reached for a very short time under constant stress and temperature. The entropy of the RVE is assumed reaching an extremum ensuring the canonic constraints as proposed by Le Bellac et al., 2004[271]. Additional models based on the statistic physic were developed by Müller

and Seelecke, 2001 and Müller, 2012 [272,273] and allowed to simulate the SMA pseudo-elastic behavior.

Some of these models are well adapted to an implementation in a finite element code in order to carry out numerical structural analysis of the response of SMA based applications subjected to thermomechanical loading. The implementation needs the determination, analytically or numerically, of tangent operators allowing to derive the stiffness matrices of finite elements. As an example, many SMA thermomechanical models are implemented in the finite element code Abaqus via the subroutine UMAT.

1.9 Conclusion

In the first chapter, we have presented the idea of energy harvesting and gave the state-of-the-art concerning SMA/piezoelectric composite systems. The main idea of the thesis is to combine the two smart materials for energy harvesting. Therefore, the introduction part dealt with the concept of piezoelectricity and thermomechanical modelling. Followed by this, we presented the different piezoelectric materials and in particular the piezoelectric polymers of the PVDF family. We are focused to develop a flexible composite coupled with SMA. Hence, the best material choice is from piezoelectric polymers, especially P(VDF-TrFE), which shows the highest piezoelectric coefficient. In this regard, we have introduced, the PVDF and its copolymers-based energy harvesting devices. Then we introduced the SMA, describing the two important properties: shape memory effects and superelasticity. Finally, the chapter concludes with the state of the art of thermomechanical behaviour modeling of the SMA.

We have selected classical NiTi SMA possessing shape memory effect and P(VDF-TrFE) as the piezoelectric polymer for the composite fabrication. We have tested different layered structures (one-layer and multiple layers) for the SMA-Piezo composite. Chapter two is dealing with the processing and characterization of the composite. The processing of the SMA/P(VDF-TrFE) composite consists of many steps such as the elaboration and deposition of the polymer. The deposition of metal electrodes and the polarization are the key factors of the fabrication of the composite. A detailed description of each step is given in chapter 2. In order to check the composite energy harvesting performance, we have conducted several characterization studies. The mechanical and thermal energy harvesting is done for both the P(VDF-TrFE) film and the composite. The electro-thermo-mechanical characterization of the composite was carried out using the tensile test. Finally, a new characterization system is developed for the continuous heating and cooling of the composite. Therefore, in chapter 2 we are presenting the experimental fabrication and characterization of the SMA/P(VDF-TrFE) composite to show the feasibility of the combination of the two-smart material for the generation of electric response using a two-step energy conversion mechanism.

Chapter 2

Experimental characterisation of the composite for energy harvesting

2.1 Processing of SMA/P(VDF-TrFE) composite 44
2.1.1 Materials and methods 45
2.1.2 Synthesis of P(VDF-TrFE) solution 45
2.1.3 Spin coating technique 45
2.1.4 SMA/(PVDF-TrFE) composite 47
2.1.5 Multi-layered SMA/(PVDF-TrFE) composite 48
2.1.6 Polarisation hysteresis 49
2.2. SMA/P(VDF-TrFE) composite with interface layer 51
2.2.1 PEN/P(VDF-TrFE) device 51
2.2.2 Polarisation hysteresis 52
2.2.3 SMA/Epoxy/PEN/P(VDF-TrFE) composite 53
2.2.5 Summary 54
2.3 Experimental characterization for energy harvesting 55
2.3.1 Mechanical energy harvesting performance 55
2.3.2 Output voltage 56
2.3.3 Output power 58
2.3.4 SMA/ P(VDF-TrFE) composite 59
2.3.7 Output voltage 61
2.4 Thermomechanical loading test in tensile machine for SMA/P(VDF-TrFE) device 62
2.4.1 Stress-strain -temperature 64
2.4.2 Voltage-strain-temperature 66
2.4.3 Summary 68
2.5 Micro energy harvester characterisation system 70
2.5.1 Support system and frame 72
2.5.2 Cooling and heating source 73
2.5.3 Optical lens system 73
2.5.4 Summary 74
2.6 Conclusion 75

Introduction

In this chapter, we will present the fabrication of the SMA/piezoelectric polymer composite and the electro-thermo-mechanical characterization for energy harvesting. We have selected P(VDF-TrFE) as the piezoelectric polymer thin layer and coupled with conventional NiTi SMA. P(VDF-TrFE) polymer was found a suitable candidate for energy harvesting applications due to its excellent flexibility, high piezoelectric coefficient. The processing of the composite involved different steps. Different configurations of the composite will be discussed with two layers and multilayers of SMA and piezoelectric P(VDF-TrFE) layer. The direct deposition of the P(VDF-TrFE) layer on the SMA and the SMA/P(VDF-TrFE) composite consisting of an interface layer is also described. The processing and elaboration of the SMA/ P(VDF-TrFE) composite are shown here for the first time. Therefore, a detailed discussion will be given concerning the fabrication and the polarization of the deposited polymer layer. In the second section of this chapter, we will give the obtained results. Also, the electro-thermo-mechanical characterization of the composite and the obtained electrical response is presented. Finally, we will introduce a new setup in order to characterize the electric response of the composite subjected to periodic heating and cooling.

2.1 Processing of SMA/P(VDF-TrFE) composite

The hybrid composite system is made by combining NiTi SMA and P(VDF-TrFE) as the piezoelectric polymer layer. The objective is to harvest thermal energy by coupling the two smart materials. The SMA/P(VDF-TrFE) composite is able to harvest both thermal and mechanical energy in a synergistic way. In order to fabricate the composite, we have tested different layered structure. The processing and the optimization of the final composite structure involved a series of steps such as elaboration, deposition of the polymer and electrodes. In order to deposit a homogeneous thin layer of P(VDF-TrFE) polymer on the NiTi SMA, we have used the spin coating technique. The electrodes layers of the thickness in the nanometres range were deposited using an E-beam evaporator. The P(VDF-TrFE) layer was subjected to a high voltage polarization (100 V/µm) using the contact method in order to achieve a significant piezoelectric coefficient of the film. The two types of the composite are discussed in the processing part. The first one is the direct deposition of polymers and the electrode layer on one face of the SMA. Then multiple layers of the polymer are deposited on both sides of the SMA. Finally, we will present the composite with an interface epoxy layer. The SMA/P(VDF-TrFE) composite with interface layer is used for further characterization studies. In fact, this composite geometry gives the better performance compared to the other layered composites. Then in the next section we will present the piezoelectric energy harvesting performance of the P(VDF-TrFE) polymer thin film. The mechanical energy harvesting is carried out by normal finger tapping and bending tests. Correspondingly, the thermal energy harvesting of the SMA/ P(VDF-TrFE) composite is done by oil bath heating. The electro-thermo-mechanical behaviour of the composite is characterized by a tensile test machine. Furthermore,

a particular electro-thermo-mechanical characterization system will be designed to measure the electric response from the composite during periodic heating/cooling.

2.1.1 Materials and methods

Commercial SMA purchased from Goodfellow, England, consisted of 125µm thin sheet of Ni_{55} Ti_{45} (wt%) with a start reverse transformation temperature A_s at about 62°C and forward transformation finish temperature M_f at about 51°C. This SMA is at the martensitic state at room temperature with a self-accommodated martensite. As we are dealing with the shape memory effect of the SMA, we have chosen this NiTi SMA. Also, studies showed that 55 at.% NiTi alloys exhibited high thermomechanical stability[17]. The poly (vinylidene difluoride-trifluoroethylene), or P(VDF-TrFE) powder (70/30 %, M_w = 350 000 $g.mol^{-1}$) comes from Piezotech S.A.S, France. Cyclopentanone comes from Sigma Aldrich.

2.1.2 Synthesis of P(VDF-TrFE) solution

Pellets of P(VDF-TrFE) were completely dissolved in cyclopentanone by continuous stirring at 80°C with a concentration of 14 wt%. After complete dissolution of the solvent, the solution was filtered at 2.7 µm, to help to eliminate large dust which may cause breakdown during polarization. Figure 2.1 (a) and (b) represents the schematic diagram and the original photographic image of the solution preparation.

2.1.3 Spin coating technique

Spin coating is a simple cost-effective technique for the preparation of uniform polymer films. The basic principle involves the transfer of a drop of polymer solution in the center of the desired substrate. The rotation of the substrate at high-speed leads to the formation of the functional film. This is due to the centrifugal force during the rotation. Most of the solution is spin off the edges of the substrate. Finally, a thin layer is formed on the surface of the substrate. Usually, a volatile solvent is preferred for the following evaporation. Characteristics of the film can be optimized by taking into account of certain important parameters such as rotation time and speed, and the viscosity of the solution[122,274]. Also, the main advantage of spin coating is that it acts as a mechanical stretching and improves the β phase crystal orientation in PVDF based polymers[122].

After the spinning, the annealing of the film also plays a vital role in the final thickness and the β phase content. The crystallization and solvent evaporation behavior can be varying depending on the annealing methods such as oven and hot plate annealing.

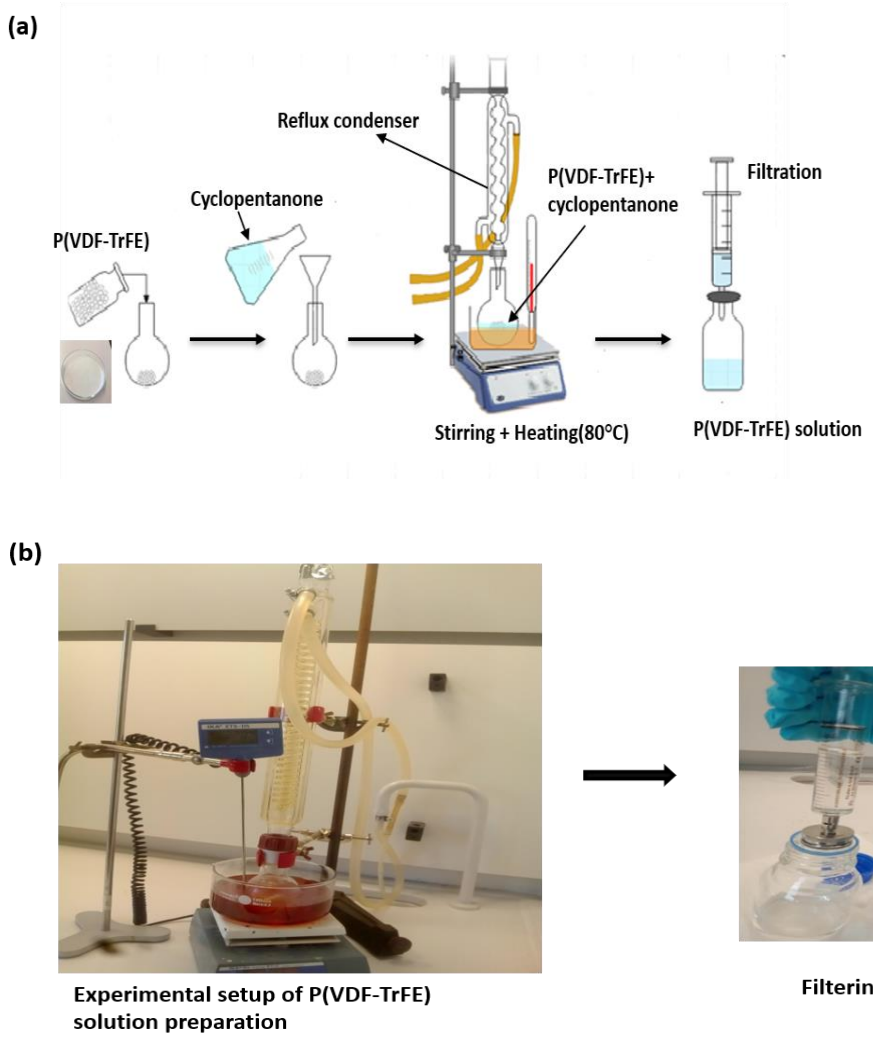

Figure 2.1 (a). Schematic diagram of the P(VDF-TrFE) solution preparation (b) Photographic image of the different steps in solution preparation setup.

For example, for the annealing in the oven, the deposited PVDF film is exposed to isotropic heating from surface to inner. That induces more crystallization of the film surface. Nevertheless, the evaporation of the solvent is weakened in the inner portion. In the case of the hot plate, annealing offers unidirectional heating of the sample from top to bottom. Therefore, it promotes faster crystallization and avoids solvent trapping[116,274].

To fabricate SMA/P(VDF-TrFE) hybrid flexible composite, we used the spin coating technique to deposit a thin layer of P(VDF-TrFE) on the SMA substrate. To enhance the piezoelectric properties, we performed both hot plate heating and oven annealing at different temperatures. Hence, the first hot plate heating helps to evaporate the solvent and the oven heating induces the crystallisation. Thus, it enhances the β phase and the final piezoelectric property of the polymer.

2.1.4 SMA/(PVDF-TrFE) composite

The SMA/P(VDF-TrFE) device was fabricated by the direct deposition of the polymer solution on to the SMA film. The NiTi SMA of thickness 125 µm was taken as the substrate. A thin film of P(VDF-TrFE) was deposited on the NiTi SMA by spin coating technique (Figure 2.2a). The P(VDF-TrFE) layer of ~4 µm thickness was obtained by rotating spin coater at 2500 rpm for the 60s. The first annealing of the film was done at 80 °C for 10 minutes, which helps to evaporate the cyclopentanone solvent. The final annealing of the film was done in the oven at 138° C for 2 hr. The goal of this final annealing is to optimize the crystallization of the polymer, thereby enhancing the piezoelectric properties. NiTi itself acts as a bottom electrode during the polarization of the polymer film. Therefore, one top electrode was sufficient for the composite. This top electrode of Cr/Al (150 nm) was deposited by evaporation on the top of the polymer layer. The fabricated SMA/P(VDF-TrFE) composite with top Cr/Al electrode is shown in Figure 2.2(b).

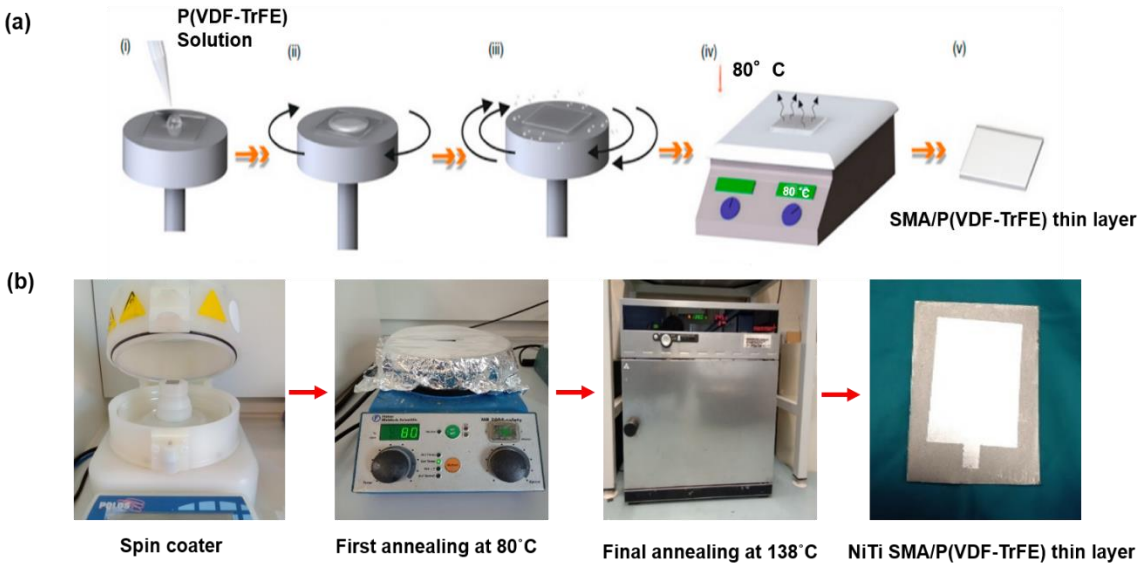

Figure 2.2. SMA/Polymer composite film preparation (a) different steps of spin coating to form the polymer layer on SMA (b) Photographic image of the spin coater and the annealing steps for SMA/P(VDF-TrFE) composite.

The electrode deposition was done using E-beam deposition in the cleanroom (
Figure 2.3a and b). The electrodes were designed with a tail geometry. This tail geometry is required for the polarization in the proceeding steps. The tail end of the electrodes is connected to the radiant testing system, shown in figure 2.4. The electrodes are deposited on top of the P(VDF-TrFE) layer with the help of masks. The polyethylene naphthalate (PEN) is used for the fabrication of the mask. The mask with a tail end was made using laser cutting. The SMA/P(VDF-TrFE) composite was loaded inside the E-beam evaporator. The mask was put on top of the polymer, in this way, it is possible to deposit the electrodes only in the required area of the polymer with different electrode patterns. The schematic illustration of the electrode deposition using a mask is given in Figure 2.3(c). In order to get a sufficient vacuum for the polymer, the

composite is kept for 12 hours inside the evaporator. The chromium (Cr) electrode of thickness 10nm was first deposited on the polymer, which functions as an adhesive layer. Finally, the Aluminum (Al) layer of thickness 150 nm was deposited on the top of the Cr layer. The schematic illustration and the original image of the SMA/P(VDF-TrFE) composite with an active area of 1.6 cm×2.3 cm is shown in Figure2.3(c).

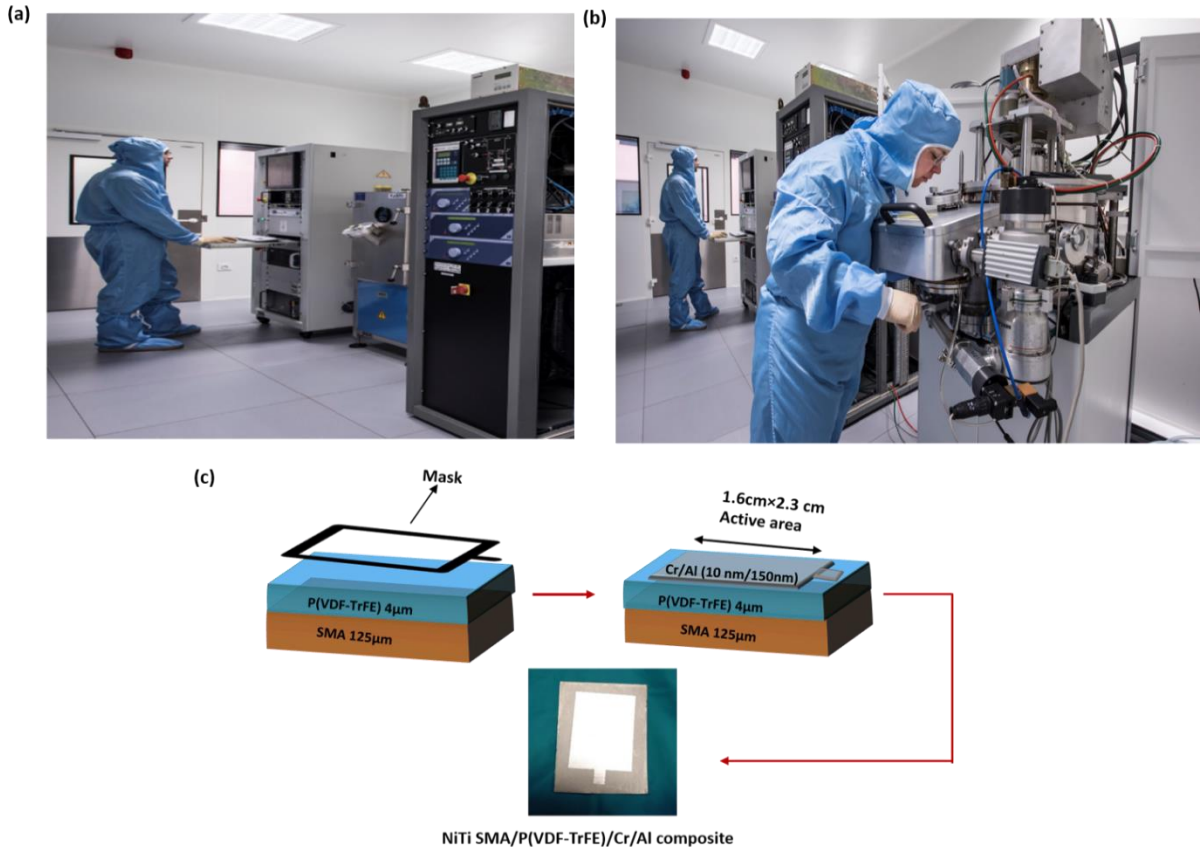

Figure 2.3 Electrode deposition process (a) Image of the E-beam evaporator (b) The whole view of the cleanroom for material deposition (c) schematic representation of the electrode deposition and the image of the SMA/P(VDF-TrFE)/Cr/Al composite.

2.1.5 Multi-layered SMA/(PVDF-TrFE) composite

In this composite, thin layers of P(VDF-TrFE) film have been deposited on both sides of SMA. The same procedure as one-layer SMA-polymer deposition was followed. The main benefit is that SMA serves the function of the bottom electrode for the polarization of the polymer on both sides. To fabricate the multiple layers the solution of P(VDF-TrFE) was spin-coated on both sides of the SMA substrate. On each side, the thickness of the polymer layer was ~4.3µm +/- 1 µm. It was attained by using the same parameters of rotation at 2500 rpm for the 60s. Then the film was pre-heated at 60° C for 10 minutes and followed by annealing in air at 138° C for 2 hr. Finally, the top electrode of Cr/Al (150 nm) was deposited on both sides of the polymer layers by evaporation (Figure 2.4).

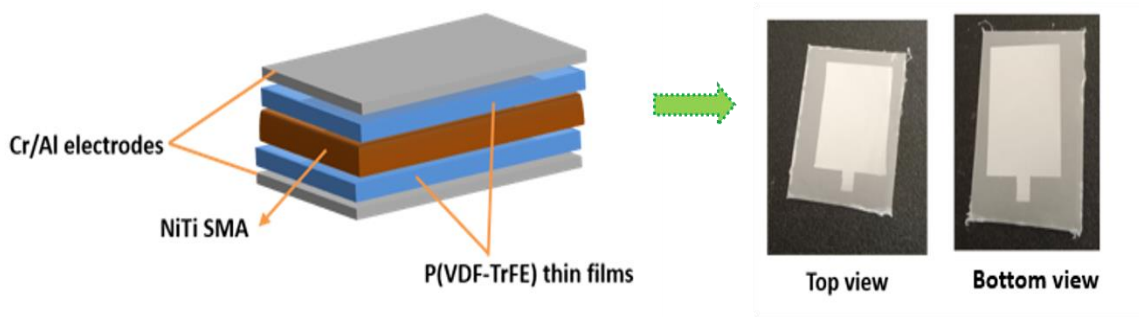

Figure 2.4.SMA/P(VDF-TrFE) multilayer composite structure and photographic image of the device top view and bottom layer view on the right.

2.1.6 Polarisation hysteresis

The P(VDF-TrFE) polymer was subjected to poling to orient the polarization of the ferroelectric domains to enhance the piezoelectric properties. The electric polarization is achieved by the direct contact method. The polarization (P)- voltage (V) hysteresis loops were obtained from the ferroelectric testing system (Radiant Technologies, Precision LCII) connected to a high voltage interface, applying an electric field of a maximum of 100 V/µm at 0.2Hz along the thickness direction at room temperature.

The high voltage is applied using the ferroelectric test system, along with a Vision software capable of generating sample stimulus signals by executing small sub-programs known as tasks. The system consists of a High-Voltage-Interface (HVI), High-Voltage Amplifier (HVA) and a precision tester. The HVI functions as an interface between the HVA and the precision tester. The HVI provides security for equipment and human operators by guarding against high voltage being applied to the sample. HVI also provides a logical signal to the vision software through the precision tester to indicate it is present. HVI also contribute to the enabling of high voltage measurement. The HVA provide high voltage by taking the low voltage input signals and scales them upwards by a constant gain factor to produce the high voltage output. The signal reaches the sample through the HVI. The signals to and from the sample are provided by and to the High-Voltage Interface. One sample electrode is connected directly to the HV DRIVE port and the other to the HV RETURN port. The whole system with the sample connected to the drive and returns ports are shown in Figure 2.5.

The electric poling of the P(VDF-TrFE) film on NiTi SMA substrates was done by the application of an electric field of 100V/µm to align the dipoles in the film with the thickness direction. The electric field is increased by applying the potential between the two electrodes. Here NiTi SMA is taken as the bottom electrode and the deposited Cr/Al top electrode. The maximum electric field (100V/µm) was achieved by several cycles of the voltage increment. For each cycle, a short increment of the voltage of 10 V/µm was applied, which helps to avoid the breakdown of the film.

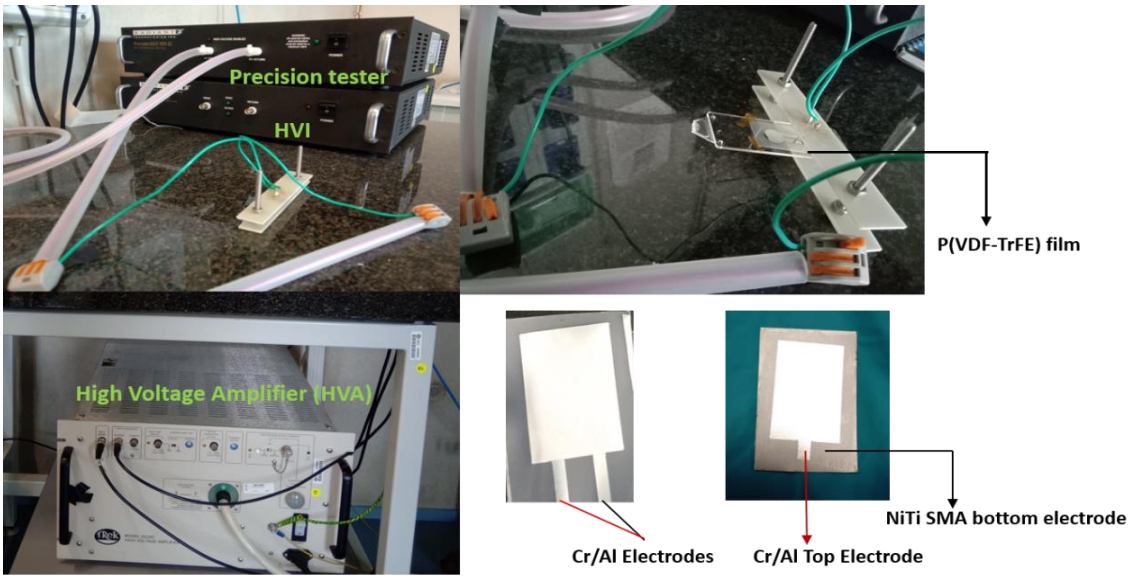

Figure 2.5. Precision system applying A high voltage through the HVI with P(VDF-TrFE) samples connected.

The polarization versus the electric field (P-V loop, voltage normalized in voltage per micrometer) for both the top and bottom layers of P(VDF-TrFE) on SMA is represented in Figure 2.6.

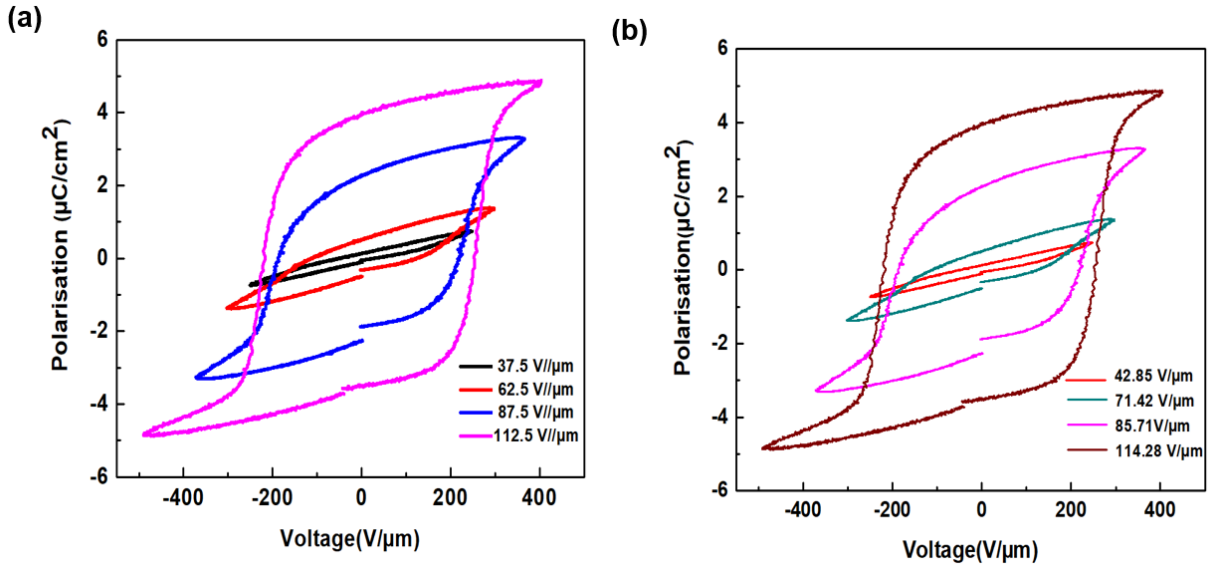

Figure 2.6 Polarisation hysteresis loop of SMA/P(VDF-TrFE) composite (a) bottom layer (b) top layer.

The polymer exhibits a P-V loop with a coercive field (Ec) of 260 V/μm and saturation polarization (Ps) of 4.9 μC/cm^2. Polarization saturation (Ps) of about 7 μC/cm^2 is reported for P(VDF-TrFE) films[275,276].These values are less compared to the reported Ps value for pure P(VDF-TrFE) polymer, related to an electric breakdown of the sample observed when the voltage increased above 400V. The obtained d_{33} values for SMA/P(VDF-TrFE) device is 22.8 pC/N. The

poling was achieved by an electric field of 112.5 V/µm for the bottom layer and 114.28 V/µm for the top layer of the polymer on SMA. The small difference in the electric field is due to small variation in thickness of the film on both sides of the SMA.

2.2. SMA/P(VDF-TrFE) composite with interface layer

For our first samples, the polymer solution was directly deposited on the SMA and poling of the polymer layers was done. However, it showed some drawback for energy harvesting because, after poling, the charge was disappearing through the SMA layer. Furthermore, this configuration is not suitable for repeated cyclic heating-cooling or bending of the device due to the delamination of the PVDF layer from SMA. To enhance the interface bounding and the voltage output from the device, we have introduced an additional layer in between the P (VDF-TrFE) and SMA layer. For that, we have deposited the P(VDF-TrFE) on top of a flexible polyethylene naphthalate (PEN) substrate, and which is bonded well with the SMA sheet using epoxy glue. The detailed steps for the fabrication process are discussed below.

2.2.1 PEN/P(VDF-TrFE) device

The device was fabricated on a flexible sheet of polyethylene naphthalate (PEN) with a thickness of about 50 µm used as a substrate. The bottom electrode consisted of 150 nm thick Aluminum (Al) layer and a 10 nm thick Chromium (Cr) as an adhesion layer. The Cr/Al (150nm) was deposited by evaporation on the PEN. Thin film was deposited on the metallized PEN substrate by a spin coating technique. The P(VDF-TrFE) film of ~5 µm thickness was made by rotating spin coater at 2500 rpm for the 60s. After that, the film was pre-heated at 60° C for 10 minutes, this helping to evaporate the cyclopentanone solvent. Afterwards, the film was exposed to annealing in air at 138° C for 2 hr. The goal of this final annealing is to maximize the crystallization of the polymer thereby enhancing the piezoelectric properties. Finally, the top electrode of Cr/Al (150 nm) was deposited by evaporation. The fabrication steps are illustrated in Figure 2.7

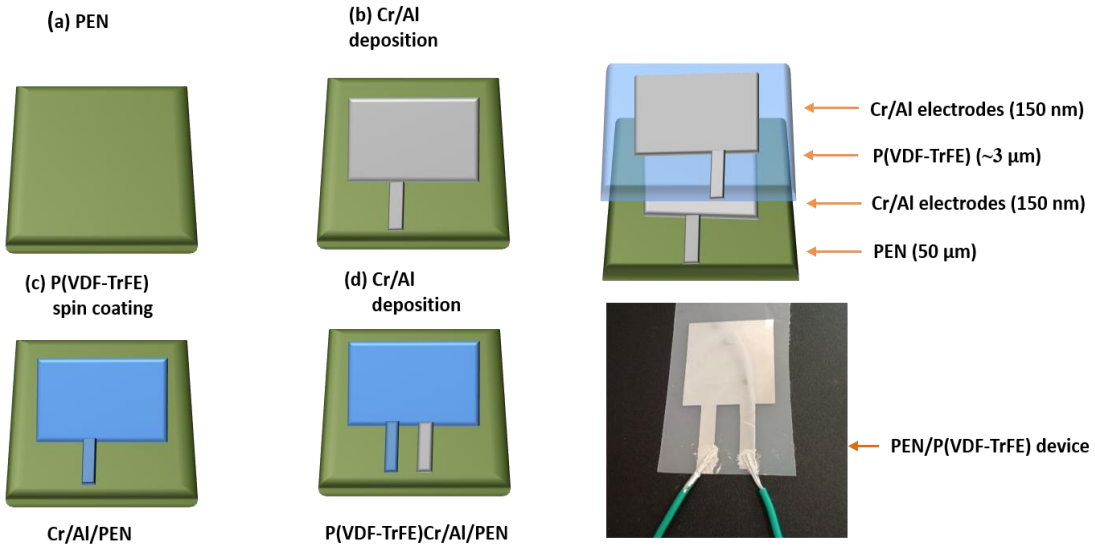

Figure 2.7 Schematic diagram of the fabrication process of the flexible piezoelectric energy harvesters. Different steps of the processing of the PEN/P(VDF-TrFE) film and the photographic image of the original composite.

2.2.2 Polarisation hysteresis

The electric poling of the P(VDF-TrFE) on PEN sheet was done as the same way as mentioned above for the SMA/polymer system. The P-E loop for the material is represented in Figure 2.8. It shows a saturation polarization (P_s) of about 7.6 µC/cm^2, which is in good agreement with the reported literature values [277,278].

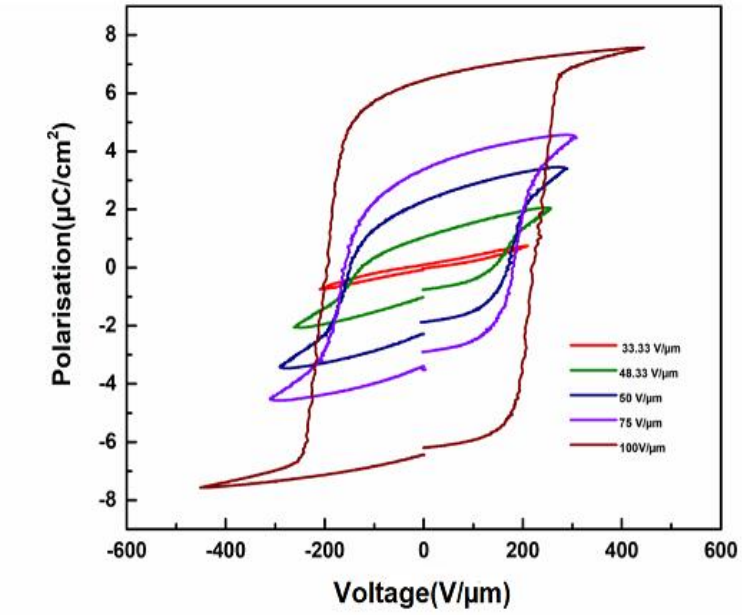

Figure 2.8 Polarization hysteresis loop of P(VDF-TrFE) on PEN.

2.2.3 SMA/Epoxy/PEN/P(VDF-TrFE) composite

To study the performance of SMA/P(VDF-TrFE) composite, several geometries and configurations were tested. To assemble SMA thin-film sheet on P(VDF-TrFE), a flexible epoxy glue was used as an interface. The SMA thin plate of thickness 125 µm with an area of 1.8 cm × 2.5 cm was cleaned with acetone and isopropanol, then spin coating technique was used to homogenize the thickness of the interface epoxy layer (Figure 2.9). After that, the PEN/Al/P(VDF-TrFE)/Al device was glued together, followed by at least 24 h drying at room temperature. The epoxy layer plays the role of a bonding layer that also allows and follow the deformation made by SMA and effectively transfer the stress to the polymer layer. Therefore, it improves the coupling between the two active layers and the final output energy harvesting performance.

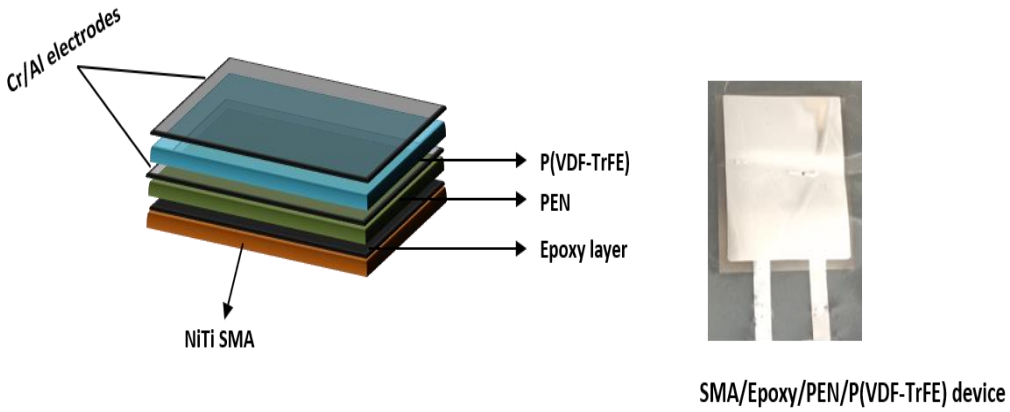

Figure 2.9 . SMA/PEN/P(VDF-TrFE) composite multilayer structure with epoxy as an interface bonding layer and photographic image of the final device.

2.2.4. Differential scanning calorimetry (DSC) measurements

The DSC results obtained for the $Ni_{55}Ti_{45}$ SMA are illustrated in Figure 2.10 . During heating, the endothermic peaks appear. The transformation to austenite starts (A_s) at 62° C and finishes the transformation (A_f) at 71° C. Similarly, during cooling process, the exothermic transformation from austenite to martensite takes place. The martensitic start (M_s) and finish (M_f) are recorded at 58° C and 51° C respectively. The SMA is martensitic at room temperature.

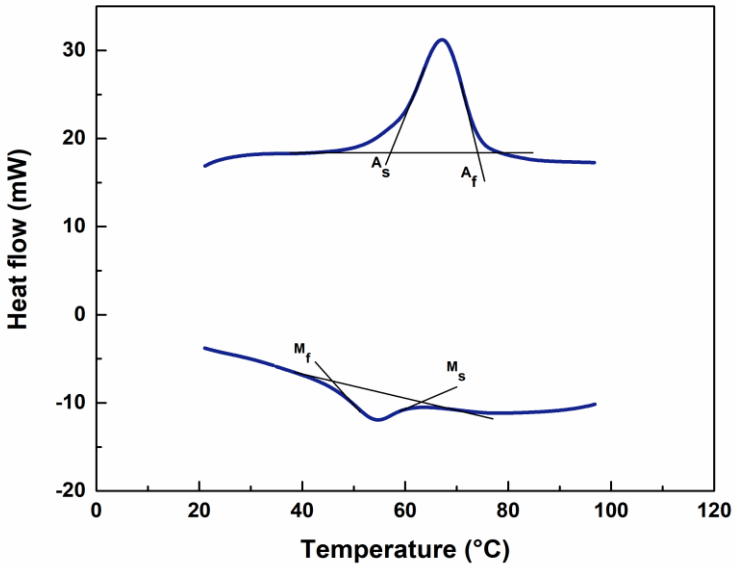

Figure 2.10 DSC curve for Ni55Ti 45 SMA showing transformation temperatures.

2.2.5 Summary

A novel hybrid composite composed of a fully flexible SMA film and a thin layer of the piezoelectric polymer was successfully fabricated and tested. The experimental preparation of the polymer, the deposition of the thin layer of the polymer on the SMA and the piezoelectric properties of the composite were studied. At first, the direct deposition of a thin polymer layer on SMA using spin coating technique showed some drawbacks such as electric breakdowns of the polymer after a certain applied electric field and losing the piezoelectric properties. In addition, the interface bonding between the SMA and polymer layer was not adequate. The delamination was observed due to the plastic behaviour of the polymer layer. Therefore, to improve the interface adhesion, we have developed a new composite structure, where the polymer layer is deposited on a thin flexible PEN substrate and sticked with SMA using a thin layer of flexible epoxy glue. This composite shows better performance and good adhesion strength.

However, there are still possibilities to increase the device flexibility and bonding by different methods. For example, certain chemical treatments and etching of the SMA surface can increase the bonding between the polymer layers. Also, silane coupling agents are considered to be an effective solution for interface adhesion. The addition of ceramic or nanofillers to the polymer membrane will also improve the piezoelectric properties and enhanced composite performance for energy harvesting.

2.3 Experimental characterization for energy harvesting

The following section presents the specific characterization of the P(VDF-TrFE) thin film and the SMA/P(VDF-TrFE) composite with regards to energy harvesting applications. There are immense research activities performed and published in this area. However, a limited number of studies are reported in the field of coupling different smart materials to improve the functionalities and energy harvesting performance. In this regard, some of the literature studies are carried out on the coupling of SMA and piezoelectric materials for energy harvesting. Here we are going further on this topic to demonstrate the experimental characterization of the hybrid composite. In this section, we present the thermal and mechanical energy harvesting performance of the composite.

We present two different sorts of device, one using P(VDF-TrFE) on PEN and the second one is P(VDF-TrFE) coupled with SMA. The characterization includes the simultaneous conversion of mechanical and thermal energy into electrical energy. In addition, the electro-thermo-mechanical response of the composite is tested using a tensile machine having a heat chamber. Here we obtain some recent significant improvements of this composite. The final goal is to convert the waste heat into useful electrical energy to power small scale electronic devices. Therefore, the characterization process needs the acquisition of an additional system for the faster heating and cooling of the composite. Henceforth, we gave designed a new microharvesting device to characterize the electrical response of the composite providing periodic heating and cooling. These results will serve as a baseline for this kind of composite devices.

2.3.1 Mechanical energy harvesting performance

In order to check the energy harvesting performance of the manufactured composite, we have applied the mechanical force by finger tapping and bending. Due to the flexible nature of the composite, the several bending and releasing test is carried out to show the working mechanism of the piezoelectric composite. The piezoelectric properties of the P(VDF-TrFE) film on the PEN substrate and the P(VDF-TrFE) film coupled with SMA have been measured by using an oscilloscope (Keysight DS01012A) and picoammeter (Keithley 6485). The PEN/ P(VDF-TrFE) and SMA/ P(VDF-TrFE) devices are subjected to repeated human finger tapping and bending and the voltage, current and power output are measured. The voltage, current and power output from the composite is recorded. Figure 2.11 illustrates the experimental setup for the piezoelectric energy harvesting.

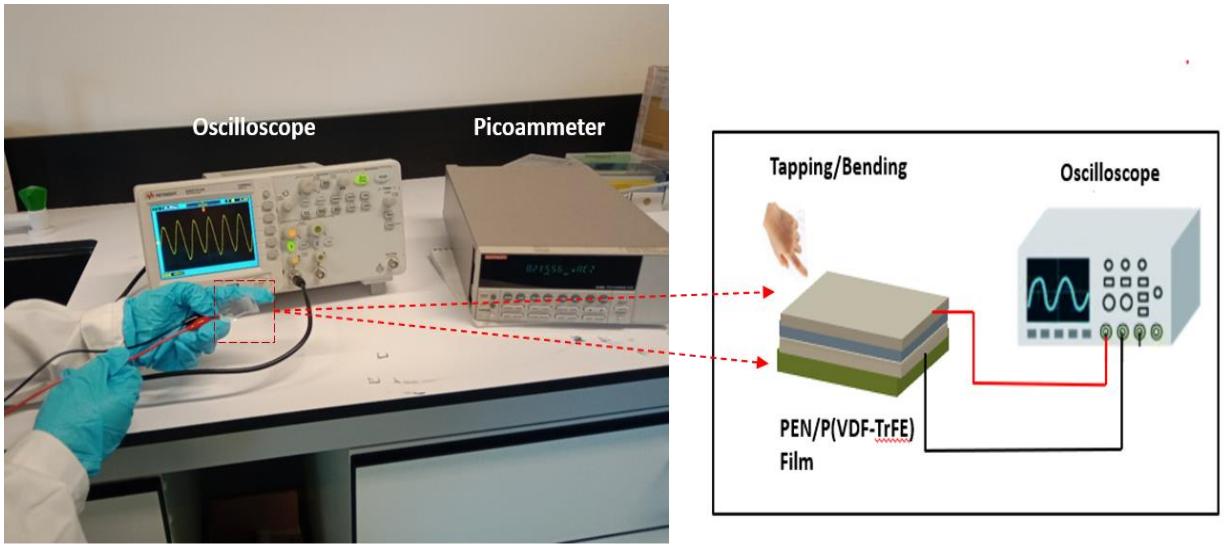

Figure 2.11 The experimental setup and the schematic representation for the piezoelectric energy harvesting.

2.3.2 Output voltage

To check the ability of the piezoelectric energy harvesting performance of the PEN/P(VDF-TrFE) film, compressive uniaxial stress was applied on the device by repeated human finger tapping. The device is able to convert the human finger tapping movements into electricity under pressing and releasing motion. It was observed that during finger tapping an output voltage of 4.5V to 5 V and current of ~1.1 µA was obtained from the device (voltage is measured in an open circuit and current in short circuit). The voltage output from the PEN/P(VDF-TrFE) film is represented in Figure 2.12(a). The fact is that during the finger pressing the piezoelectric potential is developed due to the alteration of the polarization in the material. The piezo potential is developed and induced between the top and bottom electrodes (Figure 2.13). The potential difference between the two-electrodes transient the passing of free electrons (i.e., current) in the electrodes leading to a positive voltage peak. When the stress is released immediately, the negative voltage output is developed due to the decreasing of the piezoelectric potential and the discharging of the accumulated electrons. This process is repeated several times under pressing and releasing state to obtain the periodic output electric signal from the piezo device.

The output performance of the device is also measured during the cyclic bending and releasing motion using human finger impression (Figure 2.12b). This result demonstrates the high flexibility and sensitive nature of the device. During bending, the device generated an output voltage of 8 V and current of 2 µA.

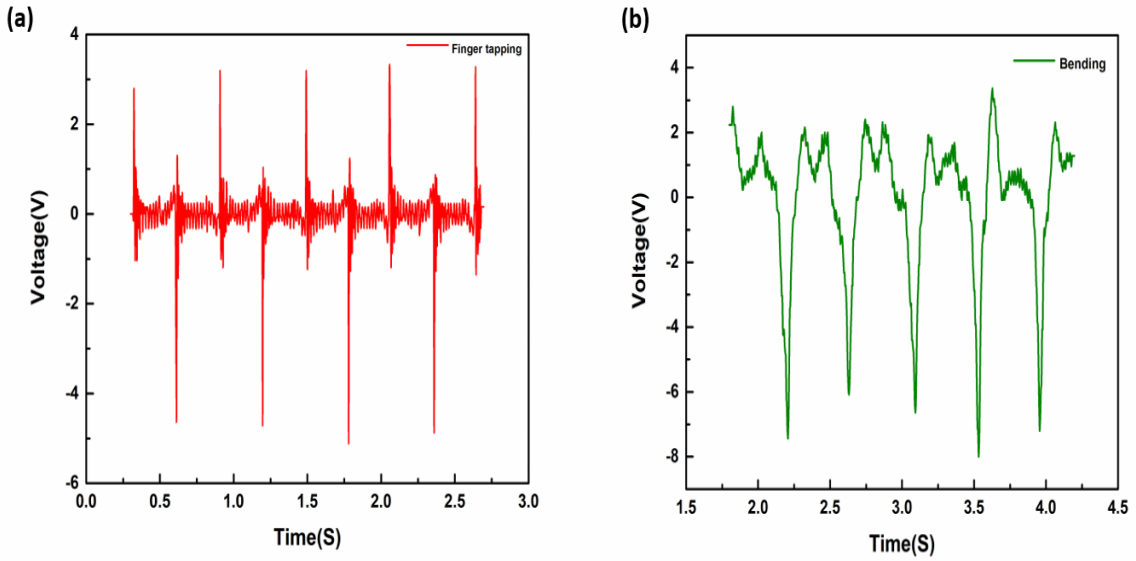

Figure 2.12. Output voltage generated from the PEN/P(VDF-TrFE) composite subjected to different deformation (a) finger tapping (b) bending.

A high output voltage and current is produced from the composite during bending and releasing motion compared to the finger tapping. This is due to the high area of deformation under bending deformation. The voltage peaks are wider for bending because the time taken for bending is quite high compared to that of the finger tapping. This peak output is calculated based on the maximum voltage generated in a cycle.

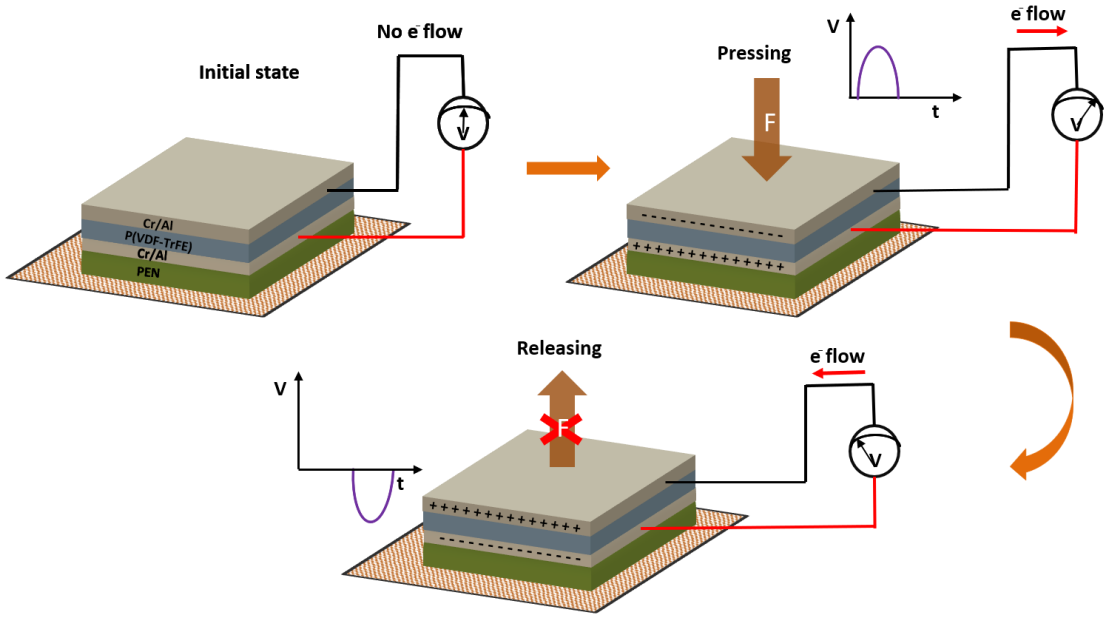

Figure 2.13 Schematically showing the working mechanism of the PEN/P(VDF-TrFE) film.

2.3.3 Output power

The power output (P = VI) is first calculated from the open circuit voltage and short circuit current measurement by considering the peak output values. During finger impression and bending, the power output of the P(VDF-TrFE) film is 5.5 µW cm^{-2} and 16 µW cm^{-2} respectively. This method is not the best practical solution for a real-time application, this kind of power output measurements giving an overestimated power value since the voltage is measured across a very high resistance and the current across a very low resistance. In this regards, it is more appropriate to measure the voltage across resistance[279]. Hence, the best practical test for energy harvesting technologies is to measure the voltage across a range of resistive loads[279,280]. Therefore, in this study, we performed the test for the PEN/P(VDF-TrFE) device by bending and recorded the peak voltage across various load resistors. Figure 2.14 represents the power and current output measured across resistors ranging from 1 KΩ to 5 MΩ (0.001, 0.046, 0.5, 1, 5 MΩ). A maximum power value of 6.25 µW cm^{-2} was observed, across a load resistor of 1 MΩ (Figure 2.15).

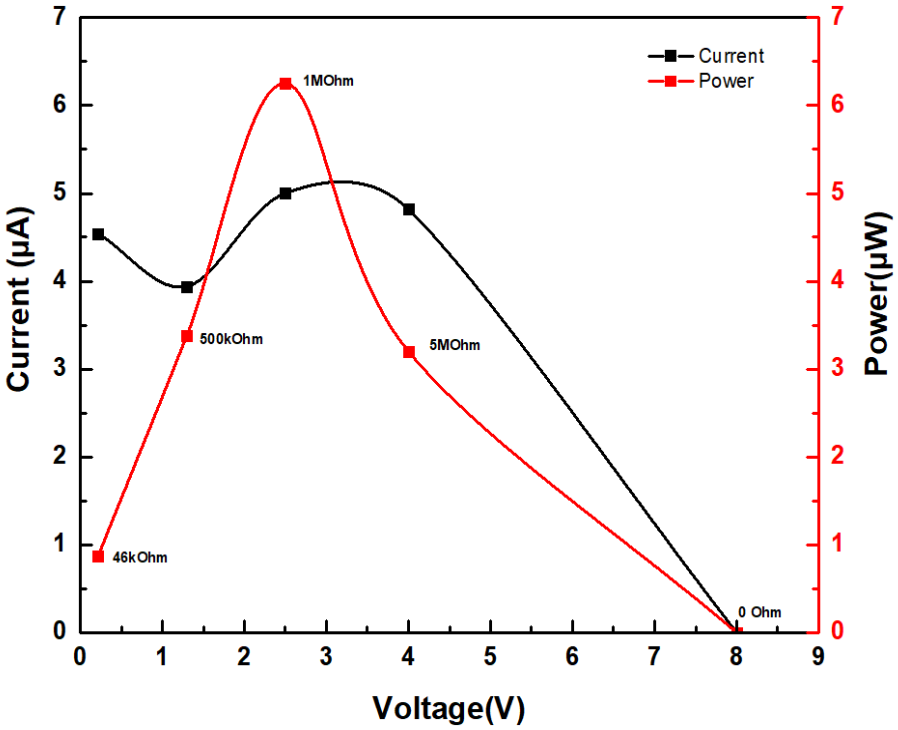

Figure 2.14. Power and current output of the PEN/P(VDF-TrFE) film.

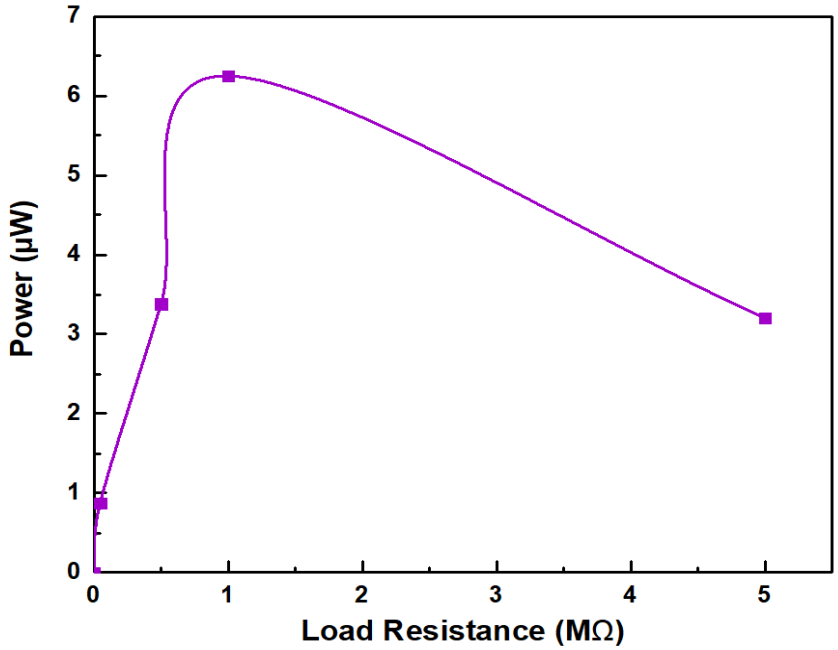

Figure 2.15 Power output of the PEN/P(VDF-TrFE) film across various load resistors.

From, the power output measurement; it is observed that a higher power output was observed on bending deformation. It is due to the higher area of deformation of the film during bending compared to finger tapping. In other words, the voltage response depends on the conditions of the application of mechanical constraints (swept area and effect of time). It is also possible to increase the peak value merely by increasing the strain rate that we apply to the device.

2.3.4 SMA/ P(VDF-TrFE) composite

First, we performed the energy harvesting on SMA/P(VDF-TrFE) composite and implemented it by doing the normal finger impression. It was observed that the charges created on the piezopolymer layer were disappearing due to the conducting nature of the SMA substrate. Therefore, to overcome this problem, another device was made using an interface layer in flexible epoxy. The processing of the composite is described in section 2.2.3. SMA/PEN/P(VDF-TrFE) shows good flexibility and the whole device follow easily the deformation made by the SMA layer. The mechanical and thermal energy harvesting performance of the P(VDF-TrFE) film coupled with NiTi SMA composite will be discussed in the following sections. The mechanical force is applied using finger tapping in the same method implemented for the PEN/P(VDF-TrFE) film. The thermal energy harvesting is performed in an oil bath heating. In both cases, the piezoelectric output voltage is measured with an oscilloscope. The electro-thermo-mechanical characterisation of the SMA/P(VDF-TrFE) composite is carried out using a tensile machine.

2.3.5 Mechanical energy harvesting

In order to implement the mechanical energy harvesting, normal finger tapping was carried out on the whole six-layer assembled sample. The results showed good agreement with the PEN/P(VDF-TrFE) device. The device produces an output voltage of 2.5 to 3 V, current of 1 µA and power output of 3 µW (P = V/I, calculated from open circuit voltage and short circuit current) during the finger tapping (Figure 2.16).

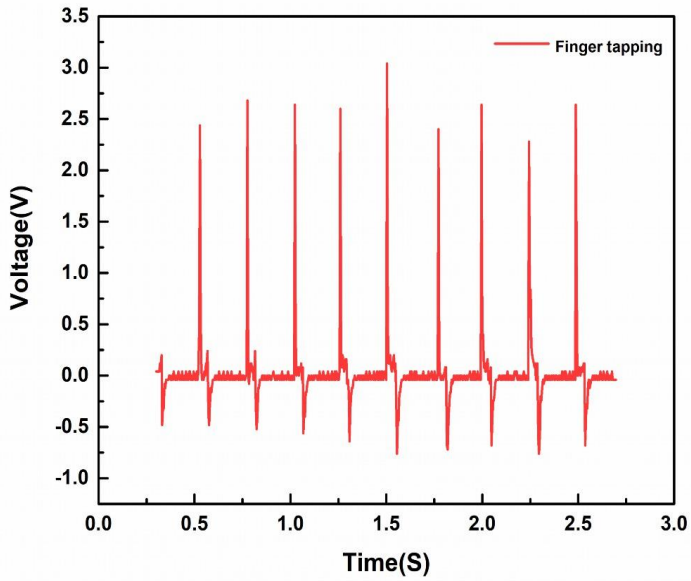

Figure 2.16 Output voltage generated from the SMA/PEN/P(VDF-TrFE) composite under finger tapping.

From the voltage output graph, it is noticed that the arising positive output is higher than the negative peak because of the fast finger impartation and slow-releasing motion of the human finger demonstrating the dependence of the output voltage on the strain rate.

2.3.6 Thermal energy harvesting

In order to evaluate the prepared composite and the impact of the NiTi SMA layer during the heating induced deformation, the sample should be heated at a temperature above A_s. Moreover, the heating should be carried out in a well-controlled and measurable way. Several methods exist to heat the SMA material such as electric current heating, water bath heating and oil bath heating[281,282]. Each of these methods has its own advantages and disadvantages depending on the working conditions, composite configuration, and applications. In this study, we are using oil bath heating because it will provide homogeneous heating of the system.

The heating system consists of a silicone oil bath. The temperature was set manually in a thermal heater provided with a sensor to accurately measure the temperature. Prior to the

measurement, the oil bath was stabilized at a given temperature for 15 minutes, and the accurate temperature can be seen in the temperature sensor. The cooling was done at room temperature by natural cooling. The sample was placed inside the oil bath and the voltage output was measured in an oscilloscope. The following section gives the measurement results from the oil bath heating. Figure 2.17 presents the oil bath heating system along with the SMA/P(VDF-TrFE) sample connected to the oscilloscope.

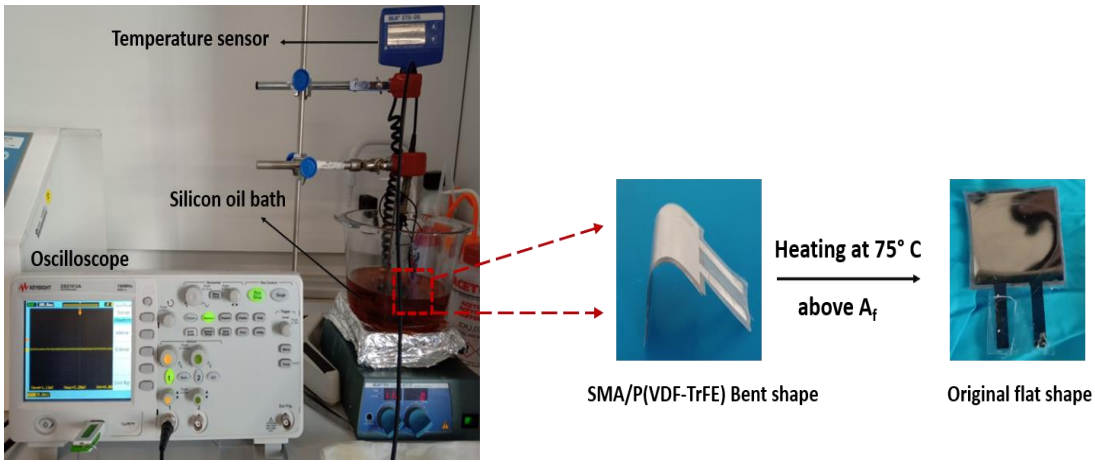

Figure 2.17 Oil bath heating system along with the sample and oscilloscope.

2.3.7 Output voltage

To demonstrate the thermal energy harvesting from the device, the whole device was bent at room temperature. Then the bent device was placed in a silicon oil bath and the temperature was progressively set as 75° C. Upon heating above 62°C, the NiTi shape memory alloy underwent a structural phase transition and was restored to its original flat shape. Accordingly, the P(VDF-TrFE) device also follows a drastic shape change, which yields an output voltage. An oscilloscope was used to measure the voltage from the device. An output voltage of ~2 V is obtained during the reverse phase transformation of the SMA (Figure 2.18). When the device returns to its original shape, the stress is created in the piezoelectric layer. During heating due to the reverse martensitic transformation, a change associated with the SMA induces the strain recovery and, it was transformed into a piezoelectric voltage. Therefore, this result gives the feasibility of the device, for one cycle of heating, to successfully transforming the thermal to mechanical to electrical energy. To demonstrate performance over multiple cycles, we have designed a microharvester device. This new setup is developed in such a way that, it can measure the electric response by subjecting to periodic heating and cooling of the composite. Hence, the obtained results show the feasibility of the hybrid composite coupled with SMA which can convert the thermal-mechanical energy into electrical energy. This approach opens the development of a new hybrid composite to power small scale electronic devices.

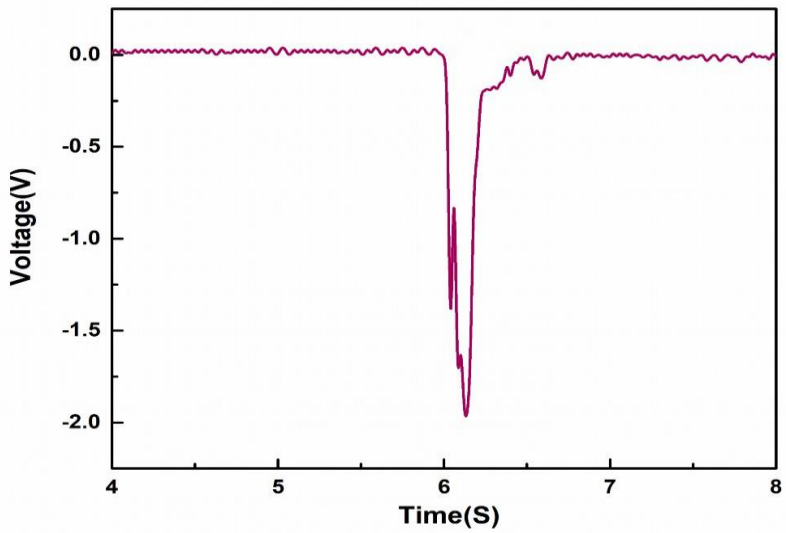

Figure 2.18 Output voltage generated from the SMA/P(VDF-TrFE) composite during thermal loading.

2.4 Thermomechanical loading test in tensile machine for SMA/P(VDF-TrFE) device

For SMA/P(VDF-TrFE) composite, tensile loading, unloading, and heating tests are conducted in a tensile machine to investigate the electrical response from the piezoelectric polymer layer on the deformation of the SMA layer. The uniaxial tests are carried out on a Zwick© LTM1 tensile machine equipped with a temperature chamber integrated with the testing machine (Figure 2.19a). The corresponding longitudinal strain is evaluated from the displacement measurement. The voltage measurements were recorded using the LabVIEW software with the help of an Arduino board. The SMA/P(VDF-TrFE) composite specimen have a rectangular shape with a total length (L) of 50 mm and width (W) of 5 mm respectively. The active area of the sample presents a length of 35.32 mm between the clamps. The dimension and the specification of the specimen used for the test are illustrated in Figure 2.19(b).

The tensile test is implemented by several steps as follows: (1) tensile loading the sample to 80 ˚C MPa (σ_{max}) at room temperature (24 °C) with a stress rate was set as 2 MPa.s^{-1} (2) unloading the sample to a zero-stress level; and (3) heating up to about 80 °C with a heating rate of 10°C/minute. The induced voltage is measured during this step (4) cooling to room temperature. The induced voltage is measured between the two Cr/Al electrodes deposited on each side of the polymer layer. The evolution of the whole process during the tensile test is graphically presented in Figure 2.20. The austenite (A_f) and martensite (M_f) finish temperatures were 71 °C and 51 °C, respectively as measured by a differential scanning calorimetry (DSC) test.

(a) Zwick© LTM1 tensile machine with thermal chamber

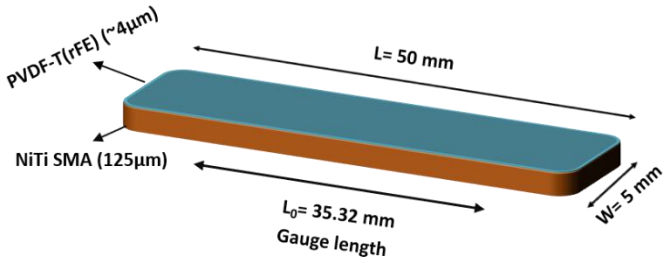

(b) Dimension of the SMA/P(VDF-TrFE) composite for tensile test

Figure 2.19. The tensile machine with its thermal chamber (b) Schematic representation of the dimension of the SMA/P(VDF-TrFE) composite.

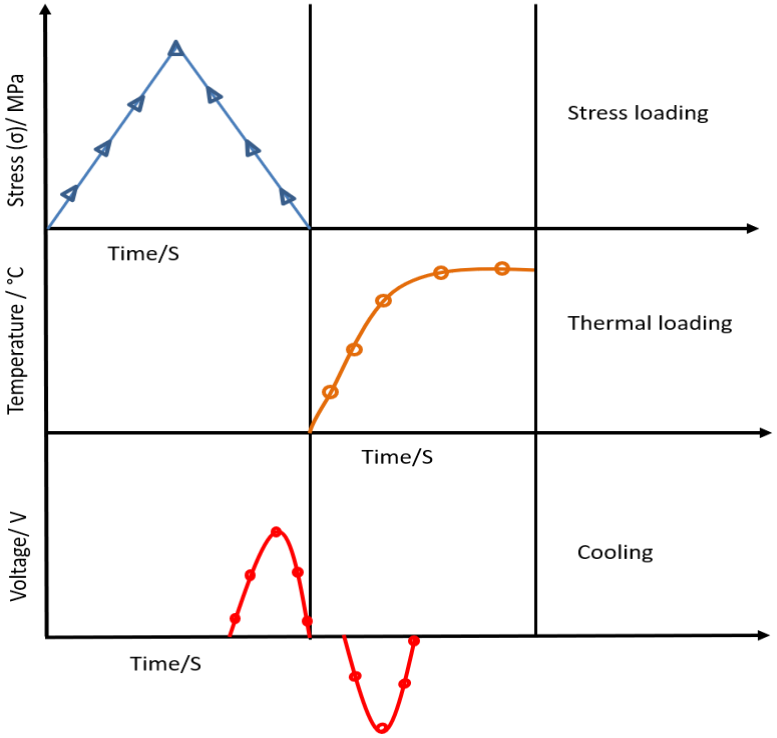

Figure 2.20. The graphical representation of the evolution of the electric voltage under thermomechanical loading.

The application of a maximum stress during the loading phase and subsequent unloading shows a complete hysteresis of the one-way shape memory effect. Figure 2.21(a) depicts the

schematic and photographic representation of the mechanical loading and subsequent measurement of the output voltage from the composite. The composite specimen is clamped inside the machine as given in Figure 2.21(b).

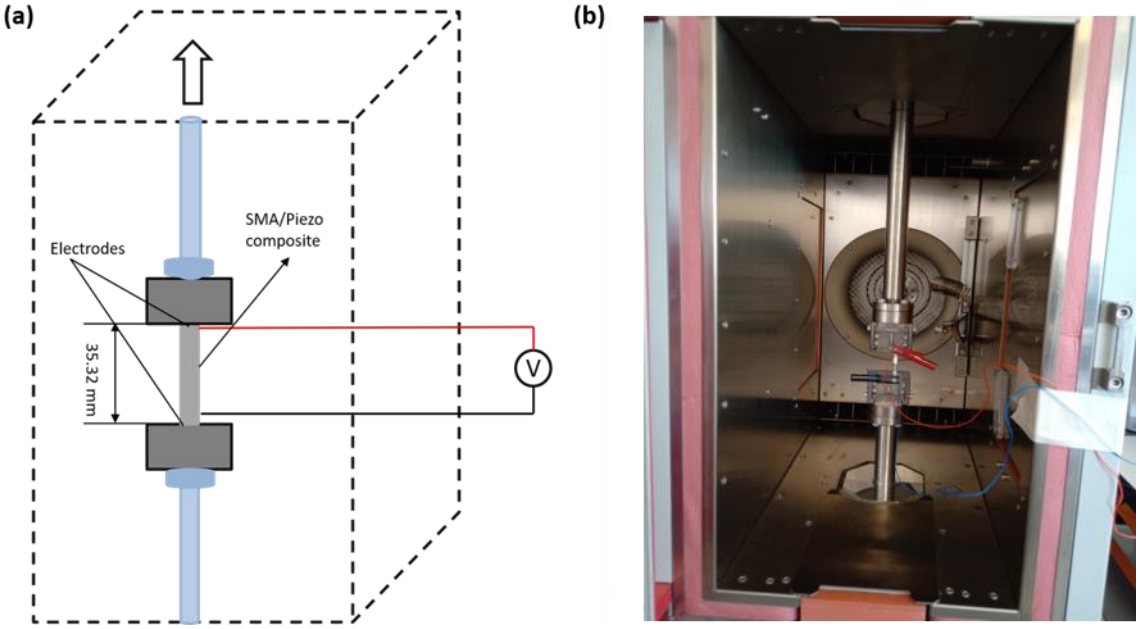

Figure 2.21. (a) Schematic diagrams of the tensile test (b) Tensile machine with SMA/P(VDF-TrFE) composite clamped inside the chamber.

2.4.1 Stress-strain -temperature

The shape memory effect was obtained during the tensile test. The maximum obtained strain is 4.2%. Figure 2.22 shows the stress-time and stress-strain relationship of NiTi SMA specimen under mechanical loading.

Initially, the NiTi SMA possesses the twinned martensitic phase because the testing temperature was lower than the M_f temperature. In this study, we are working with low stress for the reason that the application of higher stress and temperature leads to the depolarization of the thin polymer layer.

At first, during the mechanical loading, the specimen elastically deformed and inelastic deformation occurred when the applied stress reached 80 MPa, resulting from the martensitic reorientation that is interface movement of different martensite variants. After that, the mechanical unloading to a zero-stress level was carried out. In this step, the reoriented martensitic phase mainly underwent elastic unloading. However, an inelastic strain has remained even after complete unloading. Subsequent thermal loading (absence of stress), the reverse transformation initiates and the reoriented martensitic phase starts to transform into the austenite phase when the temperature reaches A_s. The increase in temperature leads to

the increase in the austenitic phase volume fraction and the inelastic strain decreases continuously. As the temperature reaches 71 °C (A_f) the transformation to the austenite phase is completed. Hence the strain retained after mechanical unloading is significantly recovered through the heating process. During the following cooling, the austenitic phase transforms into the twinned martensitic phase since the absence of the stress. Using tensile loading and unloading, we present one cyclic loading and heating of the composite specimen. The 3D graphical representation of the stress-strain-temperature relationship is shown in Figure 2.23.

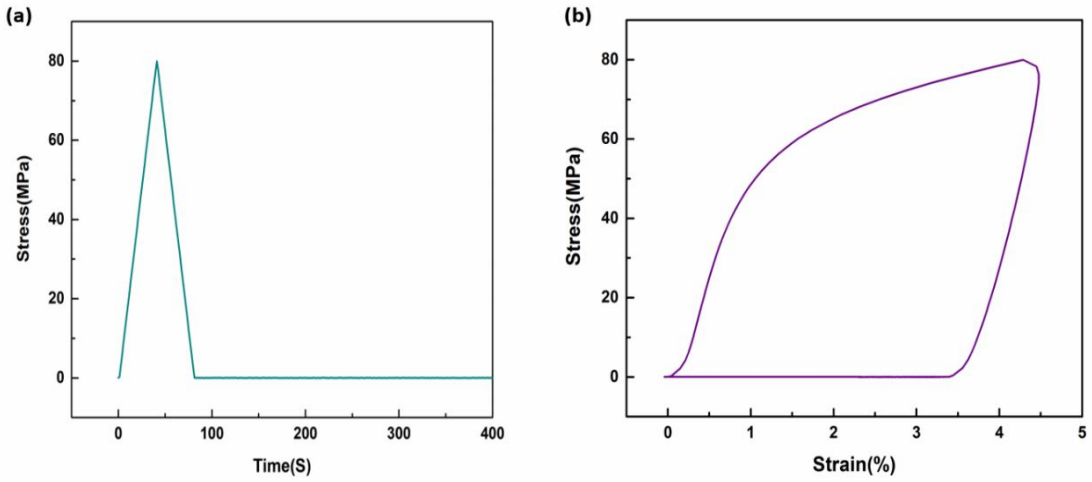

Figure 2.22. (a) Stress-time curve with σ_{max}= 80 MPa (b) Stress-strain curve for the one-way shape memory effect.

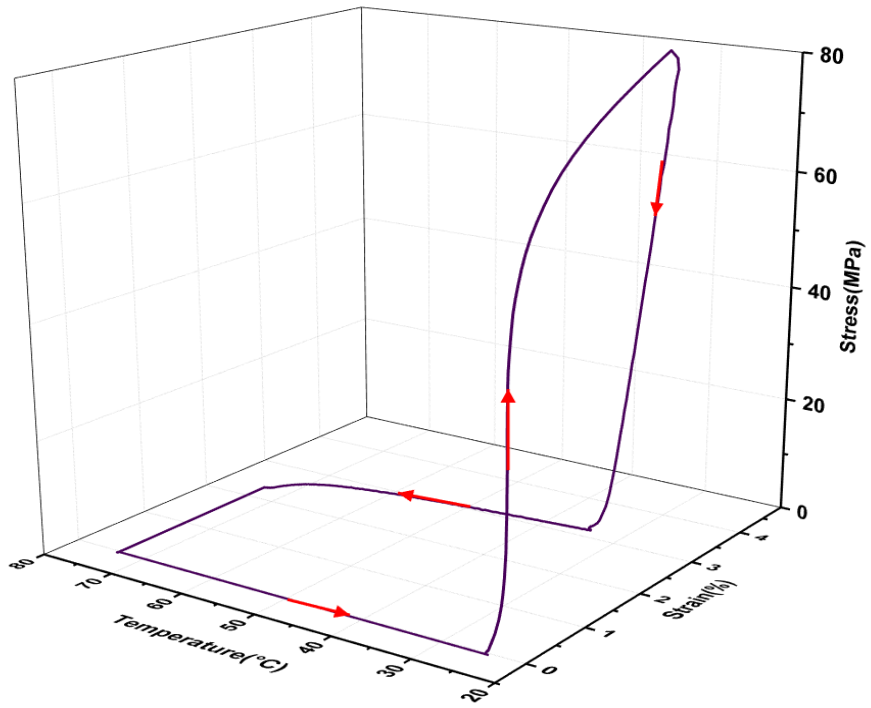

Figure 2.23. 3D representation of the stress-strain-temperature curve for one cycle of loading and heating of the SMA/P(VDF-TrFE) composite.

In chapter 3 we have simulated the tensile test for one-way shape memory effect by finite element simulation. The experimental and simulated results are well correlated with each other. Therefore, the obtained results are in agreement with the numerical simulation. A comparison study of both the experimental and simulation behavior will be presented in chapter 3.

2.4.2 Voltage-strain-temperature

The aim of this work is to demonstrate double energy harvesting, that is to convert the thermal and mechanical energy into electrical energy, using the multicoupling properties of the SMA and piezoelectric polymer. As described in Figure 2.20, during the mechanical and thermal loading the piezoelectric layer produces an output voltage.

Figure 2.24 shows the thermoelectric response of the SMA/P(VDF-TrFE) composite as a function of time for a single heating and cooling cycle. The voltage response during heating was measured in a temperature range from 40 to 75 °C. The positive and negative voltage peaks can be interpreted as the result of the two-consecutive processes during the tensile test. During mechanical loading, the forward martensitic transformation occurs in the SMA layer, which also induced deformation in the thin piezoelectric polymer layer. As a result, an output voltage of 9.2 V is generated from the polymer layer, thanks to the electromechanical coupling of the piezoelectric layer. Consequently, during heating, the activation of the reverse transformation recovers the strain in the SMA layer. Thus, the polymer layer also recovers the shape, and which produced a negative voltage peak of 3 V. The potential difference is induced between the top and bottom electrodes. During mechanical loading the positive voltage peak is developed due to the flow of electrons from one electrode to another. The negative voltage output is created when the application of thermal loading induces the decrease in strain. Thus, the piezoelectric potential decreases and leads to the discharging of the accumulated electrons. The voltage is maximum at the temperature transitions of the SMA.

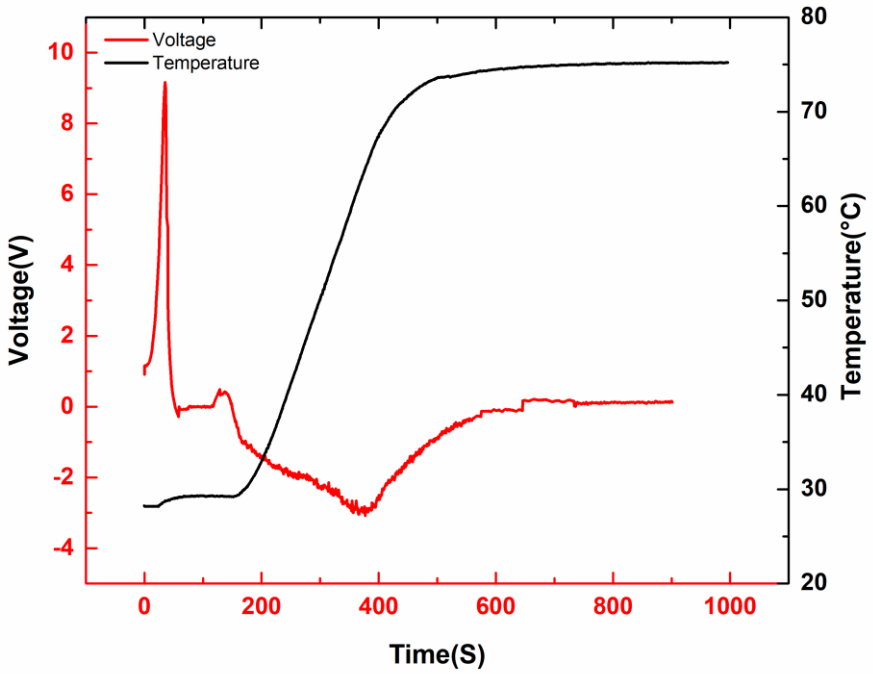

Figure 2.24. Output voltage generated by the SMA/P(VDF-TrFE) composite during the one-way shape memory effect.

The evolution of voltage, strain and temperature during the electro-thermomechanical characterization using the tensile machine is illustrated as a 3D graph in Figure 2.25. During the tensile loading and unloading process of the SMA/P(VDF-TrFE) composite, the P(VDF-TrFE) piezoelectric polymer layer also follows the deformation made by NiTi SMA. The application of a mechanical loading created a strain in the piezoelectric layer, and that induce an electric potential due to electromechanical coupling. It is evident in the 3D graph of voltage-strain-temperature (the positive voltage peak). In the next step, the heating of the composite results in a decrease in the developed strain which in turns decrease the electric potential. Thus, heating eliminates the strain and causes a decrease in electric voltage. The negative output voltage of 3V was produced during the heating loading. Thus, P(VDF-TrFE) polymer generates an electric voltage during the one-way shape memory effect exhibited by NiTi SMA. The mechanical and thermal loading processes indued an electric response from P(VDF-TrFE). The induced electric response is due to the piezoelectric properties of the polymer. Hence the feasibility of the double energy conversion mechanism of thermal to the mechanical into electrical energy is proved through this tensile test.

The obtained results show that during thermal loading, a low output voltage is generated from the piezoelectric polymer layer compared to the mechanical loading. The possible reason to explain this lower voltage could be the lesser strain in the piezo layer. That is the strain induced in the SMA layer is not completely transmitted to the polymer layer. There is an interface layer

between the SMA and the polymer. Therefore, the complete transfer of strain from the SMA layer to the piezoelectric layer does not occur.

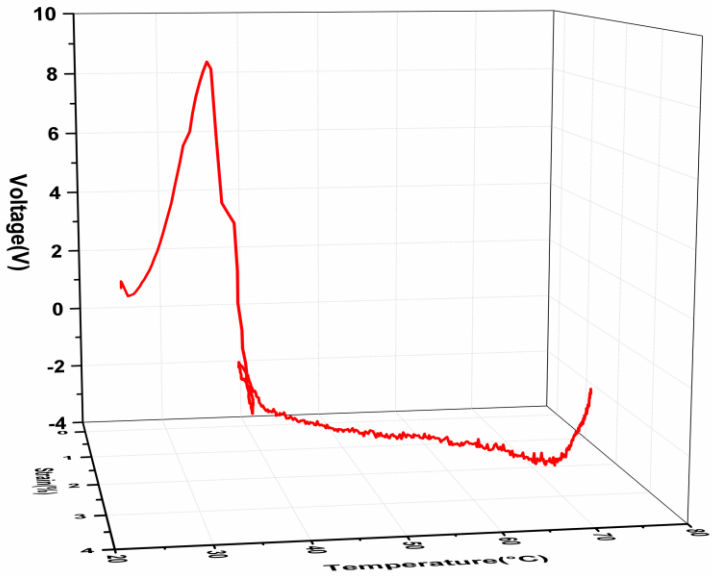

Figure 2.25. 3D representation of the Voltage-strain-temperature curve for one cycle of loading and heating of the SMA/P(VDF-TrFE) composite.

Therefore, this tensile experiment demonstrated the simultaneous conversion of the mechanical and thermal energy into electric energy. During the one-way shape memory effect, NiTi SMA undergoes the forward and reverse transformation and the polymer layer also follow the structural deformation which turns into an output voltage. Hence, the SMA/P(VDF-TrFE) composite is able to combine the thermomechanical coupling property of the NiTi SMA and electromechanical coupling of P(VDF-TrFE) piezoelectric polymer for energy harvesting. Thus, these results give a promising approach for the synergistic use of two smart materials for energy harvesting.

2.4.3 Summary

In this chapter we have exhibited the feasibility and the concept of coupling a NiTi SMA with a P(VDF-TrFE) piezoelectric polymer for thermal energy harvesting. Through this study, it was experimentally demonstrated the double energy conversion by coupling the shape memory effect of NiTi SMA and piezoelectric effect of P(VDF-TrFE) polymer. The experimental results showed the conversion of thermal into mechanical energy that is converted into electric energy.

The piezoelectric energy harvesting performance of the PEN/ P(VDF-TrFE) device was checked by applying uniaxial stress by repeated human finger tapping and bending. The device was able

to convert the human finger tapping movements into electricity under pressing and releasing motion. The power output is calculated from the open-circuit voltage and short circuit current by considering the peak output values. During finger impression and bending, the power output of the P(VDF-TrFE) film is 5.5 μW cm^{-2} and 16 μW cm^{-2} respectively. However, this power calculation method is not the best practical solution because it's gives an overestimated value of power. It is because of the voltage is measured across a very high resistance and the current across a very low resistance. Therefore, in this study, we performed the test for the PEN/P(VDF-TrFE) device by bending and recorded the peak voltage across various load resistors ranging from 1 KΩ to 5 MΩ. A maximum power value of 6.25 μW cm^{-2} was observed, across a load resistor of 1 MΩ.

The tensile test was conducted it allowed to analyze the evolution of stress versus strain and temperature and voltage versus strain and temperature. During the mechanical loading and unloading the composite generates an output voltage of 9.2 V. The developed strain was decreased at the time of heating loading, and thereby the voltage also decreased to 3V. Therefore, coupling of a flexible P(VDF-TrFE) thin layer with the NiTi SMA is able to generate an electric potential during the shape memory effect exhibited by the SMA. This proves the feasibility of this electro-thermo-mechanical coupling for energy harvesting.

However, there are various possibilities that still need to be taken into account in order to increase the efficiency of thermal energy harvesting. For example, other SMA composition can be used with sharper phase transition such as NiTiCu. The training of the NiTi SMA also needs to consider obtaining the two-way shape memory effect (TWSME). TWSME helps to exhibit the repeatable shape change under no mechanical loading in the presence of thermal loading. The smaller voltage output produced from the piezo layer during thermal loading. This could be due to the interface layer in between the SMA and piezo layer. Due to the interface layer, complete strain transferring is not possible. Therefore, it reduces the total energy harvesting performance of the composite. In order to achieve higher voltage from the composite layer by reducing the interface thickness, there are possible solution to be considered. We can use an SMA with lower thickness in the range of 20-50 μm. In this case, the whole device will be flexible and lightweight. Another possibility is that we can increase the thickness of the polymer layer by making the film using other techniques such as doctor blade or electrospinning. In order to increase the piezoelectric coefficient of the film, it will be possible to add different nanoparticles to the polymer matrix. Finally, we can fabricate the device using a reduced thickness of the interface layer.

Also, faster heating and cooling with several cycles will allow collecting more charges from the piezoelectric layer. Hence, we have designed and developed a new experimental characterization setup. This electro-thermal characterization system is able to generate periodic heating and cooling of the composite. It also, proposes to measure the electric response, temperature, displacement of the composite by controlling all these functions

simultaneously using the LabVIEW programs. In the following final section, we introduce the micro energy harvesting system.

2.5 Micro energy harvester characterisation system

We have designed an experimental setup for cyclic cooling and heating of the SMA-Piezo sample rapidly. The training of the NiTi SMA will be conducted in order to achieve the Two-way shape memory effect. Hence the composite shows repeatable shape change under zero applied mechanical load when subjected to a cyclic thermal load. This device is able to control the applied thermal loading and cooling of the sample, as well as simultaneously measuring the induced deflection and electric response from the sample. This device allows the electro-thermo-mechanical characterization of the SMA/PVDF hybrid composite. The design of this experimental test bench should allow to control the thermal loading (measurement and control of temperature) and to measure the induced deflection and electric voltage. The applied thermal cycles derive from one heating and one cooling source allowing the controlled increasing and the decreasing of the composite temperature. The control system is monitored by a specific application developed in LabVIEW.

The main aim is to perform the electro-thermo-mechanical characterization of the SMA/P (VDF-TrFE) device to harvest efficiently the thermal variation experimentally. The different components of the system are schematically illustrated in Figure 2.26.

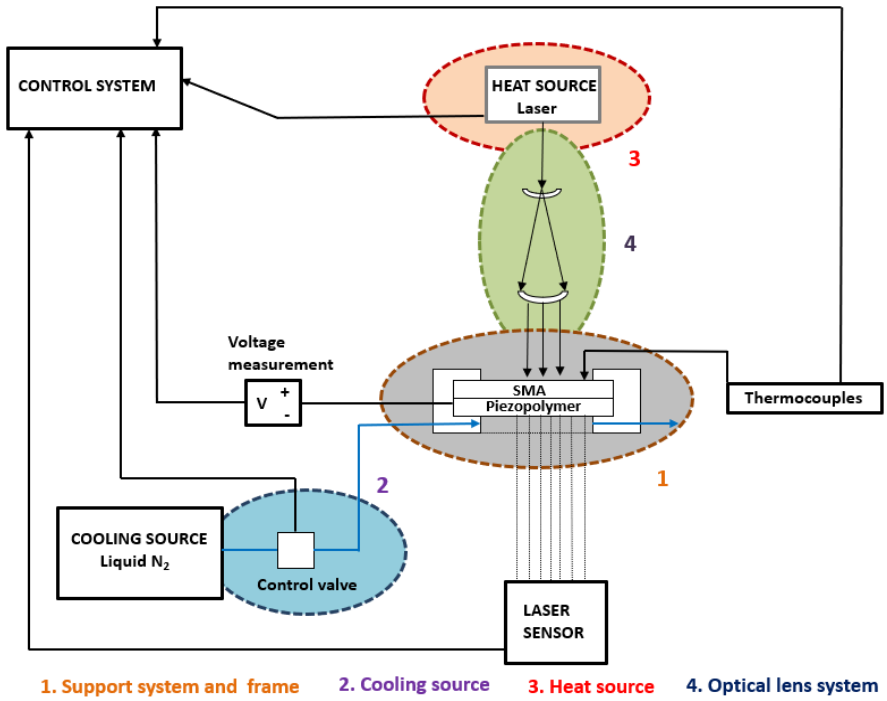

Figure 2.26. Schematic representation of the micro harvester experimental design model.

The system is mainly composed of four different subparts which include the support system and frame, cooling source, heat source and an optical lens system. Each part is described in the following section. Figure 2.27 represents the CAD model of the device designed in the Catia software.

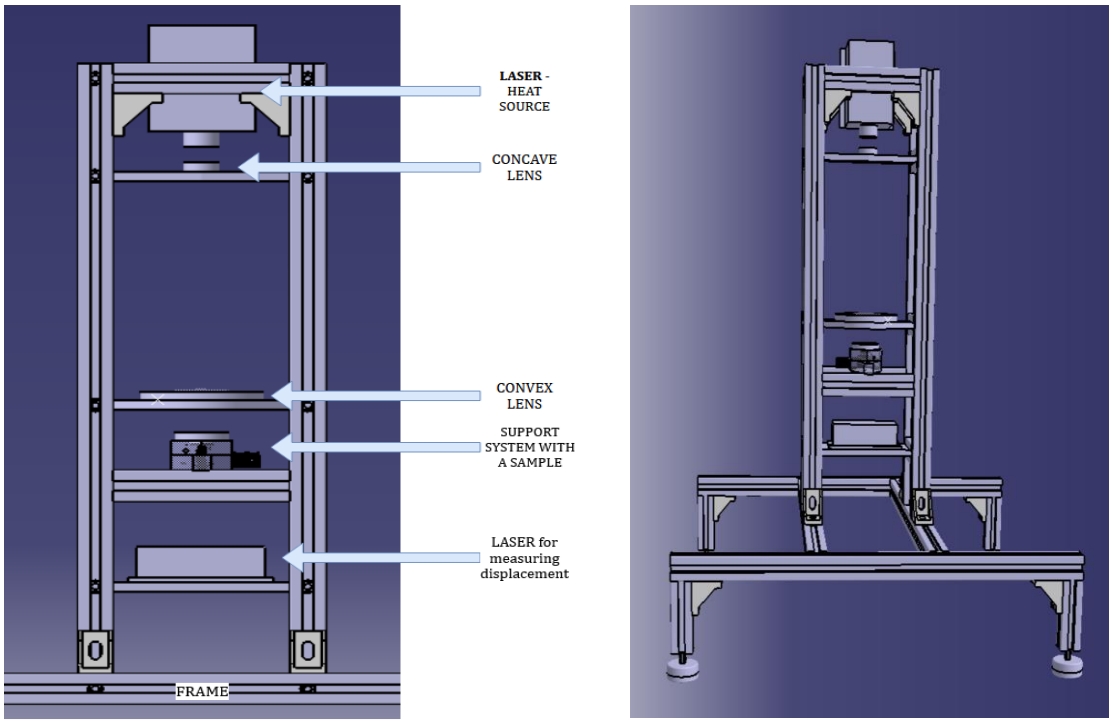

Figure 2.27. Schematic representations of the model of the micro harvester system in Catia software.

The goal of the experimental characterization is to demonstrate the thermal energy harvesting of the SMA/(PVDF-TrFE) in real-life applications. The temperature of the working system is ranging from 20 to 75 °C. That is the temperature transition of SMA, as we already proved the voltage output from the composite during the tensile test. The system is designed in such a way that, it can measure the displacement through the temperature variation using a laser sensor. Also, it is very important to ensure the efficiency of the cyclic heating and cooling of the system during the test. During temperature variation, we are focusing to obtain a continuous sinusoidal wave cycle repeated per second. If it successfully works, we can increase the frequency, and it could be possible to make it as three cycles per second.

The heating of the composite device is performed by the laser beam which is directed to the surface of the sample. The optical lens system allows the diffraction of laser beam in order to cover uniformly the sample free surface leading to a homogeneous heating. Then, the fast decrease in temperature can be carried out by using a liquid nitrogen source. The SMA/P(VDF-TrFE) composite is subjected to deformation during heating and cooling. The deformation of the sample generates an electric response. In order to get the displacement measurement, a laser sensor with less power will be used. The output voltage from the composite is also measured. Another important part that we are dealing with for this system is the control

system using the LabVIEW software. This is specially designed for combining all the subparts and to control the measurements and commands. Through this study, we are not focusing on a high output power value to compare with the existing reported energy harvesting system. However, the purpose of the test is to prove the feasibility of SMA/piezoelectric polymer composite for thermal energy harvesting by coupling the properties.

2.5.1 Support system and frame

The support system and frame enable the placement of all the components in the appropriate positions and as well as to fix each component in the right positions. The design is made in the Catia software. The structure to support all the components in our systems has consisted of a mainframe, different fixing solutions on several levels and the designed support for holding the sample. The bottom frame ensures that the position of the whole system is stable and fixed well to prevent any motion of the full system.

The composite sample composed of a circular shape, which is placed inside the sample holder. The sample holder is adapted to enable liquid nitrogen to enter through the bottom surface of the SMA/P(VDF-TrFE) composite sample and exit through the tunnel holes. The designed model and its position in both Catia software and original components are shown in Figure 2.28 and 2.29. The original sample support was made by 3D printing.

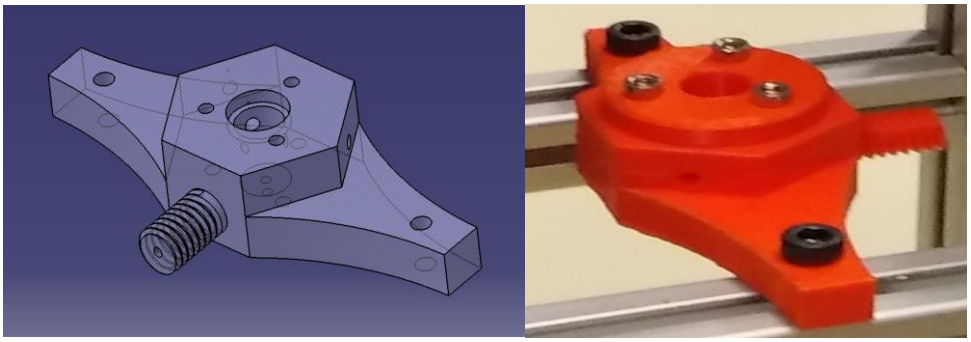

Figure 2.28. Designed model of the sample support on the left and the original photographic image of the support on the right.

The sample support system is made in a way provided with an exit output to remove the remaining liquid nitrogen cooling source and an additional hole to measure the displacement of the composite sample using a low power laser sensor.

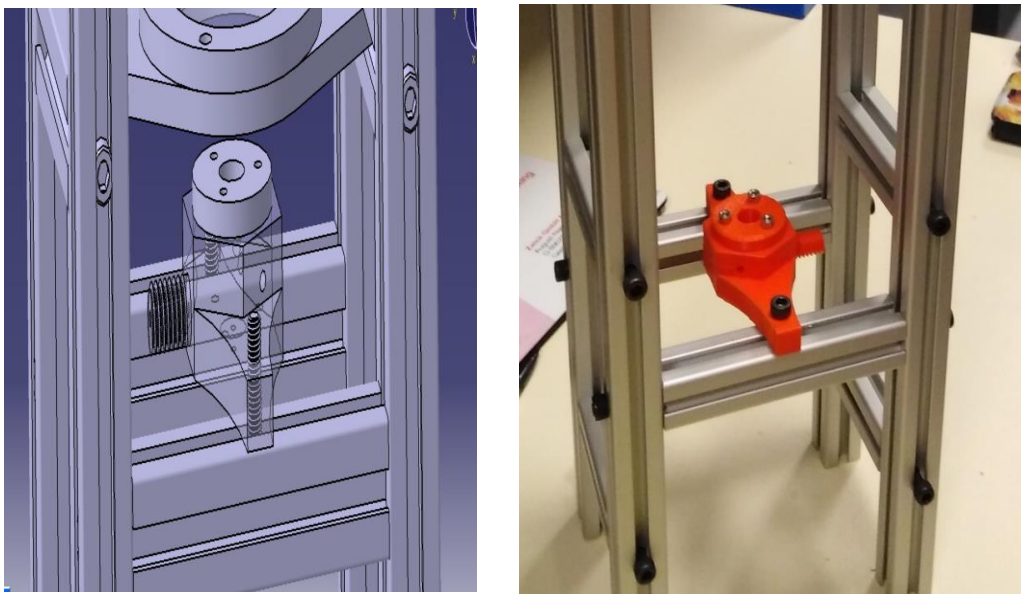

Figure 2.29. Designed model showing the position of the sample support in the mainframe on the left and the original photographic image of the support placed in the frame on the right.

2.5.2 Cooling and heating source

The cooling of the device is carried out using the liquid nitrogen source. The testing sample has a diameter of 10mm, which helps to reduce the time of cooling. Also, it helps to reduce the amount of liquid nitrogen used as well as fast cooling of the device to reach a temperature less than 20 °C. Therefore, we chose a control flux system to perform the cooling in an on and off mode. The function of the controlled flux of the material can be done by using the solenoid valve, which can be controlled using the LabVIEW software.

The laser beam is used as a heat source for the rapid heating of the sample. In our system, we have used a laser module with a power of 5W. An interface PSU-RS232 module is used in order to control the power. Therefore, the desired heating of the sample can be controlled using the LabVIEW software.

We have to also consider the safety measures to cover and protect the entire system because we are working with a high-power laser source.

2.5.3 Optical lens system

The laser heat should affect the surface of the sample equally at each point. Therefore, to get homogeneous heating of the sample, we will use an optical lens placed after the laser beam. This lens will allow us to transfer an equal amount of heat to every point on the surface of the material.

For our system, we are using one convex lens and one concave lens. Convex refers to the lens which converges the incident laser rays at a particular point (towards the principal axis), that travels through it. We have placed another concave lens after the convex lens. The concave lens can be identified as the lens which disperses the light rays around, that hits the lens. First, the laser beams passing through the convex lens and which allows the converging of the rays at a particular point. Then, the rays are passing through the concave lens, which allows the rays to disperse to the SMA/P (VDF-TrFE) composite sample. Hence, the rays that incident on the SMA/piezo sample spreads well throughout the surface.

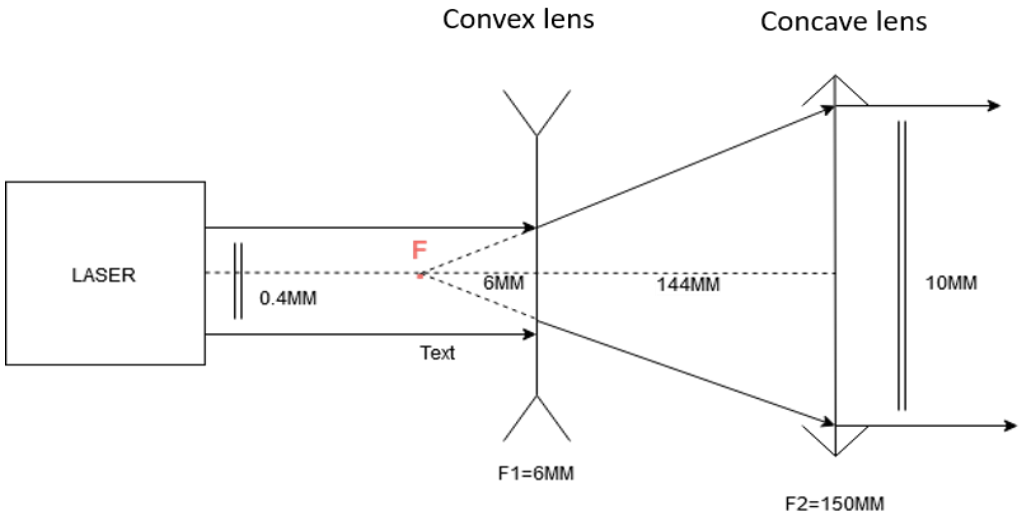

Figure 2.30. Schema of the optical lens system

For this system, we place both concave and convex lenses in order to match their focal point (F). Thanks to the properties of the concave lens, when rays go through it, they diverge and meet the next convex lens. The schematic representation of the mechanism of the laser beam passing through the two lenses is shown in Figure 2.30. The one is situated exactly to have the rays coming from the point F (the focal point of the lens) and we have obtained parallel (to the main axis) rays of light.

2.5.4 Summary

We have designed and developed an experimental device for the electro-thermo-mechanical characterization of the SMA/Piezoelectric polymer composite. The system consists of different components for heating/cooling of the composite as well as a control system to combine all the subparts. The control system is developed in the LabVIEW software to perform the controlling of the whole device with proper measurements and commands. The heating of the composite sample is done using the laser beam that has a maximum power of 5W. The power can be controlled and apply the desired power to heat the sample to a temperature of 75 °C through an interface PSU-RS232 module. The homogenous heating of the sample is done using concave and convex lens. The laser light is first passing through a convex lens that converges the

incident laser rays towards the principal axis. Further, we have placed a concave lens after the convex lenses. Hence, the concave lens spreads out the laser rays. Therefore, the rays that incident on the SMA/piezo sample spreads well throughout the surface. That means homogenous heating can be assured by this way. The immediate cooling of the sample can be performed with liquid nitrogen. The cooling of the sample is done by using a solenoid valve, which helps to control the amount of liquid nitrogen in a pulsing way in order to get a sinusoidal change of temperature in the sample.

We have developed the support system and frame that consist of the two lens holders and the sample holder. All subparts are arranged and fit well in the mainframe. We need to work further to fix the laser system, the liquid nitrogen cooling tank and all to finalize a well-operating working system. Needs to develop the electronic part to collect the voltage from the piezoelectric layer during cyclic cooling and heating. Also, further analyzing of the cooling source, because the liquid nitrogen is contained at high pressure inside the tank. Therefore, we need to decrease the pressure between the container and the valve. Another important factor we have to take into account on the safety measures and protective covers to ensure security.

2.6 Conclusion

In this chapter, we have validated the feasibility of coupling a NiTi SMA with P(VDF-TrFE) piezoelectric polymer for energy harvesting. The concept of double energy conversion mechanical to thermal to electrical energy was demonstrated experimentally. The electrical response is generated from the P(VDF-TrFE) during the one-way shape memory effect exhibited by the NiTi SMA.

A novel composite composed of NiTi SMA and P(VDF-TrFE) piezoelectric polymer was fabricated and optimized. Different configurations of SMA/P(VDF-TrFE) was tested. First, a two-layered composite was fabricated by depositing a thin P(VDF-TrFE) polymer layer on the SMA surface. The polymer layer of thickness with a few micrometers was deposited directly on top of the SMA surface using the spin coating technique. A top electrode was deposited with a few nanometer thicknesses by an E-beam evaporator. The high voltage polarization (100V/µm) was achieved by the direct contact technique to enhance the piezoelectric properties of the polymer film. Also, the multilayered composite was fabricated by depositing the polymer layer on both sides of the SMA. The polarization of the polymer on both sides of the SMA was done by taking SMA as a bottom electrode. However, the composite showed some drawbacks, such as an electric breakdown when the applied higher voltage during polarization. Also, it's showing the reduced piezoelectric properties when subjected to mechanical deformation. This finding leads to the formation of another composite with an interface layer with improved bonding using flexible epoxy glue. We have fabricated the composite, where first the P(VDF-TrFE) polymer layer was deposited on a PEN substrate and conducted the polarization by depositing Cr/Al electrodes. Then, the PEN/P(VDF-TrFE) film was bonded to SMA using the flexible epoxy

glue. The whole device is flexible and able to follow the deformation made by SMA. This composite was used to characterize further the mechanical and thermal energy harvesting performance.

The original composite made of SMA/P(VDF-TrFE) composite's performance in terms of output voltage and power was measured. The piezoelectric energy harvesting ability was checked by normal finger tapping and bending. The power output is calculated from the open-circuit voltage and short circuit current by considering the peak output values. During finger impression and bending, the power output of the P(VDF-TrFE) film is 5.5 μW cm-2 and 16 μW cm^{-2} respectively. Nevertheless, the more appropriate way to measure the power output is using resistors. Therefore, we have tested the output power using various load resistors during bending for the PEN/P(VDF-TrFE) composite. A maximum power value of 6.25 μW cm^{-2} was observed, across a load resistor of 1 MΩ. In order to demonstrate thermal energy harvesting, oil bath heating was exhibited. This test showed the generation of an output voltage from the polymer layer in the temperature range corresponding to the phase transformation in the SMA.

The electro-thermo-mechanical characterization of the composite was done by a tensile machine with thermal chamber. The evaluation of the stress-strain-temperature and the voltage-strain-temperature were measured during one cycle of heating and cooling of the composite. The composite is subjected to mechanical loading, unloading and thermal loading and unloading. During mechanical loading, the composite produces an output voltage of 9.2 V. The high output voltage is induced by the electromechanical coupling of the piezoelectric layer. Consequently, during the thermal loading, the created strain is transferred to the P(VDF-TrFE) thin layer. Then, the corresponding martensitic phase change induces the thermomechanical coupling, and the P(VDF-TrFE) film also follow the shape change. This creates a negative voltage output of 3V from the piezo layer. Hence, these characterization studies demonstrate the mechanism of double energy harvesting using smart materials possessing different coupling properties. This study is not focused to enhance energy harvesting to outperform state of the art of energy harvesting devices. However, the objective is to demonstrate the coupling of SMA and piezoelectric polymer thin layer and to prove the double energy conversion mechanism.

In addition, we have developed a new characterization system to allow the simultaneous heating and cooling of the composite. The periodic heating and cooling can be done using laser beam heating and the circulation of liquid nitrogen flux respectively. The whole support system and frame to hold the sample and the mainframe to arrange different components were made. This main idea is to do the electro-thermo-mechanical characterization by measuring the deflection and electric response from the piezoelectric layer at a given temperature range. The system can be controlled using the LabView software. Hence, this system will allow us to perform several cycling heating and cooling of the composite and thereby possible to record the electric response from the composite.

However, several possible ways can be considered to improve the composite. The interface properties can be improved by using other ways such as silane coupling agents. In addition, the SMA film with lesser thickness will improve the efficiency of the composite, where we can deposit the polymer layer with an increased thickness on the SMA. Moreover, it is interesting to add nanoparticles to the polymer matrix, which will enhance the piezoelectric properties. SMA with sharper phase transition could be used to fabricate the composite, which allows working with a small transition temperature. Different compositions such as NiTiCu or CuAlNi can meet the criteria. Also, electronic design and circuit comprise key factors in piezoelectric energy harvesting. The final performance of the composite energy conversion depends on the electronic circuits, size, dimension, SMA type and area of deformation of the composite. To predict the global response of the composite and each layer needs a double level of modeling. Therefore, the following chapter deals with the numerical analysis of the composite behaviour.

Chapter 3

Numerical analysis of the electro-thermo-mechanical response of the SMA/Piezo composite

3.1 Modeling of SMA behavior 79
3.2 Modeling of piezoelectric behavior 80
3.2.1 Linear model 80
3.3 Finite element simulation of the SMA/(PVDF-TrFE) composite 80
3.3.1 SMA thermomechanical properties 81
3.3.2 Piezoelectric properties 82
3.4 Finite element (FE) model of the device 82
3.4.1 Tensile and bending tests 83
3.5 SMA behaviour simulation with Chemisky-Duval's model 84
3.5.1 Superelastic effect 84
3.5.2 One-way shape memory effect 84
3.5.3 Assisted Two-way shape memory effect 85
3.6 Simulation of the two-layer composite material 86
3.6.1 Mesh and element type 86
3.7 Simulation results and discussion 87
3.7.1 One-way shape memory effect 88
3.7.2 Two-way shape memory effect 91
3.7.3. SMA/Piezoelectric polymer composite 92
3.8 Comparison between simulation and experimental analysis of the composite 94
3.9 Prototype geometry 96
3.10 Conclusion 97

Introduction

This chapter deals with developing a finite element model (FEM) for the SMA/Piezoelectric polymer composite. The global response of the composite requires a connected double level of modeling. The first level concerns the prediction of the multi-physical local behavior of each layer. First, the numerical modeling of SMA's thermomechanical behavior is done using Chemisky Duval's model. The electromechanical behavior of the piezoelectric polymer is modeled with the linear model. This model is implemented in Abaqus finite element

commercial code. The second level involve the development of the FEM to predict the electro-thermo-mechanical response from the composite. It consists to mesh the bilayer composite by solid hexahedral continuum element with quadratic interpolation. The bending and tension loading of the composite is performed, and the corresponding stress-strain-temperature evaluation is recorded. This finite element modelling allows predicting the distribution of stress, strain, and electric responses of the composite. As well as it is possible to predict the global response of voltage as a function of temperature. Moreover, it helps to identify the appropriate geometry of the layered structure. Also, we can predict the generated output voltage from the piezoelectric polymer having different thickness. The final section of this chapter will address a comparison study between the obtained experimental results and numerical simulation results. The numerical simulation was mainly performed by Guven Muslum, a master student in LEM3.

3.1 Modeling of SMA behavior

Some different approaches exist to describe the thermomechanical behavior of SMA such as micro-mechanical and macroscopic approaches. The state of the art for different approaches for the modeling of the SMA thermomechanical behavior was given in the first chapter at section 1.8.3. In the micromechanical approach, the behavior of the material is modeled at a microscopic scale. A scale transition is then carried out to describe the behavior at a macroscopic level. This can be done for example by using Mori-Tanaka scale transition method. Generally, the micro-mechanical approaches are less adapted to finite-element analyses due to their high computation time and need to define several internal variables. Another promising approach is the macroscopic one which has a high advantage to need less computational time and uses only a few numbers of internal variables. Hence, these kinds of approaches are commonly more adapted to finite-element analysis.

The macroscopic approach is widely used in majorities of the methods to describe the thermomechanical behavior of SMAs. The energetic formulation used is based on the thermodynamic irreversible processes. Several models exist such as Tanaka[235], Brinson,[198] Lagoudas,[201]and Chemisky Duval's models describing the macroscopic phenomenological thermomechanical model. The choice of internal variables is very important for this kind of method. The choice of them is done depending on the physical phenomenon that we want to take into consideration in the method (shape memory effect, phase transformation …). We have adopted Chemisky Duval's models in order to simulate the behavior of NiTi SMA. A user subroutine UMAT coded in C++ has been implemented in Abaqus to describe SMA's behavior in Abaqus. The detailed description of the model concerning the system of equations was described in the first chapter.

3.2 Modeling of piezoelectric behavior

To simulate the electromechanical behavior of the piezoelectric materials, there are two kinds of models. One is linear in which only piezoelectricity is considered and the other is non-linear which is dealing with the ferroelectricity and ferroelasticity induced by ferroelectric domain switching under high electromechanical loading level. In our study, we use the linear model. It corresponds to the reversible electromechanical behavior induced by the small and reversible variation of polarization under the application of mechanical or electrical loading.

3.2.1 Linear model

We will consider these two effects, direct and reverse. In direct effect, the electric charge is created when subjected to mechanical loading. In reverse effect, the material becomes strained when an electric field is applied. The linear model to describe the electromechanical behavior was presented in the first chapter in equation 1.1 and 1.2.

The piezoelectric principle, the linear model, the piezoelectric modes, and tensor components were described in the first chapter section 1.4, 1.7. Generally, for most of the piezoelectric materials the 33, 31 and 32 piezoelectric modes are used. In our study, the experimental polarization of the P(VDF-TrFE) polymer is conducted in the thickness direction that is in the X_3 direction. Then all the piezoelectric stress coefficient is equal to zero. With all of that, the linear mechanical behavior of the piezoelectric polymer can be written as follows.

$$\begin{bmatrix}\sigma_1\\ \sigma_2\\ \sigma_3\\ \sigma_4\\ \sigma_5\\ \sigma_6\\ q_1\\ q_2\\ q_3\\ \end{bmatrix} = \begin{bmatrix} C_{11} & C_{12} & C_{13} & 0 & 0 & 0 & 0 & 0 & e_{31}\\ C_{12} & C_{22} & C_{23} & 0 & 0 & 0 & 0 & 0 & e_{31}\\ C_{13} & C_{23} & C_{33} & 0 & 0 & 0 & 0 & 0 & e_{31}\\ 0 & 0 & 0 & C_{44} & 0 & 0 & 0 & 0 & 0\\ 0 & 0 & 0 & 0 & C_{55} & 0 & e_{15} & 0 & 0\\ 0 & 0 & 0 & 0 & C_{66} & 0 & 0 & e_{15} & 0\\ 0 & 0 & 0 & 0 & e_{15} & 0 & k_{11} & 0 & 0\\ 0 & 0 & 0 & 0 & 0 & e_{15} & 0 & k_{11} & 0\\ e_{31} & e_{31} & e_{33} & 0 & 0 & 0 & 0 & 0 & k_{33}\end{bmatrix} \begin{bmatrix}\varepsilon_1\\ \varepsilon_2\\ \varepsilon_3\\ \varepsilon_4\\ \varepsilon_5\\ \varepsilon_6\\ E_1\\ E_2\\ E_3\end{bmatrix} \quad (3.1)$$

3.3 Finite element simulation of the SMA/(PVDF-TrFE) composite

As discussed in the second chapter, the composite is composed of 125 µm thick $Ni_{55}Ti_{45}$ SMA and P(VDF-TrFE) layer of thickness ~5µm on the top of the SMA sheet. The SMA/P(VDF-TrFE) composite specimen is designed as a rectangular shape with a total length (L) of 50 and width W) of 5 mm respectively. The composite's dimension is schematically shown in Figure 3.1.

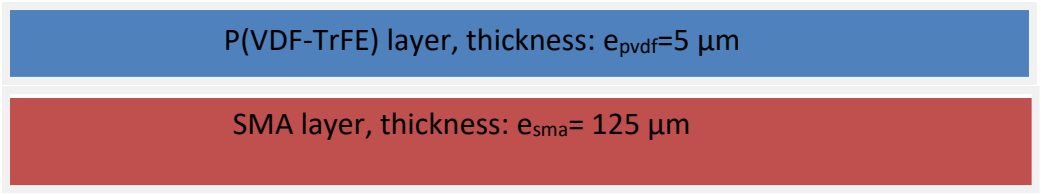

Figure 3.1. SMA/P(VDF-TrFE) composite dimension

3.3.1 SMA thermomechanical properties

The thermomechanical properties of the SMA used for the Chemisky-Dual's model for the simulation are illustrated in

Table 3.1 and 3.2.

E	Young' modulus
ν	Poisson's ration
α	Thermal dilatation coefficient
ε_{trac}^{T}	Maximal strain of transformation in tension
ε_{trac}^{TFA}	Maximal strain of transformation in tension from the self-accommodated martensite
ε_{comp}T	Maximal strain of transformation in compression
b_d	Slope of the curve (strain, temperature) in direct transformation and in tensile loading
b_r	Slope of the curve (strain, temperature) in reverse transformation and in tensile loading
M_s	Martensite start temperature
A_f	Austenite finish temperature
rf	Coefficient defining the amplitude of internal loops
F_ε^T	Martensite orientation start stress
Hf	Pseudohardening of transformation
H_ε^T	Pseudohardening of re-orientation
H_{twin}	Pseudohardening of accommodation
H_s	Temperature offset of the transformation of oriented martensite to austenite

Table 3.1. The parameters used for the numerical modelling.

E(MPa)	V	α (°C)$^{-1}$	ε_{trac}^{T}	ε_{trac}^{TFA}	$\varepsilon_{comp}T$
70000	0.3	8×10^{-6}	0.05	0.04	0.04
b_d (MPa/°C)	b_r (MPa/°C)	M_s(°C)	A_f (°C)	r_f	
5	2	58	71	0.6	
F_ε^T (MPa)	H_f (MPa)	H_ε^T (MPa)	H_{twin} (MPa)	H_s (MPa)	
				50	
100	4	1000	4000		

Table 3.2. Thermomechanical properties of the $Ni_{55}Ti_{45}$ SMA

3.3.2 Piezoelectric properties

The piezoelectric polymer P(VDF-TrFE) is polarized in the thickness direction (normal to the piezoelectric surface). The experimental details for the polarization and the obtained P-E hysteresis curve were described in the second chapter. In order to model the piezoelectric behaviour, we used the matrix notation where the X3 direction was taken normal to the piezoelectric surface. The properties of the piezopolymer taken into account for our simulation are provided in Table 3.3.

Density	1.82×10^3 kg/m^3 [105]
Relative permittivity (κ/κ_0)	12[105]
Piezoelectric strain coefficient(d31)	23 pC/N
Piezoelectric strain coefficient(d33)	22.8 pC/N
Pyroelectric voltage coefficient (Pv)	0.47 V/(µm K)
Young's Modulus	12 GPa[105]
Poisson ratio	0.3[105]

Table 3.3. Properties of P(VDF-TrFE) polymer.

All values given in the table are not measured experimentally, some of the values such as Young's modulus and Poisson ratio are taken from literature.

3.4 Finite element (FE) model of the device

The simulation of the thermomechanical coupling of the SMA layer and electromechanical coupling of the piezoelectric thin layer was conducted using the software Abaqus. Thus, it is

possible to activate the thermal, electrical, and mechanical degree of freedom. This has been performed using a static General step in Abaqus. The activation of the thermal degree of freedom is difficult in this kind of analysis. In our case, we only want to change the temperature value of SMA. Therefore, the temperature value of SMA is assumed to be uniform during the heating-cooling process. We assumed that this temperature change is very low corresponding to successive steady-state steps. The temperature changes with this step have been done by using a predefined field. Hence, it is possible to modify the temperature of the SMA between the steps.

By using a static General step, we can stimulate the thermomechanical and electromechanical behavior of the SMA and piezoelectric polymer respectively.

The next section is dealing with the simulation of the bending and tensile tests.

3.4.1 Tensile and bending tests

The right choice of the boundary conditions is the key point to simulate the tensile test of the SMA and the composite system. The boundary conditions are given below in Figure 3.2 exhibiting the upper view of the composite.

- A load is applied in direction X1 on the surface at the end of the SMA.
- The opposite surface, displacement in the direction of the applied load is blocked.
- Displacement in direction X_3, direction normal to the surface of the sample, (surface which has a normal vector in X_3 direction) has been blocked.
- Displacement in direction X_2, on one surface which has a normal vector in X_2 direction, has been blocked.

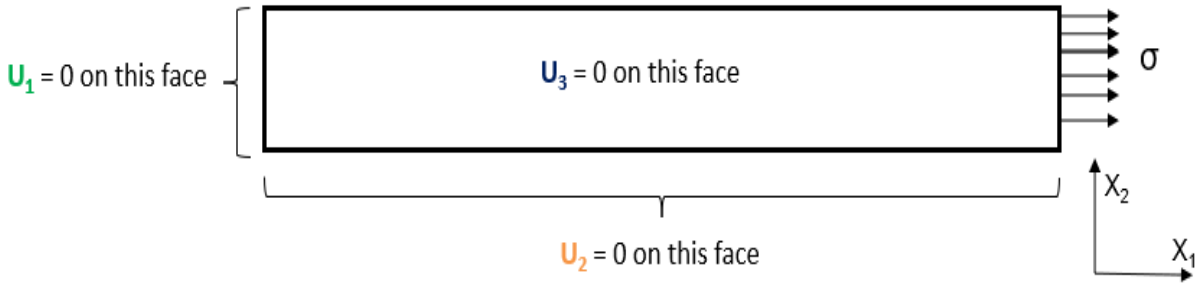

Figure 3.2 Boundary conditions for the tensile test.

These boundary conditions can help to simulate the tensile test of the sample taking into account the corresponding three symmetries.

In the case of the bending test, the circumference surface is clamped. Also, we applied a surface pressure (Figure 3.3).

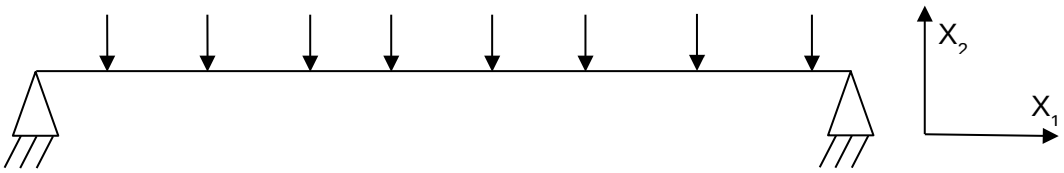

Figure 3.3. Boundary conditions used for the bending test.

3.5 SMA behaviour simulation with Chemisky-Duval's model

Here, we have simulated the behavior of an SMA plate by implementing Chemisky-Duval's model to check the efficiency of this model for the prediction of the SMA behavior. The simulation of the three main properties of the SMA, superelastic behavior, one way and assisted two-way shape memory effects are showed in the following section.

3.5.1 Superelastic effect

In order to simulate the superelastic behavior in Chemisky-Duval's model, we have carried out the tensile test on the SMA to demonstrate a high reversible deformation of the SMA. The sample was loaded and unloaded in tension at a constant temperature below A_f.

3.5.2 One-way shape memory effect

The one-way shape memory effect was simulated using two different loadings that are tensile and bending. There is a key point to consider in Chemisky-Dual's model[250], that is it always start in the austenite phase. Accordingly, to apply a load in the martensitic phase first we must cool the SMA to a temperature lower than M_f in order to lead to a fully self-accommodated martensitic state. After that, it's possible to apply any load at the martensitic phase. At this temperature, self-accommodated variants of martensite are activated. Then we apply the load either tensile or bending to start the orientation of the martensitic variants in the loading direction and until the detwinned martensite is created. Finally, the sample is unloaded and heated in order to recover the austenitic phase.

The simulation is mainly divided into four steps:

Step 1: Cooling to a temperature under M_f
Step 2: Loading
Step 3: Unloading
Step 4: Heating to a temperature beyond A_f

The thermal and mechanical loads applied during the steps are shown in Figure 3.4 and 3.5.

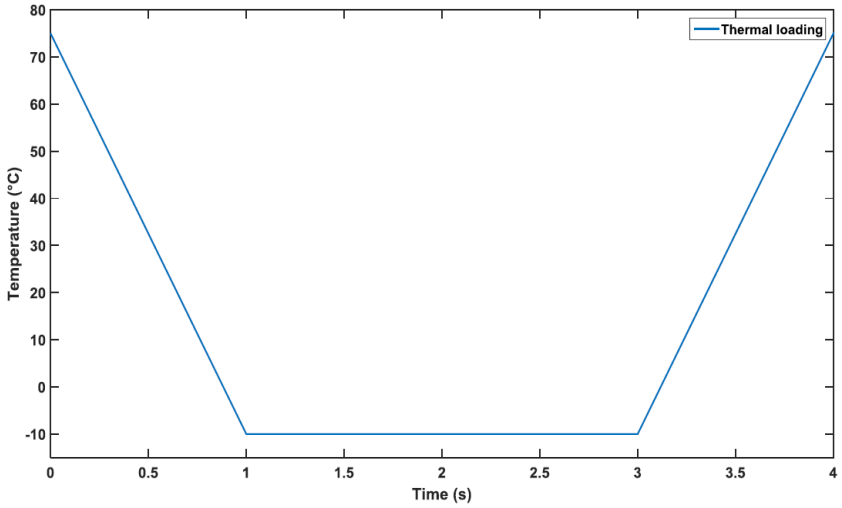

Figure 3.4. Temperature loading during the one-way shape memory effect simulation.

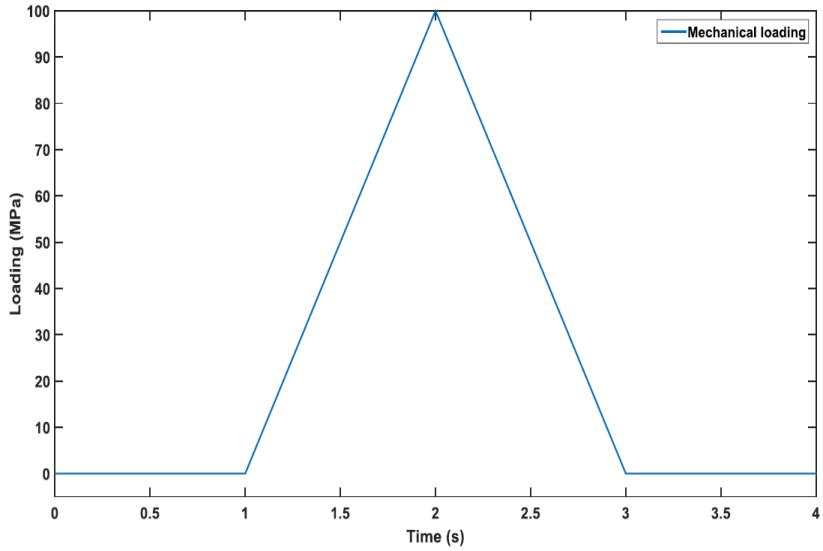

Figure 3.5.Mechanical loading during the one-way shape memory effect simulation.

3.5.3 Assisted Two-way shape memory effect

The aim of the assisted two-way shape memory effect simulation is to carry out thermal cycles to the material under a constant mechanical loading (Figure 3.6). This allows getting a shape change during thermal cooling-heating cycles. The cooling at constant stress induces a forward transformation from austenite to oriented martensite. The heating induces the recovering of the oriented martensite to austenite. The sample shape will then switch between two metastable states at low and high temperatures.

The simulation is divided mainly into five steps:

Step 1: Cooling up to a temperature lower than M_f (creation of self-accommodated martensite).
Step 2: Application of the high load sufficient to orient some variants of martensite.
Step 3: Application of the load we want (this loading is maintained for the next steps).
Step 4: Heat up to a temperature beyond A_f (beginning of thermal cycles).
Step 5: Cooling up to a temperature lower than M_f.

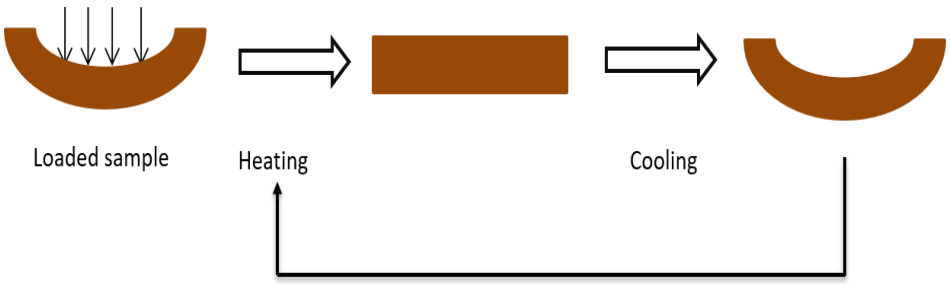

Figure 3.6. Schematic representation of the simulation of the two-way shape memory effect.

3.6 Simulation of the two-layer composite material

The finite element simulation of the composite is carried out by considering a significant contact between the SMA layer and the piezoelectric layer (no friction). Indeed, the two layers are assumed to be well bonded together during the composite processing. The SMA sheet is considered as a substrate to deposit a thin layer of the polymer on top of it.

In this study, we developed two instances for the SMA layer and for the P(VDF-TrFE) layer with an appropriate geometry. Then we merged both instances by maintaining the boundary. Once the composite material is formed, the simulation of the two-way shape memory effect was performed on the material. The goal of this work is to apply a mechanical loading to the SMA and apply thermal cycles (heating and cooling) to evaluate the electric response from the piezoelectric layer.

3.6.1 Mesh and element type

The mesh of the model is a significant part of the finite element analysis. The accuracy of the results has a major impact on the choice of the mesh. Therefore, the good choice of the mesh found an important step in the simulation. The selection of the appropriate mesh is based on the aspect ratio. In this numerical simulation, we need to predict the global multiphysical response of the composite and local state of all the physical quantities at each material point. In this regard, the basic solution is to develop a 3D finite element model for which each layer of

the composite is meshed by a 3D continuum solid element having a hexahedral shape with quadratic interpolation. Hence, the aspect ratio for a hexahedron element is defined as the ratio between the longest and shortest edge of the element.

We also have to consider the appropriate mesh refinement with the number of elements in the thickness of the model. For the 3D element, we have to use at least two elements in the thickness. The accuracy of the obtained results will increase as the number of elements increases. On the other hand, it will highly increase the computation time as the number of elements and mesh size increase. Therefore, we have to find a proper balance between the number of elements in the thickness and size of the mesh to get an accurate result along with a good computation time.

In this study, we have used two elements through the thickness of the piezoelectric layer and four elements in the thickness of the SMA layer. The size of the mesh was fixed to 0.5mm. The mesh of the model and the number of elements in each layer are presented in Figure 3.7.

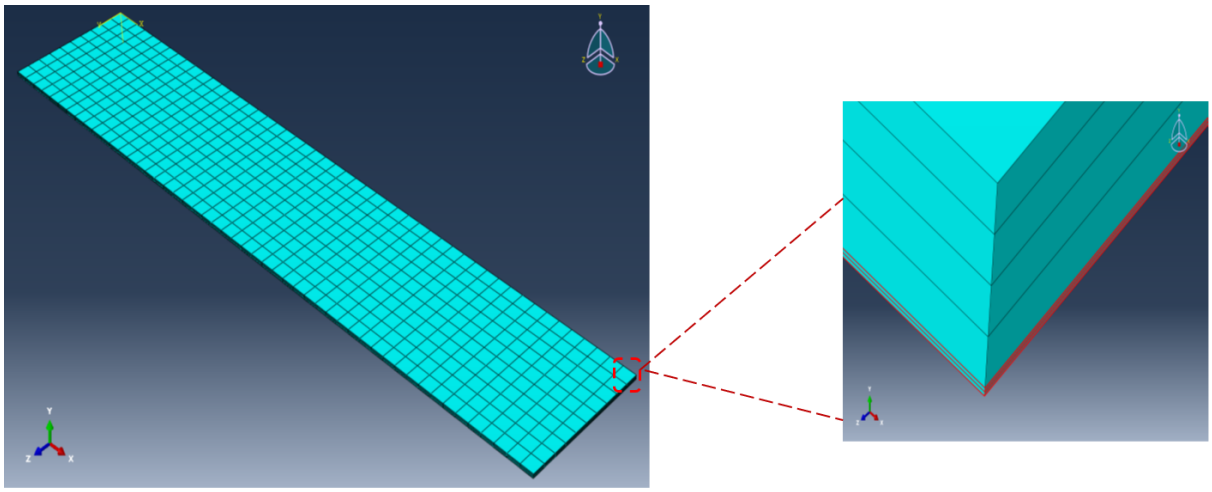

Figure 3.7. Mesh of the model in the left and the number of elements in the thickness, two for the piezoelectric layer and four in the SMA layer.

The type of element is chosen according to the type of analyze. The SMA layer is meshed with a thermomechanical 3D solid element (labeled C3D20T in Abaqus) with three displacements and temperature as degrees of freedom (dof) for each node whereas the Piezoelectric layer is meshed with an electromechanical 3D solid element (labeled C3D20E) with three displacements and the electric potential as dof for each node.

3.7 Simulation results and discussion

This section is dealing with simulated results of the properties of the SMA. The superelastic effect, one way and two-way shape memory effect of SMA were simulated on a plate composed of an SMA material. The superelastic effect of SMA is given in Figure 3.8. The NiTi

SMA is stressed at a temperature above A_f, it can exhibit superelastic or pseudoelastic behavior. This is also referred to as the ability of the material to recover its original shape upon unloading at a temperature above A_f. The stress-induced martensite transformation leads to strain generation during mechanical loading at constant temperature higher than A_f. The elastic linear behavior of austenite can be observed until the forward transformation yield stress. The martensitic transformation occurs starting from this yield stress leading to a nonlinear behavior. The saturation of forward martensitic transformation leads to the linear elastic behavior of martensite. During the unloading, always at constant temperature, the reverse transformation occurs after an elastic linear part at martensitic state. After the end of reverse transformation, the linear elastic state of austenite is observed till recovering the initial state. The reverse behavior is shifted with respect to the forward transformation leading to a hysteretic behavior.

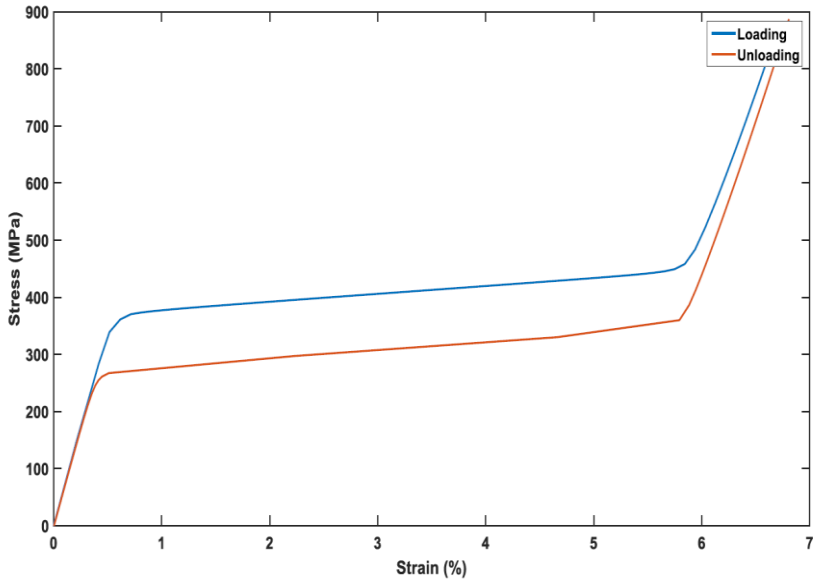

Figure 3.8. Superelastic effect of SMA

The sample was deformed up to 7% and after unloading, this high strain is completely recovered.

3.7.1 One-way shape memory effect

The tensile and bending loading results for the one-way shape memory effect are described in this section. The tensile loading simulation results of the SMA plate are illustrated in Figure 3.9 and 3.10.

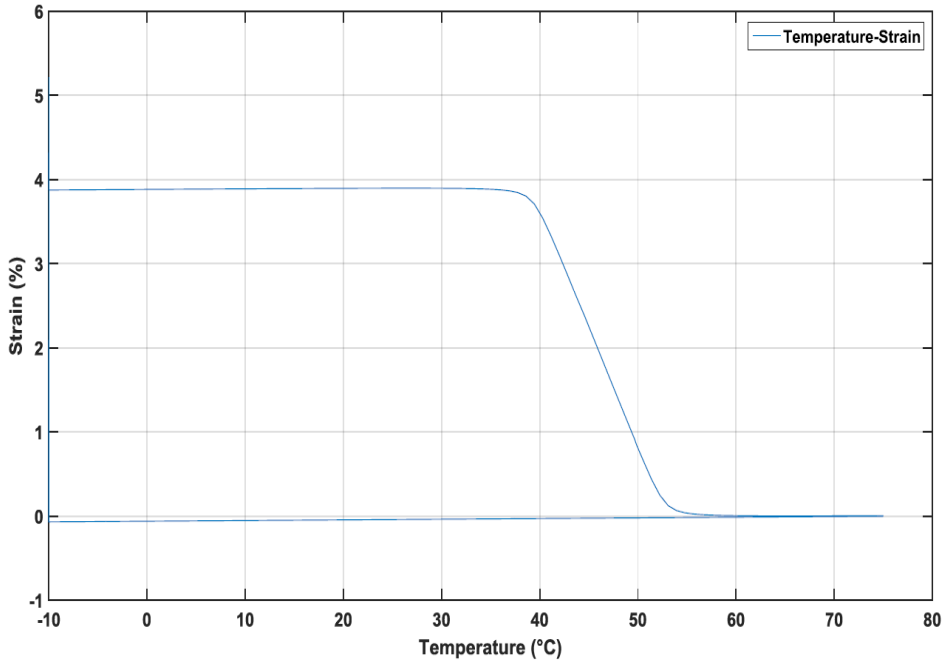

Figure 3.9 Strain -Temperature graph for the tensile test one-way shape memory effect

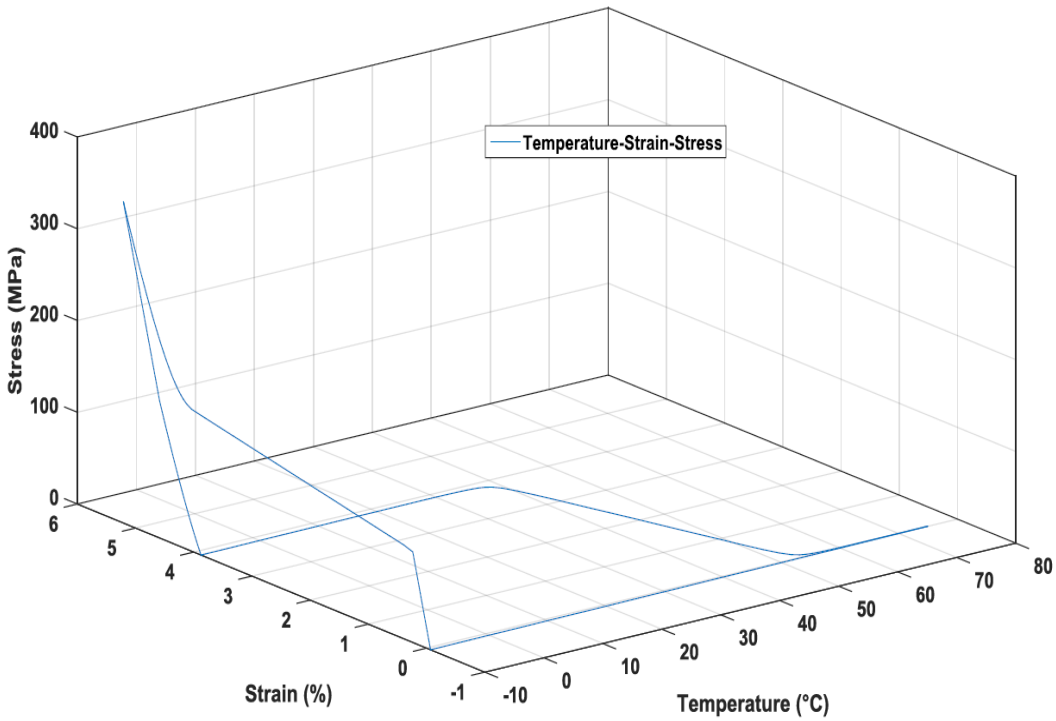

Figure 3.10 Temperature -strain-stress 3D graph for one-way shape memory effect

The simulation results for the bending test showed that the sample possesses a macroscopic strain after loading and unloading. The finite element model of the sample after the unloading process is shown in Figure 3.11(a). It is also evident that heating of the sample can eliminate the macroscopic strain, as illustrated in Figure 3.11(b).

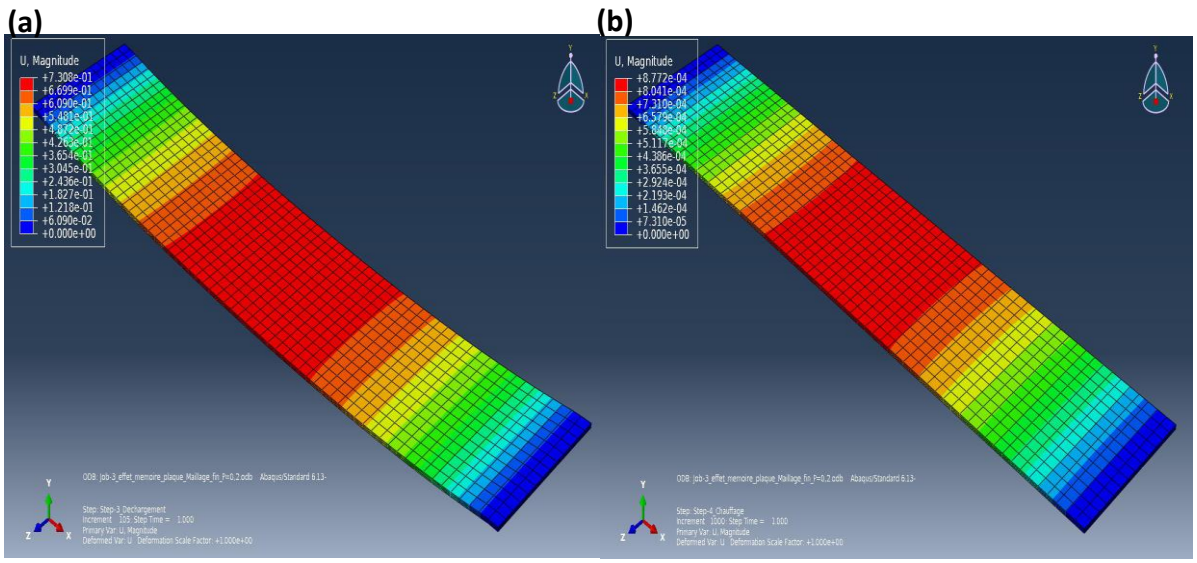

Figure 3.11. Deflection of the SMA sample after unloading process (b) The sample retains its original shape after heating.

The bending test results for one-way shape memory effect are given in figure 3.12 and 3.13.

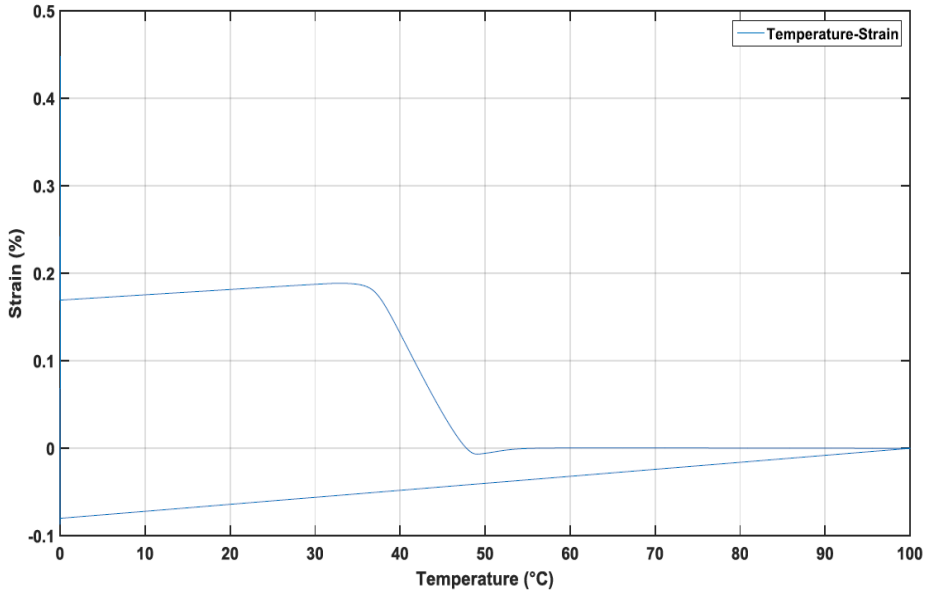

Figure 3.12 Strain-Temperature graph for bending test one-way shape memory effect.

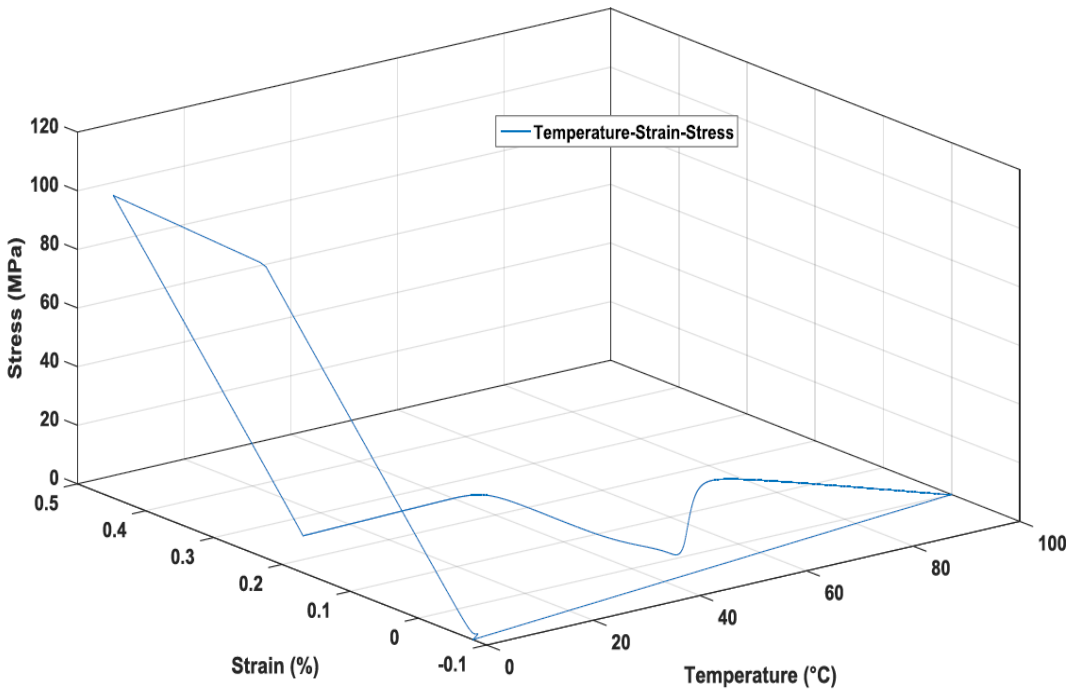

Figure 3.13. 3D graph of Temperature-strain-stress for bending test one-way shape memory effect.

We have considered the corresponding elements located in the middle of the top surface.

3.7.2 Two-way shape memory effect

In the case of the two-way shape memory effect, the thermal cycles also applied along with the mechanical loading. The tensile and bending simulation results for the two-way shape memory effect are represented in Figure 3.14 (a) and (b).

Here in our model, the changes in the deformation between thermal cycles are high or low depending on the previous load that we applied for the orientation of the martensite. Indeed, as we apply high stress in order to orient the martensite, if the heating is high, it leads to the elimination of strain caused by the activated high number of martensite.

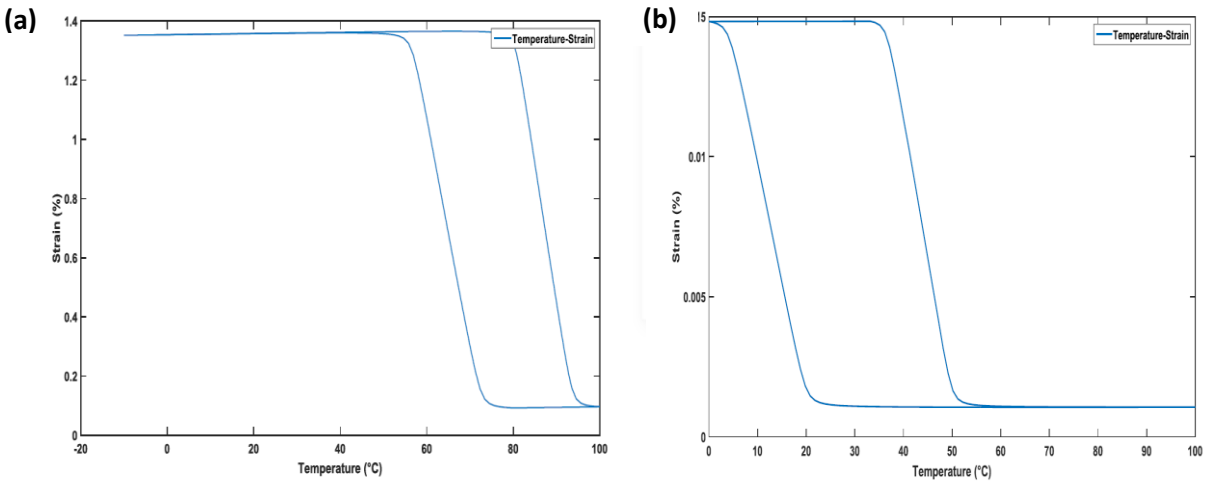

Figure 3.14. (a) Strain- Temperature graph for tensile test of two-way shape memory effect (b) Strain-Temperature graph for bending test of two-way shape memory effect.

In tensile and bending loadings, a change in deformation appears during heating and cooling of the material under mechanical loading. This confirms the two-way shape memory effect of the SMA.

3.7.3. SMA/Piezoelectric polymer composite

The composite material is subjected to both the tensile and bending tests. The thermal cycles are applied in order to induce the voltage output from the piezoelectric layer. The evaluation of electric potential as a function of temperature at different PVDF layer thicknesses for tensile loading is plotted below (Figure 3.15).

We have selected the thicknesses of the polymer layer from 3 to 8 µm to evaluate the relationship between the thickness versus the generated electric potential for different layers. The thickness of the P(VDF-TrFE) layer was 5 µm for the composite characterized experimentally. As it is evident, the electric potential increases linearly with the film thickness. Indeed, the induced electric potential increases with the increase in thickness and vice versa. During cooling, the forward martensitic transformation occurs in the SMA layer, which also induces a deformation of the piezoelectric layer: the electromechanical coupling causes the increase of the voltage. While heating, the activation of the reverse transformation recovers the transformation strain in the SMA layer. At this time the piezoelectric layer also recovers its shape and consequently the electric voltage decreases.

The increasing and decreasing of the electric voltage occurs with hysteresis related to the switching hysteresis between forward and reverse transformation in the SMA layer.

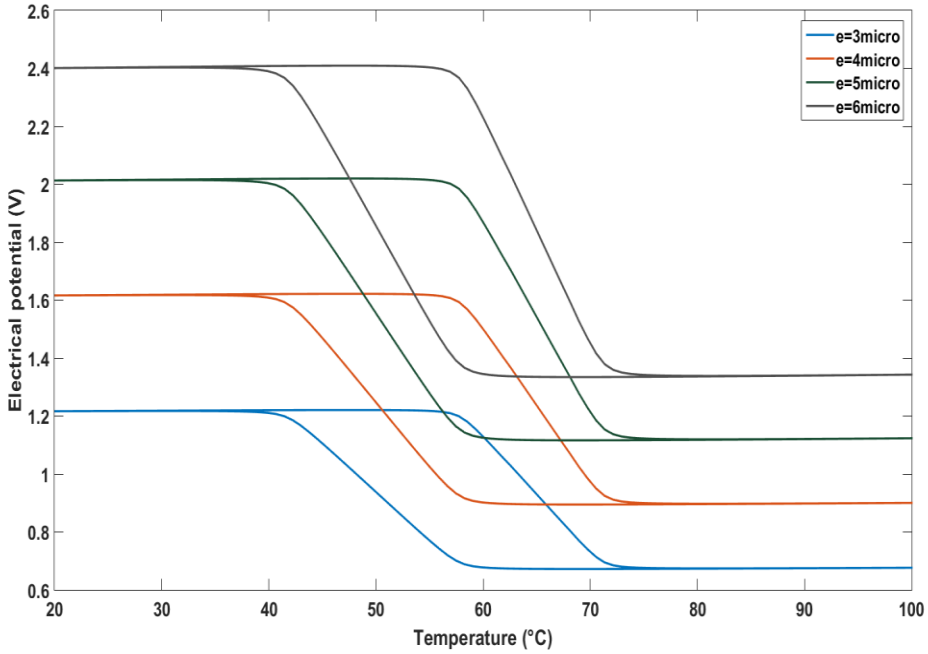

Figure 3.15 Electrical potential vs temperature graph for P(VDF-TrFE) layers with different thicknesses (3µm to 6µm) under tensile loading.

In the same way, the bending test was carried out for the different thickness layers of PVDF films, and the electrical potential was measured. The evaluation of the electric potential during thermal cycles for various thicknesses of the piezoelectric layer is plotted in the Figure 3.16.

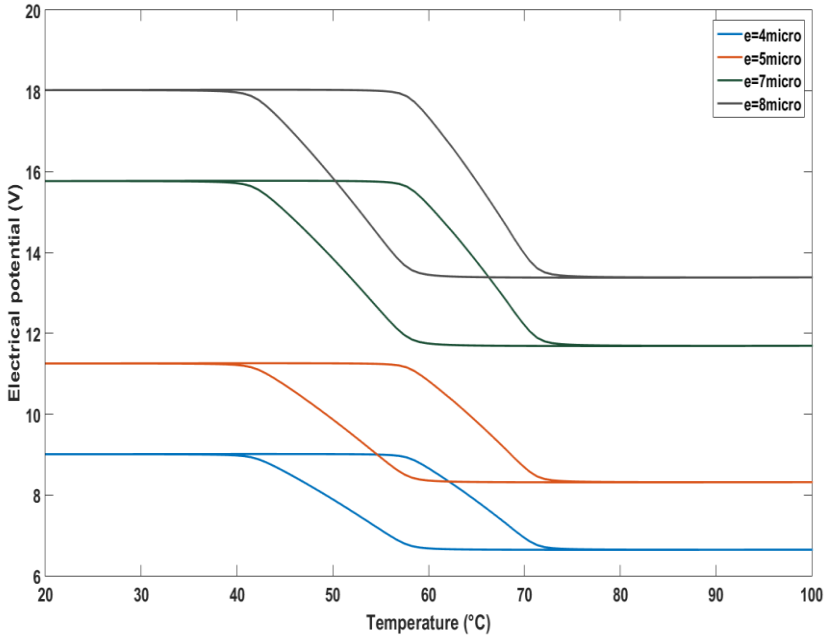

Figure 3.16 Electrical potential-temperature graph for PVDF layers with different thicknesses under bending test.

Both in tensile and bending tests, the electric potential increases with the increase in film thickness. To depict the phenomenon, we have plotted a graph showing the variation of the maximum and the minimum electrical potential created during thermal cycles for different

layer thicknesses of the piezoelectric film. The evaluation of the electrical potential versus the film thickness for both tensile and bending test is depicted in Figure 3.17.

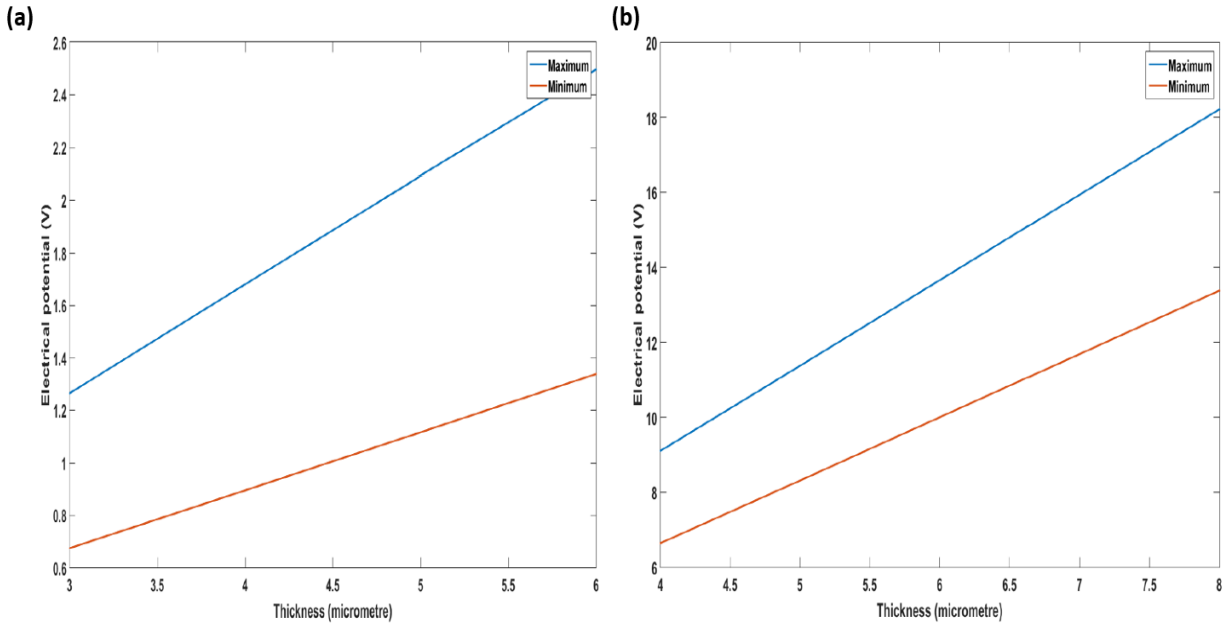

Figure 3.17. Electric potential evolution function of piezoelectric layer thickness (a) tensile (b) bending.

It is observed that the higher electrical potential output was observed on bending compared to tensile loading.

3.8 Comparison between simulation and experimental analysis of the composite

The tensile test was carried out experimentally for the SMA/piezoelectric polymer composite, which is discussed in chapter two. For the experimental test, initially, the sample was loaded to 80 MPa at room temperature (23°C). After loading, the sample was unloaded to zero stress followed by heating up to 75°C. During this process the induced electrical voltage from the piezoelectric layer were collected. Figure 3.18 illustrates the composite under the tensile loading and the corresponding finite element model. The mesh represents four elements through the thickness for the SMA layer with a thickness of 125 µm and two elements for the piezoelectric layer with thickness between 3 to 5 µm.

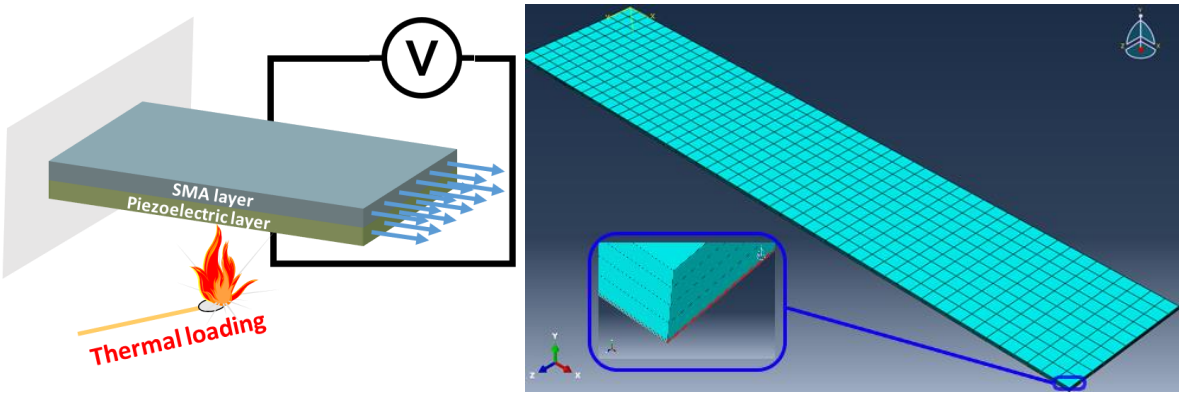

Figure 3.18. SMA/Piezo hybrid composite subjected to a heating-cooling loading under constant tension pre-loading, (b) finite element mesh for the SMA/piezo composite contains four elements for the SMA layer and two elements for piezoelectric layer along with the thickness.

The NiTi SMA tensile test was performed using a tensile machine starting from the room temperature at 23 °C. The finite element simulation and the experimental result for the stress-strain curve are shown in Figure 3.19. Both the experimental and simulated curves are in good agreement with the reported NiTi SMA stress-strain curves. After loading and unloading a remnant strain is observed on the material. Heating induces a reverse transformation allowing to recover of this remnant strain.

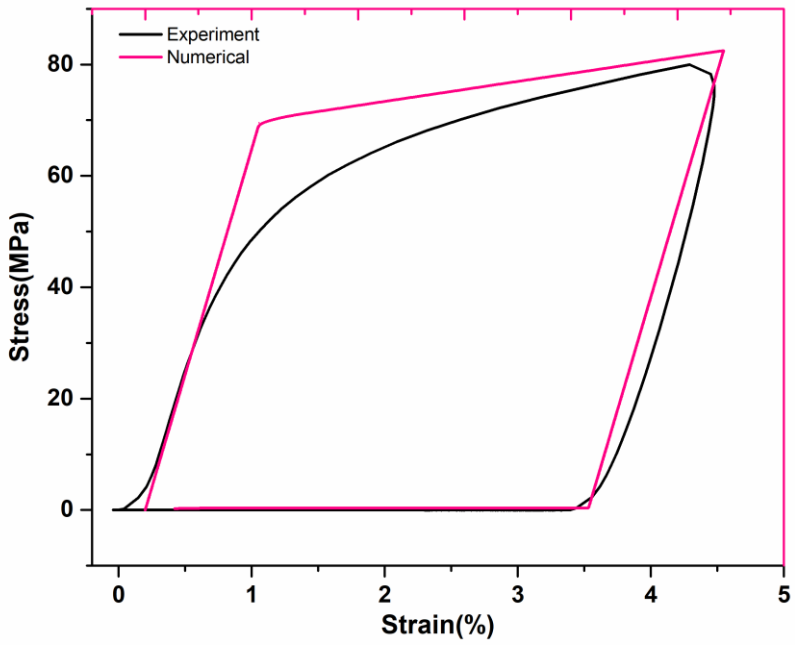

Figure 3.19. Experimental and modelling stress versus strain curve.

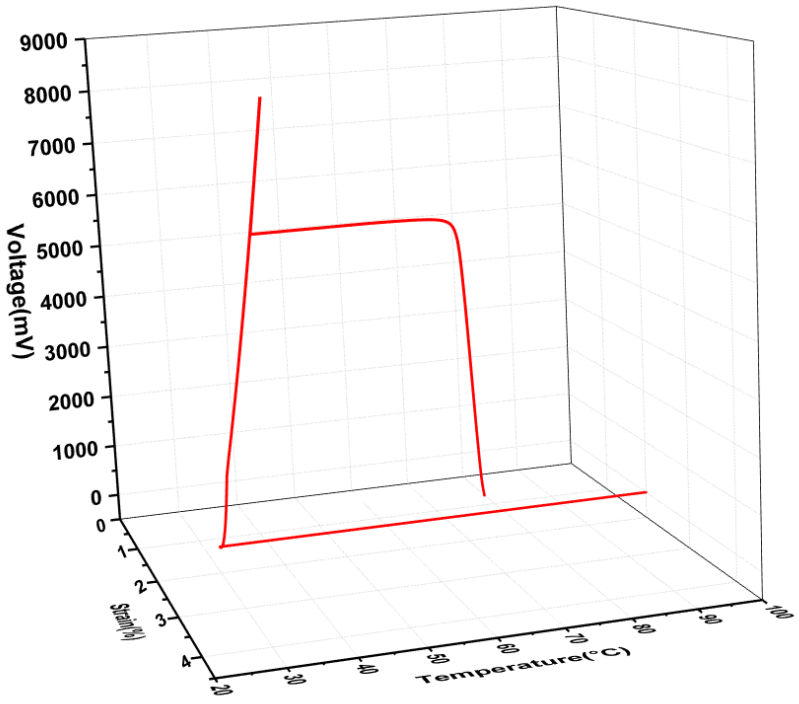

Figure 3.20. Evolution of the Voltage-Strain temperature in the numerical model.

Figure 3.20 represents the voltage-strain-temperature graph for the numerical model. The numerical simulation is carried out by the following steps: the first step represents the cooling under the M_f temperature followed by a tension pre-loading. The third step considers the unloading of the sample and finally heating of the hybrid composite above a temperature higher than A_f. The numerical results displayed a maximum voltage of 8 V generated from the composite. The electromechanical coupling induced during the phase transformation of the SMA induced the increase in voltage. However, during unloading and heating, the reverse transformation occurs and recovers the transformation strain in the SMA layer. Hence the voltage produced from the piezoelectric layer also decreases accordingly. We have obtained a voltage output of 5V during heating for the numerical simulation. While the experimental results give an output voltage of 3V. The lesser output voltage from the experimental results could be explained by the effect of the interface layer. The complete strain transfer from the SMA to the piezoelectric layer does not occurred. Therefore, we can observe a decreased voltage output for the experimental results.

3.9 Prototype geometry

The final objective of this study is to develop an energy harvester to convert the widely available waste heat into electric power. In order to perform the experimental characterization, we have developed an electro-thermo-mechanical harvester prototype. The harvester is designed in a way, that can provide simultaneous heating-cooling of the composite to amplify

the electrical response. A detailed description of the harvester prototype was shown in the second chapter section 2.5. For that, we have modified the shape of the composite sample and simulate thermal cycles on the material in the same way we did previously. The shape of the material is in the form of a disc of diameter 10mm. The thickness of the two-layer composite is the same. Prior to the composite preparation, the training of the NiTi SMA will be conducted, to achieve the shape memory effect. Therefore, it allows to get a shape change under periodic heating-cooling loadings. The configuration of the composite is shown in Figure 3.21(a). The disc is clamped on its circumference and is subjected to normal pressure. The simulation was carried out to find the evolution of electric potential as a function of temperature. We have obtained the same result for the simulation as previously. (Figure 3.21(b)).

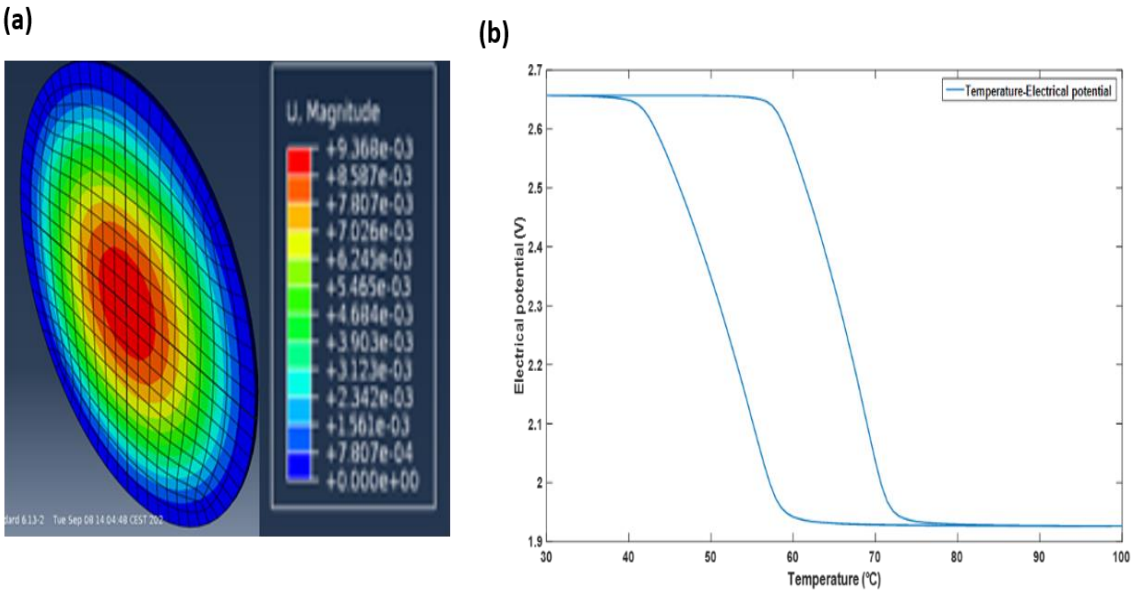

Figure 3.21. (a)Finite element model of the disc configuration for the composite material (b) Electric potential evolution function of temperature.

This solution is under investigation with the development of an experimental micro-harvester device in order apply the thermal and mechanical loadings and measure the induced electric voltage, the deflection, and the real temperature of the hybrid composite.

3.10 Conclusion

The main properties of the SMA such as superelastic behavior, one-way shape memory effect, and two-way shape memory effect were simulated using Chemisky et al., model already implemented in Abaqus via Umat. The classical and linear piezoelectric constitutive model was used to describe the electromechanical behavior of the piezoelectric layer. The one-way and two-way shape memory effect was well proved by modeling the tensile and bending loading. In this study, we want to work in a low-stress condition. However, in the two-way shape memory effect, no change in strain was observed during thermal cycles under low stress. We found this

is due to the fact that at low stress there was no orientation of martensitic variants. Therefore, at first, we loaded the sample at a stress high enough to orient the martensite before applying the thermal loading.

We have successfully developed the finite element model for the SMA/piezoelectric polymer composite. During the application of thermal loading, an electrical potential was induced on the piezoelectric layer, which is well exhibited through the model. Also, we exhibited the electrical potential depends on the piezoelectric thickness of the piezoelectric layer. This electrical potential increases with the increase of thickness. We have compared the finite element model for the one-way shape memory effect with the experimental data. The compared results showed both the experimental and simulated results have correlated with each other.

The composite shape was changed to a disc in order to perform the electro-thermo-mechanical characterization of the device. Also, we have simulated the evolution of the strain and electrical potential with the temperature. The finite element model helps to define the geometry for the micro-energy harvester prototype, the thickness of the multiple layers of the composite to predict the composite which allow to maximize the exhibited electrical potential and therefore the delivered electric power.

The coming chapter deals mainly with different aspects of piezoelectric energy recovery from the P(VDF-TrFE) film. We will present different mechanical systems in order to characterize the piezoelectric performance. As the main challenge in piezoelectric energy recovery is to collect the instantaneous charge created on the film. Hence the power conversion efficiency of the whole device is relying on the electronic circuit. For that, we have compared the performance evolution of two types of electronic circuit boards. Thus, in the final chapter, we will discuss the electronic part with the ambition of powering low-scale electronic devices.

Chapter 4

Performance evaluation for piezoelectric energy recovery

4.1. Shaker test bench for piezoelectric energy recovery 101
4.1.1 Components of the shaker test bench 102
4.1.2 Study with the shaker test bench 105
4.2 Mechanical system for bending test 106
4.2.1 Principle of operation 106
4.2.2 Study with the mechanical bending system 107
4.3 Electronic circuits for piezoelectric energy harvesting: state of the art 109
4.3.1 Electrical modelling of the piezoelectric generator 110
4.3.2 Piezoelectric energy recovery standard circuits 112
4.3.3 Optimal recovery techniques 115
4.4 Practical application to our system 119
4.4.1 Equivalent electrical circuit of a piezoelectric generator 119
4.4.2 Choice of energy harvesting electronics 120
4.4.3 Simulation of the system with the LTC 3108 board 121
4.4.4 Simulation of the system with the LTC 3588-1 board 124
4.5 Conclusion 126

Introduction

After having developed the piezoelectric film, designed, and fabricated the SMA/P(VDF-TrFE) composite, simulated its electro-thermomechanical performance, and designed a specific heating/cooling system to operate it under thermal-cycling conditions, it is necessary to test its performance in terms of piezoelectric energy recovery under different application situations.

To do so, the necessary step is to set up a piezoelectric test bench, first, we have tested the film based on a mechanical shaker setup. The experimental setup consists of a vibrating shaker, provided with a rod periodically deforming the piezoelectric film. As we show in this chapter, this setup gave interesting results, but insufficient in terms of deformation amplitude and consequently of piezoelectric response. This led us to design and develop a specific system for the actuation of flexible piezoelectric films, described in the next section. This new system, realized in 3D printing by the IJL services, proved to be very efficient for the generation of piezoelectric charges from our P(VDF-TrFE) films.

The next step, essential and non-trivial, was the collection of these piezoelectric charges and their transformation into electrical power. For this purpose, a bibliographical study was carried out to determine the most adapted electronic solutions, described in this chapter. This study directed our choice towards two electronic boards available on the market, the LTC3108 board and the LTC3588-1 board, of which we led, after having defined the conditioning of the board, the compared theoretical study through the electronic simulation software LT-Spice. The results of these simulations given for different voltages and different currents supposed to be generated by the piezoelectric device show that these two modules can constitute a solution of piezoelectric energy recovery. However, the input currents necessary for the nominal operation of these energy harvesting electronic cards are often higher, even very higher than those generated by our piezoelectric device. In this sense, the comparison of the boards leads to the choice of the LTC3588-1, although it still consumes too much current. At the end of this chapter, we discuss the possibility of overcoming the technological bottleneck of the minimum electrical current that can be harvested from a piezoelectric polymer film-based device. For this electronic part, I had the help of several students that I co-supervised in an internship or in study project during this PhD work: R. Amrane, Y. Ammour and S. Belgaid, U. Mpouette and A. Noupayou Teguia.

4.1. Shaker test bench for piezoelectric energy recovery

Energy harvesting from piezoelectric materials are one of the promising solutions for the future of micro and nanoelectronic components as well as for power electronics components. Currently, the recovery and exploitation, as well as the storage of piezoelectric energy, are at the heart of various scientific research around the world. This subject is quite complicated for many reasons, but mainly because the charges created on the surface of a piezoelectric crystal on the one hand generate a weak current, and on the other hand disappear quickly. Thus, it is necessary to develop and implement a specific electronic to recover the piezoelectric energy.

Nevertheless, the prior step was the realization of an automated test bench to study the electrical characteristics of a piezoelectric film. Our first system (Figure 4.1) is based rather classically on a mechanical shaker, powered by a function generator, which periodically exerts mechanical stress in the form of vibrations on the film surface.

Therefore, to determine the energy harvesting performance of the P(VDF-TrFE) films prepared in our work, they were first subjected to an external strain using a mechanical shaker and the output voltage was recorded. The mechanical shaker, powered by a function generator, periodically exerts mechanical stress in the form of vibrations on the film surface. Figure 4.1 shows the photographic image of the experimental setup. The setup consists of an oscilloscope (Keysight Infinii Vision DSO-X 3012T), a shaker (LDS V200), an amplifier (LDS LPA100) to drive

the shaker and a function generator (Agilent 33120a). The vibration from the shaker was applied to the P(VDF-TrFE) film by using an extended metal arm from the shaker.

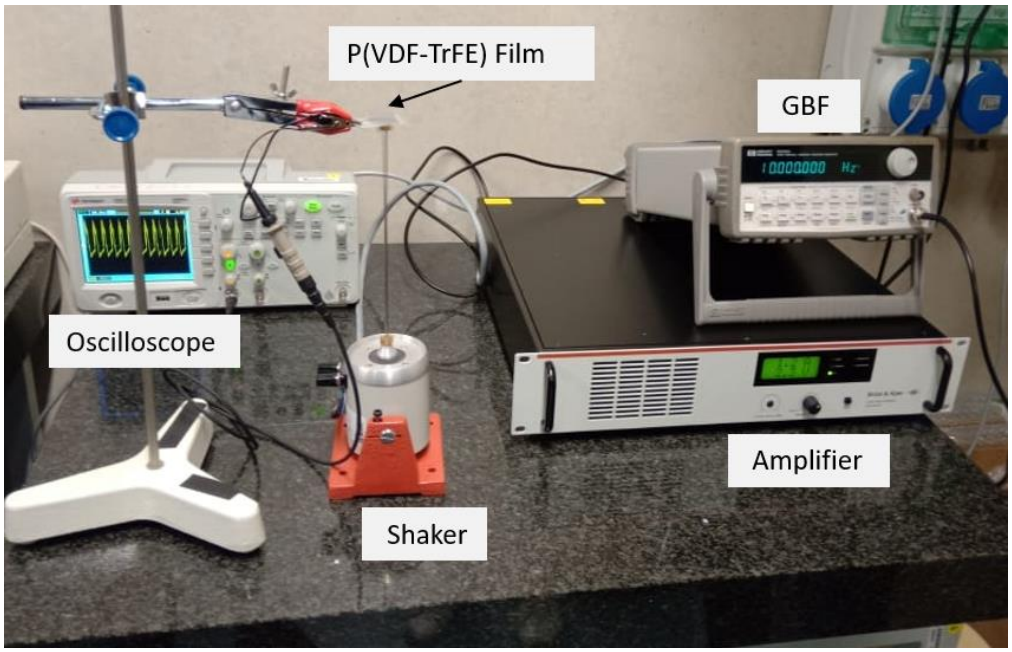

Figure 4.1 Experimental setup for the mechanical shaker system for piezoelectric energy recovery.

We automated this test bench, by realizing a LabVIEW program to control with a GPIB -IEEE488 interface card both the GBF function generator and the oscilloscope. This allowed us to perform a frequency sweep for different powers of the shaker and to visualize the response of the piezoelectric sample to distinguish the optimal frequencies for a given situation.

This shaker test bench is composed of a sample holder, shaker, the shaker being driven by its specific power supply, the sample fixed on the holder, periodically bent by the vibration of the shaker, and the generated voltage output is measured from the two electrodes which are connected to the oscilloscope, and the oscilloscope controlled like the GBF function generator by the GPIB card programmed by LabVIEW (the details are given in appendix 1 figure 1 and 2). Some of these elements are described below.

4.1.1 Components of the shaker test bench

I. Sample

The samples tested with this bench were P (VDF- TrFE) copolymer films, typically 5.3 µm thick on a surface of 1.6x2.3 cm^2, deposited by spin coating and polarized with electrodeposition on top and bottom, as described in Chapter 2 (Figure 4.2).

Figure 4.2 P(VDF-TrFE) Piezoelectric film.

II. Mechanical shaker

The V200 Electrodynamic Vibrator named here as the "shaker" (LDS V200) is a miniaturized unit designed to generate vibrations under laboratory conditions. It is widely used in educational and research institutions for applications such as dynamic study of structures and materials, electronic assembly testing, fatigue, and resonance testing, use as a velocity transducer or actuator. The shaker can be driven by any suitable oscillator/amplifier combination. In this study we used the LDS LPA100 amplifier, as shown in Figure 4.3.

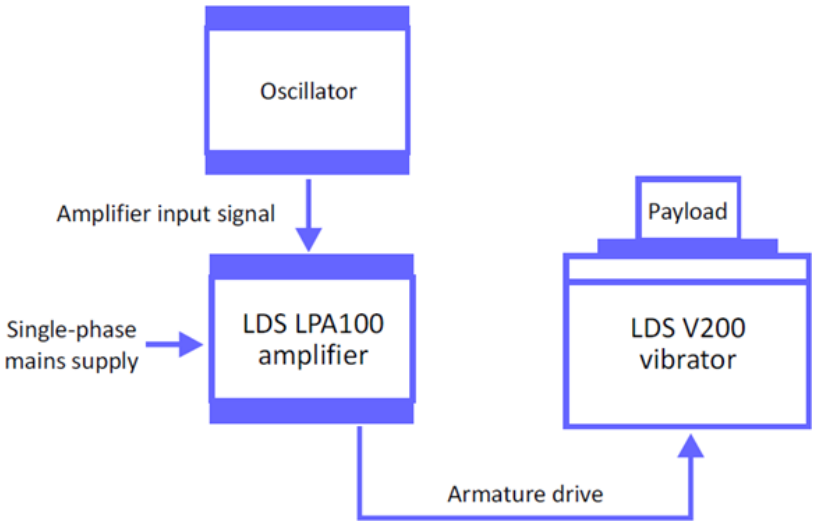

Figure 4.3 Schematic diagram for the shaker.

The vertical displacement of the shaker varies depending on the mass of the sample studied. To calculate it we have the formula below:

$$D = S - (2 \times \frac{W}{K}) \qquad (4.1)$$

The calculated values for displacement are provided in Table 4.1.

Abbreviations	Denominations	Values
S	Maximum permitted peak-to-peak displacement [mm]	5
D	Maximum available displacement, peak to peak [mm]	(m=0) => 5
K	Stiffness without auxiliary	2.8 N/mm
W	Sample mass (mass x 9.81) [N]	(m=0) => 0

Table 4.1 Calculation parameters of the displacement performed by the mechanical shaker.

However, in any case, the maximum vertical displacement is limited to 5 millimeters peak to peak, as given by the technical specifications of the LDS V200 shaker powered by the amplifier (LDS LPA100) and given in Appendix 1.

III. Support of the piezoelectric film

In order to ensure a solid support of the P(VDF-TrFE) film, we imagined a support in the form of a bracket at the end of which would sit a clamp coated internally with an insulating element, to ensure the separation between the film electrodes. The photographic image of the support system to hold the sample is given in Figure 4.4.

Figure 4.4 (P(VDF-TrFE) film holder view (a) Front view (b) Side view

(a) (b)

IV. LabVIEW program

After the shaker was mounted and tested for operation, we performed the programming of a LabVIEW command to automate the test bench. The aim was to perform frequency sweeps at different voltages in order to visualize and exploit the piezoelectric response of the P(VDF-TrFE) film and identify the most interesting frequency ranges in terms of energy efficiency. To this end, we used a GPIB-IEEE488 interface board to connect the function generator (Agilent 33120a) and oscilloscope (Keysight Infinii Vision DSO-X 3012T) to the PC via a USB input, initializing the GBF and oscilloscope ports via Digilent's "KeySight" software.

The procedure for the initialization of the GBF ports and oscilloscope, as well as the two steps of the design of the LabVIEW control and the LabVIEW command dashboard are given in Appendix 1 (Figure 2).

4.1.2 Study with the shaker test bench

To determine the optimum operating frequencies of our piezoelectric samples, we made two sweeps for two frequency ranges with a step of 5 Hz in "Tapping" mode, with different vibration amplitudes, corresponding to different voltages applied on the shaker.

[10, 50] (Hz) for voltages [0.6, 0.8, 1, 1; 2] (V)
[40, 80] (Hz) for voltages [1.5, 1.7, 1.9] (V)

Beyond 80 Hz the vibrations are no longer perceptible and the security that we have applied to the current level does not allow the voltage to exceed 1.9 V. Note that, the lower the frequency used, the higher the current through the shaker, so at low frequency the maximum amplitude is around 1.9 V. The values highlighted in Table 4.2 and 4.3 showed that for high voltages, the frequency range allowing the highest voltage responses is [60,65] Hz against [35,40] Hz for low voltages.

Frequencies [Hz] / Amplitude [V]	10	15	20	25	30	35	40	45	50
0.6	0.38	1.3	0.25	0.9	0.75	0.38	1.3	0.9	0.5
0.8	0.4	0.25	0.25	0.3	0.5	0.5	0.25	0.22	0.4
1	0.26	0.39	0.25	0.24	0.61	0.6	0.38	0.25	0.49
1.2	0.4	0.6	0.38	0.5	0.5	1.1	0.7	0.7	0.4

Table 4.2 Frequency sweep [10,50] Hz

Frequencies [Hz] / Amplitude [V]	40	45	50	55	60	65	70	75	80
1.5	0.6	0.25	0.25	0.5	0.6	1	0.8	1.2	1.1
1.7	0.75	0.5	0.75	0.6	2.6	1.95	0.9	0.6	0.9
1.9	0.82	0.6	0.49	0.82	3.4	2.9	1.6	0.75	1.3

Table 4.3 Frequency sweep [40,80] Hz.

Although the results of this test bench (Table 4.2 and 4.3) are interesting, with voltages obtained exceeding 3V at 60Hz, they do not serve our expectations because as we will see later in this chapter, the proper functioning of electronic cards of piezoelectric energy recovery often require higher input voltages. That is why we have developed a specific test bench more adapted to our samples. For this new test bench, it will be essential to find a system that allows us to apply a 'bending' deformation to the film. Bending deformation gives higher voltage output due to the high area of deformations for the piezoelectric film.

4.2 Mechanical system for bending test

Our previous setup using the shaker leading to the recovery of rather low voltages related in fact to limited deformations, we developed a specific mechanical bench for the test of flexible piezoelectric films. The aim was to set up a system that would allow us to bring the stresses in a repetitive and precise way on the PVDF type piezoelectric film, and to read the voltage delivered by the piezoelectric film when it is subjected to these stresses.

The design of our mechanical bench was developed with SolidWorks software. After the design phase came the 3D printing by the mechanical engineers of the Institute Jean Lamour laboratory. The design of the mechanical test bench developed in Solidworks is shown in Figure 4.5.

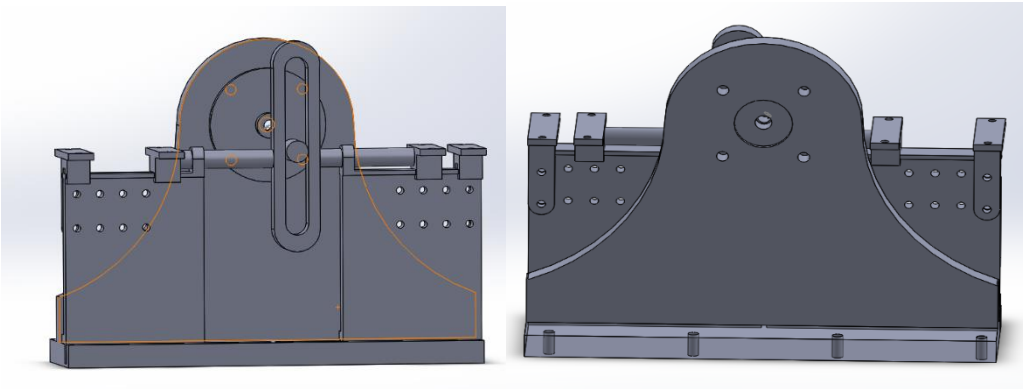

Figure 4.5. Front and back view of the mechanical test bench design with SolidWorks.

4.2.1 Principle of operation

Our model combines the system crank rod and the excentricity of the cam. Indeed, we have a wheel which is driven by rotation by a stepper motor. On this wheel we put an exocentric tube, which drives in turn the connecting rod connected on both sides to the supports on which are fixed the piezoelectric film(s) to be tested. This support is driven in translation by the rotation of the stepper motor, the other end of the support being fixed. The maximum distance between the two supports is 28.34mm and the minimum 2mm (length of the whole system 180 mm). Thus, the film is deformed at each cycle in a much stronger way than in the previous system.

The mechanical operation of the bench, controlled by an Arduino board via the stepper motor, is detailed in appendix 1. This appendix 1 (figures 3,4 and 5) provides the characteristics of the stepper motor, the wiring circuit of the motor with the Arduino module, the control program of the stepper motor and the particular connections of the pins of the Arduino Shield module for a bipolar motor.

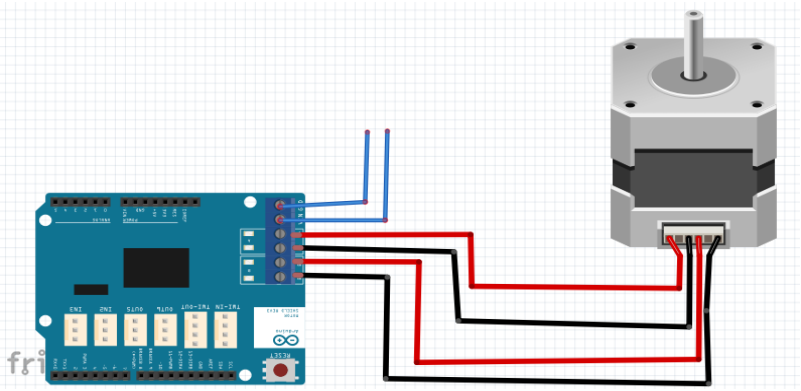

Figure 4.6 Arduino board and stepper motor.

4.2.2 Study with the mechanical bending system

We have taken direct measurements of the voltage that our 1.6x2.3 cm^2 area piezoelectric film can deliver. The purpose of this operation is to know the maximum voltage that can be delivered by the piezoelectric film when it undergoes stresses in a precise and constant way by the mechanical bench that we have designed. We have calibrated the stabilized power supply at 6 V to make our motor turn. With this setting, the motor rotates by 20 right turns and 20 left turns. The oscillation frequency was 5.551Hz. For this measurement, we calculated the maximum and minimum distance of the stress oscillation exerted on the piezoelectric film: 1.5mm and 3.3mm respectively. A photographic image of the mechanical test setup is shown in Figure 4.7. The test results are recorded with an oscilloscope and an example of obtained result is presented in
Figure 4.8.

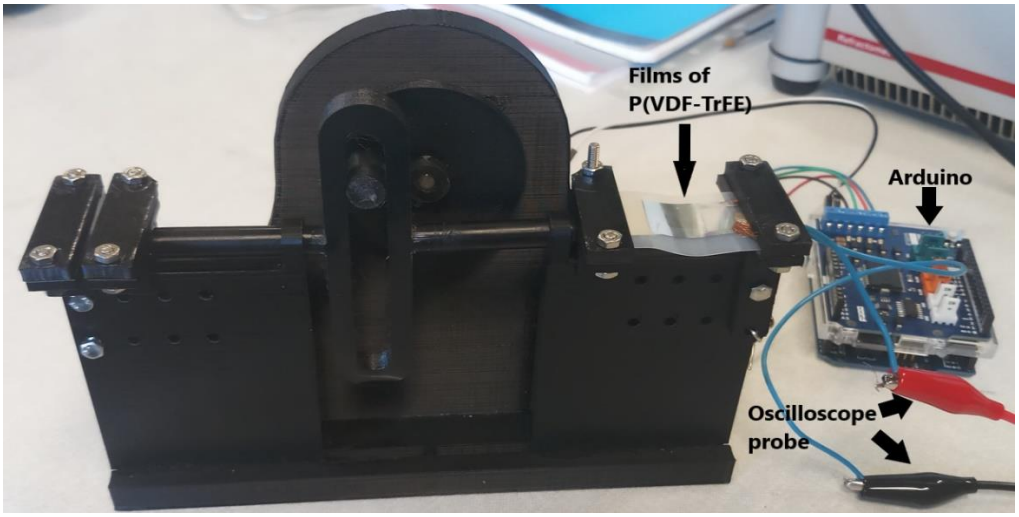

Figure 4.7 The experimental setup of the mechanical bending system.

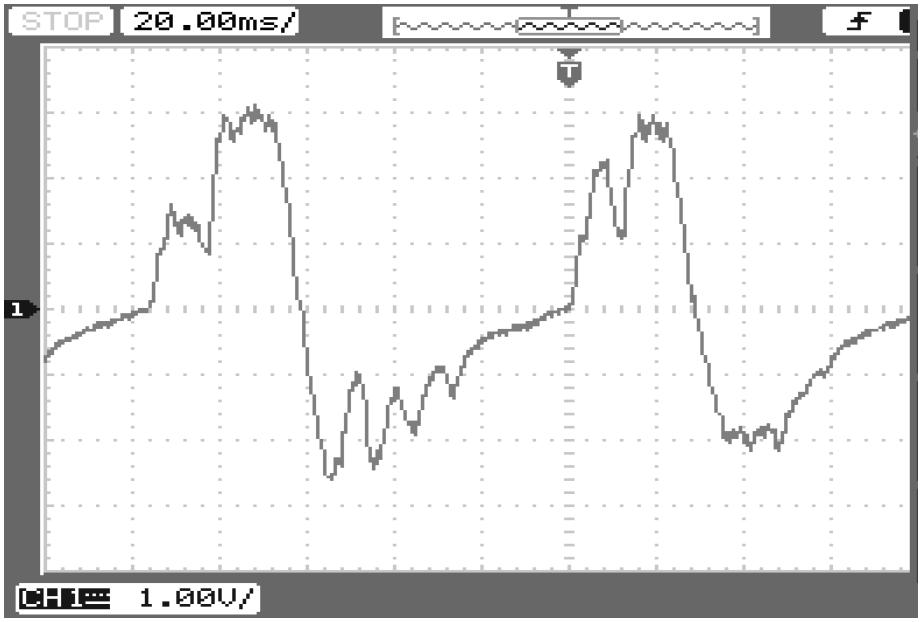

Figure 4.8 The generated output voltage from the piezoelectric P(VDF-TrFE) film

In this example, we observed a peak-to-peak voltage delivered by the piezoelectric PVDF film of 5,70V. The shape of the signal is almost periodic. The slight difference in the shape of the graph between the two periods is probably due to the rigidity of the P(VDF-TrFE) film used in this manipulation, as we visually observed that the motor of the mechanical folding system wasn't powerful enough to apply a uniform and regular stress on the film.

Then other tests were carried out on P(VDF-TrFE) films with the same physical, mechanical, and electrical characteristics, but thinner and more flexible, so that they can be folded properly by the mechanical folding system (Figure 4.9).

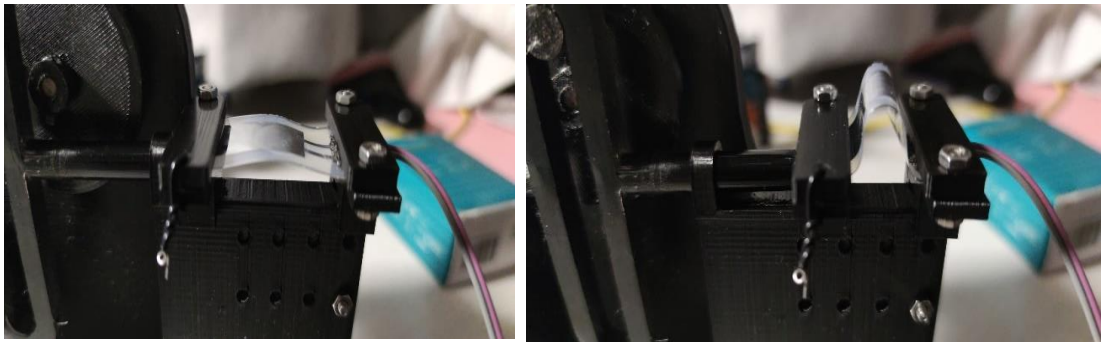

Figure 4.9 Folding and unfolding of the P(VDF - TrFE) film by the mechanical folding system during handling.

The oscilloscope being connected to the output of the piezoelectric film during the application of mechanical stresses, we have recorded the output signal from the second piezoelectric film, which is given in Figure 4.10.

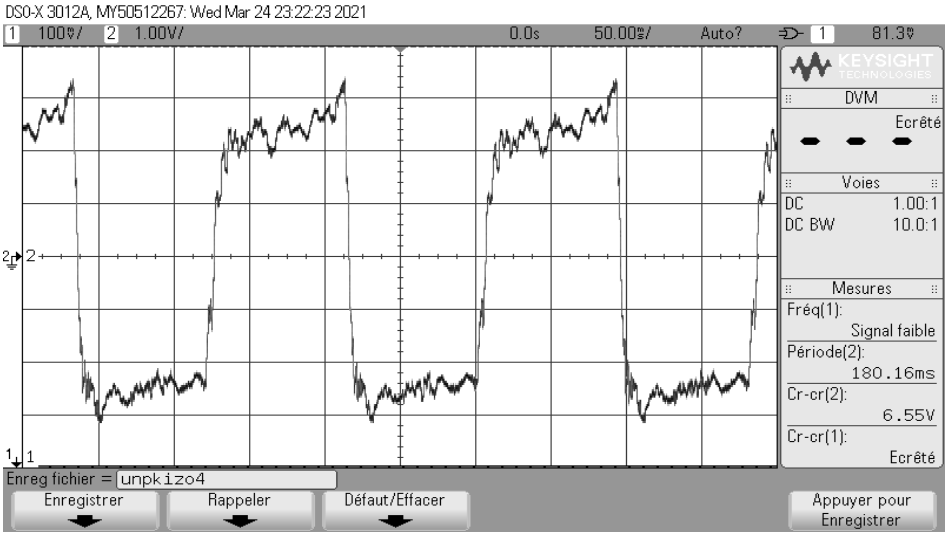

Figure 4.10 Output voltage from the P(VDF-TrFE) film.

In this case we have obtained a higher peak-to-peak voltage, of 6.55V. We can also see that the shape of the signal is more regular and periodic, which allows us to confirm our hypothesis: indeed when the film is flexible enough the contraction applied by the mechanical folding system is better which leads to a higher voltage (almost 1V difference between the two films) and a periodic signal.

The piezoelectric current delivered by different individual piezoelectric films mounted on this test bench was also measured using a picoammeter. We obtain a current peak of about 0.4 to 0.5µA for each mechanical activation of the film. For all samples, the voltage delivered by the films was always higher or equal to 5V (oscilloscope measurement)**.**

As shown in Figure 4.7, this machine can perform this manipulation with two samples: in order to carry out the test, two films can be placed on both sides of the mechanical bench. Thus, this test bench is equivalent to a push-pull setup: the samples are bent alternately. For our sma/piezo device, this could illustrate for example an application where two items would alternately pass through a heat source, and at each instant one SMA/P(VDF-TrFE) device would be fold and the other unfold. In this configuration, by collecting both voltages, we can tend to a rectified voltage signal at the output of the piezoelectric film and to increase the energy harvesting.

4.3 Electronic circuits for piezoelectric energy harvesting: state of the art

The next step is the choice and optimization of the energy extraction circuit ensuring the conversion of the produced electric charges into exploitable electric power to feed an electronic component. We have developed a mechanical system to create the bending and vibration motion for the P(VDF-TrFe) film. However, the aim of this study is to convert mechanical or thermal energy into electrical energy to power small scale electronic device.

In this regard, it is essential to collect the charges from the film and to power electronic devices. Therefore, the studies on electronic parts pay much attention to the efficient energy harvesting from the piezoelectric polymers.

The electronic circuit is a major part in piezoelectric energy harvesting systems, which plays a significant role in power conversion efficiency of the whole system. The main problem is to convert the electronic charge into electric power because there are few charges generated by piezoelectric effect. Mostly, the piezoelectric energy harvesting system interface circuit contains three key elements. They are an AC-DC rectifier which rectify the AC voltage generated from the piezoelectric element into DC. Another one is the voltage regulator that regulate the DC power supply to the storage device like capacitor. The third important element is the storage device which stores the harvested energy[283,284].

4.3.1 Electrical modelling of the piezoelectric generator

To recover part of the ambient mechanical energy in the form of electrical energy, by exploiting the direct piezoelectric effect, the electromechanical behaviour of the piezoelectric system and its modelling must be known in order to optimize the energy transfer. In practice, the piezoelectric element is either independent or associated with a mechanical resonator.

I. Piezoelectric element associated with a mechanical resonator

In most applications of energy recovery from mechanical vibrations, the piezoelectric element is inserted between a frame integral with the vibrating body and a moving mass called seismic mass. Part of the external mechanical energy is thus converted into kinetic energy by this mass and then converted into electrical energy by the piezoelectric structure. The mechanical model of this generator is conventionally represented by a second-order diagram consisting of the seismic mass, a spring and a damper[284,285] (Figure 4.11a).

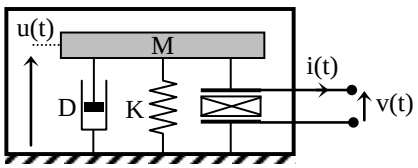

Figure 4.11(a). Mechanical model with localized constants of a piezoelectric resonator generator.

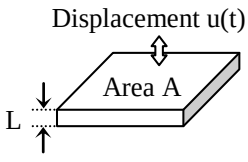

(b). Vibrating piezoelectric element in thickness mode

The frequency characteristics of the mechanical resonator are generally different from those specific to the piezoelectric element. They are adapted to the dynamics of the vibratory source and, to simplify the problem, we can consider that the generator is excited around its resonance frequency. In the following, the piezoelectric element is considered as a blade with a thickness L and a surface "A" vibrating in thickness direction. (Figure 4.11b.)

We can note some parameters for the piezoelectric element as:

u [m]	:	displacement of the blade plane under the action of a stress
k (ou k^2)	:	piezoelectric coupling factor
C_0 [F]	:	blocked capacitance of the piezoelectric element
e_{33} [C/m^2]	:	piezoelectric constant of the piezoelectric element
$\alpha = -e_{33}\frac{A}{L}$ [C/m]:		effective piezoelectric coefficient

For the mechanical resonator the important parameters are,

M [kg]	:	equivalent seismic mass
K [N/m]	:	spring stiffness constant
D [N/ms^{-1}]	:	damping coefficient

In dynamic mode the electromechanical system obeys the following equations:

$$M\ddot{u}(t) + D\dot{u}(t) + Ku(t) + \alpha v(t) = F(t) \quad (4.2)$$

$$\alpha\dot{u}(t) - C\dot{v}(t) = i(t) \quad (4.3)$$

Where the second equation corresponds to an electrical equivalent circuit consisting of a current generator of intensity proportional to the speed of travel in parallel on the blocked capacitance C_0 (Figure 4.12a). It should be noted that the various electrical losses are neglected here. They can be represented by the addition of a parallel parasitic resistance.

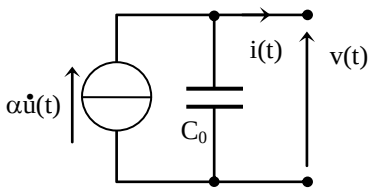

Figure 4.12(a). Simplified electrical model of a piezoelectric element.

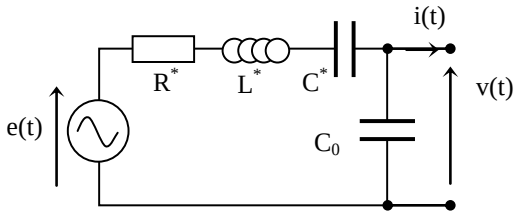

(b). Electric model of a piezoelectric resonator.

The current source depends on the mechanical parameters of the resonator. In case the vibrations can be assimilated to a harmonic pulsation excitation, the piezoelectric resonator can be replaced by an equivalent electrical diagram formed by a voltage generator associated with an internal impedance of type[286] R*-L*-C* (Figure 4.12b)

$$R^* = \frac{D}{\alpha^2} \qquad L^* = \frac{M}{\alpha^2} \qquad C^* = \frac{\alpha^2}{K} \qquad (4.4)$$

II.Independent piezoelectric element

For a piezoelectric element subjected to any forced regime, the model to be used remains that of Figure 4.11. The difficulty lies in the knowledge of the speed profile imposed by external stress.

4.3.2 Piezoelectric energy recovery standard circuits

1. Simple circuits

Piezoelectric elements only deliver electrical energy when their structure is in motion. The output voltage and current are therefore of AC mode and most often of pulse type. An AC-DC conversion stage, with or without regulation, is required to supply a load.

The base circuits shown in Figure 4.13(a) and (b) can be used to recover energy from isolated impacts on a piezoelectric plate or film. Low conduction threshold diodes (Schottky) are recommended. R represents the terminal electrical charge (battery). These assemblies accumulate the energy of the impacts in the storage capacitor C which must have a very low leakage resistance[62]. The second assembly theoretically doubles the DC output voltage. In both cases, the energy recovery rate remains low.

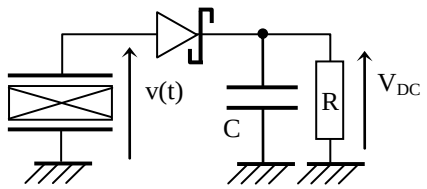

Figure 4.13.(a) Simple rectifier

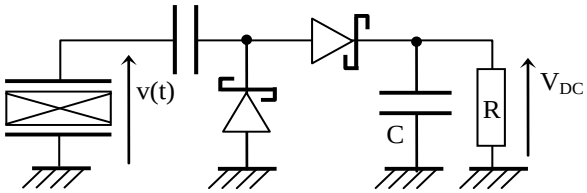

(b). Simple rectifier with voltage doubler

2. Standard circuit with double alternating rectifier

The standard piezoelectric energy recovery circuit (Figure 4.14a) uses a double alternating rectifier bridge.

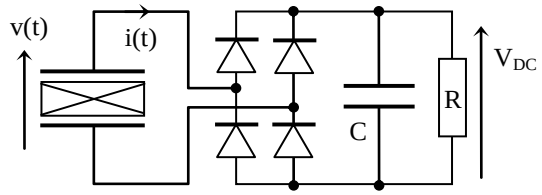

Figure 4.14(a). Standard circuit for piezo energy harvesting.

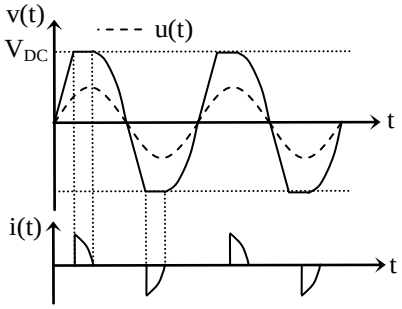

(b) Voltage and current waveforms of standard circuit

A sinusoidal displacement u(t) of pulsation and amplitude U_0 is considered. Storage capacity C is assumed to be high enough to assume that V_{DC} remains constant during a vibration cycle.
By neglecting the conduction thresholds of the diodes, the current i(t) is zero as long as the absolute value of v(t) is lower than V_{DC}. The piezoelectric element is in this case in an open circuit and v(t) varies proportionally to the displacement u(t).

When $|v(t)|$ reaches V_{DC}, the rectifier enters into conduction and energy extraction begins. The current is then proportional to the speed of the movement. Conduction stops at extremes of displacement for which the speed is zero. The evolution of the current i(t) shown in Figure 4.14(b) shows that the energy transfer is carried out during a small part of the vibration cycle.
The average electrical power in the load R, the maximum harvestable power and the optimal load can be determined using the expressions presented in Table 4.4[287].

Average electrical power	Theoretical maximum power	Optimal load value
$P = \frac{4\alpha^2 R\omega^2}{(2RC_0\omega + \pi)^2} U_0^2$	$P_{max} = \frac{\alpha^2 \omega}{2\pi C_0} U_0^2$	$R_{opt} = \frac{\pi}{2\omega C_0}$

Table 4.4. The harvesting and optimal load value for standard piezoelectric energy recovery circuit.

The reusable electrical power is dependent on the load R which is a disadvantage. Theoretical methods to dynamically adapt this load have been proposed but are not used in practice.

3. Circuits with double alternating rectifier and output regulator

The level of the rectified voltage V_{DC} is proportional to the amplitude of the displacement U_0 which in practice is not constant. The addition of a downstream voltage regulator is generally necessary. The assembly shown in Figure 4.15 uses a simple linear regulator to lower and regulate the V_{DC} voltage. The Zener diode protects the controller against possible overvoltage's[288].

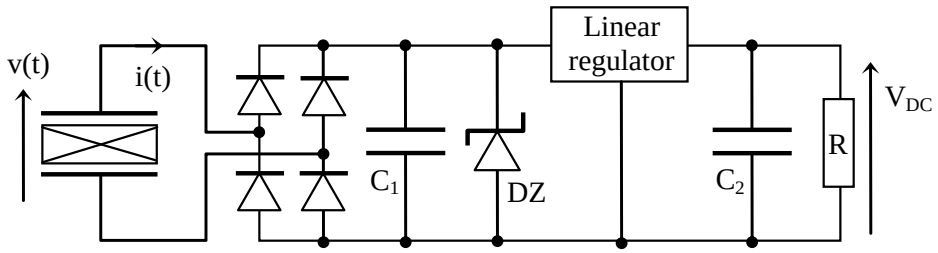

Figure 4.15 Standard interface circuit with DC voltage linear regulator.

This simple solution reduces the overall efficiency of energy conversion. It cannot be used for low power systems.

In a recent application[64], the authors use a similar strategy to extract energy from a PVDF-TrFE multilayer. In the proposed set-up (Figure 4.16), the LTC4071 integrated circuit is used to control and regulate the charge of a LI-Ion battery.

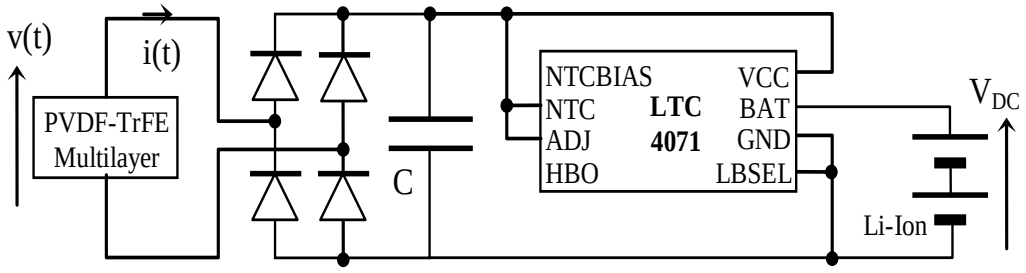

Figure 4.16 Standard interface circuit with battery charger system.

4. Specific integrated circuits

In order to regulate the VDC voltage without compromising extraction efficiency, Linear Technology has developed the LTC3588 integrated circuit designed specifically for the piezo energy harvesting[289]. Its internal diagram (Figure 4.17a) includes a low-loss rectifier and a buck converter regulator. Its operation requires only a few passive components, including a coil (Figure 4.17b).

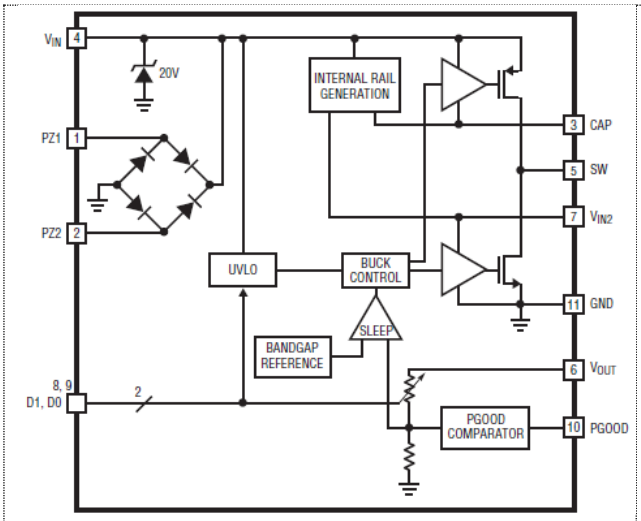

Figure 4.17(a). Internal circuit diagram of LTC3588

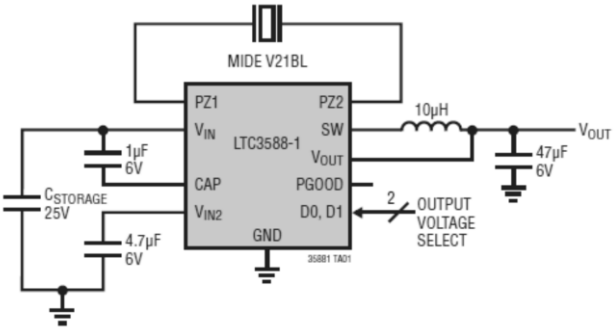

(b). Piezoelectric Energy Harvesting Power Supply with LTC3588

This circuit operates for voltages after rectification (VIN) between 2.7 and 20 V. However, in many applications involving micro or nano piezoelectric generators[101,105], this voltage is too low to function for a buck regulator converter. In this case, Zhao et al[290] suggests to add an adaptive DC-DC boost converter after the rectifier. A similar, faster approach is to use the LTC3108 integrated converter step-up as shown in Figure 4.18. This converter can work with very low VIN input levels (20 mV) but is not adaptive, so its efficiency is less than 40%.

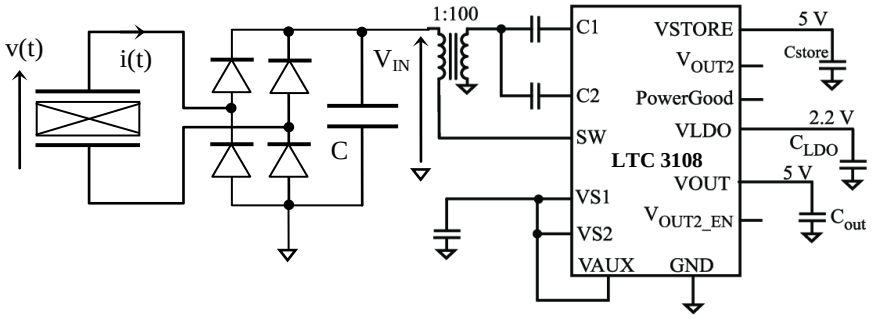

Figure 4.18. LTC3108 Boost converter for low voltage piezoelectric energy harvesting.

4.3.3 Optimal recovery techniques

These techniques have been developed to optimize the transfer of energy to the load to be supplied. They are based on a non-linear treatment of the piezoelectric voltage in synchronism with the vibration. Various circuits based on Synchronized Switch Harvesting (SSH) have been available since 2001.

1. Parallel SSHI system

The parallel-synchronized switch harvesting on Inductor (Figure 4.19) shows P-SSHI system.

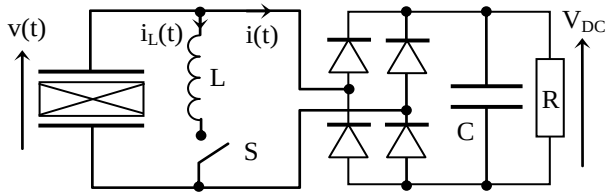

Figure 4.19 (a). P-SSHI interface circuit.

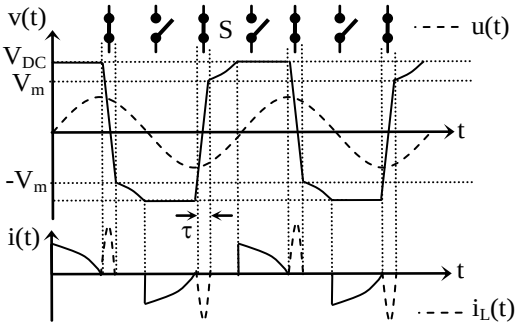

(b) Voltage and current waveforms of P-SSHI circuit

Its principle for the system is, when the S switch is open, the system behaves like the standard recovery circuit. By neglecting the conduction thresholds of the diodes and assuming a sufficiently high storage capacity C, the amplitude of the voltage v(t) is limited to the value V_{DC}.

When the switch S is closed, the proper capacitance C_0 of the piezoelectric element forms an oscillating circuit parallel to the L coil.

Over a period $\tau = \pi\sqrt{LC_0}$ equals to half a pseudo oscillation period, the voltage v(t) changes sign.

Due to the damping, the amplitude V_m after inversion is smaller than the initial amplitude V_M (Figure 4.20). The V_M/V_m ratio depends on the quality factor Q of the circuit according to the relationship :

$$\gamma = \frac{V_m}{V_M} = e^{-\pi/2Q} \qquad (4.5)$$

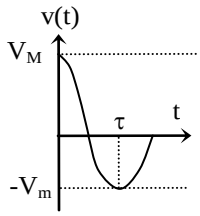

Figure 4.20. Pseudo period of the LC0 circuit.

An electronic detector closes the switch at times when the vibration elongation is at its maximum (times when the extraction speed and current cancel each other out) and reopens it

a delay T later. As shown in Figure 4.19(b), the synchronized inversion of the v(t) sign allows the energy extraction time zone to be reached more quickly at each half vibration cycle.

By not taking into account the electrical power consumed by the control and command electronics, the optimal power and load resistance can be determined as indicated in Table 4.5.

Average electrical power	Theoretical maximum power	Optimal load value
$P = \frac{4\alpha^2 R}{\left(RC_0\omega(1-\gamma)+\pi\right)^2}\omega^2 U_0^2$	$P_{max} = \frac{\alpha^2\omega}{(1-\gamma)\pi C_0}U_0^2$	$R_{opt} = \frac{\pi}{(1-\gamma)\omega C_0}$

Table 4.5. The harvesting and optimal load value in P-SSHI method.

2) Serial SSHI circuit (Series-Synchronized Switch Harvesting on Inductor)

In the S-SSHI circuit (Figure 4.21a) the coil is in series with the piezoelectric element. As in the previous process, the switch S is closed synchronously with the maximum elongation moments. During a large part of the vibration cycle, the piezoelectric element is isolated from any charge. Its voltage, which then changes in proportion to the displacement, loads the proper capacity C_0, which makes it possible to reach a maximum voltage level V_M just before S is closed (Figure 4.21b). Unlike P-SSHI, the transfer of energy to storage capacity C is only done during the closing phases of S, which lead to the inversion of the v(t) sign.

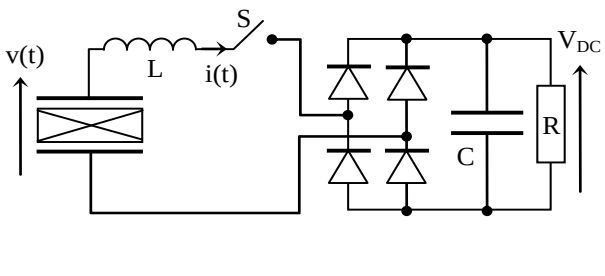

Figure 4.21(a) S-SSHI interface circuit

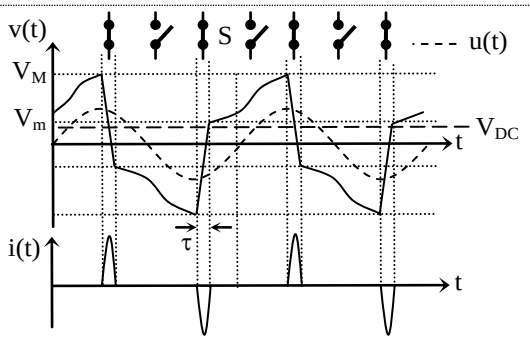

(b). Voltage and current waveforms of S-SSHI circuit

Average electrical power	Theoretical maximum power	Optimal load value
$P = \frac{4\alpha^2 R(1+\gamma)^2}{\left(2RC_0\omega(1+\gamma)+\pi(1-\gamma)\right)^2}\omega^2 U_0^2$	$P_{max} = \frac{\alpha^2}{2\pi C_0}\frac{1+\gamma}{1-\gamma}\omega U_0^2$	$R_{opt} = \frac{\pi}{2C_0\omega}\cdot\frac{1+\gamma}{1-\gamma}$

Table 4.6. The harvesting and optimal load value in S-SSHI method

The energy transfer obtained with this process (Table 4.6) is slightly lower than that of the P-SSHI.

3) SECE recovery system

In the SECE (Synchronous Electric Charge Extraction) circuit (Figure 4.22) the energy transfer is carried out after the rectifier bridge. It is always carried out at the extremes of the voltage v(t) which coincide with those of the vibrational displacement. When S is closed, the energy stored in the capacity C_0 is transferred to the self L until v(t) is cancelled. During these transfers, diode D is blocked, which isolates the storage capacity.

When (u)t=0 v(t), S is reopened and the electrokinetic energy of the coil is transferred to C.

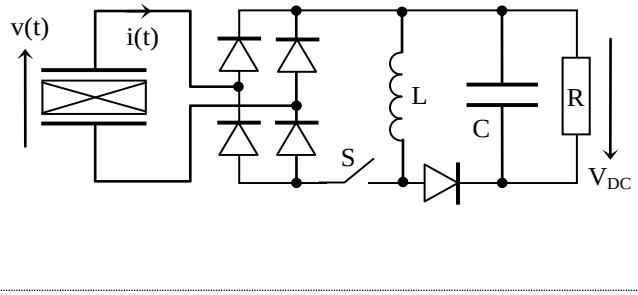

Figure 4.22(a). SECE interface circuit

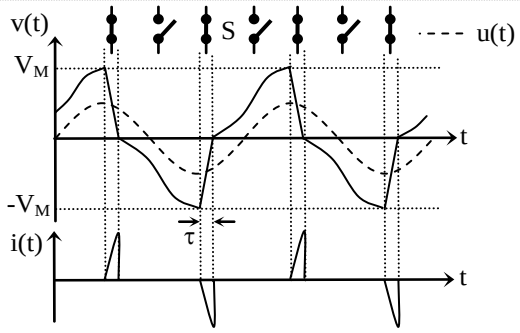

(b) Voltage and current waveforms of SECE circuit

This technique has the great advantage of collecting electrical power independent of the load and given by:

$$P = \frac{2\alpha^2\omega}{\pi C_0}U_0^2 \qquad (4.6)$$

4) Variants

Other non-linear techniques, derived from previous methods, have been proposed. For example DSSH : Double Synchronized Switch Harvesting[291] and OSECE[283,292] .

5) Comparative curves

The graph in Figure 4.23 shows the electrical powers collected using the different techniques summarized above. To facilitate comparison, power and load are normalized according to the following reference parameters:

For charging : $R_{ref} = \frac{\pi}{2\omega C_0}$

For power : P_{ref} = the maximum power delivered by the standard circuit

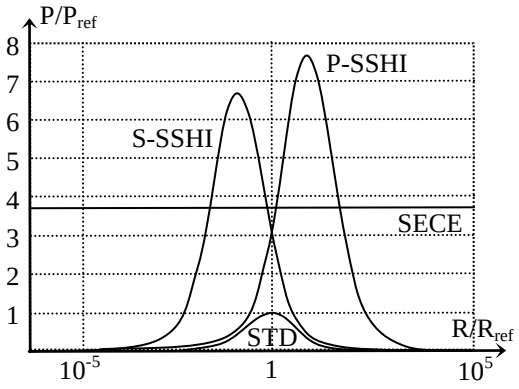

Figure 4.23. Electrical powers collected according to the charging resistor.

For example, we can see that the SECE technique theoretically allows almost four times the maximum power obtained with the standard recovery circuit.

4.4 Practical application to our system

4.4.1 Equivalent electrical circuit of a piezoelectric generator

To simulate the operation of the energy recovery electronics, it is essential to model the response of the piezoelectric film to a mechanical stimulation, i.e. to propose an equivalent electrical circuit for a piezoelectric generator.

As we have seen in chapter 1, in quasi-static conditions the piezoelectricity equations link two electrical quantities (E the electric field and D the electric dispalcement) and two mechanical quantities (Ɛ the strain and σ the stress). These equations allow to calculate an electrical or mechanical quantity from the two others and from the boundary conditions. For example, we can take the equation linking the electrical displacement D to the applied stress σ and the electric field E to which it is subjected:

$$D = d^E \mathcal{E} + k^T E \qquad (4.7)$$

By deriving this equation with respect to time, we obtain equation (4.7)

$$\frac{dD}{dt} = d^E \frac{d\mathcal{E}}{dt} + k^T \frac{dE}{dt} \qquad (4.8)$$

It will be assumed that the applied stress, when a force is exerted on the piezoelectric film corresponds to only bending state. Thus, the problem becomes scalar and therefore easier to model. Here E is the image of the voltage V across the piezoelectric film (E=V/e where e is the thickness of the film), D is the image of the amount of charge Q on the electrodes (D=Q/A where A is the area of the film), and σ =F/A, where F is the force applied to the membrane. From these considerations we obtain:

$$i = i_0 - C_p \frac{dV}{dt} \qquad (4.9)$$

With: $i_0 = d^E \frac{dF}{dt}$ and $C_p = \frac{Ak^T}{h}$ (4.10)

This equation refers to the simplified electrical circuit in Figure 4.12, or the one in Figure 4.24 with $R_0 \rightarrow \infty$.

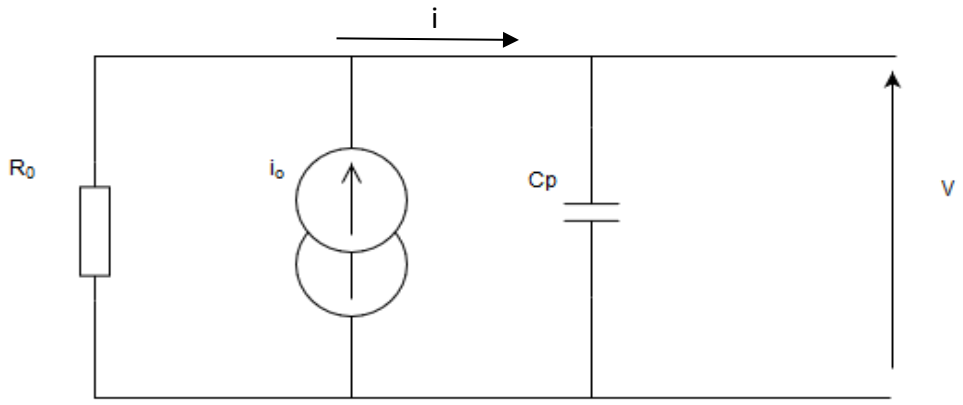

Figure 4.24. Equivalent schematic of a direct mode piezoelectric device.

In the schematic diagram shown in Figure 4.24, R_0 represents the dielectric losses: this resistance is calculated with the formula $R_0=\rho e/A$ where ρ is the resistivity of the material.

4.4.2 Choice of energy harvesting electronics

In the section 4.3 we presented the different electronic approaches to harvest energy. In practice, there are currently a limited number of electronic cards on the market for recovering electrical energy from piezoelectric or more often photovoltaic devices. A specialized manufacturer, Linear Technology, offers several models for energy harvesting and each model has characteristics that make it more suitable for one application rather than another. Among these models, two of them seemed to us of particular interest: the LTC3108 and LTC3588-1 modules, which are optimized for energy recovery from low power sources.

To recover piezoelectric energy, in applications involving micro or nano piezoelectric generators, the voltage is often too low to operate a step-down regulator converter. In this case, the LTC3108 integrated step-up converter has the advantage of being able to operate with very low VIN input levels (from 20 mV). Before our experimental measurements (see section 4.5), showing that we could obtain several volts, this card seemed the most appropriate. The LTC3588-1 converter, on the other hand, requires a higher voltage, typically 5V, but a lower current. Indeed, the current obtained from a piezoelectric film is generally extremely low and this is the other, if not the most important, potentially blocking point of energy recovery and storage by these devices.

We have investigated the possibility of using either of these modules, LTC3108 and LTC3588-1, as an electronic medium to recover energy from PVDF-TrFE films and hybrid composites with

SMA. Their block diagrams are given in Appendix 3 (Figure 6,7 and 8). We have simulated and compared their operation under different conditions using LTSpice software, a computer-aided design tool that allows to conceptualize and simulate circuits to verify their proper operation. This evaluation will allow us to characterize these energy recovery circuits and to determine which one is best suited to our specifications.

4.4.3 Simulation of the system with the LTC 3108 board

The LTC 3108 module is originally designed to extract energy from a low DC voltage source. Therefore, after verification of the classical behavior of the LTC 3108 module with a DC voltage source at its input for which it is originally dedicated (see Appendix 3), we modeled the piezoelectric charges and discharges appearing periodically during a cyclic deformation of the piezoelectric film. As shown in section 4.4.1, the classical way is to assimilate the piezoelectric film (PVDF-TrFE) to a current source I connected in parallel to a capacitor. Therefore, to simulate the piezoelectric generator on the software, we used the circuit given in Figure 4.25, setup proposed by the manufacturer for a model of a piezoelectric transducer as generator.

More in detail, we have modeled our P(VDF-TrFE) film with a current generator with which we fix the value of the input current Iin, a resistor R2 adjustable according to the current in the simulations to maintain the value of the input voltage Vin at 5V, and a capacitance C_{piezo} which represents the internal capacity of the film. Note that the effective resistance of the piezoelectric film is of the order of MΩ, this value has been measured experimentally when polarizing the films under high voltage. In this configuration, the LTC3108 is used without the input amplifier which is integrated in the board: the integrated circuit is directly attacked in AC mode by the piezoelectric source, and the inputs of the “External rectifier”, “step up transformer” and “switching circuit” are not used (Figure 4.25).

The current peaks generated by the film subjected to bending are represented by a sinusoidal current at the input of the circuit, with a frequency of 5 Hz, a low frequency supposed to correspond to that of thermal variations. The LTSpice software allows to model electronic circuits and to collect information about their precise behavior in given situations, complex.

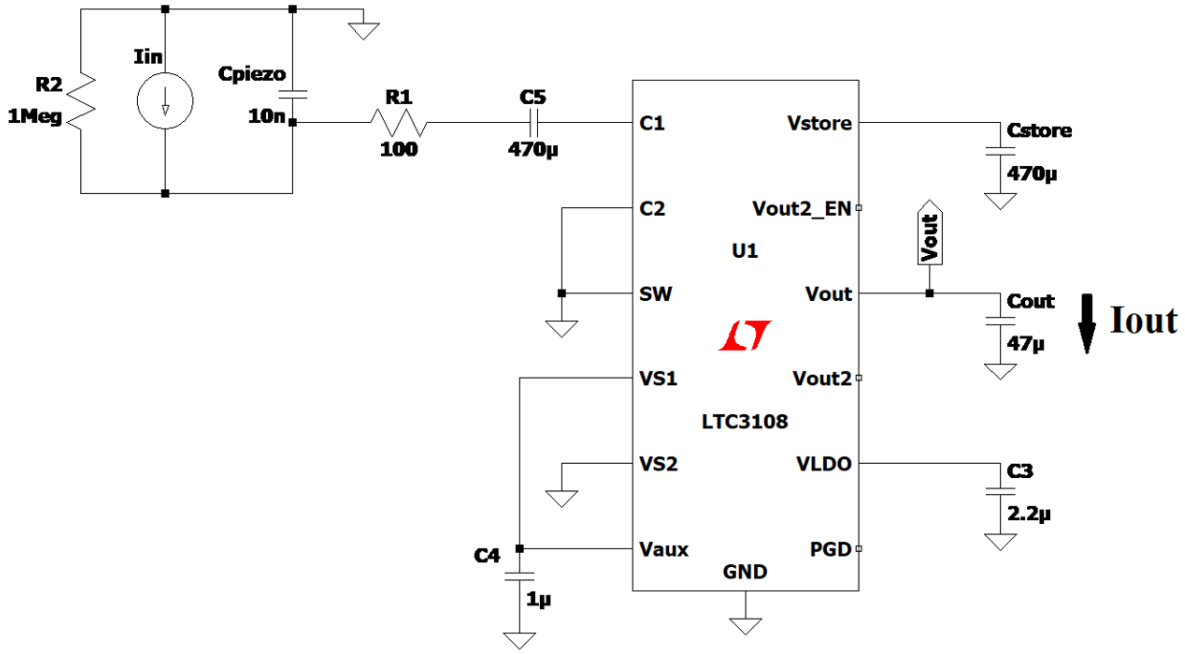

Figure 4.25. Simulation setup of the LTC 3108 board with an AC input.

With this set-up the input voltage evolves dynamically and could theoretically reach 200V across the capacitor C1 (after for example a few hours), but in the simulation we consider the values obtained for 2.5V, consistent with our first experimental values. For a piezoelectric device which can provide 200 µA, the temporal evolution of output voltage and output current are shown in Figures 4.26.

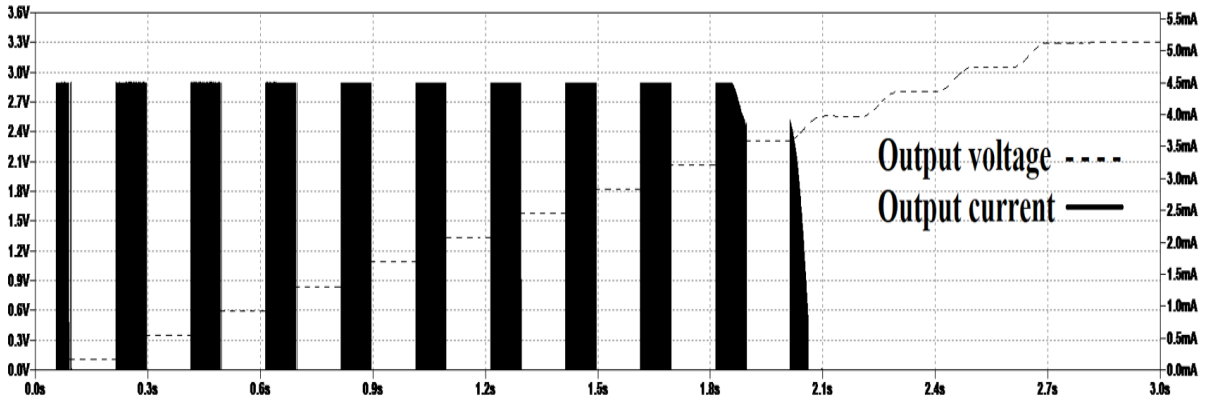

Figure 4.26. Temporal Evolution of the output voltage and output current

In that case, as we can see in Figure 4.26, the output current periodically delivered is 4.5 mA and the output voltage increase step by step up to 3.3V, the nominal values delivered by the electronic module.

The value of the output energy of the card can then be estimated with the following equation:

$$Eout = \frac{Cout \times Vout^2}{2} \qquad (4.11)$$

With:

$Eout$: Output energy in Joule
$Cout$: Capacitor of the load at the output in Farad
$Vout$: Output voltage in Volts

For an input current of Iin=200 µA and an input voltage Vin=2.5V, the corresponding energy is therefore:

$$Eout = \frac{(47 \times 10^{-6}) \times 3{,}3^2}{2} = 255{,}91\ \mu J$$

However, in fact, this value for the input current is much too high to account for our experimental piezoelectric values. Then, keeping the frequency of 5Hz, we tried a range of input currents, supposed to be delivered by the piezoelectric generator, from 20µA to 220µA (Table 4.7).

Input current I_{IN}	**Input voltage V_{IN}**	**Output voltage V_{OUT}**	**Load current I_{OUT}**	**Output Energy Eout**
20 µA	2,3 V	140 µV (unregulated)	2.2 nA	460 µJ
40 µA	2.3 V	330 mV (unregulated)	4.5 mA	2.55 µJ
60 µA	2.5 V	700 mV (unregulated)	4.5 mA	11.5 µJ
80 µA	2.5 V	1.1 V (unregulated)	4.5 mA	28.43 µJ
100 µA	2.5 V	1.5 V (unregulated)	4.5 mA	52.87 µJ
120 µA	2.5 V	1.9 V (unregulated)	4.5 mA	84.83 µJ
140 µA	2.5 V	2.3 V (unregulated)	4.5 mA	124.31 µJ
160 µA	2.5 V	2.7 V (unregulated)	4.5 mA	171.31 µJ
180 µA	2.5 V	3.2 V (unregulated)	4.5 mA	240.64 µJ
200 µA	2.5 V	3.3 V (regulated)	4.5 mA	255.91 µJ
220 µA	2.5 V	3.3 V (regulated)	4.5 mA	255.91 µJ

Table 4.7. Evaluation of the LTC3108 board with different intensities.

Table 4.7 shows several evaluations of the LTC 3108 board in this configuration. It can be seen that I_{IN}=200 µA is the minimum value to get an output voltage V_{OUT} regulated at its nominal value of 3.3V (corresponding to a nominal output energy of 255.91µJ). Under typically 80µA in input it is impossible to get 1V in output, and under 20µA, the card delivers almost no current in output. The conclusion is that for very low currents such as those delivered by small size polymer piezoelectric films (in our case Iin=0,5µA<<I=200µA), this energy harvesting board is not suitable.

4.4.4 Simulation of the system with the LTC 3588-1 board

While the LTC3108 board is particularly well adapted to the storage of DC energy such as photovoltaic energy, although it can be used with AC signals, provided that the input current amplitudes are greater than 200µA for nominal operation, the LTC 3588-1 board appears to be a solution directly adapted to the recovery of energy from ambient vibrations via piezoelectric generator sensors, and it is optimized for low power sources.

With the setup Figure 4.27, we modeled the piezoelectric generator after a parametric study of each of the components, to best simulate its current and voltage response to the periodic application of mechanical stress. The piezoelectric film was finally modeled with a current generator that delivers a sinusoidal signal, with a frequency of 5 Hz. The resistor R1 and the capacitor Cpiezo of the circuit allow us to control the value of the generated voltage and to approximate as closely as possible the real electrical characteristics of the film, as seen with the mechanical bench.

This systematic study of the different components of the signal led to the setup shown in Figure 4.27 with adjusted experimental values: C5 = 1nF, and R1 adjusted in the range of MΩ to keep the voltage Vin at 5V.

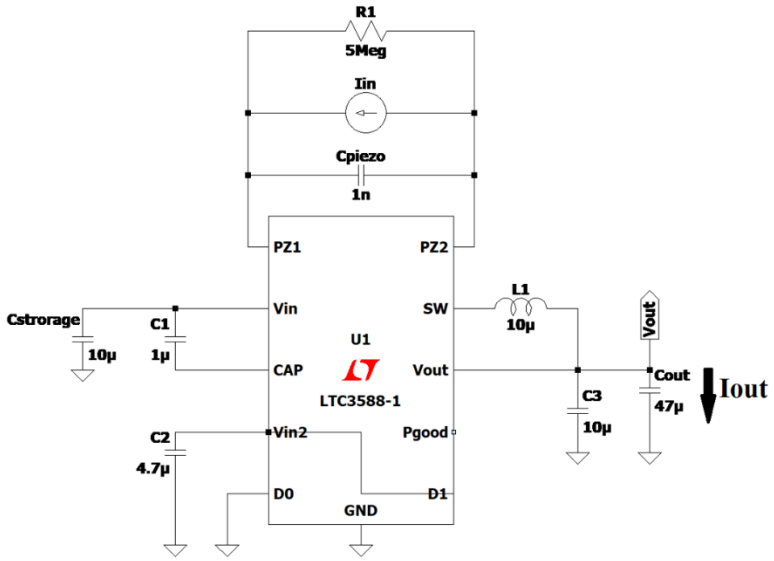

Figure 4.27. Simulation circuit with the LTC 3588 board.

Table 4.8 shows that with sufficient voltage in entry, i.e. 5V, the hinge value of the input current allowing the switching of the card in its energy harvesting operation is strongly reduced compared to the previous electronic card, to 1.71µA.

Input curent Iin	Input voltage Vin	Output curent Iout	Output voltage Vout	Output Energy Eout
0.80 µ	2.3 V	300 pA	5.00 mV	587.5 pJ
1.00 µ	2.8 V	368 pA	5.80 mV	790.5 pJ
1.50 µ	4.3 V	525 pA	8.70 mV	1.77 nJ
1.6 0µ	4.7 V	600 pA	11 mV	2.84 nJ
1.70 µ	5.0 V	650 pA	12 mV	3.38 nJ
1.71 µ	5.0 V	220 mA	1.20 V	33.84 µJ
2.00 µ	5.0 V	220 mA	2.60 V	158.86 µJ
2.10 µ	5.0 V	220 mA	3.18 V	237.64 µJ
2.20 µ	5.0 V	220 mA	3.35 V	263.73 µJ
2.50 µ	5.0 V	220 mA	3.35 V	263.73 µJ
3.00 µ	5.0 V	220 mA	3.35 V	263.73 µJ
3.50 µ	5.0 V	220 mA	3.35 V	263.73 µJ
5.00 µ	5.0 V	220 mA	3.35 V	263.73 µJ
10.00 µ	5.0 V	220 mA	3.35 V	263.73 µJ

Table 4.8. Parametric study of the LTC 3588-1 board.

Therefore, at this value of input current of 1.71 µA for an input voltage of 5 V, this card switches in a very interesting operation, with a power production of nearly 0.3W after a loading time of 750s. With 1.71µA, the current at the output of our circuit reaches periodically 220 mA and the voltage is 1.2 V, even if this voltage is not well regulated here. At this value, the current delivered by the card, 220mA, is multiplied by 3×10^{8} compared to the operating limit value 1.70µA and we can consider that it is functional.

Moreover, 2.20µA is sufficient to obtain the nominal power of the card, which delivers from this value its nominal voltage 3.3V and current 220mA. From 2.2µA, we reach the nominal operation with more than 0.7W obtained in output. Figure 4.28 show the output current and voltage for the nominal operation of the card, for a current input signal Iin =2.20 µA and a voltage Vin = 5V.

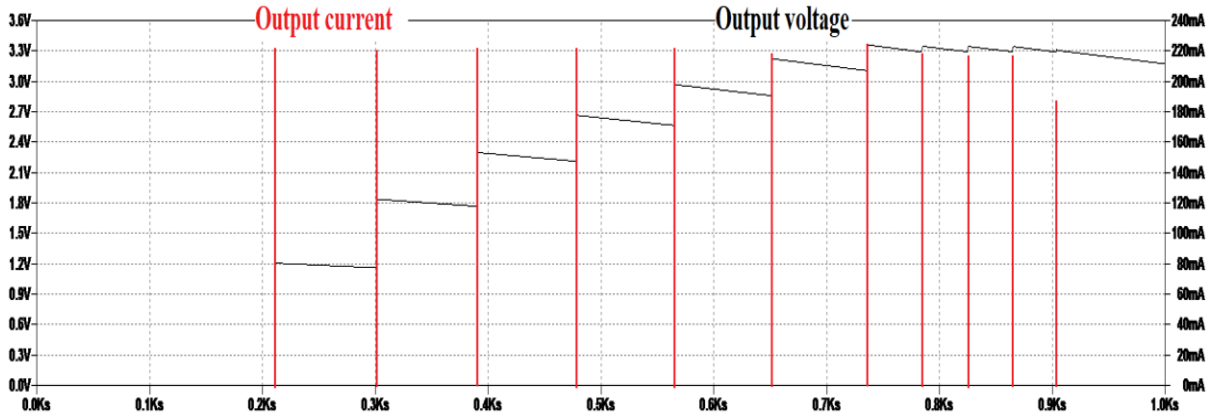

Figure 4.28. Output voltage and output current for Iin = 2.20µA and Vin = 5V.

The simulation reveals also an important information: the charging time of the energy harvesting board's capabilities required before starting to produce energy. Of course for these very low currents this time can be very long. It is limited in these two examples to 750s (Figure 4.30), or 12.5mn.

Thus, by comparing the two models of cards used, the LTC3588-1 card appears clearly more suitable for our specifications, since the minimum value of current imposed to obtain the regulation at 5V is 1.71µA. The obtained results allow us to validate the conditioning circuit and are very encouraging for the continuation of the project. Indeed, our device with a single layer of piezoelectric film allowed us to obtain voltages higher than 5V and currents of the order of 0.4-0.5µA. In the future, the superposition of a multilayer system should allow to obtain a multiplied current, and to reach quite easily this low limit for the effective collection of piezoelectric charges.

4.5 Conclusion

In this chapter, we presented the piezoelectric test benches performed to put our piezoelectric films under cyclic deformation conditions, such as on a thermally cycling SMA substrate. Then we presented the state of the art on the approach to recover and store piezoelectric charges to convert them into electrical power. We discussed the equivalent circuit of a piezoelectric generator, defined from the electrical induction equation, and then the practical choice of an electronic board to harvest the piezoelectric energy, selecting two boards that we then studied and compared by LTSpice: the LTC3108 and LTC3588-1 modules.

With the LTC 3108 module, we observe a good operation but current ranges at the card input, supposed to be generated by the piezoelectric film, are very important compared to the experimentally measured values. Hence the study of the second card, LTC3588-1, which shows a lower consumption for a nominal and regulated operation, but still clearly too high.

By working on the different parameters to refine the electrical modeling of the piezoelectric film and to adjust the experimental measurements as well as possible, we finally demonstrate that the LTC3588-1 board should be able to efficiently store the piezoelectric energy resulting from a mechanical excitation at 5Hz, provided that the generated piezoelectric current reaches 2.2µA, and after an initial charging time of 750s.

Our first measurements, on a simple film of small size 1.6cm x 2.3cm, showed currents of the order of 0.5µA. In the perspectives of this work, the elaboration of flexible multilayer systems in the spirit of the ceramic multilayer piezoelectric stack actuators, whose feasibility has been demonstrated in chapter 2, should allow to reach the required performances. A perspective is to use for example a storage battery Nickel-metal hydride NimH, modeled in our simulations by the C_{out} capacitor which represents the load of the circuit, in order to store the energy recovered by the piezo film via the LTC 3588 card.

5. General conclusions and perspective

Smart materials with the combined effect of different properties represent a promising approach for improved functionalities. A hybrid system composed of shape memory alloys (SMAs) and piezoelectric materials provides significant enhancement of the characteristics of the composite system. The advantage of the SMA/piezoelectric material hybrid device is that it allows the coupling of various properties such as thermomechanical and electromechanical behavior in a synergetic way. These hybrid systems have applications mainly in energy harvesting. The tremendous increase in the field of small-scale energy harvesting to power self-powered electronic devices using such composite system found an attractive area. In this context, the ability to combine thermal and mechanical harvesting using smart materials deserves more attention to study further. So far most of the studies reported on the combined effect of SMA and ceramic composite. Hence, it will be interesting to focus on the development of a hybrid system composed of SMA and piezoelectric polymer P(VDF-TrFE) film because of the excellent flexibility and the high piezoelectric coefficient of the P(VDF-TrFE) polymer suits well for the fabrication of the device with SMA.

We have successfully designed, fabricated and characterized a novel layered composite device composed of shape memory alloy (SMA) and piezoelectric polymer for energy harvesting application. We conclude the feasibility of the composite for energy harvesting by exploiting the multiple energy conversion pathways officered by the two stacking layers of SMA and P(VDF-TrFE) piezoelectric polymer. We have experimentally demonstrated a fully flexible NiTi SMA/P(VDF-TrFE) composite that is able to convert the mechanical-thermal energy into electrical energy synergistically. The finite element simulation was carried out in order to understand the multicoupling behaviour of each layer (piezoelectric and SMA layer) and the composite effective behavior. To demonstrate the working mechanism of the device, we have conducted an electro-thermo-mechanical characterization using the tensile test. The results showed the generation of electric response during the one-way shape memory effect of SMA for a single heating/cooling cycle. The obtained experimental results were validated using the finite element simulation. The simulated results found a good agreement with the experimental results. In addition, the modelling of the composite device found an interesting tool to predict the generated output voltage for a given heating/cooling loading. Finally, we have developed the electronic circuit for the piezoelectric polymer layer. The power conversion efficiency of the whole system strongly depends on the electronic circuit. Thus, we have introduced an integrated converter step-up LTC3588-1 which can work under small output current from the composite device. This allows the storage of the produced energy in a battery for future usage or can deliver the power for the operation of small electronic devices such as wireless sensors, MEMS, and biomedical devices in an autonomous way.

In the first chapter, we have introduced the concept of energy harvesting and we have presented the state of the art of the existing SMA/piezoelectric composites. We studied in a

detailed way the advantages and limitations of the existing studies and we proposed to develop a new flexible composite both experimentally and numerically. Therefore, the first chapter contains the principle of piezoelectricity and the piezoelectric materials for energy harvesting. Then, we have introduced the P(VDF-TrFE) polymer and its application for energy harvesting and different mechanisms to improve the piezoelectric properties of the polymer. In addition, to understand the behavior of the composite, it needs a connected double level of modelling. Hence, for the first step, we have introduced the modeling behavior for piezoelectric part. The second step deals with SMA and its properties and various models describing the thermomechanical behavior of SMA.

In the second chapter, we showed how we fabricated a novel composite system composed of NiTi SMA and P(VDF-TrFE) as a piezoelectric polymer layer. The first composite was made by the direct deposition of the thin polymer layer on the SMA sheet by the spin coating method. A Cr/Al electrode layer of thickness 150nm was deposited on top of the polymer layer. The electric poling was performed by contact technique with a maximum electric field of 100V/µm for enhancing the piezoelectric properties. The electric poling was done by considering SMA as a bottom electrode. The piezoelectric characterization of the SMA/P(VDF-TrFE)/Cr/Al composite showed a higher piezoelectric coefficient of 22.8 pC/N. A multi-layered composite were also fabricated by depositing two thin layers of polymer of thickness ~ 4 µm on each side of the SMA sheet. However, this composite type showed some drawbacks such as electric breakdowns of the polymer after a certain applied electric field and losing the piezoelectric properties. In addition, we have observed delamination of the polymer layer from the SMA surface due to the plastic behavior of the P(VDF-TrFE) layer. Therefore, to improve the interface adhesion, we have developed a new composite structure, where the polymer layer is deposited on a thin flexible PEN substrate. The electric poling was carried out in the same way by depositing two electrodes of Cr/Al on each side of the polymer layer. The P-E hysteresis loop demonstrated a good saturation polarization (P_s) of 7.6 µC/cm^2. Then, the PEN/ P(VDF-TrFE) film was sticked with SMA using a thin layer of flexible epoxy glue. This composite shows better performance and good adhesion strength. This finalized composite structure with an active area of 1.8 cm × 2.5 cm was used for our experimental characterization.

The main objective of the work is to exploit the multiphysical properties of the SMA/(PVDF-TrFE) stacking layered composite for energy harvesting. Especially the composite that enable waste heat recovery at low heat source temperatures at the centimeter length scale of the composite. Therefore, in the chapter 2, the section 2.6, we were performed mechanical, thermal, and electro-thermo-mechanical characterisation of the SMA/(PVDF-TrFE). The experimental characterisation showed the two-way energy conversion of mechanical to thermal to electric energy. In this aspect, it is necessary to first optimize the piezoelectric response of the P(VDF-TrFE) film. Hence, we first performed the piezoelectric energy harvesting of the PEN/ P(VDF-TrFE) film by the application of mechanical pressure. A uniaxial stress was applied to the PEN/ P(VDF-TrFE) film by repeated human finger tapping and bending. The

device was able to convert the human finger tapping movements into electricity under pressing and releasing motion. The power output is calculated from the open-circuit voltage and short circuit current by considering the peak output values. During finger impression and bending, the power output of the P(VDF-TrFE) film is 5.5 μW cm^{-2} and 16 μW cm^{-2} respectively. However, this power calculation method is not the best practical solution because it gives an overestimated value of power. It is because of the voltage is measured across a very high resistance and the current across a very low resistance. Therefore, in this study, we performed the test for the PEN/P(VDF-TrFE) film by bending and recorded the peak voltage across various load resistors ranging from 1 kΩ to 5 MΩ. A maximum power value of 6.25 μW cm^{-2} was observed, across a load resistor of 1 MΩ.

The thermal energy harvesting was carried out for the SMA/(PVDF-TrFE) composite using silicon oil bath heating at a temperature of 75° C. The transformation temperature of the NiTi SMA was between 50 to 75 ° C which is measured using DSC studies. Consequently, during heating above 62°C, the NiTi SMA underwent a martensitic transformation and was restored to its original flat shape. Accordingly, the P(VDF-TrFE) device also follows a drastic shape change, which yields an output voltage ~2V from the piezoelectric layer during the reverse transformation of SMA. In order to identify simultaneously, the electro-thermo-mechanical performance of the composite, we have done a tensile test and analyzed the stress-strain-temperature and voltage-strain-temperature during thermo-mechanical loading. We have obtained an electric response during mechanical loading and heating of the device. Hence, the SMA/P(VDF-TrFE) composite is able to combine the thermomechanical coupling property of the NiTi SMA and electromechanical coupling of P(VDF-TrFE) piezoelectric polymer for energy harvesting. Thus, the results offer a promising approach for the synergetic use of two smart materials for energy harvesting. The voltage and power output from the composite are lower compared to existing devices. However, in these first results, we are demonstrating the feasibility of coupling two smart material composite for thermal energy harvesting at low temperature.

Finally, the second chapter concluded with the development of a characterization setup. We have designed and developed an experimental device for the electro-thermo-mechanical characterization of the SMA/Piezoelectric polymer composite. The system consists of different components for heating/cooling of the composite as well as a control system to combine all the subparts. The control system is developed in the LabVIEW software to perform the controlling of the whole device with proper measurements and commands. The heating of the composite sample is done using the laser beam that has a maximum power of 5W. The power can be controlled to apply the desired power to heat the sample to a temperature of 75 °C through an interface PSU-RS232 module. The homogenous heating of the sample is done using concave and convex lenes. The laser light is first passing through a convex lens that converges the incident laser rays towards the principal axis. Further, we have placed a concave lens after the convex lens. Hence, the concave lens spreads out the laser rays. Therefore, the rays incident on

the SMA/piezo sample spreads well throughout the surface. That means homogenous heating can be assured by this way. The immediate cooling of the sample can be performed with liquid nitrogen. The cooling of the sample is done by using a solenoid valve, which helps to control the amount of liquid nitrogen in a pulsing way in order to get a sinusoidal change of temperature in the sample. We have developed the support system and frame that consist of the two lens holders and the sample holder. All subparts are arranged and fit well in the mainframe.

In chapter 3, we have validated the finite element analysis for the composite in order to optimize the electromechanical coupling of the piezoelectric polymer layer and the thermomechanical coupling of the SMA layer. Finally, the combination of these constitutive models enables to identify the global effective electro-thermo-mechanical behavior of the composite. In the third chapter, we have simulated the main properties of the SMA such as superelastic behavior, one-way shape memory effect and two-way shape memory effect were simulated using Chemisky et al., model already implemented in Abaqus via Umat. The classical and linear piezoelectric constitutive model was used to describe the electromechanical behavior of the piezoelectric layer. The one-way and two-way shape memory effects were proved by modelling the tensile and bending loading. Then, we have successfully developed the finite element model for the SMA/piezoelectric polymer composite. During the application of thermal loading, an electrical potential was created on the piezoelectric layer, which is well exhibited through the model. Also, we have demonstrated the relationship between the thickness of the piezoelectric layers for the electrical output. The electrical potential increases with the increase of the thickness. We have compared the finite element model for the one-way shape memory effect with the experimental data from tensile test machine. The compared results showed that the model showing good agreement with the experimental results. The numerical tool allows us to predict the evaluation of electric voltage during the thermal loading. Thus, it is an interesting predicting numerical tool that could help for enhancing the harvesting performances of such hybrid composite.

Finally, in chapter 4 the key elements were designed and realized to evaluate the performance of the P(VDF-TrFE) film for energy recovery. Two types of mechanical test benches were selected, and the test was carried out using small size (1.6cm×2.3cm) films. In the first bench, the external strain was provided to the film using a mechanical shaker. The shaker is capable of exerting mechanical stress periodically on the film. However, the deformation obtained was insufficient to account for the movements of the SMA. Hence, we have developed a specific mechanical system, that allowed to give the periodic deformation of the P(VDF-TrFE) film as well as it was designed in such a way to test two films simultaneously in alternate bending. The output voltage and current from the film were measured using an oscilloscope and picoammeter respectively.

In order to recover the piezoelectric charge produced from the film, in chapter 4 we have studied two types of electronic cards LTC3108 and LTC 3588-1, which can function at a low

voltage or current input level. We have simulated and compared the operation of both these modules under various conditions using LTSpice software. This simulation allowed us to identify the suitable one with our specification and helps to carry out the experiment accordingly. From the performed simulation tests, we got rather interesting results. The LTC3108 module gives good operation with a minimum voltage. However, it needs an input current value which is difficult to obtain from a single-layered P(VDF-TrFE) film with a small size and thickness that we are using. On the other hand, the LTC3588-1 is found more suitable for our specifications, since the minimum value of input current of 2.2 µA for a voltage of 5V, which should be easily achieved by future multilayer devices. In these conditions, an output power of nearly 0.7W is delivered after a loading time of 750s. Through this study, we have validated the conditioning circuits and it is opening new possibilities to continue this work with different multilayer composite structure to enhance the power output.

Various significant perspectives can be considered. The composite with a multilayered hybrid structure will enhance energy harvesting. We have proposed the layered SMA-piezoelectric hybrid structure, however, works still need to be done for the optimization of the composite by considering the interface bonding as well. There are different methods that can be taken into account in order to prepare the SMA and P(VDF-TrFE) composite. By considering different compositions of SMA, various combinations of the polymer by incorporating ferroelectric nanoparticles into the polymer matrix. It would be more suitable to lower the operating temperature to harvest the thermal energy at a smaller ΔT. The second step would be to perform the periodic cycling cooling and heating of the composite. During our work, we did the first measurements on a small-sized film for piezoelectric energy recovery. However, as a perspective we can use the large-sized multilayered composite to allow us to collect more energy and finally, the produced energy can be stored in a battery for future usage. This will allow to power the small-scale electronic device.

In summary, this work presents significant results towards the development of the flexible hybrid composite coupled with SMA and piezoelectric polymer. The hybrid composite will be able to convert the thermal and mechanical energy into electric energy from the ambient environment in a synergistic way. Thereby, it can deliver the produced electric charge to power the portable electronics such as wireless sensors, MEMS or NEMS and biomedical devices in an autonomous way.

Appendices

Appendix 1: « Shaker » mechanical bench

A) Technical specifications of the LDS V200 shaker powered by the amplifier (LDS LPA100):

Maximum current allowed	3 A
Maximum peak-to-peak displacement	5.0 mm
Usable frequency range	5 à 13 000 Hz
Resonance frequency (fn) of the device	13 000 Hz
Impedance at 500 Hz	2.0 Ω

Table 1. Technical specifications of the LDS V200

B) Initialization of the GBF ports and oscilloscope

Figure 1. Initialization of the GBF ports.

C) Design of the LabVIEW control

The design of the LabVIEW control was done on two stages:

- The first is to initialize the function generator (GBF) and the calculation of the frequency step to be respected during the scan.
- The second stage consisted of initializing and configuring the oscilloscope to read the signal produced by the P(VDF-TrFE) film and recovered by a probe, then displaying the results on a graphic terminal and finally saving them in an Excel file.

D) LabVIEW command dashboard

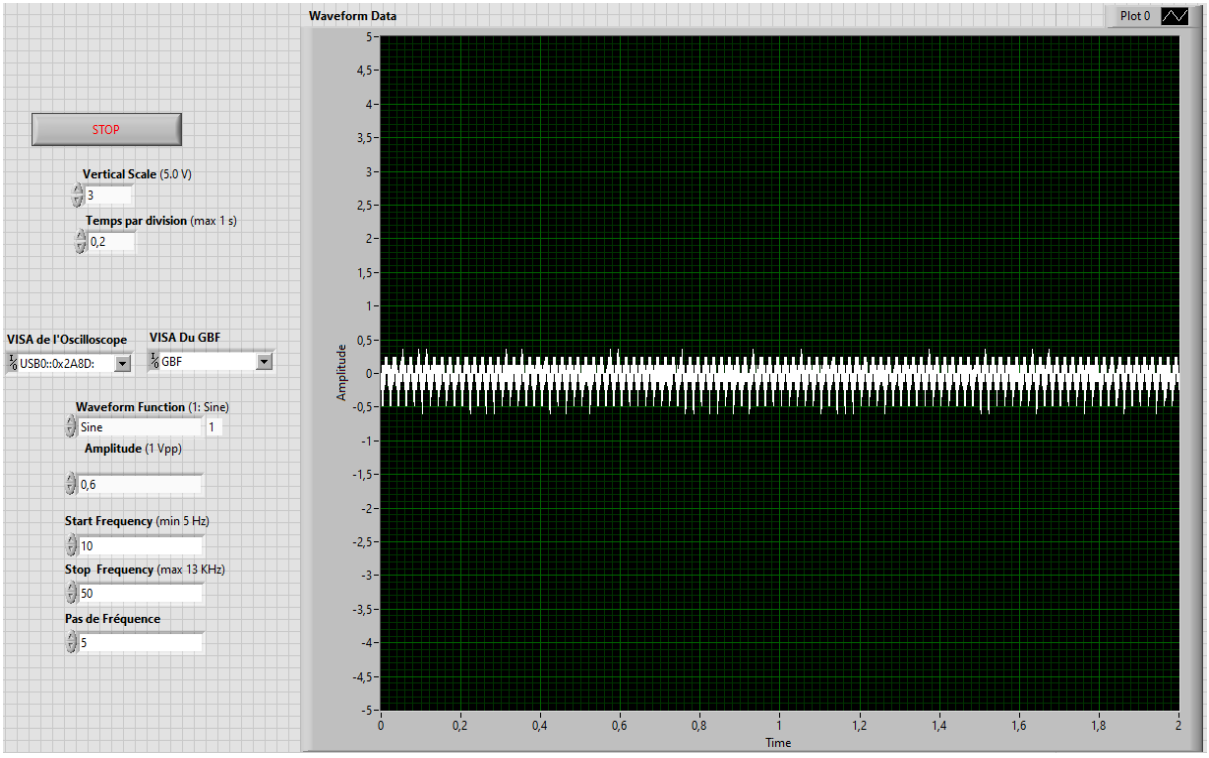

Figure 2. LabVIEW commands

E - Important points

From these manipulations we have retained some important parameters that should be highlighted, first of all the maximum and minimum values accepted by the mechanical shaker:

- Imax= 1.5 A
- Vmin = 0.6 V
- Fmin (minimum tolerated frequency) = 5 Hz
- Tmax = 0.9 s/div on the display otherwise the shaker stops.

Take into account the type of connection of the oscilloscope (GPIB, USB) since problems of data transfer occur when it is connected in USB (instability of the connection).

Appendix 2: Actuation of the mechanical bench by THE STEP MOTOR

Figure 3 to 5 below related to the section 4.2.1 describing the operation of mechanical test bench.

The step motor has the role of driving the translations on our mechanical bench. This motor is equipped with a control circuit which drives the motor by programming. We used the RS PRO High Torque hybrid motor.

Figure 3. Photo of the step motor

Here are the technical characteristics of this motor (table 2) :

Step Angle		1.8
Step Angle Accuracy (Full Step, No Load)	%	±5
Rated Voltage	V	2.8
Current/Phase	A	1.33
Resistance/Phase	Ω	2.1
Inductance/Phase	MH	2.5
Detent Torque	mNm	
Holding Torque	Ncm	0.22
Rotor Inertia	G-CM²	35
Weight	Kg	0.22
Number of Leads	N°.	4

Table 2: Summary of the characteristics of the step motor

Our stepper motor was controlled by a program developed on Arduino, with a power supply of 8 volts. The wiring circuit of the stepper motor with the Arduino module is as follows:

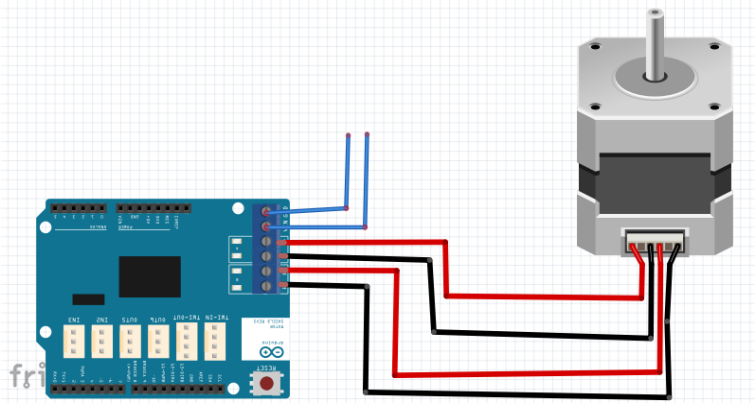

Figure 4. Wiring circuit of the stepper motor with the Arduino module

The program to operate the motor is as follows:

```
#include <Stepper.h>
const int stepsPerRevolution = 20;
Stepper myStepper(stepsPerRevolution ,12, 13);
const int pwmA = 3;
const int pwmB = 11;
const int brakeA = 9;
const int brakeB = 8;
const int dirA = 12;
const int dirB = 13;
int Distance = 60;
int VITESSSE =2000;
int x=0;
void setup() {
  Serial.begin(9600);
 pinMode(pwmA, OUTPUT);
 pinMode(pwmB, OUTPUT);
 pinMode(brakeA, OUTPUT);
 pinMode(brakeB, OUTPUT);
 digitalWrite(pwmA, HIGH);
 digitalWrite(pwmB, HIGH);
 digitalWrite(brakeA, LOW);
 digitalWrite(brakeB, LOW);
 myStepper.setSpeed(VITESSSE);
}

void loop() {
  if (Serial.available() > 0) {
    myStepper.setSpeed( Serial.read());
  }
 myStepper.step(Distance);
 delay(1);
 myStepper.step(-Distance);
 delay(1);
}
```

Figure 5. The program that controls the step motor

The program developed for our motor allows to follow the command in Waves mode. For this motor we used the pins of the Arduino Shield module because the motor is bipolar. The connections of the pins are as follows:

- Pin #3 Digital PWMA output
- Pin #11 Digital PWMB output
- Pin #12 Digital dirA Output
- Pin #13 Digital dirB Output

We have introduced the Brake pins for breaking the motor, which helps to change the direction of rotation by making a half turn, as our program allows us to make only 20 steps to the left and right.

APPENDIX 3: Energy Harvesting Electronic cards

LTC 3108 Block diagram

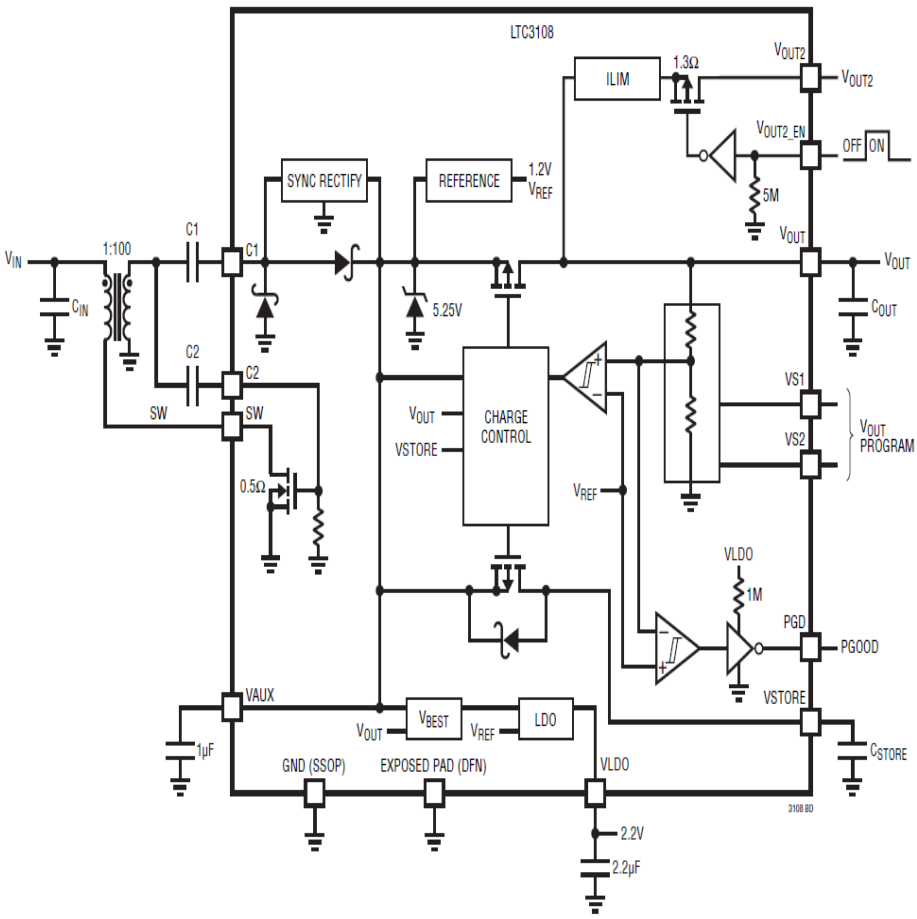

Figure 6. LTC3108 Block diagram

LTC 3588-1 Block diagram

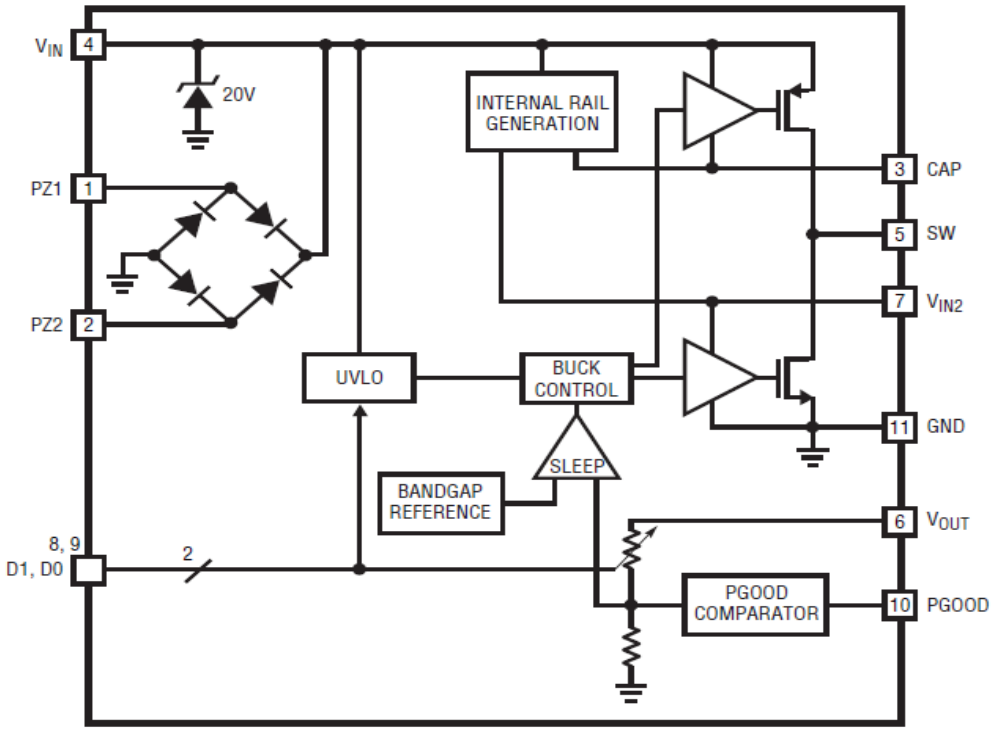

Figure 7. LTC 3588-1 Block diagram.

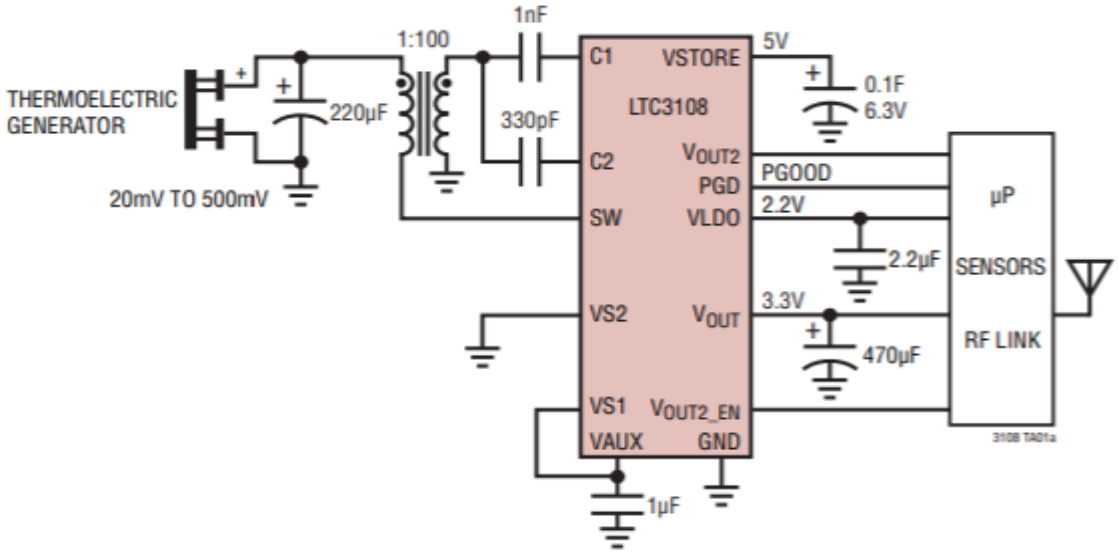

Figure 8. LTC3108 Integrated DC/DC converter, ideally for harvesting and managing energy from low input voltage source such as TEGs.

Bibliography

1. Bodkhe S, Ermanni P. 3D printing of multifunctional materials for sensing and actuation: Merging piezoelectricity with shape memory. *European Polymer Journal* 2020; 132: 109738.

2. Narayana KJ, Gupta Burela R. A review of recent research on multifunctional composite materials and structures with their applications. *Materials Today: Proceedings* 2018; 5: 5580–5590.

3. Sukumaran S, Chatbouri S, Rouxel D, et al. Recent advances in flexible PVDF based piezoelectric polymer devices for energy harvesting applications. *Journal of Intelligent Material Systems and Structures*; 1045389X20966058.

4. He H, Lu X, Hanc E, et al. Advances in lead-free pyroelectric materials: a comprehensive review. *J Mater Chem C* 2020; 8: 1494–1516.

5. Costa P, Nunes-Pereira J, Pereira N, et al. Recent Progress on Piezoelectric, Pyroelectric, and Magnetoelectric Polymer-Based Energy-Harvesting Devices. *Energy Technology* 2019; 7: 1800852.

6. Costanza G, Tata ME. Shape Memory Alloys for Aerospace, Recent Developments, and New Applications: A Short Review. *Materials* 2020; 13: 1856.

7. Zareie S, Issa AS, Seethaler RJ, et al. Recent advances in the applications of shape memory alloys in civil infrastructures: A review. *Structures* 2020; 27: 1535–1550.

8. Sun L, Huang WM, Ding Z, et al. Stimulus-responsive shape memory materials: A review. *Materials & Design* 2012; 33: 577–640.

9. Stachiv I, Alarcon E, Lamac M. Shape Memory Alloys and Polymers for MEMS/NEMS Applications: Review on Recent Findings and Challenges in Design, Preparation, and Characterization. *Metals* 2021; 11: 415.

10. Mehrpouya M, Bidsorkhi HC. MEMS Applications of NiTi Based Shape Memory Alloys: A Review. *MNS* 2017; 8: 79–91.

11. Sun H, Yin M, Wei W, et al. MEMS based energy harvesting for the Internet of Things: a survey. *Microsyst Technol* 2018; 24: 2853–2869.

12. Iannacci J. Microsystem based Energy Harvesting (EH-MEMS): Powering pervasivity of the Internet of Things (IoT) – A review with focus on mechanical vibrations. *Journal of King Saud University - Science* 2019; 31: 66–74.

13. Covaci C, Gontean A. Piezoelectric Energy Harvesting Solutions: A Review. *Sensors* 2020; 20: 3512.

14. Sezer N, Koç M. A comprehensive review on the state-of-the-art of piezoelectric energy harvesting. *Nano Energy* 2021; 80: 105567.

15. Adeodato A, Duarte BT, Monteiro LLS, et al. Synergistic use of piezoelectric and shape memory alloy elements for vibration-based energy harvesting. *International Journal of Mechanical Sciences* 2021; 194: 106206.

16. Khanna S, Marathey P, Utsav, et al. Unravelling camphor mediated synthesis of TiO2 nanorods over shape memory alloy for efficient energy harvesting. *Applied Surface Science* 2021; 541: 148489.

17. *Shape Memory Alloys*. Boston, MA: Springer US. Epub ahead of print 2008. DOI: 10.1007/978-0-387-47685-8.

18. *Molecular Dynamics Simulation of Shape-Memory Behavior.* INTECH Open Access Publisher, http://www.intechopen.com/articles/show/title/molecular-dynamics-simulation-of-shape-memory-behavior (2010, accessed 17 September 2019).

19. Achieving ultra-large elastic strains in Nb thin films on NiTi phase-transforming substrate by the principle of lattice strain matching | Elsevier Enhanced Reader. DOI: 10.1016/j.matdes.2020.109257.

20. Hubert A, Calchand NR, Gorrec YL, et al. Magnetic Shape Memory Alloys as smart materials for micro-positioning devices. 2012. Epub ahead of print 2012. DOI: 10.7716/aem.v1i2.10.

21. Sawaguchi T, Maruyama T, Otsuka H, et al. Design Concept and Applications of Fe–Mn–Si-Based Alloys—from Shape-Memory to Seismic Response Control. 2016. Epub ahead of print 2016. DOI: 10.2320/matertrans.mb201510.

22. Stošić Z, Manasijević D, Balanović L, et al. Effects of Composition and Thermal Treatment of Cu-Al-Zn Alloys with Low Content of Al on their Shape-memory Properties. *Materials Research* 2017; 20: 1425–1431.

23. S S, Mallik US, Raju TN. Microstructure and Shape Memory Effect of Cu-Zn-Ni Shape Memory Alloys. *Journal of Minerals and Materials Characterization and Engineering* 2014; 02: 71–77.

24. Mohd Jani J, Leary M, Subic A, et al. A review of shape memory alloy research, applications and opportunities. *Materials & Design (1980-2015)* 2014; 56: 1078–1113.

25. M.A. J, Kolla LG, G.N.V.R. V, et al. Pulsed DC magnetron sputtered titanium nitride thin films for localized heating applications in MEMS devices. *Sensors and Actuators A: Physical* 2018; 272: 199–205.

26. Jayachandran S, Mani Prabu SS, Manikandan M, et al. Exploring the functional capabilities of NiTi shape memory alloy thin films deposited using electron beam evaporation technique. *Vacuum* 2019; 168: 108826.

27. Ishida A, Martynov V. Sputter-Deposited Shape-Memory Alloy Thin Films: Properties and Applications. *MRS Bulletin* 2002; 27: 111–114.

28. Šittner P, Stalmans R. Developing hybrid polymer composites with embedded shape-memory alloy wires. *JOM* 2000; 52: 15–20.

29. Merlin M, Scoponi M, Soffritti C, et al. On the improved adhesion of NiTi wires embedded in polyester and vinylester resins. *Frattura ed Integrità Strutturale* 2014; 9: 127–137.

30. Cohades A, Michaud V. Shape memory alloys in fibre-reinforced polymer composites. *Advanced Industrial and Engineering Polymer Research* 2018; 1: 66–81.

31. Neuking K, Abu-Zarifa A, Eggeler G. Surface engineering of shape memory alloy/polymer-composites: Improvement of the adhesion between polymers and pseudoelastic shape memory alloys. *Materials Science and Engineering: A* 2008; 481–482: 606–611.

32. Avirovik D, Kumar A, Bodnar RJ, et al. Remote light energy harvesting and actuation using shape memory alloy—piezoelectric hybrid transducer. *Smart Mater Struct* 2013; 22: 052001.

33. Gosliga JS, Ganilova DOA. Energy Harvesting based on the Hybridisation of two Smart Materials. 12.

34. Xu R, Bouby C, Zahrouni H, et al. 3D modeling of shape memory alloy fiber reinforced composites by multiscale finite element method. *Composite Structures* 2018; 200: 408–419.

35. Merzouki T. Finite Element analysis of a shape memory alloy actuator for a micropump. *Simulation Modelling Practice and Theory* 2012; 15.

36. Chen J, Xu QC, Blaszkiewicz M, et al. Lead Zirconate Titanate Films on Nickel-Titanium Shape Memory Alloys: SMARTIES. *Journal of the American Ceramic Society* 1992; 75: 2891–2892.

37. Sappati K, Bhadra S. Piezoelectric Polymer and Paper Substrates: A Review. *Sensors* 2018; 18: 3605.

38. Safaei M, Sodano HA, Anton SR. A review of energy harvesting using piezoelectric materials: state-of-the-art a decade later (2008–2018). *Smart Materials and Structures* 2019; 28: 113001.

39. Chen X, Han X, Shen Q-D. PVDF-Based Ferroelectric Polymers in Modern Flexible Electronics. *Advanced Electronic Materials* 2017; 3: 1600460.

40. Liu C. Recent Developments in Polymer MEMS. *Advanced Materials* 2007; 19: 3783–3790.

41. Chorsi MT, Curry EJ, Chorsi HT, et al. Piezoelectric Biomaterials for Sensors and Actuators. *Advanced Materials* 2019; 31: 1802084.

42. Jing Q, Kar-Narayan S. Nanostructured polymer-based piezoelectric and triboelectric materials and devices for energy harvesting applications. *Journal of Physics D: Applied Physics* 2018; 51: 303001.

43. Gusarov B, Gusarova E, Viala B, et al. Thermal energy harvesting by piezoelectric PVDF polymer coupled with shape memory alloy. *Sensors and Actuators A: Physical* 2016; 243: 175–181.

44. Wang S, Shao H-Q, Liu Y, et al. Boosting piezoelectric response of PVDF-TrFE via MXene for self-powered linear pressure sensor. *Composites Science and Technology* 2021; 202: 108600.

45. Calavalle F, Zaccaria M, Selleri G, et al. Piezoelectric and Electrostatic Properties of Electrospun PVDF-TrFE Nanofibers and their Role in Electromechanical Transduction in Nanogenerators and Strain Sensors. *Macromol Mater Eng* 2020; 305: 2000162.

46. Augustine R, Sarry F, Kalarikkal N, et al. Surface Acoustic Wave Device with Reduced Insertion Loss by Electrospinning P(VDF–TrFE)/ZnO Nanocomposites. *Nano-Micro Letters* 2016; 8: 282–290.

47. Hadji R, Nguyen VS, Vincent B, et al. Preparation and characterization of P(VDF-TrFE)/Al_2O_3 nanocomposite. *IEEE Transactions on Ultrasonics, Ferroelectrics and Frequency Control* 2012; 59: 163–167.

48. Ramadan KS, Sameoto D, Evoy S. A review of piezoelectric polymers as functional materials for electromechanical transducers. *Smart Materials and Structures* 2014; 23: 033001.

49. Naito Y, Uenishi K. Electrostatic MEMS Vibration Energy Harvesters inside of Tire Treads. *Sensors* 2019; 19: 890.

50. Toshiyoshi H, Ju S, Honma H, et al. MEMS vibrational energy harvesters. *Science and Technology of Advanced Materials* 2019; 20: 124–143.

51. Nagakannan M, Inbaraj CJ, Mukesh Kannan K, et al. A RECENT REVIEW ON IOT BASED TECHNIQUES AND APPLICATIONS. In: *2018 2nd International Conference on I-SMAC (IoT in Social, Mobile, Analytics and Cloud) (I-SMAC)I-SMAC (IoT in Social, Mobile, Analytics and Cloud) (I-SMAC), 2018 2nd International Conference on*. Palladam, India: IEEE, pp. 70–75.

52. Landaluce H, Arjona L, Perallos A, et al. A Review of IoT Sensing Applications and Challenges Using RFID and Wireless Sensor Networks. *Sensors* 2020; 20: 2495.

53. Madakam S, Ramaswamy R, Tripathi S. Internet of Things (IoT): A Literature Review. *Journal of Computer and Communications* 2015; 03: 164–173.

54. Iannacci J. Microsystem based Energy Harvesting (EH-MEMS): Powering pervasivity of the Internet of Things (IoT) – A review with focus on mechanical vibrations. *Journal of King Saud University - Science* 2019; 31: 66–74.

55. Wu H, Huang Y, Xu F, et al. Energy Harvesters for Wearable and Stretchable Electronics: From Flexibility to Stretchability. *Advanced Materials* 2016; 28: 9881–9919.

56. Lee J-H, Kim J, Kim TY, et al. All-in-one energy harvesting and storage devices. *J Mater Chem A* 2016; 4: 7983–7999.

57. Liu H, Zhong J, Lee C, et al. A comprehensive review on piezoelectric energy harvesting technology: Materials, mechanisms, and applications. *Applied Physics Reviews* 2018; 5: 041306.

58. Tang X, Wang X, Cattley R, et al. Energy Harvesting Technologies for Achieving Self-Powered Wireless Sensor Networks in Machine Condition Monitoring: A Review. *Sensors* 2018; 18: 4113.

59. Li H, Tian C, Deng ZD. Energy harvesting from low frequency applications using piezoelectric materials. *Applied Physics Reviews* 2014; 1: 041301.

60. Bowen CR, Kim HA, Weaver PM, et al. Piezoelectric and ferroelectric materials and structures for energy harvesting applications. *Energy Environ Sci* 2014; 7: 25–44.

61. Mitcheson PD, Yeatman EM, Rao GK, et al. Energy Harvesting From Human and Machine Motion for Wireless Electronic Devices. *Proceedings of the IEEE* 2008; 96: 1457–1486.

62. Khan A, Abas Z, Soo Kim H, et al. Piezoelectric thin films: an integrated review of transducers and energy harvesting. *Smart Materials and Structures* 2016; 25: 053002.

63. Elahi H, Eugeni M, Gaudenzi P. A review on mechanisms for piezoelectric-based energy harvesters. *Energies 2018,11,1850*

64. Kang M-G, Jung W-S, Kang C-Y, et al. Recent Progress on PZT Based Piezoelectric Energy Harvesting Technologies. *Actuators* 2016; 5: 5.

65. Liu L, Pang Y, Yuan W, et al. A self-powered piezoelectric energy harvesting interface circuit with efficiency-enhanced P-SSHI rectifier. *Journal of Semiconductors* 2018; 39: 045002.

66. Kudela P, Radzienski M, Ostachowicz W, et al. Structural Health Monitoring system based on a concept of Lamb wave focusing by the piezoelectric array. *Mechanical Systems and Signal Processing* 2018; 108: 21–32.

67. Song H-C, Kumar P, Maurya D, et al. Ultra-Low Resonant Piezoelectric MEMS Energy Harvester with High Power Density. *Journal of Microelectromechanical Systems* 2017; 26: 1226–1234.

68. Dannier A, Brando G, Ruggiero F.N. The piezoelectric phenomenon in energy harvesting scenarios: A theoretical study of viable applications in unbalanced rotor systems. Energies 2019,12,708.

69. Caliò R, Rongala U, Camboni D, et al. Piezoelectric Energy Harvesting Solutions. *Sensors* 2014; 14: 4755–4790.

70. Sozinov A, Likhachev AA, Lanska N, et al. Giant magnetic-field-induced strain in NiMnGa seven-layered martensitic phase. *Applied Physics Letters* 2002; 80: 1746–1748.

71. Curtis SM, Wolff N, Dengiz D, et al. Integration of AlN piezoelectric thin films on ultralow fatigue TiNiCu shape memory alloys. *Journal of Materials Research* 2020; 35: 1298–1306.

72. Rubel RI, Akram W, Jafor A, et al. Review on Shape Memory Alloy Substrate with Thermoelectric and Piezoelectric Behavior for Thermo-piezo-electric Generation Unit. 7.

73. Zhan M, Wang S, Zhang L, et al. Experimental Evaluation of Smart Composite Device with Shape Memory Alloy and Piezoelectric Materials for Energy Dissipation. *Journal of Materials in Civil Engineering* 2020; 32: 04020079.

74. Pandya S, Velarde G, Zhang L, et al. New approach to waste-heat energy harvesting: pyroelectric energy conversion. *NPG Asia Materials*; 11. Epub ahead of print December 2019. DOI: 10.1038/s41427-019-0125-y.

75. Thakre A, Kumar A, Song H-C, et al. Pyroelectric Energy Conversion and Its Applications—Flexible Energy Harvesters and Sensors. *Sensors* 2019; 19: 2170.

76. Lagoudas DC, Bo Z. The cylindrical bending of composite plates with piezoelectric and SMA layers. *Smart Mater Struct* 1994; 3: 309–317.

77. Lester B, Baxevanis T, Chemisky Y, et al. Review and Perspectives: Shape Memory Alloy Composite Systems. 62.

78. Garcia E, Lobontiu N. Induced-strain multimorphs for microscale sensory actuation design. 9.

79. Lee J-K, Taya M. Modeling for piezoelectric-shape memory alloy composites. *Arch Appl Mech* 2011; 81: 629–640.

80. Namli OC, Lee J-K, Taya M. Modeling of piezo-SMA composites for thermal energy harvester. In: *Behavior and Mechanics of Multifunctional and Composite Materials 2007*. International Society for Optics and Photonics, p. 65261L.

81. Namli OC, Taya M. Design of Piezo-SMA Composite for Thermal Energy Harvester Under Fluctuating Temperature. *Journal of Applied Mechanics* 2011; 78: 031001.

82. Shen X, Han J-H, Lee I. Study of a reduced and internally biased oxide wafer PZT actuator and its integration with shape memory alloy. 6.

83. Lebedev GA, Gusarov BV, Viala B, et al. Thermal energy harvesting using shape memory/piezoelectric composites. In: *2011 16th International Solid-State Sensors, Actuators and Microsystems Conference*. Beijing, China: IEEE, pp. 669–670.

84. Zakharov D, Lebedev G, Cugat O, et al. Thermal energy conversion by coupled shape memory and piezoelectric effects. *Journal of Micromechanics and Microengineering* 2012; 22: 094005.

85. Zakharov D, Gusarov B, Gusarova E, et al. Combined Pyroelectric, Piezoelectric and Shape Memory Effects for Thermal Energy Harvesting. *Journal of Physics: Conference Series* 2013; 476: 012021.

86. Avirovik D, Kumar A, Bodnar RJ, et al. Remote light energy harvesting and actuation using shape memory alloy—piezoelectric hybrid transducer. *Smart Materials and Structures* 2013; 22: 052001.

87. Sato H. Multifunctional devices combining shape-memory alloy and piezoelectric materials. In: Goulbourne NC, Naguib HE (eds). San Diego, California, USA, p. 90581I.

88. Radousky H, Qian F, An Y, et al. Harvesting Mechanical and Thermal Energy by Combining ZnO Nanowires and NiTi Shape Memory Alloy. 8.

89. Pusty M, Sinha L, Shirage PM. A flexible self-poled piezoelectric nanogenerator based on a rGO–Ag/PVDF nanocomposite. *New Journal of Chemistry* 2019; 43: 284–294.

90. Chen X, Tian H, Li X, et al. A high performance P(VDF-TrFE) nanogenerator with self-connected and vertically integrated fibers by patterned EHD pulling. *Nanoscale* 2015; 7: 11536–11544.

91. Hu X, Ding Z, Fei L, et al. Wearable piezoelectric nanogenerators based on reduced graphene oxide and in situ polarization-enhanced PVDF-TrFE films. *Journal of Materials Science* 2019; 54: 6401–6409.

92. Yan J, Liu M, Jeong YG, et al. Performance enhancements in poly(vinylidene fluoride)-based piezoelectric nanogenerators for efficient energy harvesting. *Nano Energy* 2019; 56: 662–692.

93. Dineva P, Gross D, Müller R, et al. Piezoelectric Materials. In: *Dynamic Fracture of Piezoelectric Materials*. Cham: Springer International Publishing, pp. 7–32.

94. Jean-Mistral C, Basrour S, Chaillout J-J. Comparison of electroactive polymers for energy scavenging applications. *Smart Materials and Structures* 2010; 19: 085012.

95. Kholkin AL, Pertsev NA, Goltsev AV. Piezoelectricity and Crystal Symmetry. In: Safari A, Akdoğan EK (eds) *Piezoelectric and Acoustic Materials for Transducer Applications*. Boston, MA: Springer US, pp. 17–38.

96. Dineva P, Gross D, Müller R, et al. Piezoelectric Materials. In: *Dynamic Fracture of Piezoelectric Materials*. Cham: Springer International Publishing, pp. 7–32.

97. Ramadan KS, Sameoto D, Evoy S. A review of piezoelectric polymers as functional materials for electromechanical transducers. *Smart Mater Struct* 2014; 23: 033001.

98. Dahiya RS, Valle M. *Robotic Tactile Sensing*. Dordrecht: Springer Netherlands. Epub ahead of print 2013. DOI: 10.1007/978-94-007-0579-1.

99. Dineva P, Gross D, Müller R, et al. Piezoelectric Materials. In: *Dynamic Fracture of Piezoelectric Materials*. Cham: Springer International Publishing, pp. 7–32.

100. Covaci C, Gontean A. Piezoelectric Energy Harvesting Solutions: A Review. *Sensors* 2020; 20: 3512.

101. Mishra S, Unnikrishnan L, Nayak SK, et al. Advances in Piezoelectric Polymer Composites for Energy Harvesting Applications: A Systematic Review. *Macromolecular Materials and Engineering* 2019; 304: 1800463.

102. Song J, Zhao G, Li B, et al. Design optimization of PVDF-based piezoelectric energy harvesters. *Heliyon* 2017; 3: e00377.

103. Setter N, Damjanovic D, Eng L, et al. Ferroelectric thin films: Review of materials, properties, and applications. *Journal of Applied Physics* 2006; 100: 051606.

104. Fan FR, Tang W, Wang ZL. Flexible Nanogenerators for Energy Harvesting and Self-Powered Electronics. *Advanced Materials* 2016; 28: 4283–4305.

105. Piezo Film Sensors Technical Manual. 89.

106. Fraga MA, Furlan H, Pessoa RS, et al. Wide bandgap semiconductor thin films for piezoelectric and piezoresistive MEMS sensors applied at high temperatures: an overview. *Microsyst Technol* 2014; 14.

107. Crossley S, Whiter RA, Kar-Narayan S. Polymer-based nanopiezoelectric generators for energy harvesting applications. *Materials Science and Technology* 2014; 30: 1613–1624.

108. Stevenson T, Martin DG, Cowin PI, et al. Piezoelectric materials for high temperature transducers and actuators. *J Mater Sci: Mater Electron* 2015; 26: 9256–9267.

109. Septiyani Arifin DE, Ruan JJ. Study on the curie transition of P(VDF-TrFE) copolymer. *IOP Conf Ser: Mater Sci Eng* 2018; 299: 012056.

110. Jiang H, Yang J, Xu F, et al. VDF-content-guided selection of piezoelectric P(VDF-TrFE) films in sensing and energy harvesting applications. *Energy Conversion and Management* 2020; 211: 112771.

111. Ruan L, Zhang D, Tong J, et al. Preparation and Device Applications of Ferroelectric β-PVDF Films. In: Irzaman H (ed) *Ferroelectrics and Their Applications*. InTech. Epub ahead of print 3 October 2018. DOI: 10.5772/intechopen.77167.

112. Jing Q, Kar-Narayan S. Nanostructured polymer-based piezoelectric and triboelectric materials and devices for energy harvesting applications. *Journal of Physics D: Applied Physics* 2018; 51: 303001.

113. Voet VSD, ten Brinke G, Loos K. Well-defined copolymers based on poly(vinylidene fluoride): From preparation and phase separation to application. *Journal of Polymer Science Part A: Polymer Chemistry* 2014; 52: 2861–2877.

114. Cardoso V, Correia D, Ribeiro C, et al. Fluorinated Polymers as Smart Materials for Advanced Biomedical Applications. *Polymers* 2018; 10: 161.

115. Ruan L, Yao X, Chang Y, et al. Properties and Applications of the β Phase Poly(vinylidene fluoride). *Polymers* 2018; 10: 228.

116. Shaik H, Rachith SN, Rudresh KJ, et al. Towards β-phase formation probability in spin coated PVDF thin films. *Journal of Polymer Research*; 24. Epub ahead of print March 2017. DOI: 10.1007/s10965-017-1191-x.

117. Chen X, Han X, Shen Q-D. PVDF-Based Ferroelectric Polymers in Modern Flexible Electronics. *Advanced Electronic Materials* 2017; 3: 1600460.

118. Bodkhe S, Rajesh PSM, Kamle S, et al. Beta-phase enhancement in polyvinylidene fluoride through filler addition: comparing cellulose with carbon nanotubes and clay. *Journal of Polymer Research*; 21. Epub ahead of print May 2014. DOI: 10.1007/s10965-014-0434-3.

119. Harstad S, D'Souza N, Soin N, et al. Enhancement of $\boldsymbol{\beta}$-phase in PVDF films embedded with ferromagnetic Gd_5Si_4 nanoparticles for piezoelectric energy harvesting. *AIP Advances* 2017; 7: 056411.

120. Seo J, Son JY, Kim W-H. Structural and ferroelectric properties of P(VDF-TrFE) thin films depending on the annealing temperature. *Materials Letters* 2019; 238: 294–297.

121. Mirzazadeh Z, Sherafat Z, Bagherzadeh E. Physical and mechanical properties of PVDF/KNN composite produced via hot compression molding. *Ceramics International* 2021; 47: 6211–6219.

122. Ruan L, Yao X, Chang Y, et al. (2018) Properties and Applications of the β Phase Poly(vinylidene fluoride). *Polymers* 10(3): 228. DOI: 10.3390/polym10030228.

123. Polat K. Energy harvesting from a thin polymeric film based on PVDF-HFP and PMMA blend. 8.

124. Oh WJ, Lim H S et al. Preparation of PVDF/PAR composites with piezoelectric properties by Post-Treatment. Polymers 2018, 10, 1333; doi:10.3390/polym10121333.

125. Li J, Zhao C, Xia K, et al. Enhanced piezoelectric output of the PVDF-TrFE/ZnO flexible piezoelectric nanogenerator by surface modification. *Applied Surface Science* 2019; 463: 626–634.

126. Ng KE, Ooi PC, Shazni Mohammad Haniff MA, et al. Performance of all-solution-processed, durable 2D MoS2 flakes−BaTiO3 nanoparticles in polyvinylidene fluoride matrix nanogenerator devices using N-methyl-2-pyrrolidone polar solvent. *Journal of Alloys and Compounds* 2020; 820: 153160.

127. Shi K, Sun B, Huang X, et al. Synergistic effect of graphene nanosheet and BaTiO3 nanoparticles on performance enhancement of electrospun PVDF nanofiber mat for flexible piezoelectric nanogenerators. *Nano Energy* 2018; 52: 153–162.

128. Wan C, Bowen CR. Multiscale-structuring of polyvinylidene fluoride for energy harvesting: the impact of molecular-, micro- and macro-structure. *Journal of Materials Chemistry A* 2017; 5: 3091–3128.

129. Feng Y, Peng C, Deng Q, et al. Annealing and Stretching Induced High Energy Storage Properties in All-Organic Composite Dielectric Films. *Materials* 2018; 11: 2279.

130. Du C, Zhu B-K, Xu Y-Y. Effects of stretching on crystalline phase structure and morphology of hard elastic PVDF fibers. *Journal of Applied Polymer Science* 2007; 104: 2254–2259.

131. Sencadas V, Moreira MV, Lanceros-Méndez S, et al. α- to β Transformation on PVDF Films Obtained by Uniaxial Stretch. *Materials Science Forum* 2006; 514–516: 872–876.

132. Li L, Zhang M, Rong M, et al. Studies on the transformation process of PVDF from α to β phase by stretching. *RSC Adv* 2014; 4: 3938–3943.

133. Damjanovic D. Hysteresis in Piezoelectric and Ferroelectric Materials. In: *The Science of Hysteresis*. Elsevier, pp. 337–465.

134. Park C, Ounaies Z, Wise KE, et al. In situ poling and imidization of amorphous piezoelectric polyimides. *Polymer* 2004; 45: 5417–5425.

135. Jones GD, Assink RA, Dargaville TR, et al. *Characterization, performance and optimization of PVDF as a piezoelectric film for advanced space mirror concepts.* SAND2005-6846, 876343. Epub ahead of print 1 November 2005. DOI: 10.2172/876343.

136. Mahadeva SK, Berring J, Walus K, et al. Effect of poling time and grid voltage on phase transition and piezoelectricity of poly(vinyledene fluoride) thin films using corona poling. *J Phys D: Appl Phys* 2013; 46: 285305.

137. Li M, Katsouras I, Piliego C, et al. Controlling the microstructure of poly(vinylidene-fluoride) (PVDF) thin films for microelectronics. *Journal of Materials Chemistry C* 2013; 1: 7695.

138. Sharma M, Srinivas V, Madras G, et al. Outstanding dielectric constant and piezoelectric coefficient in electrospun nanofiber mats of PVDF containing silver decorated multiwall carbon nanotubes: assessing through piezoresponse force microscopy. *RSC Advances* 2016; 6: 6251–6258.

139. Yuan X, Gao X, Yang J, et al. The large piezoelectricity and high power density of a 3D-printed multilayer copolymer in a rugby ball-structured mechanical energy harvester. *Energy & Environmental Science* 2020; 13: 152–161.

140. Yang Y, Pan H, Xie G, et al. Flexible piezoelectric pressure sensor based on polydopamine-modified BaTiO3/PVDF composite film for human motion monitoring. *Sensors and Actuators A: Physical* 2020; 301: 111789.

141. Wankhade SH, Tiwari S, Gaur A, et al. PVDF–PZT nanohybrid based nanogenerator for energy harvesting applications. *Energy Reports* 2020; 6: 358–364.

142. Hu X, Ding Z, Fei L, et al. Wearable piezoelectric nanogenerators based on reduced graphene oxide and in situ polarization-enhanced PVDF-TrFE films. *Journal of Materials Science* 2019; 54: 6401–6409.

143. Kar E, Bose N, Dutta B, et al. 2D SnO2 nanosheet/PVDF composite based flexible, self-cleaning piezoelectric energy harvester. *Energy Conversion and Management* 2019; 184: 600–608.

144. You S, Zhang L, Gui J, et al. A Flexible Piezoelectric Nanogenerator Based on Aligned P(VDF-TrFE) Nanofibers. *Micromachines* 2019; 10: 302.

145. Khadtare S, Ko EJ, Kim YH, et al. A flexible piezoelectric nanogenerator using conducting polymer and silver nanowire hybrid electrodes for its application in real-time muscular monitoring system. *Sensors and Actuators A: Physical* 2019; 299: 111575.

146. Li J, Chen S, Liu W, et al. High Performance Piezoelectric Nanogenerators Based on Electrospun ZnO Nanorods/Poly(vinylidene fluoride) Composite Membranes. *The Journal of Physical Chemistry C* 2019; 123: 11378–11387.

147. Wu L, Jing M, Liu Y, et al. Power generation by PVDF-TrFE/graphene nanocomposite films. *Composites Part B: Engineering* 2019; 164: 703–709.

148. Parangusan H, Ponnamma D, Al-Maadeed MAA. Stretchable Electrospun PVDF-HFP/Co-ZnO Nanofibers as Piezoelectric Nanogenerators. *Scientific Reports*; 8. Epub ahead of print December 2018. DOI: 10.1038/s41598-017-19082-3.

149. Sahatiya P, Kannan S, Badhulika S. Few layer MoS2 and in situ poled PVDF nanofibers on low cost paper substrate as high performance piezo-triboelectric hybrid nanogenerator: Energy harvesting from handwriting and human touch. *Applied Materials Today* 2018; 13: 91–99.

150. Jella V, Ippili S, Eom J-H, et al. Enhanced output performance of a flexible piezoelectric energy harvester based on stable MAPbI3-PVDF composite films. *Nano Energy* 2018; 53: 46–56.

151. Hu P, Yan L, Zhao C, et al. Double-layer structured PVDF nanocomposite film designed for flexible nanogenerator exhibiting enhanced piezoelectric output and mechanical property. *Composites Science and Technology* 2018; 168: 327–335.

152. Fu J, Hou Y, Gao X, et al. Highly durable piezoelectric energy harvester based on a PVDF flexible nanocomposite filled with oriented BaTi2O5 nanorods with high power density. *Nano Energy* 2018; 52: 391–401.

153. Khalifa M, Mahendran A, Anandhan S. Durable, efficient, and flexible piezoelectric nanogenerator from electrospun PANi/HNT/PVDF blend nanocomposite. *Polymer Composites* 2019; 40: 1663–1675.

154. Liu J, Yang B, Lu L, et al. Flexible and lead-free piezoelectric nanogenerator as self-powered sensor based on electrospinning BZT-BCT/P(VDF-TrFE) nanofibers. *Sensors and Actuators A: Physical* 2020; 303: 111796.

155. Fu J, Hou Y, Zheng M, et al. Flexible Piezoelectric Energy Harvester with Extremely High Power Generation Capability by Sandwich Structure Design Strategy. *ACS Applied Materials & Interfaces*. Epub ahead of print 14 February 2020. DOI: 10.1021/acsami.9b21201.

156. Kamlah M. Ferroelectric and ferroelastic piezoceramics – modeling of electromechanical hysteresis phenomena. *Continuum Mech Thermodyn* 2001; 13: 219–268.

157. Chen PJ. Three dimensional dynamic electromechanical constitutive relations for ferroelectric materials. *International Journal of Solids and Structures* 1980; 16: 1059–1067.

158. Chen PJ, Montgomery ST. A macroscopic theory for the existence of the hysteresis and butterfly loops in ferroelectricity. *Ferroelectrics* 1980; 23: 199–207.

159. Bassiouny E, Ghaleb AF, Maugin GA. Thermodynamical formulation for coupled electromechanical hysteresis effects—I. Basic equations. *International Journal of Engineering Science* 1988; 26: 1279–1295.

160. Bassiouny E, Maugin GA. Thermodynamical formulation for coupled electromechanical hysteresis effects—III. Parameter identification. *International Journal of Engineering Science* 1989; 27: 975–987.

161. Cocks ACF, Mcmeeking RM. A phenomenological constitutive law for the behaviour of ferroelectric ceramics. *Ferroelectrics* 1999; 228: 219–228.

162. Elhadrouz M, Zineb TB, Patoor E. Constitutive law for ferroelectric and ferroelastic single crystals: a micromechanical approach. *Computational Materials Science* 2005; 32: 355–359.

163. Elhadrouz M, Zineb TB, Patoor E. Constitutive Law for Ferroelastic and Ferroelectric Piezoceramics. *Journal of Intelligent Material Systems and Structures* 2005; 16: 221–236.

164. Kamlah M, Böhle U. Finite element analysis of piezoceramic components taking into account ferroelectric hysteresis behavior. *International Journal of Solids and Structures* 2001; 38: 605–633.

165. Kamlah M, Tsakmakis C. Phenomenological modeling of the non-linear electro-mechanical coupling in ferroelectricsfn2fn2Dedicated to Professor Dr D. Munz on the occasion of his 60th birthday. *International Journal of Solids and Structures* 1999; 36: 669–695.

166. Klinkel S. A phenomenological constitutive model for ferroelastic and ferroelectric hysteresis effects in ferroelectric ceramics. *International Journal of Solids and Structures* 2006; 43: 7197–7222.

167. McMeeking RM, Landis CM. A phenomenological multi-axial constitutive law for switching in polycrystalline ferroelectric ceramics. *International Journal of Engineering Science* 2002; 40: 1553–1577.

168. Zouari W, Ben Zineb T, Benjeddou A. A FSDT—MITC Piezoelectric Shell Finite Element with Ferroelectric Non-linearity. *Journal of Intelligent Material Systems and Structures* 2009; 20: 2055–2075.

169. Hwang SC, Huber JE, McMeeking RM, et al. The simulation of switching in polycrystalline ferroelectric ceramics. *Journal of Applied Physics* 1998; 84: 1530–1540.

170. Hwang SC, McMeeking RM. A finite element model of ferroelectric polycrystals. *Ferroelectrics* 1998; 211: 177–194.

171. Hwang SC, McMeeking RM. A finite element model of ferroelastic polycrystals. *International Journal of Solids and Structures* 1999; 36: 1541–1556.

172. Jayendiran R. Finite element analysis of switching domains using ferroelectric and ferroelastic micromechanical model for single crystal piezoceramics. *Ceramics International* 2016; 15.

173. Kamlah M, Liskowsky AC, McMeeking RM, et al. Finite element simulation of a polycrystalline ferroelectric based on a multidomain single crystal switching model. *International Journal of Solids and Structures* 2005; 42: 2949–2964.

174. Mcmeeking RM, Hwang SC. On the potential energy of a piezoelectric inclusion and the criterion for ferroelectric switching. *Ferroelectrics* 1997; 200: 151–173.

175. Michelitsch T, Kreher WS. A simple model for the nonlinear material behavior of ferroelectrics. *Acta Materialia* 1998; 46: 5085–5094.

176. Choudhary N, Kaur D. Shape memory alloy thin films and heterostructures for MEMS applications: A review. *Sensors and Actuators A: Physical* 2016; 242: 162–181.

177. Tsuchiya K. Mechanisms and properties of shape memory effect and superelasticity in alloys and other materials: a practical guide. In: *Shape Memory and Superelastic Alloys*. Elsevier, pp. 3–14.

178. Fultz B. *Phase Transitions in Materials*. Cambridge: Cambridge University Press. Epub ahead of print 2014. DOI: 10.1017/CBO9781107589865.

179. Singh A, Gangwar H. Synthesis and Thermo Mechanical Behaviour of Shape Memory Alloys: A Review. 2015; 3: 9.

180. Ortín J, Delaey L. Hysteresis in shape-memory alloys. *International Journal of Non-Linear Mechanics* 2002; 37: 1275–1281.

181. Pfeifer R, Müller CW, Hurschler C, et al. Adaptable Orthopedic Shape Memory Implants. *Procedia CIRP* 2013; 5: 253–258.

182. Lobo PS, Almeida J, Guerreiro L. Shape Memory Alloys Behaviour: A Review. *Procedia Engineering* 2015; 114: 776–783.

183. Velmurugan C, Senthilkumar V, Dinesh S, et al. Review on phase transformation behavior of NiTi shape memory alloys. *Materials Today: Proceedings* 2018; 5: 14597–14606.

184. Naresh C, Bose PSC, Rao CSP. Shape memory alloys: a state of art review. *IOP Conference Series: Materials Science and Engineering* 2016; 149: 012054.

185. Stoeckel D. THE SHAPE MEMORY EFFECf • Phenomenon, AUoys and Applications. 14.

186. Tadaki T, Otsuka K, Shimizu K. Shape Memory Alloys. *SHAPE MEMORY ALLOYS*; 23.

187. Baxevanis T, Landis CM, Lagoudas DC. On the Effect of Latent Heat on the Fracture Toughness of Pseudoelastic Shape Memory Alloys. *Journal of Applied Mechanics*; 81. Epub ahead of print 1 October 2014. DOI: 10.1115/1.4028191.

188. Thompson SA. An overview of nickel–titanium alloys used in dentistry. *International Endodontic Journal* 2000; 33: 297–310.

189. Wang XB, Verlinden B, Van Humbeeck J. R-phase transformation in NiTi alloys. *Materials Science and Technology* 2014; 30: 1517–1529.

190. Ren X, Otsuka K. Origin of rubber-like behaviour in metal alloys. *Nature* 1997; 389: 579–582.

191. Chen HR (ed). *Shape memory alloys: manufacture, properties and applications*. New York: Nova Science Publishers, 2010.

192. Ma J, Karaman I, Noebe RD. High temperature shape memory alloys. *International Materials Reviews* 2010; 55: 257–315.

193. Miller DA, Lagoudas DC. Influence of cold work and heat treatment on the shape memory effect and plastic strain development of NiTi. *Materials Science and Engineering: A* 2001; 308: 161–175.

194. Sreekumar M, Nagarajan T, Singaperumal M. Application of trained NiTi SMA actuators in a spatial compliant mechanism: Experimental investigations. *Materials & Design* 2009; 30: 3020–3029.

195. Mertmann M, Vergani G. Design and application of shape memory actuators. *Eur Phys J Spec Top* 2008; 158: 221–230.

196. Zarinejad M, Liu Y. DEPENDENCE OF TRANSFORMATION TEMPERATURES OF SHAPE MEMORY ALLOYS ON THE NUMBER AND CONCENTRATION OF VALENCE ELECTRONS. 23.

197. Mihálcz I. FUNDAMENTAL CHARACTERISTICS AND DESIGN METHOD FOR NICKEL-TITANIUM SHAPE MEMORY ALLOY. *Periodica Polytechnica Mechanical Engineering* 2001; 45: 75–86.

198. Brinson LC. One-Dimensional Constitutive Behavior of Shape Memory Alloys: Thermomechanical Derivation with Non-Constant Material Functions and Redefined Martensite Internal Variable. *Journal of Intelligent Material Systems and Structures* 1993; 4: 229–242.

199. Liang C, Rogers CA. One-Dimensional Thermomechanical Constitutive Relations for Shape Memory Materials. *Journal of Intelligent Material Systems and Structures* 1990; 1: 207–234.

200. Cisse C, Zaki W, Ben Zineb T. A review of constitutive models and modeling techniques for shape memory alloys. *International Journal of Plasticity* 2016; 76: 244–284.

201. Lagoudas DC, Bo Z, Qidwai MA. A UNIFIED THERMODYNAMIC CONSTITUTIVE MODEL FOR SMA AND FINITE ELEMENT ANALYSIS OF ACTIVE METAL MATRIX COMPOSITES. *Mechanics of Composite Materials and Structures* 1996; 3: 153–179.

202. Patoor E, Eberhardt A, Berveiller M. Thermomechanical Behavior of Shape Memory Alloys. In: *ESOMAT 1989 - Ist European Symposium on Martensitic Transformations in Science and Technology*. Bochum, Germany: EDP Sciences, pp. 133–140.

203. Falk F. Ginzburg-Landau theory of static domain walls in shape-memory alloys. *Z Physik B - Condensed Matter* 1983; 51: 177–185.

204. Falk F. Model free energy, mechanics, and thermodynamics of shape memory alloys. *Acta Metallurgica* 1980; 28: 1773–1780.

205. Abeyaratne R, Knowles JK. On the driving traction acting on a surface of strain discontinuity in a continuum. *Journal of the Mechanics and Physics of Solids* 1990; 38: 345–360.

206. Ball JM, James RD. Fine Phase Mixtures as Minimizers of Energy. In: Antman SS, Brezis H, Coleman BD, et al. (eds) *Analysis and Continuum Mechanics: A Collection of Papers Dedicated to J. Serrin on His Sixtieth Birthday*. Berlin, Heidelberg: Springer, pp. 647–686.

207. Barsch GR, Krumhansl JA. Nonlinear and nonlocal continuum model of transformation precursors in martensites. *Metall Mater Trans A* 1988; 19: 761–775.

208. Dhote RP, Melnik RNV, Zu J. Dynamic multi-axial behavior of shape memory alloy nanowires with coupled thermo-mechanical phase-field models. *Meccanica* 2014; 49: 1561–1575.

209. Levitas VI, Preston DL. Three-dimensional Landau theory for multivariant stress-induced martensitic phase transformations. I. Austenite$\ensuremath{\leftrightarrow}$martensite. *Phys Rev B* 2002; 66: 134206.

210. Levitas VI, Preston DL. Three-dimensional Landau theory for multivariant stress-induced martensitic phase transformations. II. Multivariant phase transformations and stress space analysis. *Phys Rev B* 2002; 66: 134207.

211. Wang LX, Melnik RVN. Thermo-Mechanical Wave Propagations in Shape Memory Alloy Rod with Phase Transformations. *Mechanics of Advanced Materials and Structures* 2007; 14: 665–676.

212. Alder BJ, Wainwright TE. Studies in Molecular Dynamics. I. General Method. *J Chem Phys* 1959; 31: 459–466.

213. Rahman A. Correlations in the Motion of Atoms in Liquid Argon. *Phys Rev* 1964; 136: A405–A411.

214. Parrinello M, Rahman A. Polymorphic transitions in single crystals: A new molecular dynamics method. *Journal of Applied Physics* 1981; 52: 7182–7190.

215. Ozgen S, Adiguzel O. Investigation of the thermoelastic phase transformation in a NiAl alloy by molecular dynamics simulation. *Journal of Physics and Chemistry of Solids* 2004; 65: 861–865.

216. Suzuki T, Shimono M. A simple model for martensitic transformation. *J Phys IV France* 2003; 112: 129–132.

217. Daw MS, Baskes MI. Embedded-atom method: Derivation and application to impurities, surfaces, and other defects in metals. *Phys Rev B* 1984; 29: 6443–6453.

218. Blanc P, Lexcellent C. Micromechanical modelling of a CuAlNi shape memory alloy behaviour. *Materials Science and Engineering: A* 2004; 378: 465–469.

219. Huang M, Gao X, Brinson LC. A multivariant micromechanical model for SMAs Part 2. Polycrystal model. *International Journal of Plasticity* 2000; 16: 1371–1390.

220. Levitas VI, Ozsoy IB. Micromechanical modeling of stress-induced phase transformations. Part 1. Thermodynamics and kinetics of coupled interface propagation and reorientation. *International Journal of Plasticity* 2009; 25: 239–280.

221. Sadjadpour A, Bhattacharya K. A micromechanics inspired constitutive model for shape-memory alloys: the one-dimensional case. *Smart Mater Struct* 2007; 16: S51–S62.

222. Sun QP, Hwang KC. Micromechanics modelling for the constitutive behavior of polycrystalline shape memory alloys—I. Derivation of general relations. *Journal of the Mechanics and Physics of Solids* 1993; 41: 1–17.

223. Kudoh Y, Tokonami M, Miyazaki S, et al. Crystal structure of the martensite in Ti-49.2 at.%Ni alloy analyzed by the single crystal X-ray diffraction method. *Acta Metallurgica* 1985; 33: 2049–2056.

224. Sun QP, Hwang KC, Yu SW. A micromechanics constitutive model of transformation plasticity with shear and dilatation effect. *Journal of the Mechanics and Physics of Solids* 1991; 39: 507–524.

225. Wang XM, Xu BX, Yue ZF. Micromechanical modelling of the effect of plastic deformation on the mechanical behaviour in pseudoelastic shape memory alloys. *International Journal of Plasticity* 2008; 24: 1307–1332.

226. Yu C, Kang G, Song D, et al. Micromechanical constitutive model considering plasticity for super-elastic NiTi shape memory alloy. *Computational Materials Science* 2012; 56: 1–5.

227. Lu ZK, Weng GJ. A self-consistent model for the stress–strain behavior of shape-memory alloy polycrystals. *Acta Materialia* 1998; 46: 5423–5433.

228. Šittner P, Novák V. Anisotropy of martensitic transformations in modeling of shape memory alloy polycrystals. *International Journal of Plasticity* 2000; 16: 1243–1268.

229. Thamburaja P, Anand L. Polycrystalline shape-memory materials: effect of crystallographic texture. *Journal of the Mechanics and Physics of Solids* 2001; 49: 709–737.

230. Batdorf: A mathematical theory of plasticity based... - Google Scholar, https://scholar.google.com/scholar_lookup?title=A%C2%A0Mathematical%20Theory%20of%20Plasticity%20Based%20on%20the%20Concept%20of%20Slip&publication_year=1949&author=S.B.%20Batdorf&author=B.%20Budiansky (accessed 8 April 2021).

231. Bažant: Microplane model for strain controlled inelastic... - Google Scholar, https://scholar.google.com/scholar_lookup?title=Microplane%20Model%20for%20Strain%20Controlled%20Inelastic%20Behaviour&publication_year=1984&author=Z.%20Ba%C5%BEant (accessed 8 April 2021).

232. Collard C, Ben Zineb T. Simulation of the effect of elastic precipitates in SMA materials based on a micromechanical model. *Composites Part B: Engineering* 2012; 43: 2560–2576.

233. Niclaeys C, Ben Zineb T, Arbab-Chirani S, et al. Determination of the interaction energy in the martensitic state. *International Journal of Plasticity* 2002; 18: 1619–1647.

234. Xolin P, Collard C, Engels-Deutsch M, et al. Finite element and experimental structural analysis of endodontic rotary file made of Cu-based single crystal SMA considering a micromechanical behavior model. *International Journal of Solids and Structures* 2021; S0020768321000238.

235. Tanaka K, Nagaki S. A thermomechanical description of materials with internal variables in the process of phase transitions. *Ing arch* 1982; 51: 287–299.

236. Auricchio F, Taylor RL. Shape-memory alloys: modelling and numerical simulations of the finite-strain superelastic behavior. *Computer Methods in Applied Mechanics and Engineering* 1997; 143: 175–194.

237. Bertram A. Thermo-mechanical constitutive equations for the description of shape memory effects in alloys. *Nuclear Engineering and Design* 1983; 74: 173–182.

238. Raniecki B, Lexcellent C, Tanaka K. Thermodynamic models of pseudoelastic behaviour of shape memory alloys. 24.

239. RANIECKI B, LEXCELLENT C. RL-models of pseudoelasticity and their specification for some shape memory solids. *Eur j mech, A Solids* 1994; 13: 21–50.

240. Raniecki B, Lexcellent Ch. Thermodynamics of isotropic pseudoelasticity in shape memory alloys. *European Journal of Mechanics - A/Solids* 1998; 17: 185–205.

241. Raniecki B, Lexcellent Ch. Thermodynamics of isotropic pseudoelasticity in shape memory alloys. *European Journal of Mechanics - A/Solids* 1998; 17: 185–205.

242. Souza AC, Mamiya EN, Zouain N. Three-dimensional model for solids undergoing stress-induced phase transformations. *European Journal of Mechanics - A/Solids* 1998; 17: 789–806.

243. Auricchio F, Petrini L. Improvements and algorithmical considerations on a recent three-dimensional model describing stress-induced solid phase transformations. *International Journal for Numerical Methods in Engineering* 2002; 55: 1255–1284.

244. Bouvet C, Calloch S, Lexcellent C. A phenomenological model for pseudoelasticity of shape memory alloys under multiaxial proportional and nonproportional loadings. *European Journal of Mechanics - A/Solids* 2004; 23: 37–61.

245. Evangelista V, Marfia S, Sacco E. Phenomenological 3D and 1D consistent models for shape-memory alloy materials. *Comput Mech* 2009; 44: 405.

246. Lexcellent Ch, Boubakar ML, Bouvet Ch, et al. About modelling the shape memory alloy behaviour based on the phase transformation surface identification under proportional loading and anisothermal conditions. *International Journal of Solids and Structures* 2006; 43: 613–626.

247. Saint-Sulpice L, Arbab-Chirani S, Calloch S. Thermomechanical cyclic behavior modeling of Cu-Al-Be SMA materials and structures. *International Journal of Solids and Structures* 2012; 49: 1088–1102.

248. Thiebaud F, Lexcellent C, Collet M, et al. Implementation of a model taking into account the asymmetry between tension and compression, the temperature effects in a finite element code for shape memory alloys structures calculations. *Computational Materials Science* 2007; 41: 208–221.

249. Boyd JG, Lagoudas DC. A thermodynamical constitutive model for shape memory materials. Part I. The monolithic shape memory alloy. *International Journal of Plasticity* 1996; 12: 805–842.

250. Chemisky Y, Duval A, Patoor E, et al. Constitutive model for shape memory alloys including phase transformation, martensitic reorientation and twins accommodation. *Mechanics of Materials* 2011; 43: 361–376.

251. Leclercq S, Lexcellent C. A general macroscopic description of the thermomechanical behavior of shape memory alloys. *Journal of the Mechanics and Physics of Solids* 1996; 44: 953–980.

252. Moumni Z, Zaki W, Nguyen QS. Theoretical and numerical modeling of solid–solid phase change: Application to the description of the thermomechanical behavior of shape memory alloys. *International Journal of Plasticity* 2008; 24: 614–645.

253. Peultier B, Ben Zineb T, Patoor E. Macroscopic constitutive law of shape memory alloy thermomechanical behaviour. Application to structure computation by FEM. *Mechanics of Materials* 2006; 38: 510–524.

254. Auricchio F, Marfia S, Sacco E. Modelling of SMA materials: Training and two way memory effects. *Computers & Structures* 2003; 81: 2301–2317.

255. Duval A, Haboussi M, Ben Zineb T. Modelling of localization and propagation of phase transformation in superelastic SMA by a gradient nonlocal approach. *International Journal of Solids and Structures* 2011; 48: 1879–1893.

256. Hazar S, Zaki W, Moumni Z, et al. Steady State Crack Growth in Shape Memory Alloys. American Society of Mechanical Engineers Digital Collection. Epub ahead of print 20 February 2014. DOI: 10.1115/SMASIS2013-3071.

257. Morin C. *A comprehensive approach for fatigue analysis of shape memory alloys*. Phdthesis, Ecole Polytechnique X, https://pastel.archives-ouvertes.fr/pastel-00608205 (2011, accessed 8 April 2021).

258. Stebner AP, Brinson LC. Explicit finite element implementation of an improved three dimensional constitutive model for shape memory alloys. *Computer Methods in Applied Mechanics and Engineering* 2013; 257: 17–35.

259. Zaki W. An efficient implementation for a model of martensite reorientation in martensitic shape memory alloys under multiaxial nonproportional loading. *International Journal of Plasticity* 2012; 37: 72–94.

260. Anand L, Gurtin ME. Thermal effects in the superelasticity of crystalline shape-memory materials. *Journal of the Mechanics and Physics of Solids* 2003; 51: 1015–1058.

261. Arghavani J, Auricchio F, Naghdabadi R, et al. An improved, fully symmetric, finite-strain phenomenological constitutive model for shape memory alloys. *Finite Elements in Analysis and Design* 2011; 47: 166–174.

262. Arghavani J, Auricchio F, Naghdabadi R, et al. On the robustness and efficiency of integration algorithms for a 3D finite strain phenomenological SMA constitutive model. *International Journal for Numerical Methods in Engineering* 2011; 85: 107–134.

263. Christ D, Reese S. A finite element model for shape memory alloys considering thermomechanical couplings at large strains. *International Journal of Solids and Structures* 2009; 46: 3694–3709.

264. Müller Ch, Bruhns OT. A thermodynamic finite-strain model for pseudoelastic shape memory alloys. *International Journal of Plasticity* 2006; 22: 1658–1682.

265. Reese S, Christ D. Finite deformation pseudo-elasticity of shape memory alloys – Constitutive modelling and finite element implementation. *International Journal of Plasticity* 2008; 24: 455–482.

266. Stupkiewicz S, Petryk H. Finite-strain micromechanical model of stress-induced martensitic transformations in shape memory alloys. *Materials Science and Engineering: A* 2006; 438–440: 126–130.

267. Thamburaja P. A finite-deformation-based phenomenological theory for shape-memory alloys. *International Journal of Plasticity* 2010; 26: 1195–1219.

268. Ziólkowski A. Three-dimensional phenomenological thermodynamic model of pseudoelasticity of shape memory alloys at finite strains. *Continuum Mech Thermodyn* 2007; 19: 379–398.

269. Bhattacharyya A, Lagoudas DC. A stochastic thermodynamic model for the gradual thermal transformation of SMA polycrystals. *Smart Mater Struct* 1997; 6: 235–250.

270. Fischlschweiger M, Oberaigner ER. Kinetics and rates of martensitic phase transformation based on statistical physics. *Computational Materials Science* 2012; 52: 189–192.

271. Bellac ML, Bellac ML, Mortessagne F, et al. *Equilibrium and Non-Equilibrium Statistical Thermodynamics*. Cambridge University Press, 2004.

272. Müller I. Pseudo-elastic hysteresis in shape memory alloys. *Physica B: Condensed Matter* 2012; 407: 1314–1315.

273. Müller I, Seelecke S. Thermodynamic aspects of shape memory alloys. *Mathematical and Computer Modelling* 2001; 34: 1307–1355.

274. Lu L, Ding W, Liu J, et al. Flexible PVDF based piezoelectric nanogenerators. *Nano Energy* 2020; 78: 105251.

275. Ullah A, ur Rahman A, Won Ahn C, et al. Enhancement of dielectric and energy density properties in the PVDF-based copolymer/terpolymer blends. *Polym Eng Sci* 2015; 55: 1396–1402.

276. Dietze M, Es-Souni M. Structural and functional properties of screen-printed PZT–PVDF-TrFE composites. *Sensors and Actuators A: Physical* 2008; 143: 329–334.

277. Dietze M, Es-Souni M. Structural and functional properties of screen-printed PZT–PVDF-TrFE composites. *Sensors and Actuators A: Physical* 2008; 143: 329–334.

278. Neumann N, Köhler R, Hofmann G. Pyroelectric thin film sensors and arrays based on P(VDF/TrFE). *Integrated Ferroelectrics* 1995; 6: 213–230.

279. Bhavanasi V, Kumar V, Parida K, et al. Enhanced Piezoelectric Energy Harvesting Performance of Flexible PVDF-TrFE Bilayer Films with Graphene Oxide. *ACS Applied Materials & Interfaces* 2016; 8: 521–529.

280. Briscoe J, Jalali N, Woolliams P, et al. Measurement techniques for piezoelectric nanogenerators. *Energy & Environmental Science* 2013; 6: 3035.

281. Huang W. On the selection of shape memory alloys for actuators. 2002; 9.

282. Sreekumar M, Singaperumal M, Nagarajan T, et al. Recent advances in nonlinear control technologies for shape memory alloy actuators. *J Zhejiang Univ - Sci A* 2007; 8: 818–829.

283. Wu Y, Badel A, Formosa F, et al. Self-powered optimized synchronous electric charge extraction circuit for piezoelectric energy harvesting. *Journal of Intelligent Material Systems and Structures* 2014; 25: 2165–2176.

284. Badel A, Guyomar D, Lefeuvre E, et al. Piezoelectric Energy Harvesting using a Synchronized Switch Technique. *Journal of Intelligent Material Systems and Structures* 2006; 17: 831–839.

285. Shu YC, Lien IC. Efficiency of energy conversion for a piezoelectric power harvesting system. *Journal of Micromechanics and Microengineering* 2006; 16: 2429–2438.

286. Shu YC, Lien IC, Wu WJ. An improved analysis of the SSHI interface in piezoelectric energy harvesting. *Smart Materials and Structures* 2007; 16: 2253–2264.

287. Lefeuvre E, Badel A, Richard C, et al. A comparison between several vibration-powered piezoelectric generators for standalone systems. *Sensors and Actuators A: Physical* 2006; 126: 405–416.

288. Gambier P, Anton SR, Kong N, et al. Piezoelectric, solar and thermal energy harvesting for hybrid low-power generator systems with thin-film batteries. *Measurement Science and Technology* 2012; 23: 015101.

289. LTC3588-1 - Nanopower Energy Harvesting Power Supply. 20.

290. Zhao Y, Wang K, Guan M. An adaptive boost converter for low voltage piezoelectric energy harvesting. *Ferroelectrics* 2016; 502: 107–118.

291. Lallart M, Garbuio L, Petit L, et al. Double synchronized switch harvesting (DSSH): a new energy harvesting scheme for efficient energy extraction. *IEEE Transactions on Ultrasonics, Ferroelectrics and Frequency Control* 2008; 55: 2119–2130.

292. Arroyo E, Badel A. Electromagnetic vibration energy harvesting device optimization by synchronous energy extraction. *Sensors and Actuators A: Physical* 2011; 171: 266–273.

Résumé français

Les matériaux intelligents avec l'effet combiné de différentes propriétés représentent une approche prometteuse pour améliorer leurs fonctionnalités. Un système hybride composé d'alliages à mémoire de forme (AMF) et de matériaux piézoélectriques permet une amélioration significative des caractéristiques du système composite. L'avantage du dispositif hybride AMF/matériau piézoélectrique est qu'il permet le couplage de diverses propriétés telles que le comportement thermomécanique et électromécanique de manière synergique. Ces systèmes hybrides peuvent avoir des applications dans la récolte d'énergie. Un domaine est celui de la récolte d'énergie à petite échelle pour alimenter des dispositifs électroniques auto-alimentés. Dans ce contexte, la capacité de combiner la récolte thermique et mécanique à l'aide de matériaux intelligents méritait d'être étudiée plus en profondeur. Jusqu'à présent, la plupart des études avaient porté sur l'effet combiné de d'un AMF et d'une céramique piézoélectrique. Il était donc intéressant de se concentrer sur le développement d'un système hybride composé d'AMF et d'un film de polymère piézoélectrique P(VDF-TrFE), car l'excellente flexibilité et le coefficient piézoélectrique élevé du polymère P(VDF-TrFE) conviennent parfaitement à la fabrication du dispositif avec AMF.

Nous avons ainsi conçu, fabriqué et caractérisé avec succès un nouveau dispositif composite composé d'un stratifié d'un alliage à mémoire de forme (AMF) et d'un polymère piézoélectrique pour une application de récolte d'énergie. Nous concluons dans cette étude la faisabilité du composite pour la récolte d'énergie en exploitant les multiples voies de conversion d'énergie offertes par les deux couches superposées d'AMF et de polymère piézoélectrique P(VDF-TrFE). Nous avons réalisé expérimentalement un composite en AMF NiTi/P(VDF-TrFE) entièrement flexible, capable de convertir l'énergie mécanique-thermique en énergie électrique de manière synergique. La simulation par éléments finis a aussi été réalisée afin de comprendre le comportement de chaque couche (couche piézoélectrique et AMF) et le comportement effectif du composite. Pour démontrer le bon de fonctionnement du dispositif, nous avons effectué une caractérisation électro-thermomécanique en utilisant le test de traction. Les résultats ont montré la génération d'une réponse électrique pendant l'effet de mémoire de forme unidirectionnel de l'AMF pour un seul cycle de chauffage/refroidissement. Les résultats expérimentaux obtenus ont été validés à l'aide de la simulation par éléments finis. Les résultats simulés ont trouvé un bon accord avec les résultats expérimentaux. En outre, la modélisation du dispositif composite s'est avérée être un outil intéressant pour prédire la tension de sortie générée pour une charge de chauffage/refroidissement donnée.

Enfin, nous avons développé le circuit électronique de la couche polymère piézoélectrique. L'efficacité de la conversion de puissance de l'ensemble du système dépend fortement du circuit électronique.

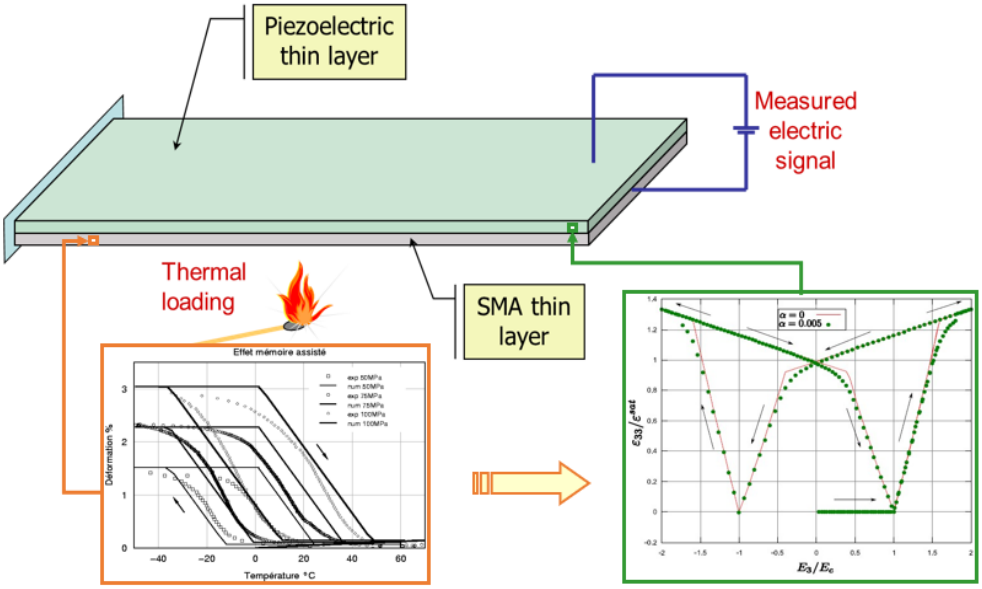

Figure 1. Représentation schématique du principe de fonctionnement du composite AMF-couche fine piézoélectrique.

Ainsi, nous avons introduit un convertisseur élévateur intégré LTC3588-1 qui peut fonctionner avec un très faible courant de sortie du dispositif composite. Cela permet de stocker l'énergie produite dans une batterie pour une utilisation ultérieure ou de fournir la puissance nécessaire au fonctionnement de petits appareils électroniques.

Dans le premier chapitre, nous avons introduit le concept de récolte d'énergie et nous avons présenté l'état de l'art des composites AMF/piézoélectriques existants. Nous avons étudié de manière détaillée les avantages et les limites des études existantes et nous avons proposé de développer un nouveau composite flexible à la fois expérimentalement et numériquement. Le premier chapitre contient donc le principe de la piézoélectricité et les matériaux piézoélectriques pour la récolte d'énergie. Ensuite, nous avons présenté le polymère P(VDF-TrFE) et son application pour la récolte d'énergie ainsi que différents mécanismes pour améliorer les propriétés piézoélectriques du polymère. Ensuite, pour comprendre le comportement du composite, il fallait un double niveau de modélisation couplé. Ainsi, pour la première étape, nous avons introduit la modélisation du comportement de la partie piézoélectrique. La deuxième étape traite de l'AMF et de ses propriétés ainsi que des différents modèles décrivant son comportement thermomécanique.

Dans le deuxième chapitre, nous avons montré comment nous avons fabriqué un nouveau système composite composé d'une couche d'AMF NiTi et d'une couche de polymère piézoélectrique P(VDF-TrFE). Le premier composite a été réalisé par le dépôt direct de la fine couche de polymère d'une épaisseur de ~4 µm sur la feuille en AMF (épaisseur 125 µm) par la méthode du spin coating. Une couche d'électrode Cr/Al d'une épaisseur de 150nm a été déposée sur le dessus de la couche de polymère. La polarisation électrique a été réalisée par

la technique du contact avec un champ électrique maximum de 100V/µm pour améliorer les propriétés piézoélectriques. La polarisation électrique a été réalisée en considérant l'AMF comme une électrode inférieure. La caractérisation piézoélectrique du composite AMF/P(VDF-TrFE)/Cr/Al a montré un coefficient piézoélectrique plus élevé de 22,8 pC/N. Un composite multicouche a également été fabriqué en déposant deux fines couches de polymère d'une épaisseur de ~ 4 µm sur chaque côté de la feuille de AMF. Cependant, ce type de composite a montré quelques inconvénients tels que le claquage électrique du polymère après un certain champ électrique appliqué et la perte des propriétés piézoélectriques. En outre, nous avons observé une délamination de la couche de polymère de la surface de l'AMF en raison du comportement plastique de la couche de P(VDF-TrFE). Par conséquent, pour améliorer l'adhésion à l'interface, nous avons développé une nouvelle structure composite, où la couche de polymère est déposée sur un substrat polyéthylène naphtalate (PEN) mince et flexible. La polarisation électrique a été réalisée de la même manière en déposant deux électrodes de Cr/Al de chaque côté de la couche de polymère. La boucle d'hystérésis P-E a démontré une bonne polarisation de saturation (Ps) de 7,6 µC/cm2. Ensuite, le film PEN/ P(VDF-TrFE) a été collé avec l'AMF en utilisant une fine couche de colle époxy flexible. Ce composite montre de meilleures performances et une bonne force d'adhésion. Cette structure composite finalisée avec une surface active de 1,8 cm × 2,5 cm a été utilisée pour notre caractérisation expérimentale.

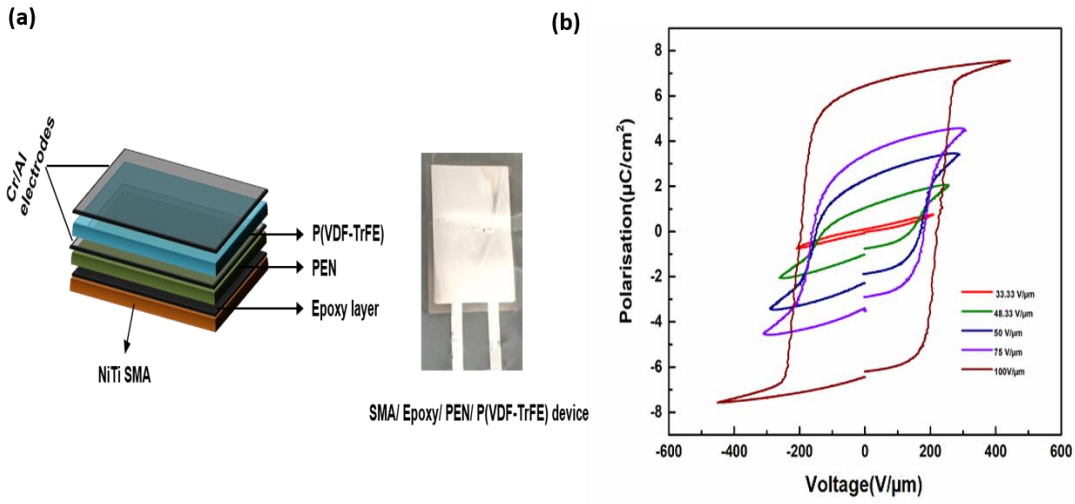

Figure 2 (a). Structure multicouche composite AMF/PEN/P(VDF-TrFE). (b) Boucle d'hystérésis de polarisation de P(VDF-TrFE) sur PEN.

L'objectif principal de ce travail était d'exploiter les propriétés multiphysiques du composite à couches superposées AMF/(PVDF-TrFE) pour la récolte d'énergie. En particulier, ce composite qui permet la récupération de la chaleur perdue à de faibles températures de la source de chaleur à l'échelle centimétrique du composite. Par conséquent, dans le chapitre 2, nous avons aussi effectué la caractérisation mécanique, thermique et électro-thermomécanique du composite AMF/(PVDF-TrFE). La caractérisation expérimentale a montré la double conversion de l'énergie thermique en énergie mécanique qui est à son tour convertie en énergie

électrique. Dans cet aspect, il est nécessaire d'optimiser d'abord la réponse piézoélectrique du film P(VDF-TrFE). Par conséquent, nous avons d'abord effectué la récolte d'énergie piézoélectrique du film PEN/ P(VDF-TrFE) par l'application d'une pression mécanique. Une contrainte uniaxiale a été appliquée au film PEN/ P(VDF-TrFE) par le tapotement d'un doigt humain ou la flexion répétés. Le dispositif a été capable de convertir les mouvements de tapotement du doigt humain correspondant à une sollicitation de pression et de relâchement en électricité. La puissance de sortie est calculée à partir de la tension en circuit ouvert et du courant de court-circuit en considérant les valeurs de sortie maximales. Pendant le tapage par le doigt et la flexion, la puissance de sortie du film P(VDF-TrFE) est respectivement de 5,5 µW cm-2 et 16 µW cm^{-2}. Cependant, cette méthode de calcul de la puissance n'est pas la meilleure solution pratique car elle donne une valeur de puissance surestimée. Cela est dû au fait que la tension est mesurée à travers une résistance très élevée et le courant à travers une résistance très faible. Par conséquent, dans cette étude, nous avons effectué le test pour le film PEN/P(VDF-TrFE) par flexion et enregistré la tension de crête à travers diverses résistances de charge allant de 1 kΩ à 5 MΩ. Une valeur de puissance maximale de 6,25 µW cm-2 a été observée, à travers une résistance de charge de 1 MΩ.

Par ailleurs la récolte d'énergie thermique a été réalisée pour le composite AMF/(PVDF-TrFE) en utilisant un bain d'huile de silicium chauffé à une température de 75°C. Les températures de début et de fin de transformation directe et inverse de l'AMF en NiTi étaient comprises entre 50 et 75°C, mesurées par des études DSC. Pendant le chauffage au-dessus de 62°C, l'AMF en NiTi a subi une transformation martensitique inverse et a retrouvé sa forme plate d'origine. En conséquence, le dispositif P(VDF-TrFE) suit également un changement de forme drastique, qui donne une tension de sortie ~2V de la couche piézoélectrique pendant la transformation inverse de l'AMF. Afin d'identifier simultanément les performances électro-thermomécaniques du composite, nous avons effectué un test de traction et analysé les évolutions contrainte-déformation-température et tension-déformation-température pendant le chargement thermomécanique. Nous avons obtenu une réponse électrique pendant le chargement mécanique et le chauffage du dispositif. Ainsi, le composite AMF/P(VDF-TrFE) est capable de combiner la propriété de couplage thermomécanique de l'AMF en NiTi et le couplage électromécanique du polymère piézoélectrique P(VDF-TrFE) pour la récolte d'énergie. Ainsi, les résultats offrent une approche prometteuse pour l'utilisation synergique de deux matériaux intelligents pour la récolte d'énergie. La tension et la puissance de sortie du composite sont plus faibles par rapport aux dispositifs existants. Cependant, dans ces premiers résultats, nous démontrons la faisabilité du couplage de deux matériaux intelligents composites pour la récolte d'énergie thermique à basse température.

Enfin, dans ce deuxième chapitre, nous avons également présenté une nouvelle configuration de caractérisation. Le dispositif expérimental conçu est capable de réaliser la caractérisation électro-thermomécanique du composite AMF/polymère Piézoélectrique. Le système est

constitué de différents composants pour le chauffage/refroidissement du composite ainsi que d'un système de contrôle pour combiner toutes les sous-parties.

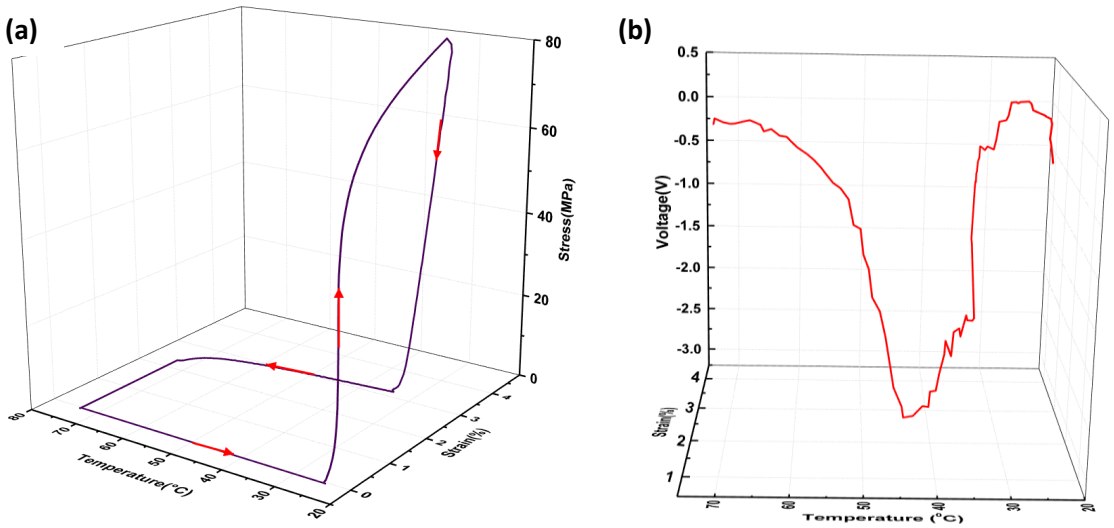

Figure 3(a). Représentation 3D de la courbe contrainte-déformation-température du composite AMF/ P(VDF-TrFE). Représentation 3D de la courbe tension-déformation-température du composite AMF/ P(VDF-TrFE).

Le système de contrôle est développé dans le logiciel LabVIEW pour effectuer le contrôle de l'ensemble du dispositif avec des mesures et des commandes appropriées. Le chauffage de l'échantillon composite est effectué à l'aide d'un faisceau laser d'une puissance maximale de 5W. La puissance peut être contrôlée pour appliquer la puissance désirée afin de chauffer l'échantillon à une température de 75 °C par le biais d'un module d'interface PSU-RS232. Le chauffage homogène de l'échantillon se fait à l'aide de lentilles concaves et convexes. La lumière laser passe d'abord par une lentille convexe qui fait converger les rayons laser incidents vers l'axe principal. Ensuite, nous avons placé une lentille concave après la lentille convexe. Ainsi, la lentille concave étale les rayons laser. Par conséquent, les rayons incidents sur l'échantillon AMF/piezo se propagent bien sur toute la surface. Cela signifie qu'un chauffage homogène peut être assuré de cette manière. Le refroidissement immédiat de l'échantillon peut être effectué avec de l'azote liquide. Le refroidissement de l'échantillon est effectué à l'aide d'une électrovanne, qui permet de contrôler la quantité d'azote liquide de manière pulsée afin d'obtenir un chargement sinusoïdal de la température de l'échantillon. Nous avons développé le système de support et le cadre qui se compose des deux supports de lentilles et du support d'échantillon. Toutes les sous-parties sont disposées et s'intègrent bien dans le cadre principal.

Dans le chapitre 3, nous avons validé l'analyse par éléments finis pour le composite afin d'optimiser le couplage électromécanique de la couche polymère piézoélectrique et le couplage thermomécanique de la couche AMF. La combinaison de ces modèles constitutifs permet d'identifier le comportement électro-thermomécanique effectif global du composite.

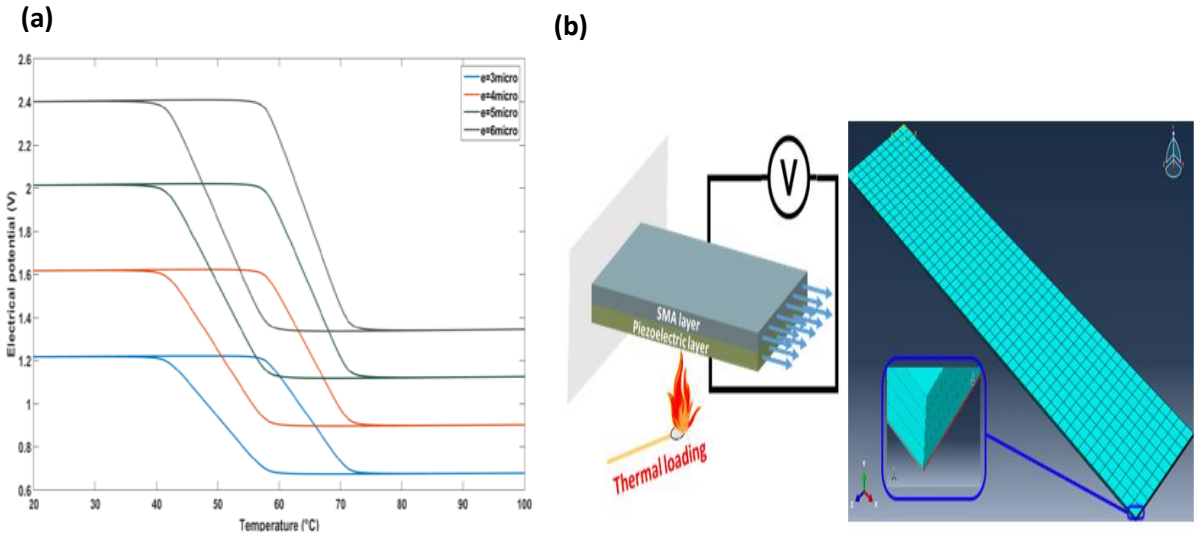

Figure 4. Graphique du potentiel électrique en fonction de la température pour des couches de P(VDF-TrFE) de différentes épaisseurs soumises à une charge de traction. Composite hybride AMF/Piezo soumis à une charge de chauffage-refroidissement sous précharge de tension constante et maillage par éléments finis.

Dans ce chapitre, nous avons simulé les principales propriétés de l'AMF telles que le comportement superélastique, l'effet de mémoire de forme unidirectionnel et l'effet de mémoire de forme bidirectionnel ont été simulés en utilisant le modèle de Chemisky et al. déjà implémenté dans Abaqus via Umat. Le modèle constitutif piézoélectrique classique et linéaire a été utilisé pour décrire le comportement électromécanique de la couche piézoélectrique. Les effets de mémoire de forme ont été prouvés en modélisant les charges de traction et de flexion. Ensuite, nous avons développé avec succès le modèle d'éléments finis pour le composite AMF / polymère piézoélectrique. Pendant l'application d'une charge thermique, un potentiel électrique a été créé sur la couche piézoélectrique, ce qui est bien illustré par le modèle.

Nous avons également démontré la relation entre l'épaisseur des couches piézoélectriques et le rendement électrique. Le potentiel électrique augmente avec l'augmentation de l'épaisseur. Nous avons comparé le modèle d'éléments finis pour l'effet de mémoire de forme avec les données expérimentales de la machine d'essais de traction. La comparaison entre les résultats expérimentaux et numériques a montré que le modèle présente un bon accord avec les résultats expérimentaux. L'outil numérique nous permet de prédire l'évaluation de la tension électrique pendant le chargement thermique. Ainsi, il s'agit d'un outil numérique de prédiction intéressant qui pourrait aider à améliorer les performances de récolte d'énergie de ce type de composite hybride.

Le circuit électronique joue un rôle important dans le système de récolte d'énergie. L'efficacité de la conversion d'énergie de l'ensemble du système dépend fortement du circuit électronique.

Le problème principal de ce type de système est de convertir la charge électronique en énergie électrique car il y a peu de charges électriques générées par la couche mince piézoélectrique. Afin de récolter efficacement l'énergie du dispositif, le chapitre 4 présente les éléments clés qui ont été conçus et réalisés pour évaluer les performances du film P(VDF-TrFE) pour la récupération d'énergie.

Nous avons aussi développé un banc de test automatisé pour étudier les caractéristiques électriques d'un film piézoélectrique, pour cela nous avons sélectionné deux types de bancs de test mécaniques. Le test a été réalisé avec des films de petite taille (1.6cm×2.3cm). Dans le premier banc, la contrainte externe a été fournie au film en utilisant un shaker mécanique. L'agitateur est capable d'exercer périodiquement une contrainte mécanique sur le film. Cependant, la déformation obtenue était insuffisante pour rendre compte des mouvements de l'AMF. Nous avons donc développé un système mécanique spécifique, qui a permis de donner la déformation périodique du film P(VDF-TrFE) et qui a été conçu de manière à tester deux films simultanément en flexion alternée. La tension et le courant de sortie du film ont été mesurés en utilisant respectivement un oscilloscope et un pico-ampèremètre.

Afin de récupérer la charge piézoélectrique produite par le film, nous avons enfin étudié dans le chapitre 4 deux types de cartes électroniques LTC3108 et LTC 3588-1, qui peuvent fonctionner à un faible niveau de tension ou de courant d'entrée. Nous avons simulé et comparé le fonctionnement de ces deux modules dans différentes conditions en utilisant le logiciel LTSpice. Cette simulation nous a permis d'identifier celui qui correspondait le mieux à nos spécifications et nous a aidé à réaliser l'expérience en conséquence.

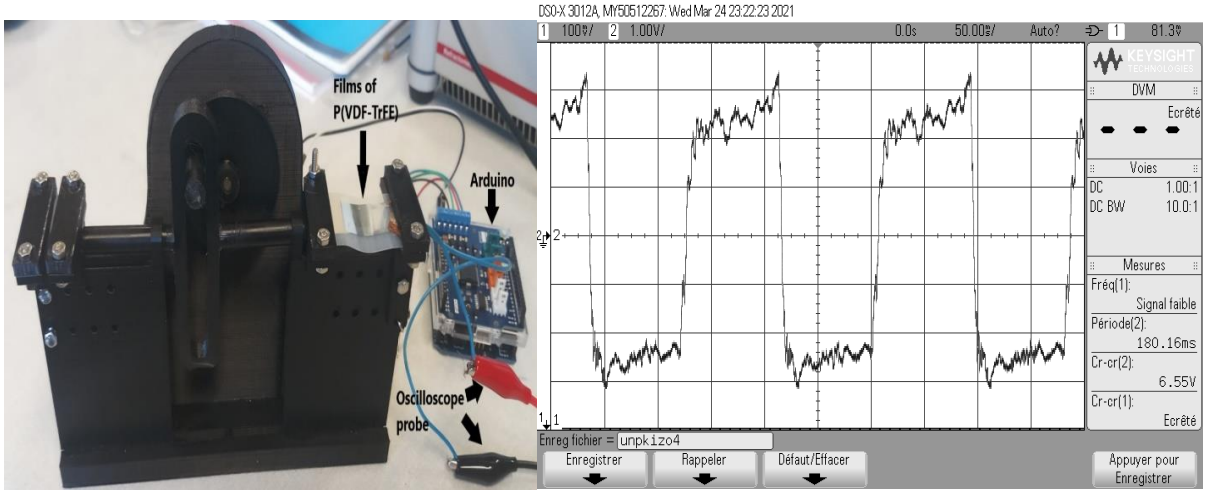

Figure 5. Le montage expérimental du système de flexion mécanique et la tension de sortie du film P(VDF-TrFE).

A partir des tests de simulation effectués, nous avons obtenu des résultats plutôt intéressants. Le module LTC3108 donne un bon fonctionnement avec une tension minimale. Cependant, il a besoin d'une valeur de courant d'entrée qui est difficile à obtenir à partir d'un film P(VDF-TrFE)

monocouche de petite taille et de faible épaisseur que nous utilisons. D'autre part, le LTC3588-1 est jugé plus adapté à nos spécifications, puisque la valeur minimale du courant d'entrée est de 2.2 µA pour une tension de 5V, ce qui devrait être facilement atteint par les futurs dispositifs multicouches. Dans ces conditions, une puissance de sortie de près de 0,7W est délivrée après un temps de chargement de 750s. Grâce à cette étude, nous avons validé les circuits de conditionnement et cela ouvre de nouvelles possibilités pour continuer ce travail avec différentes structures composites multicouches pour améliorer la puissance de sortie.

En conclusion, ce travail présente des résultats significatifs pour le développement d'un composite hybride flexible constitué d'un AMF et d'un polymère piézoélectrique. Le composite hybride sera capable de convertir l'énergie thermique en énergie mécanique qui est convertie en énergie électrique à partir de l'environnement ambiant de manière synergique. Ainsi, il pourra délivrer la charge électrique produite pour espérer alimenter l'électronique portable telle que les capteurs sans fil, les MEMS ou les NEMS de manière autonome.

Abstract

Small-scale energy harvesting to power self-powered electronic devices is tremendously increasing. In this regard, the ability to combine thermal and mechanical harvesting using smart materials pays more attention. We have presented the feasibility of using P(VDF-TrFE) piezoelectric polymer coupled with NiTi shape memory alloy (SMA) to harvest both mechanical and thermal energy in simple scalable devices. A novel multi-layered SMA-P(VDF-TrFE) composite was fabricated and carried out their electro-thermo-mechanical performance. We have designed and developed an experimental bench to perform the electro-thermomechanical characterization of the composite, allowing us to measure the piezoelectric response when it is subjected to periodic heating and cooling. Furthermore, we performed the finite element analysis of the SMA-Piezoelectric composite and simulated the main properties of SMA such as superelastic behavior, one-way shape memory effect, and two-way shape memory effect, to finally identify the overall effective electro-thermomechanical behavior of the SMA-piezoelectric polymer composite. Finally, in order to efficiently harvest the electric charge generated from the P(VDF-TrFE) film, we have studied and compared two types of integrated converters and determined the conditions for effective energy harvesting. These results are promising, which showing the feasibility of this multilayered composite to power small electronics such as wireless sensors, MEMS and biomedical devices in an autonomous way.

Keywords: Shape Memory Alloy, P(VDF-TrFE) Piezoelectric polymer, hybrid composite, energy harvesting, small scale electronic device.

Résumé

La récupération d'énergie à petite échelle pour alimenter les appareils électroniques autoalimentés se développe considérablement. À cet égard, la possibilité de combiner la récolte thermique et mécanique à l'aide de matériaux intelligents fait l'objet d'une plus grande attention. Nous avons présenté la faisabilité de l'utilisation d'un polymère piézoélectrique P(VDF-TrFE) couplé à un alliage à mémoire de forme (AMF) NiTi pour récolter à la fois l'énergie mécanique et thermique dans des dispositifs évolutifs simples. Un composite multicouche AMF-P(VDF-TrFE) a été élaboré et a démontré ses performances électro-thermo-mécaniques. Nous avons conçu un banc expérimental pour effectuer la caractérisation électro-thermomécanique du composite, permattant de mesurer la réponse piézoélectrique lorsqu'il est soumis à un chauffage et un refroidissement périodique. De plus, nous avons réalisé l'analyse par éléments finis du composite AMF/Piézoélectrique et simulé les principales propriétés du SMA telles que le comportement superélastique, l'effet de mémoire de forme unidirectionnel et l'effet de mémoire de forme bidirectionnel, pour finalement identifier le comportement électro-thermomécanique effectif global du composite AMF-polymère piézoélectrique. Enfin, afin de récolter efficacement la charge électrique générée à partir du film P(VDF-TrFE), nous avons étudié et comparé deux types de convertisseurs élévateurs intégrés, et déterminé les conditions pour une collecte d'énergie effective. Ces résultats sont prometteurs et montrent la faisabilité de ce composite multicouche pour alimenter de manière autonome de petits appareils électroniques tels que des capteurs sans fil, des MEMS et des dispositifs biomédicaux.

Mots-clés : Alliage à mémoire de forme, P(VDF-TrFE) Polymère piézoélectrique, composite hybride, récupération d'énergie, dispositif électronique à petite échelle.